JOURNAL AerospaceLab

ONERA
THE FRENCH AEROSPACE LAB

return on innovation

Issue 6
June 2013

Flow Control: the Renewal of Aerodynamics?

AL06-00 - Flow control : an Overview
E. Garnier

AL06-01 - Buffet Characterization and Control for Turbulent Wings
J. Dandois, P. Molton, A. Lepage, A. Geeraert, V. Brunet, J.-B. Dor, E. Coustols

AL06-02 - Boundary Layer Transition Control using DBD Plasma Actuators
A. Kurz, S. Grundmann, C. Tropea, M. Forte, A. Seraudie, O. Vermeersch, D. Arnal, N. Goldin, R. King

AL06-03 - Overview of Onera Actuators for Active Flow Control
F. Ternoy, J. Dandois, F. David, M. Pruvost

AL06-04 - Active Flow Control for Helicopters
A. Le Pape, C. Lienard, J. Bailly

AL06-05 - Recent Onera Flow Control Research on High-Lift Configurations
V. Brunet, J. Dandois, C. Verbeke

AL06-06 - NARX Modeling and Extremum-Seeking Control of a Separation
J. Dandois, P.Y. Pamart

AL06-07 - Closed-Loop Control of Fluid Flow: a Review of Linear Approaches and Tools for the Stabilization of Transitional Flows
D. Sipp, P. Schmid

AL06-08 - Passive Control of Cavity Flows
S. Yamouni, C. Mettot, D. Sipp, L. Jacquin

AL06-09 - Numerical and Experimental Investigations of Flow Control in Axial Compressors
J. Marty, L. Castillon, J.-C. Boniface, S. Burguburu, A. Godard

AL06-10 - The Plasma Synthetic Jet Actuator, Physics, Modeling and Flow Control Application on Separation
D. Caruana, F. Rogier, G. Dufour, C. Gleyzes

AL06-11 - Empirical Model for the Evolution of a Vortex-Pair Introduced into a Boundary Layer
T. Yehoshua, A. Seifert

AL06-12 - An Overview of Recent DLR-Contributions on Active Flow-Separation Control Studies for High-Lift Configurations
V. Ciobaca, J. Wild

ISSN: 2107-6596

Flow Control: an Overview

Eric Garnier
Research Engineer
Applied Aerodynamics Department

Current airframes being already highly optimized nowadays, further aerodynamic performance improvements may only be reached by the implementation of flow manipulation techniques. The sixth issue of Aerospace Lab Journal is aimed at providing the reader with a comprehensive overview of the current developments of these methods.

The papers presented successively review main aspects of flow control, both from the point of view of technology and that of the applications. Technologies consist not only in fluidic and plasma actuator development, but also in the specific know-how relative to closed-loop algorithms, reduced order models and actuator effect on the flow. Additionally, the potential of flow control techniques is presented on civil aircraft (both for low speed and cruise conditions), helicopters and turbomachinery applications.

A historical perspective

The beginning of the 20th century has witnessed the introduction of the seminal concept of boundary layer by L. Prandtl. The relevance of this concept was in particular shown by implementing boundary layer suction, which eventually became the first flow manipulation technique of the modern era. The investigation of blowing techniques followed in the late twenties. A theoretical step was passed in 1948 by Poisson-Quinton, who introduced the momentum coefficient and the important distinction between boundary layer control and circulation control. Concomitantly with these theoretical progresses, many applications of the circulation control concept were proposed in the fifties. This period witnessed its operational use on military aircraft and its large scale evaluation on the Boeing 707 prototype. Nevertheless, this concept suffers from its inherent complexity and added weight and, in the last fifty years, the only flow control technique routinely used, in particular on Boeing commercial airplanes, is the passive vortex generator. With the development of the stability theory and of the important idea that a flow can be supersensitive to some specific, well-chosen perturbations, flow control has been the subject of renewed interest, the general idea being that the introduction of unsteady perturbations is a much more efficient way to manipulate a flow than a steady actuation. These progresses and the current difficulties to further improve already well-optimized airframes have given a new impetus to flow control, which is now a very active research topic. The sixth issue of the Aerospace Lab Journal is aimed at making a survey of the current development in this field.

Control objective

Inherent to the idea of flow control are the notions of control objective and of the state that the flow should eventually reach. Currently, most of the effort of the community is devoted to separation control and this issue of Aerospace Lab Journal is no exception [4][5][6][9][12]. Nevertheless, keeping the flow laminar remains an important topic, which is treated in ref [2], and the reduction of the fluctuations in cavity flows is the objective of ref. [8].

Actuators & sensors

Actuators are the common denominator of all of the study presented. The development of these devices, which necessitate multi-disciplinary teams skilled in micro-technologies, has been impressive during the last decade. Paper [3] provides a comprehensive overview of fluidic actuator development at Onera. Highly innovative plasma synthetic jets are presented in ref. [10] and an example of the application of DBD actuators to transition control can be found in ref. [2]. A crucial point is that specific means must be developed, both to characterize their performance and to correctly interpret subsequent flow control experiments. Comparatively, sensors are less developed, since existing devices are sufficient for most separation control applications. Nevertheless, one can anticipate that sensor improvement will be necessary for drag reduction related applications.

Closing the loop

In order to maximize flow control efficiency, the characteristics of the perturbations introduced in the flow (frequency, flow rate, movement) must be adapted as quickly as possible. This necessitates not only sensors and actuators, but also a close-loop control algorithm in between. The theoretical basis of the control theory is presented in ref. [7]. In some cases, a model representing the relationship between sensors and actuators must be built. A possible treatment of this specific issue relying on NARX (Non-linear Auto-Regressive with eXogeneous input) modeling is proposed in ref. [6].

Simulation & Experiments

Nowadays, the evaluation of flow control concepts strongly relies on numerical simulation. It raises the issue of the way in which actuators are introduced in the simulation. The scale disparity between the individual actuator and the airframe to be controlled induces a significant additional computational cost. In practice, computations of controlled flows can be based either on a full representation of the actuator, as in refs. [1],[4],[9] and [12], or on approximated models, as in Ref [5]. The experimental basis for a new model is proposed in ref. [11]. Close-loop control is currently assessed numerically, either using Direct Numerical Simulation (DNS), as in [7], or using unsteady RANS as in ref. [6]. Even though simulation has been at the origin of significant progresses, the experimental demonstration is still indispensable to substantiate the developed flow control strategy. Examples of experimental validation of the latter can be found in references [1],[2],[4],[5],[9],[10] and [12].

Applications

The reader of this sixth issue of the Aerospace Lab Journal may be convinced that relevant flow control strategies exist for civil aircraft, both in the low speed [5][12] and the high speed flight domains [1]. Interesting perspectives have been reported for helicopters and for turbomachinery applications in refs. [4] and [9] respectively. For every aforementioned application, a global systemic analysis of the proposed control strategies must be undertaken in close collaboration with industrial partners ■

References

[1] J. DANDOIS, P. MOLTON, A. LEPAGE, A. GEERAERT, V. BRUNET, J.-B. DOR, E. COUSTOLS - *Buffet Characterisation and Control for Turbulent Wings*. Aerospace Lab Issue 6, June 2013

[2] A. KURZ, S. GRUNDMANN, C. TROPEA, M. FORTE, A. SERAUDIE, O. VERMEERSCH, D. ARNAL, N. GOLDIN, R. KING - *Boundary Layer Transition Control using DBD Plasma Actuators*. Aerospace Lab Issue 6, June 2013

[3] F. TERNOY, J. DANDOIS, F. DAVID, M. PRUVOST - *Overview of Onera Actuators for Active Flow Control.* Aerospace Lab Issue 6, June 2013

[4] A. LE PAPE, C. LIENARD, J. BAILLY - *Active Flow Control for Helicopters*. Aerospace Lab Issue 6, June 2013

[5] V. BRUNET, J. DANDOIS, C. VERBEKE - *Recent Onera Flow Control Research on High-Lift Configurations*. Aerospace Lab Issue 6, June 2013

[6] J. DANDOIS, P.Y. PAMART - *NARX Modeling and Extremum-Seeking Control of a Separation*. Aerospace Lab Issue 6, June 2013

[7] D. SIPP, P. J. SCHMID - *Closed-Loop Control of Fluid Flow: a Review of Linear Approaches and Tools for the Stabilization of Transitional Flows*. Aerospace Lab Issue 6, June 2013

[8] S. YAMOUNI, C. METTOT, D. SIPP, L. JACQUIN - *Passive Control of Cavity Flows*. Aerospace Lab Issue 6, June 2013

[9] J. MARTY, L. CASTILLON, J.-C. BONIFACE, S. BURGUBURU, A. GODARD - *Numerical and Experimental Investigations of Flow Control in Axial Compressors*. Aerospace Lab Issue 6, June 2013

[10] D. CARUANA, F. ROGIER, G. DUFOUR, C. GLEYZES - *The Plasma Synthetic Jet Actuator, Physics, Modeling and Flow Control Application on Separation.* Aerospace Lab Issue 6, June 2013

[11] T. YEHOSHUA, A. SEIFERT - *Empirical Model for the Evolution of a Vortex-Pair Introduced into a Boundary Layer.* Aerospace Lab Issue 6, June 2013

[12] V. CIOBACA, J. WILD - *An Overview of Recent DLR-Contributions on Active Flow-Separation Control Studies for High-Lift Configurations.* Aerospace Lab Issue 6, June 2013

J. Dandois, P. Molton,
A. Lepage, A. Geeraert,
V. Brunet, J.-B. Dor
E. Coustols
(Onera)

E-mail: julien.dandois@onera.fr

Buffet Characterization and Control for Turbulent Wings

The objective of this paper is to present an overview of the work performed at Onera over the last decade on the characterization and control of the buffet phenomenon. This aerodynamic instability induces strong wall pressure fluctuations and as such limits its aircraft envelope, consequently it is interesting to understand the origin of this instability and to try to delay its onset, in order to improve aircraft performance, but also to provide more flexibility during the design phase. First, results from wind tunnel tests on 2D airfoils are presented to explain the 2D buffet phenomenon and since it is used as validation test case for numerical simulations. Then, results from several wind tunnel tests on a 3D configuration are presented. The 3D buffet phenomenon is characterized using steady and unsteady wall pressure measurements and LDV. Then, several types of flow control have been investigated, either passive (mechanical vortex generators) or active (fluidic VGs, fluidic trailing-edge device (TED)). It is shown than mechanical and fluidic VGs are able to delay buffet onset in the angle-of-attack domain by suppressing the separation downstream of the shock. The effect of the fluidic TED is different, the separation is not suppressed but the rear wing loading is increased and consequently the buffet onset is not delayed in the angle-of-attack domain, but only in the lift domain. Closed-loop control of the fluidic VGs is also investigated, to adapt the mass flow rate to the aerodynamic conditions.

Introduction

The shock-wave/boundary layer interaction on the upper side of a wing at high Mach number and/or high angle of attack induces a massive flow separation, which can lead to instability. This phenomenon is a global flow instability known as "buffet" and can further lead to structural vibrations (“buffeting”). Buffet results in lift and drag variations that greatly affect the aircraft aerodynamics and, as such, limit the aircraft flight envelope, since a margin of 30% on the lift coefficient at cruising conditions must be respected by design standards.

For the last twenty-five years or so, a structured multi-disciplinary research program has been defined at Onera for addressing buffet characterization and control on, firstly turbulent airfoils, and then wings. This research program had comprised very detailed complementary experimental and numerical studies.

Two complementary devices/technologies had been developed for buffet control:

- either a "VG-type" (Vortex Generator) actuator, the effect of which is to add momentum and kinetic energy to the turbulent boundary layer which develops upstream of the shock and the induced separation, in order to suppress, or at least to delay, the appearance of separated unsteady flows, which is at the origin of the buffet phenomenon;
- or a "TED-type" (Trailing Edge Device/Deflector) actuator, which behaves as a trailing edge, or cambered trailing edge, by increasing the rear loading of an aerofoil and then postponing the buffet onset at a higher lift coefficient.

Thus, several reports and publications have been made for 2D rigid airfoils ([1]-[3] [7]-[8], [11]-[12], [15]-[17]). In particular, the efficiency of a closed-loop approach using mechanical “TEDs” was shown, the control laws being extracted from a semi-empirical model [8]. Furthermore, very few studies were made for 2.5D ([2], [15] or [17]) or 3D transonic wings [5]; early attempts of control via mechanical TEDs in open-loop have not been very successful for a 3D wing [8], as yet. These aforementioned studies referred mainly to mechanical devices.

Therefore, a new joint Onera research project was launched at the beginning of 2007, aimed at addressing buffet studies on 3D turbulent wings [9]. The focus was to investigate buffet control via the use of fluidic devices, which should be easier to handle than “mechanical TEDs for closed-loop” control applications. In parallel to this research project, the EU-funded AVERT “Aerodynamic Validation of Emission Reducing Technologies” project, coordinated by Airbus Operations

Ltd, was launched in January 2007. For high speed technologies, demonstration tests were focused on buffet control and were performed on a 3D half wing/fuselage body at the Onera S2MA facility, in March 2010 [10]. Thus, the efficiency of delaying the buffet onset was shown using an open loop approach, with either fluidic VG or fluidic TED, at constant flow rate. The main characteristics of fluidic VGs and TED were defined by Onera and LEA Poitiers, respectively.
Later on, Onera pursued buffet investigations on a 3D wing, the geometry of which being similar to that of the model tested at the Onera S2MA wind tunnel, but adapted to fit in the test section of the "research-type" Onera S3Ch wind tunnel [6], [14]. Flow topologies on both wings – either at the S3Ch or at the S2MA wind tunnel – were very consistent at the buffet onset and beyond. Blowing at rather large values of constant flow rates was applied for different angles of attack, at a Mach number close to 0.815; furthermore, various pulsed flow rates (duty cycle = 0.5) at frequencies in the range 100 to 500 Hz, were investigated for strong buffet conditions.

Later on, within the framework of the Clean Sky SFWA-ITD (Smart Fixed Wing Aircraft – Integrated Technology Demonstrator), complementary high-speed tests were carried out on the 3D turbulent wing at the Onera S3Ch wind tunnel, using fluidic devices at continuous and pulsed flow rates. First of all, the open loop approach was applied at relatively low values of constant flow rates, for several fluidic VGs conditions. Then, a closed loop approach was applied by establishing a feedback between the fluidic VG opening and:

- Either the r.m.s. value of an unsteady pressure sensor close to the trailing edge;
- Or, the average value of the shock position, estimated from 10 unsteady pressure sensors that were monitored continuously, in order to estimate the shock location in real time.

Last, but not least, within the framework of the Onera joint research project [9], closed loop control using fluidic VGs or fluidic TEDs was applied rather recently, at the beginning of 2012, on the 3D half wing/fuselage body at the Onera S2MA wind tunnel. The results are currently under analysis and are not mentioned in this review paper.

There is a huge amount of literature on the control of the shock/boundary layer interaction. The control methods can be gathered into two main categories. In the first category, the objective is to weaken the shock by splitting it to have a bifurcated λ shock structure. Several studies over the last decade have examined passive control devices to bring about the modified shock pattern: a cavity covered with a perforated plate [20], grooves and stream-wise slots [21]-[22] underneath the shock foot. These various concepts have led to moderate success, the reduction in wave drag being sometimes outweighed by viscous penalties [23]. This can be alleviated by using active devices, such as boundary layer suction through a slot, but these devices require auxiliary equipment, which offsets any drag reduction benefits [24]-[25]. A promising method to lower the total pressure loss through the shock system is the control by a bump. In the beginning, 2D-shape bumps were investigated and led to significant wave drag reductions with moderate viscous penalties, but were found to perform very badly under off-design conditions [25]-[26]. More recent studies were performed with 3D bumps, which have a limited spanwise extent, to enhance the off-design performance [27]-[29]. The λ shock structure has been found to propagate between the bumps, giving total pressure decreases across the span. Moreover, streamwise vortices developed along the bump sidewalls have a beneficial effect on the downstream boundary layer behavior, rendering this passive control device as a promising concept.

The second category is aimed at energizing the boundary layer upstream of the shock, making it more resistant to the adverse pressure gradient and consequently less likely to separate downstream of the shock. Mechanical vortex generators [30]-[36], fluidic vortex generators and synthetic jet fall in this category. Previous studies done at Onera [37] have shown that mechanical VGs are able to delay the buffet onset to higher angles of attack. However, even though they have shown their efficiency for buffet onset delay, mechanical vortex generators have the drawback of increasing drag under nominal cruising conditions. This is the reason why fluidic VGs, which can be turned off, are also investigated. Moreover, they can be used in a closed-loop strategy to optimize the flow control and consequently to reduce auxiliary equipment for actuation, which is an important constraint for aircraft manufacturers. Concerning these fluidic VGs, they have mostly been studied to control the shock/boundary layer in internal flows [38]-[41], but there are also few papers on 2D airfoils [42]-[44].

This review papers is aimed at providing the main outcomes from all these experimental tests, as well as from the computational investigations performed from the high-quality database generated through all of these afore-mentioned testing campaigns.

Buffet Characterization: Experiments and Simulations

2D Turbulent Airfoil

First, the buffet phenomenon has been investigated on a 2D airfoil. The study was carried out in the continuous closed-circuit transonic S3Ch wind tunnel of the Onera Meudon Center. This facility has a test section size of 0.78 × 0.78 × 2.2 m. The upper and lower walls are flexible, so as to reduce wall interferences near the model, the adaptation technique being based on a steady flow hypothesis [14]. The side walls are equipped with Schlieren quality windows. The experimental arrangement is shown in figure 1. The model is an OAT15A profile with a relative thickness of 12.3%, a chord length c = 230 mm, a span of 780 mm (which gives an aspect ratio of 3.4) and a thick trailing edge of 0.5% of the chord length. The central region of the profile is equipped with 68 static pressure orifices and 36 unsteady Kulite pressure transducers.

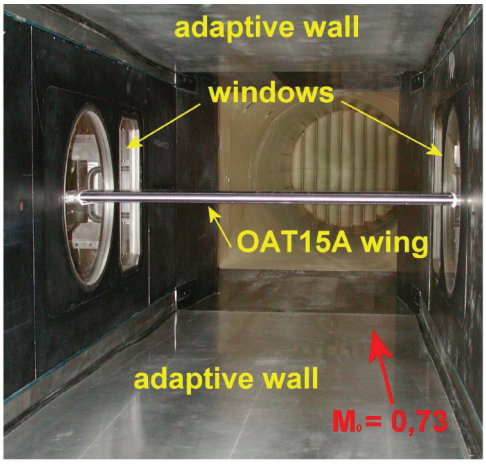

Figure 1 - OAT15A supercritical profile in the S3Ch transonic wind tunnel

Schlieren films were recorded using a high-speed camera allowing acquisitions of 1000 frames per second, which means 14 images per period since the shock oscillation frequency is 70 Hz (see figure 5). The exposure time is set equal to 1.9 10^{-6} s or 1.3 10^{-4} the oscillation period. Examples of pictures obtained for $M_0 = 0.73$ and $\alpha = 3.5°$ are shown in figure 2 (these conditions are those of the other investigations presented next). The two pictures correspond to the most upstream (red upward pointing arrow) and downstream locations (green upward pointing arrow) of the shock during its oscillation for these conditions. The wave observed upstream of the field is due to the transition triggering strip. Its apparent importance is amplified by the spanwise integration of light deviation, which tends to magnify the image contrast. In reality, surface pressure measurements showed that the variations of the flow conditions across this wave were negligible. The picture in figure 2a reveals a lambda-shaped region typical of the transonic shock wave/boundary-layer interaction with a shear layer (in white), which develops along the slip line originating from the lambda structure triple point. The separated boundary layer above the profile, behind the shock (in black), is also visible. When the shock wave moves upstream, the separation size increases, as well as the corner flow separation on each side wall. Deformations of the shock surface associated with these corner flows are visible in figure 2a, when the shock is at its most upstream location.

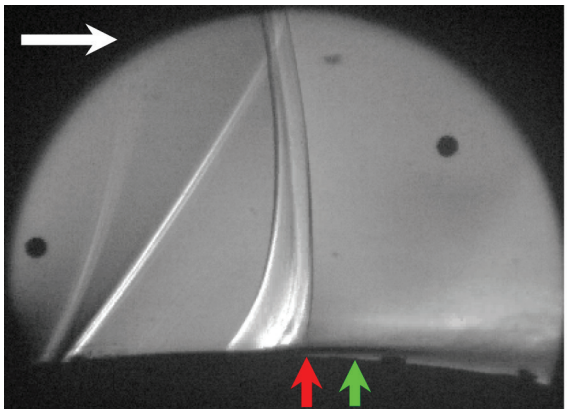

a) Shock most upstream location

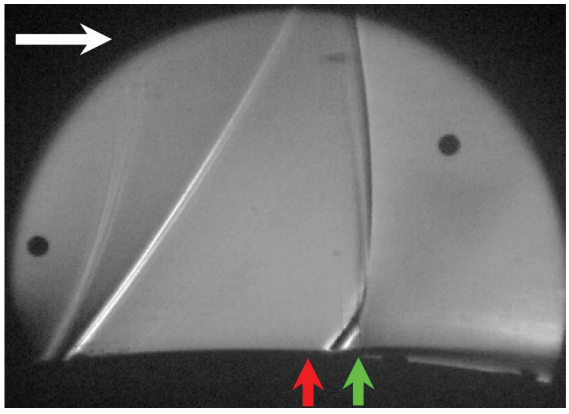

b) Shock most downstream location

Figure 2 - Instantaneous Schlieren pictures for $\alpha = 3.5°$, $M = 0.73$
(a) Shock most upstream location, (b) Shock most downstream location

The oil flow visualization in figure 3 reveals that the time-averaged shock remains parallel to the leading edge on nearly 80% of the wing. Flow deviations are apparent in the lateral wall region. These corner flow separations, which are due to interactions with the side wall boundary layers, remain confined to nearly 10% of the profile span at each end.

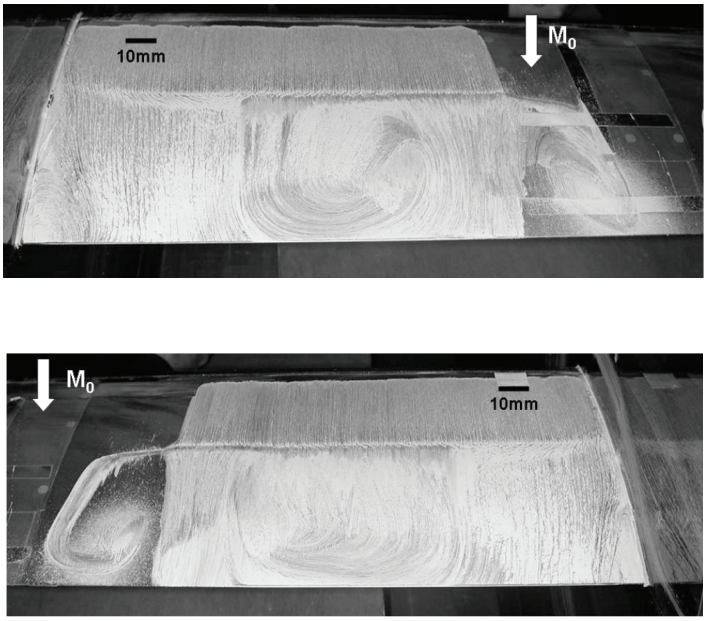

Figure 3 - Oil flow visualization of the upper surface of the wing for $\alpha = 3.5°$, $M = 0.73$, viewed from downstream: a) left side, b) right side. The center region of the airfoil is free from oil flow.

Figure 4 shows the distributions of the wall pressure coefficient Cp measured for $M_0 = 0.73$ and four incidence angles ($2.5 < \alpha < 3.9°$). As shown in this figure, a supercritical profile is characterized by a pressure plateau preceding the compression due to the shock. For $\alpha = 2.5$ and 3°, the shock remains steady (no buffet) and is located at $x/c = 0.48$. The shock starts to oscillate for $\alpha = 3.5°$, with a maximum upstream excursion detected at $x/c = 0.3$ for $\alpha = 3.9°$. The spreading of the recompression region in figure 4 results from the temporal integration of flow intermittency during shock oscillation. Note also that the pressure decreases at the trailing edge when α increases, which corresponds to an increase of the separation extending from the shock foot to the trailing-edge.

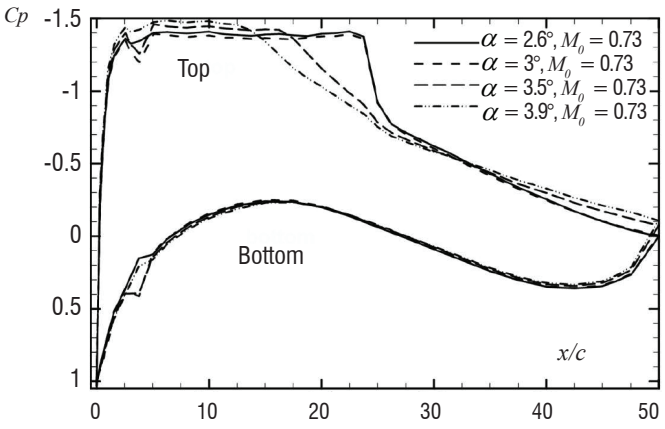

Figure 4 - Time-averaged wall pressure coefficient

Power spectra obtained with the unsteady pressure transducer located at $x/c = 0.45$ are plotted in figure 5 for $\alpha = 3$, 3.1, 3.25, 3.5, 3.9°. The frequency resolution was set to 1/3 Hz. For $\alpha = 3°$, the shock is stable, the signal energy remaining low and distributed over all frequencies. However, a bump can be detected between 40 and 95 Hz, the amplitude of this bump increasing for $\alpha = 3.1°$ with a peak emerging at 70 Hz, together with its first harmonic. This peak corresponds to the buffet frequency, as shown by the curves obtained at higher incidences ($\alpha = 3.25$ and 3.5°). Beyond buffet

onset, the spectra are marked by high harmonics and by background turbulence. One can note that the energy background overshoots for $\alpha = 3.25°$ before settling down to a lower level for higher incidences.

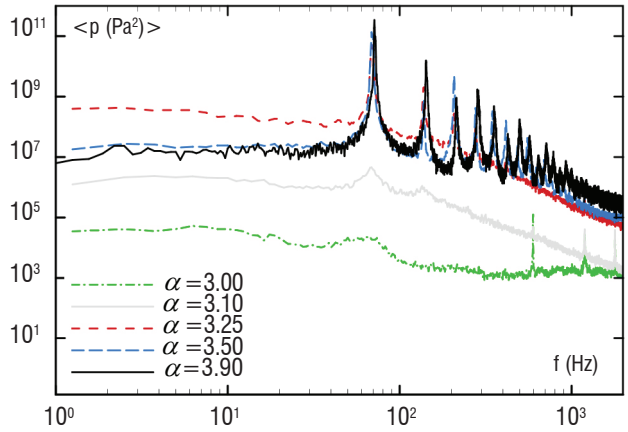

Figure 5 - Influence of the incidence on the pressure power spectrum at $x/c = 0.45$ ($M = 0.73$)

This experimental test case has been computed by several numericists at Onera with various levels of turbulence modeling: in URANS by Deck [11] and Brunet [1][3], in ZDES by Deck [11] and Brunet et al. [4] and in LES by Garnier & Deck [12].

3D Turbulent Wings

First, it appears important to define the buffet onset limit to answer, for example, the question of how much this limit has been delayed using flow control. The buffeting is the dynamic structural response to the aerodynamic buffet excitation. The buffeting limit during flight tests corresponds to a value of the acceleration measured at the pilot seat. However, in wind tunnel tests, since the dynamic response of the model structure is different from a real aircraft, new definitions of the buffeting onset must be defined. There are global criteria (based on the kink in the lift curve, the divergence of RMS value of C_L or the RMS value of the accelerometers, etc.) but also local criteria (based on the divergence of the Cp value at the trailing edge, the RMS value of the pressure, etc.).

The main problem with the local criteria is that they may be inappropriate for the case, for example, where the spanwise spacing of the fluidic VGs is varied and where there will be attached and separated zones, depending on the spanwise section. Figure 6 shows an example of the application of three criteria on a 3D configuration without control at $M = 0.82$ and $Pi = 0.6$ bar. In this case, all criteria are in a good agreement with a buffet onset angle of attack equal to 3° ±0.1°, but the starting point of divergence of the r.m.s. pressure curve is very subjective.

Before being performed in an “industrial-type” wind tunnel, tests have been carried out in the S3Ch wind tunnel of the Onera Meudon Center. The objective of this test was to assess the efficiency of the fluidic VGs, by comparison with a more classical solution based on mechanical VGs. The experimental set-up is shown in figure 7. The model is composed of a swept wing attached on a half-fuselage. This model was designed during the $BUFET'N\ Co$ project and most of the wing is based on the supercritical OAT15A airfoil. The swept angle at the leading edge is equal to 30°. The wing twist was adapted to ensure a constant pressure along the span under cruising conditions, as well as a shock parallel to the leading edge. Due to the significant confinement of the model in the wind tunnel test sections, all wind tunnel walls were taken into account during the design phase of the model in CFD. From root to tip, the chord varies between 240 mm and 200 mm over a span of 704 mm. In the end, no separation at the wing root was ensured using adapted profiles and twist in that region.

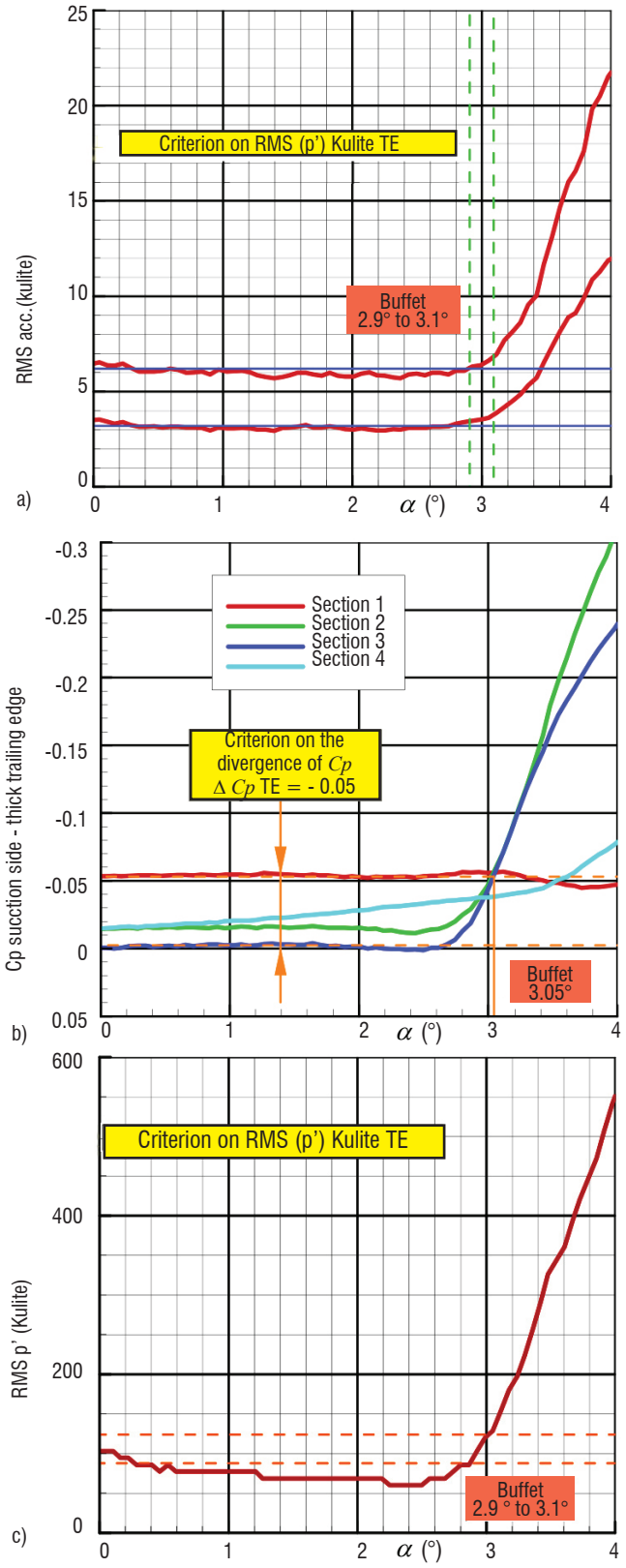

Figure 6 - Comparison of the different buffet entry criteria based on:
a) RMS value of accelerometer, b) Cp at the trailing-edge, c) RMS value of pressure

Figure 7 - Experimental set-up in the S3Ch wind tunnel

Oil flow visualization for $\alpha = 2.8°$, 3° and 3.5° at $M_0 = 0.82$ on the upper side of the model are shown in figure 8. The trace of the shock wave at the wall is clearly visible, as well as the supersonic region upstream. It starts at about 20% of the root and extends over 92% of the span. At $\alpha = 2.8°$ (figure 8 (top)), before buffet onset, there is no separation even though the skin friction lines start to be parallel to the trailing-edge at $y/b = 50$ and 60%. At $\alpha = 3°$ (figure 8 (center)), at buffet onset, a small separated zone is visible between 55 and 75% of the span and on 25% of the chord. Indeed, oil comes from the lower side of the model and goes backwards towards the shock foot. The shock is also located more upstream compared to $\alpha = 2.8°$. At $\alpha = 3.5°$ (figure 8 (bottom)), these conditions correspond to a well-established buffet regime. Downstream of the shock foot, the flow is fully separated. The massive separated flow extends from the foot shock up to the trailing edge of the wing.

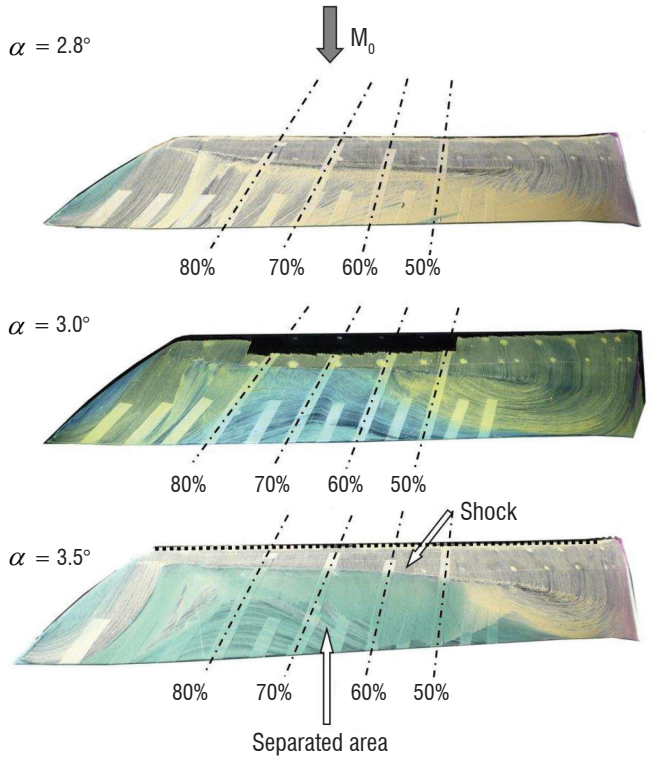

Figure 8 - Oil flow visualization for the uncontrolled case $\alpha = 2.8$, 3 and 3.5°, $M_0 = 0.82$

The wall pressure coefficient distributions for $\alpha = 2.5$, 2.6, 2.8 and 3° at $y/b = 0.7$ are plotted in figure 9. The appearance of the flow separation at the trailing-edge of the model is marked by the divergence of the pressure from the previous angles-of-attacks and by the displacement of the shock in the upstream direction. Figure 9 shows that these conditions are fulfilled for $\alpha = 3°$, which corresponds to the buffet onset. Then, like for the 2D configuration in "2D turbulent airfoil", the higher the angle-of-attack, the lower the pressure at the trailing-edge is.

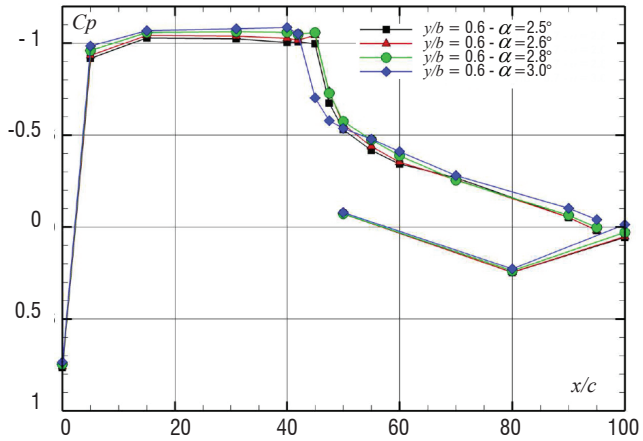

Figure 9 - Wall pressure distributions at $y/b = 0.7$ for the uncontrolled case $\alpha = 2.5$ to 3.0°, $M_0 = 0.82$

The unsteady aspects of the buffet phenomenon are analyzed from pressure measurements obtained by the Kulite sensors at $y/b = 0.6$. The Strouhal number (St) is defined by

$$St = \frac{f.c_m}{U_0},$$

where f is the frequency, c_m is the mean aerodynamic chord length and U_0 is the freestream velocity.

The results are presented for four sensors located respectively at $x/c = 0.45$ (at the shock foot) and $x/c = 0.5$, 0.6 and 0.7 downstream of the shock in the separated area. The sampling frequency is equal to 20 kHz ($St = 16$) and the length of the signal is 4 s. The number of overlapping blocks is 163, which results in a 20 Hz ($St = 0.016$) resolution frequency. The results (figure 10) show the power spectral density (PSD) of the pressure signal as a function of the Strouhal number.

At $x/c = 0.45$, in the shock displacement region, there is a significant increase of the PSD and one can note the presence of a bump on the PSD between $St = 0.2$ and $St = 0.6$. It is important to note that this is the typical signature of the 3D buffet phenomenon at the shock foot. The 3D buffet has a completely different characteristic than the 2D buffet, which is characterized by well-marked peaks in the spectra (see figure 5).

Downstream from the shock, at $x/c = 0.6$, the energy level in the signal is lower than at the shock foot. Then, the PSD level increases with x/c. The Strouhal number bump remains, but is less clear than at the shock foot and its center of mass seems to be shifted to lower frequencies.

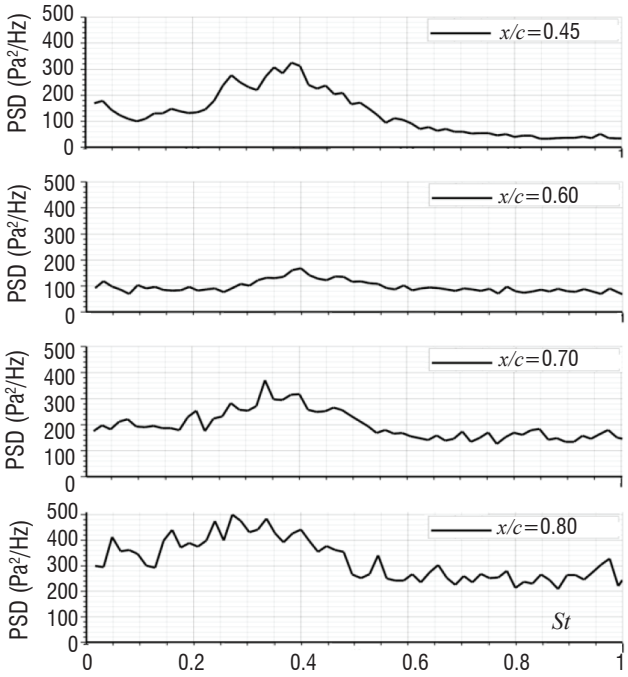

Figure 10 - Pressure spectra at $Y/b = 0.6$ for the uncontrolled configuration – $\alpha = 3.5°$, $M_0 = 0.82$

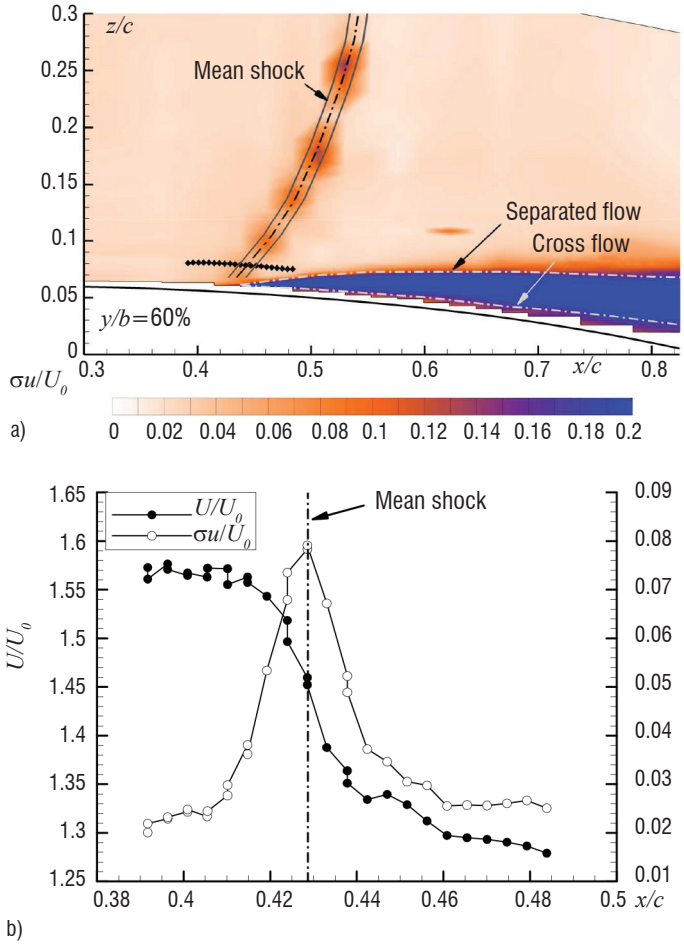

Figure 11 - Uncontrolled configuration $\alpha = 3.5°$, $M_0 = 0.82$ - Estimation of the shock oscillation amplitude at $y/b = 0.6$ - (a) LDV iso-contours of RMS longitudinal velocity, (b) time-averaged and RMS longitudinal velocity distributions

Figure 11a presents fields of root-mean-square (RMS) values of the longitudinal velocity, obtained by LDV 3C measurements in the plane $y/b = 0.6$ ($\sigma u/U_0$: RMS of the longitudinal velocity, non-dimensionalized by the free stream velocity). The average location of the leading shock is represented by a dash-dot line. These results show two regions of high RMS values. The first one is around the time-averaged shock location, the second one is in the separated region. The maximum velocity fluctuations are concentrated in the mixing layer above the separated zone, where large vortex structures are present. Below this second region, the backflow characterized by the oil flow visualization exhibits a small level of RMS values. This result confirms the unsteady wall pressure measurements in this region. Indeed, fluctuations levels are smaller than at the separation point.

The unsteadiness of the shock location can be characterized by high fluctuation levels of the axial component of the velocity at the crossing of the shock. The regions of high RMS values are represented by the gray lines around the time-averaged shock position. This behavior is explained partly by a strong deceleration of the flow at the crossing of the shock, on the one hand and by the shock unsteadiness, on the other hand.

Measurements along a line across the shock (gray dots) are performed to quantify the shock displacement (see figure 11a). A large number of samples (one million) have been acquired to insure statistical convergence. For each position, it is possible to compute histograms for each component of the velocity. Figure 11b shows the change in the longitudinal velocity and its fluctuation along this exploration line. The decrease of the axial velocity extends over 4% of the chord, which is very limited compared to the one on a 2D profile. The velocity fluctuation profile has a maximum at the average shock position.

This test case has been computed in ZDES by Brunet & Deck (see [5] for more details on the numerical method). The mesh size is 190.10^6 cells. Figure 18 shows a Q-criterion iso-surface of the instantaneous flow.

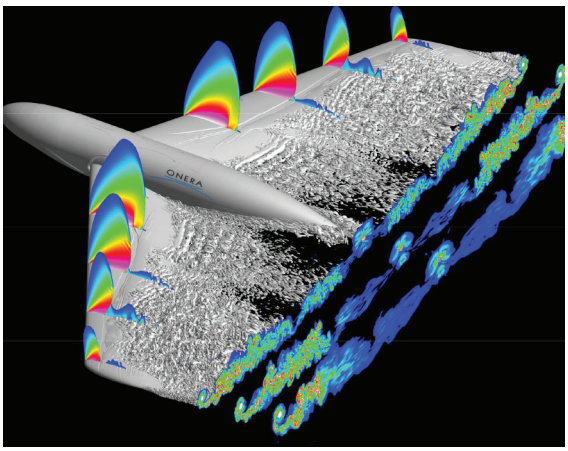

Figure 12 - Q-criterion iso-surface $\alpha = 3.5°$, $M_0 = 0.82$

Then, after these first validation tests, wind tunnel test have been performed in the S2Ma wind tunnel of the Onera Modane-Avrieux Center. This wind tunnel allows larger models to be tested. Moreover, it is equipped with a balance, which enables to study the buffet onset by varying the angle of attack of the model.

Figure 13 shows the AVERT model in the S2Ma wind tunnel. The half-model geometry consists in a wing, a fuselage and a peniche. The wing cross-section geometry is based on the OAT15A airfoil, as for the S3Ch model in figure 7. The wing span is larger (1.225 m) and the sweep angle is the same (30°). The chord length is 0.450 m at the wing root and 0.225 m at the wing tip. The mean aerodynamic chord is 0.3375 m.

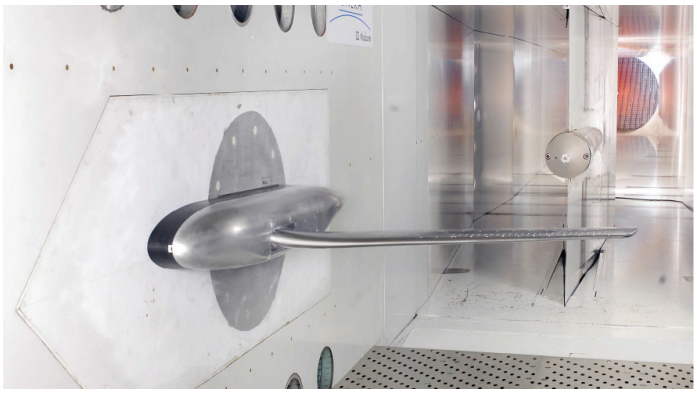

Figure 13 - AVERT model in the S2MA wind tunnel.

First results are provided from oil-flow visualizations at different angles of attack (figure 14). When increasing the angle of attack up to 2.5°, the wall flow is fully attached. At $\alpha = 3.5°$, there is some separated flow between 42.5% and 82.5% of the spanwise extent; indeed, the flow from the lower side is contaminating the upper side (figure 14(b)). For higher angles of attack, the separated areas increase greatly. Thus, it can be guessed that the buffet onset corresponds to an angle of attack of between 2.5° and 3°, which is fully consistent with the divergence of the r.m.s. pressure curve in figure 6, which comes from this wind tunnel test.

Pressure distribution curves are provided in figure 15, for a Mach number of 0.82 and a stagnation pressure of 0.6 bar. Considering, for instance, the spanwise section $y/b = 72.5\%$, when the angle of attack increases up to 2.5°, the shock position is moving backwards and the supersonic "plateau" level ahead of the shock increases. Then, from 3.0°, the shock is moving upwards while the "plateau" level still increases and separation occurs just upstream of the trailing edge with a more pronounced effect at 3.5°. These pressure distributions are fully consistent with the onset of buffeting recorded from either oil-flow visualizations or r.m.s. curves. These observations are valid also at the internal spanwise section ($y/b = 55\%$).

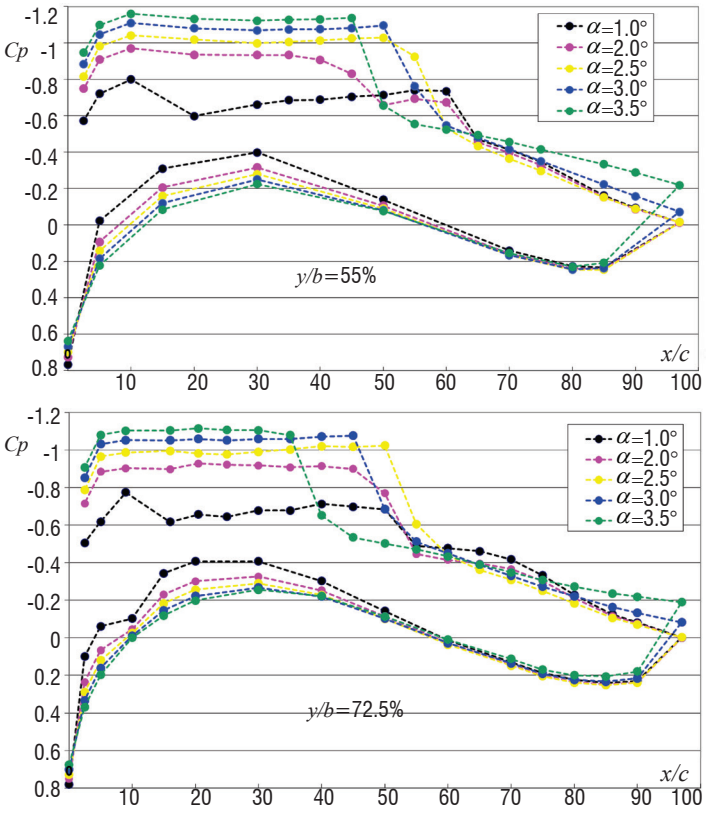

Figure 15 - Wall pressure distribution for different spanwise section and different angles-of-attack (M=0.82, Re_c=2.83 10⁶)

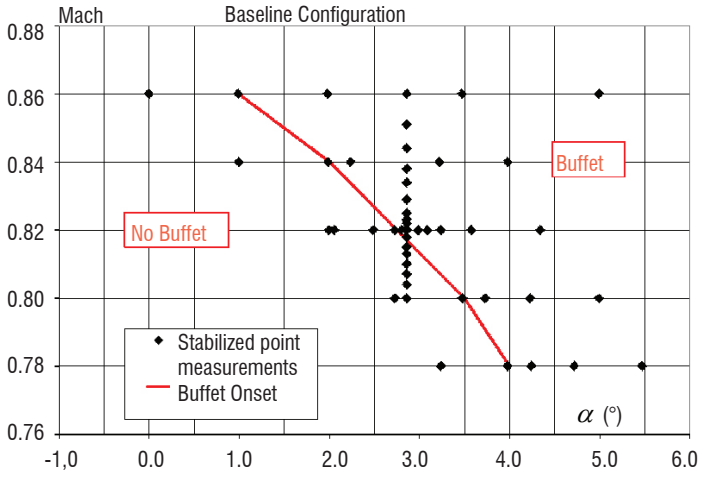

Figure 16 - Buffet appearance limit in the ($M - \alpha$) plane

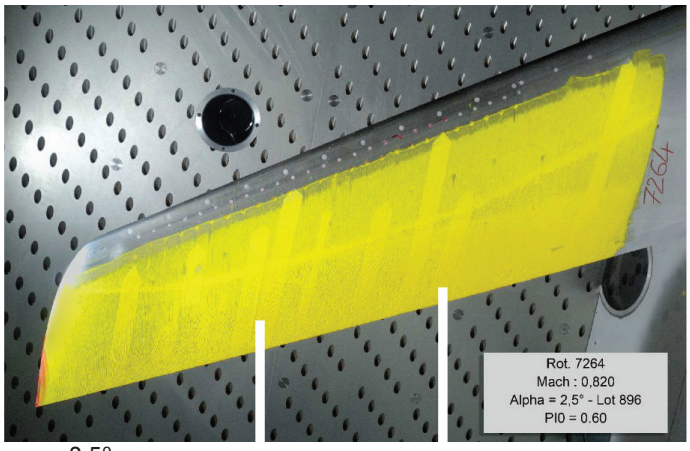

a) $\alpha = 2.5°$

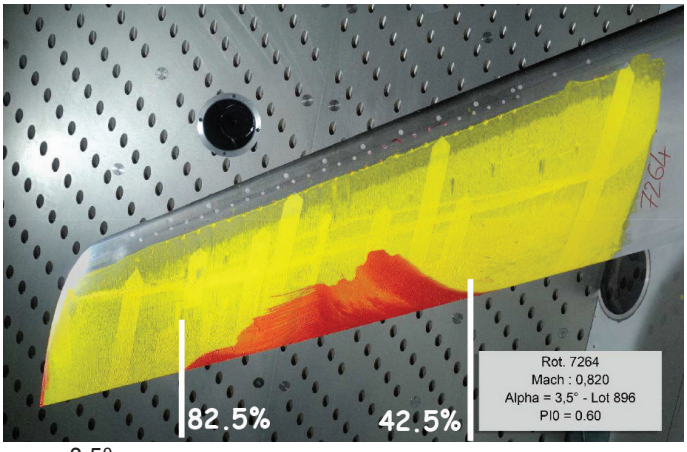

b) $\alpha = 3.5°$

Figure 14 - Oil flow visualizations of the baseline for different angles-of-attack (M=0.82, Re_c=2.83 10⁶)

To summarize, figure 16 shows the buffet onset in the (Mach, Angle of Attack) domain for the baseline configuration at $Pi = 0.6$ bar in the S2Ma wind tunnel.

Buffet Control: Open Loop Approach for 3D Turbulent Wings

Mechanical VG

As explained in the section "Buffet Characterization: Experiments and Simulations", the first objective was to define a reference configuration with control, in order to compare the efficiency of fluidic VGs. It is well known that mechanical VGs are able to postpone buffet onset, so they have been chosen as a reference. Since the wing is swept, only co-rotating VGs are considered here. The VGs, whose vertices are located at 20% of the chord, consist in 27 small triangles with a height $h = \delta = 1.3$ mm and a length equal to 5 h. Their skew angle has been defined using numerical simulations [18] and is equal to $h = 30°$ with respect to the freestream direction (and so $\beta = 0°$ with respect to the leading edge normal). The first VG is located at 51% of the span (b), the last one at 89%, and the spacing between the VGs is 1.7% of the span ($\lambda = 12\ h$).

Figure 17 shows an oil flow visualization of the controlled configurations with mechanical VGs. By comparing against figure 8, one can observe that flow separation has been suppressed over most of the wing span, except between $y/b = 0.5$ and 0.6 where a recirculation zone remains. Let us recall that VGs are only located at between 50% and 90% of the span, which leaves the first half of the wing uncontrolled and prone to separation, like for the baseline. Just downstream of the VGs, an interesting 3D flow pattern can be observed in the shock foot region and the footprint of the longitudinal vortices (darker lines normal to the leading-edge) created by the mechanical VGs. These vortices deform the shock along the span leading to a very complex but almost periodic 3D shock / vortices interaction.

This test case has also been computed by Dandois et al. [18]. Figure 18 shows a Q-criterion iso-surface ($Q = 100 U_\infty^2 / h^2$) colored by the Mach number and the separated zone (in black) for the fine grid. The streamwise vortices created by the co-rotating mechanical VGs are clearly visible. A small separated zone (in black) at between 20 and 50% of the span remains as observed in figure 17 (in green). The small separated zones at the shock foot between the streamwise vortices observed in the experiment are also visible. Figure 18 also shows the wall pressure distribution for the controlled flow with mechanical VGs. If the mesh is sufficiently refined in the wake of the VGs, the agreement between the numerical simulation and the experimental data is very good. The shock location, as well as the pressure level downstream, are very well predicted.

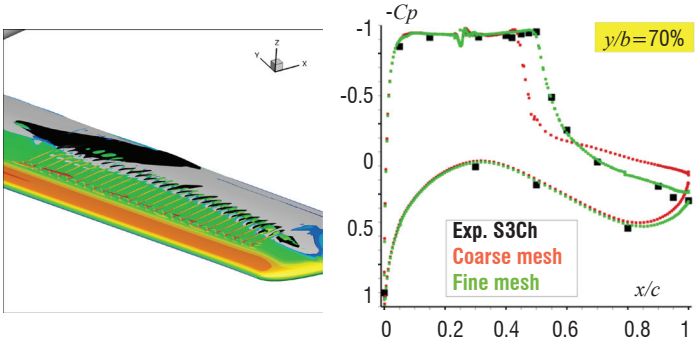

Figure 18 - Q-criterion iso-surface ($Q = 100 U_\infty^2 / h^2$) colored by Mach number and separated zone (in black) and comparison of wall pressure distributions between experiment and RANS computation

Fluidic VG (continuous flow rate)

On the S3Ch model, a cover with 40 co-rotating fluidic VGs has been manufactured to try to reproduce the effect of the mechanical VGs, with the advantage of being able to activate them only when they are necessary. The fluidic VGs consist in small nozzles with a conical shape and a supersonic exit flow at $M_{SVG} = 2$. The exit diameter of the nozzles (d) is equal to 1 mm and the pitch angle (defined between the jet direction and the local wall tangent, see figure 19 (left)) is $\alpha = 30°$. The 40 continuous fluidic VGs are located at between 53 and 82% of the span, with a spacing equal to 0.85% of the span ($\lambda = 6$mm). A different cover with 25 pulsed fluidic VGs has also been manufactured. They are located at between 50 and 84% of the span with a spacing equal to 1.63% of the span ($\lambda = 11.5$mm).

The orientation of the jets with respect to the leading edge of the model β being an important parameter, it has been studied numerically (Dandois et al. [18]), in order to define the most interesting skew angles to be tested. Thus, on the S3Ch model, two skew angles for continuous fluidic VGs have been tested: $\beta = 30°$ and 60° (and are named VGF4 and VGF5 respectively) and one for the pulsed fluidic VGs: $\beta = 60°$ (named VGFp). These pulsed fluidic VGs consist in Onera home-made piezoelectric actuators supplied with compressed air and driven by an electric square signal. They are located at 23% of the chord.

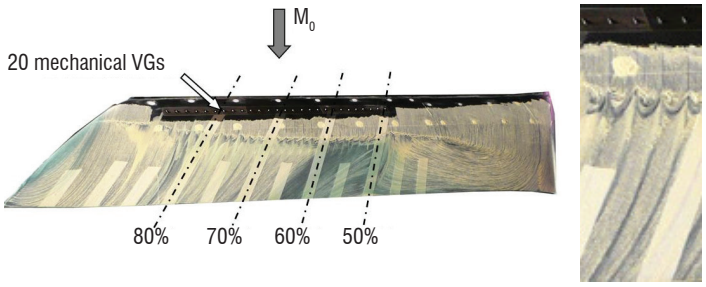

Figure 17 - Oil flow visualization with mechanical VGs (left) and zoom at y/b=75% (right) ($\alpha = 3.5°$, $M_0 = 0.82$)

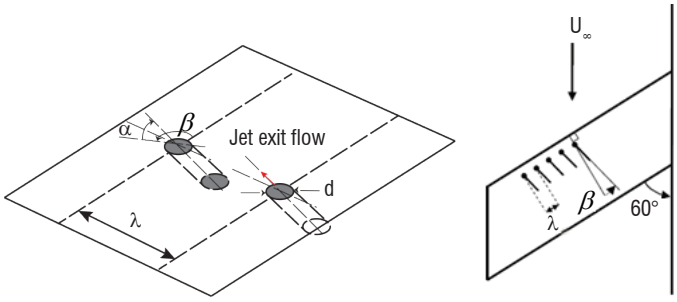

Figure 19 - Sketch showing the definitions of the main parameters of the fluidic VGs

For the fluidic VGs, the momentum coefficient Cμ is defined by:

$$C_\mu = \frac{\rho_j S_j U_j^2}{\frac{1}{2}\rho_0 S U_0^2} = \frac{q_m U_j}{\frac{1}{2}\rho_0 S U_0^2}$$

where ρ_j and U_j are respectively the density and velocity of the jets (time-averaged in the pulsed blowing case), S_j the sum of all of the orifice surface area based on the hole diameter (not the projected surface) and q_m is the mass flow rate (time-averaged in the pulsed blowing case). When the flow at the exit of the nozzles is supersonic, the Mach number ($M = 2$) and thus U_j are fixed and only the mass flow rate continues to increase with the air supply stagnation pressure. The variables ρ_o and U_0 are, respectively, the freestream density and velocity of the main flow, the wing area corresponding to a half span being denoted by S.

Figure 20 shows a comparison of the Cp distributions at $y/b = 0.7$ between the baseline, mechanical and fluidic VGs configurations. This spanwise section is representative of the most separated region on the upper wing. The results show that the control effect on the pressure plateau level upstream of the shock is negligible. The shock location has been shifted more downstream on the wing, at around $x/c = 0.55$, because of the separation alleviation for all controlled cases. The shock seems to be located more downstream in the fluidic VGs case than for the mechanical VGs. For this value of the momentum coefficient C_μ, which corresponds to a saturated effect of the fluidic VGs, the skew angle β seems to have no effect on the wall pressure distribution.

The RMS pressure chordwise distributions at $y/b = 0.6$ (only section equipped with Kulite sensors) of the clean and controlled configurations are compared in figure 21. The RMS values are computed on a signal length of 4s. For the three controlled configurations, the maximum level corresponding to the crossing of the shock is located at about $x/c = 0.55$. More downstream, the pressure fluctuation levels are lower in all controlled configurations than for the baseline. This confirms that unsteadiness in the separated region has been damped with either passive or active control. One can also note that the lowest levels are obtained by fluidic VGs. However, pressure fluctuation levels at the shock location are greater in the controlled cases than for the baseline, because the shock is located between two sensors for the baseline (see the shock position in figure 21) and consequently the peak is not visible in the figure. As for the Cp distribution, there is no significant effect of the skew angle of the fluidic VGs on the RMS pressure distributions.

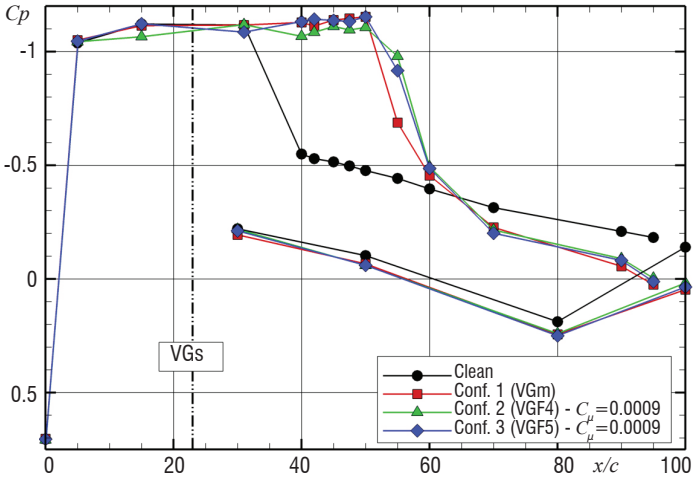

Figure 20 - Effect of the fluidic VGs mass flow rate on Cp distributions at $y/b = 0.7$ - $\alpha = 3.5°$, $M_0 = 0.82$

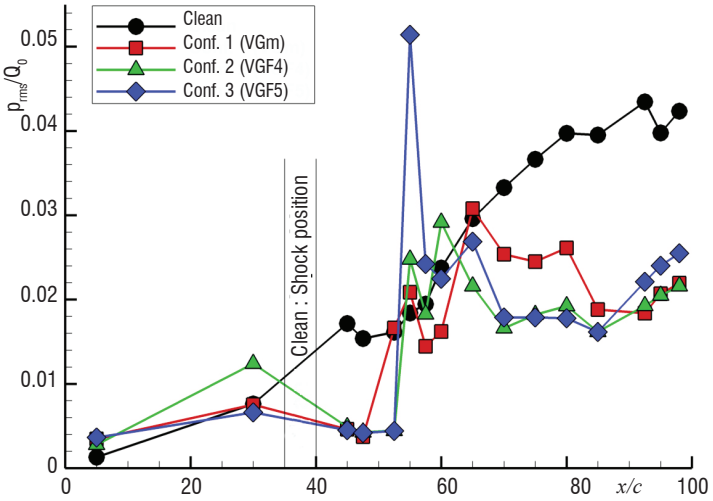

Figure 21 - Comparison of RMS pressure distributions at $y/b = 0.6$ $\alpha = 3.5°$, $M_0 = 0.82$

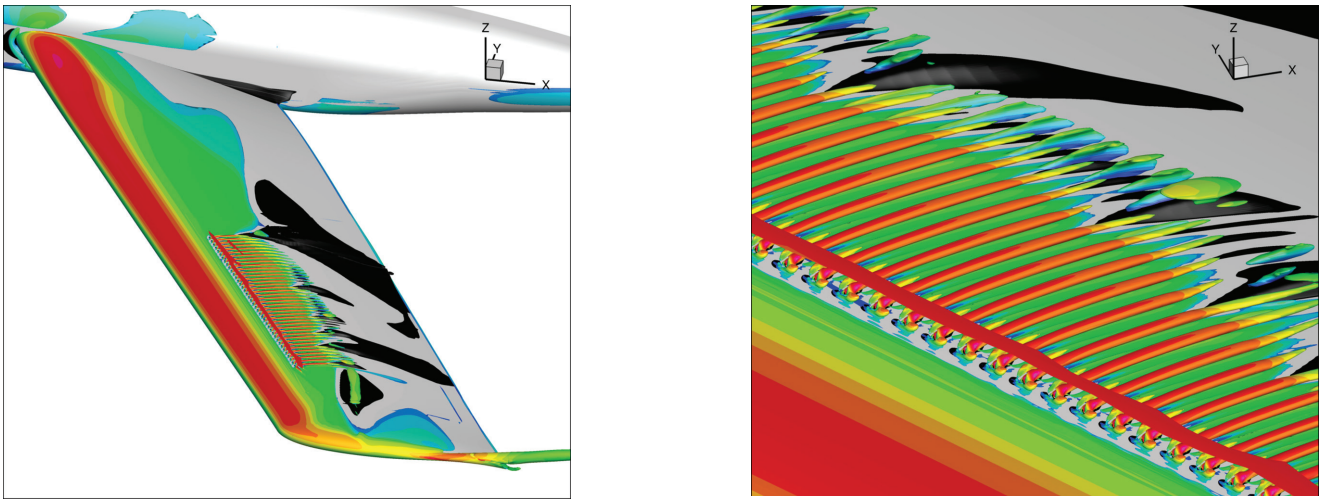

Figure 22 - Q-criterion iso-surface ($Q = 100 U_\infty^2 / h^2$) colored by the Mach number and separated zone (in black) showing the streamwise vortices created by the co-rotating fluidic VGs

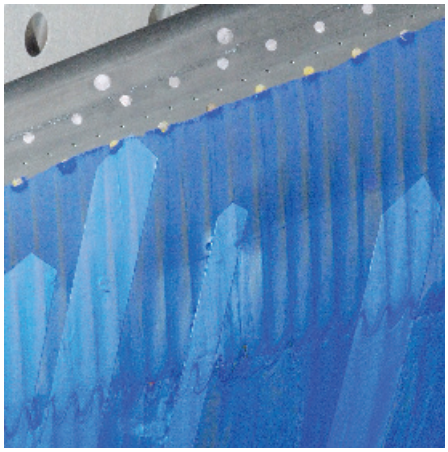

Figure 23 - Close-up view of the oil flow visualization around the fluidic VGs at $\alpha = 3°$ and $C_\mu = 5.8\ 10^{-4}$

This test case has also been computed by Dandois et al. [18]. Figure 22 displays a Q-criterion iso-surface ($Q = 100 U_\infty^2 / h^2$) colored by the Mach number and the iso-surface $Vx = 0$ (streamwise velocity = 0, in black) for the fine overset grid. The streamwise vortices created by the co-rotating fluidic VGs are clearly visible. As observed in the experiment, there remains a small separated zone between 50 and 60% of the span.

For the S2MA model, like for the S3Ch model, micro-nozzles with a throat diameter of 0.8 mm and an exit diameter $d = 1$ mm have been used. Since the model is larger than the S3Ch model, there are 50 fluidic VGs instead of 40. They are also located closer to the leading edge at 15% of the chord, in order to be outside the fuel tank region on a real aircraft. They are located between 46% and 89% of the wing span. The spacing between each hole is $\lambda = 14.4\ d$. Like for the S3Ch model, the pitch angle α is fixed equal to 30°. Since on the S3Ch model no difference was observed between the two tested skew angles, only $\beta = 60°$ (taken from the normal to the leading edge line) has been tested on this model. The maximum mass flow is 0.5 g.s^{-1} per hole and the fluidic VGs can operate in continuous blowing mode, or in pulsed blowing mode (between 0 and 700 Hz) using piezoelectric actuators inside the model.

Figure 23 shows a close-up view of the oil flow visualization of the controlled flow by fluidic VGs ($C_\mu = 5.8\ 10^{-4}$) at $\alpha = 3^o$. The streamwise vortices created by the VGs are traced by the streamwise line of oil washing between accumulations of blue oil. The shock foot is also modified by the interaction with the streamwise vortices. For a higher angle of attack $\alpha = 4.25^o$ (see figure 24), in the uncontrolled case, the flow is separated on one third of the span in the central part, whereas in the controlled case with fluidic VGs, a flow separation starts to appear at around 40% of the span where the flow is not controlled (the fluidic VGs are located between 46 and 89% of the span). Thus, the fluidic VGs are able to delay the separation appearance as well as the mechanical VGs.

Since the S2MA wind tunnel is equipped with a balance, the effect of the fluidic VGs on lift and drag can be investigated. The lift change with the angle of attack is given in figure 25 for the baseline, the mechanical VGs case and the fluidic VGs for some selected values of C_μ. The control has no influence on the lift curves for $\alpha < 2.5^o$. For $\alpha > 2.5^o$, the lift curves of the baseline and the controlled case start to diverge, the control increases the lift. Then, for $\alpha > 4^o$, the lift increment is nearly constant. The lift increment, observed for angles-of-attack larger than the buffet onset at $\alpha = 3^o$, increases with C_μ but quickly reaches a saturation for $C_\mu \geq 4.6\ 10^{-4}$,which corresponds to a low value C_μ (5% of the maximum C_μ) and the mass flow rate (5.9 g.s^{-1} = ¼ of the maximum masse flow rate). The micro-nozzles are not even shocked. In figure 25, the lift curves for $C_\mu = 4.6\ 10^{-4}$ and $1.7\ 10^{-3}$ are superimposed. The effect of the fluidic VGs on lift is comparable to the mechanical VGs one for a very low value of C_μ equal to $1.5\ 10^{-4}$ (3 g.s^{-1})

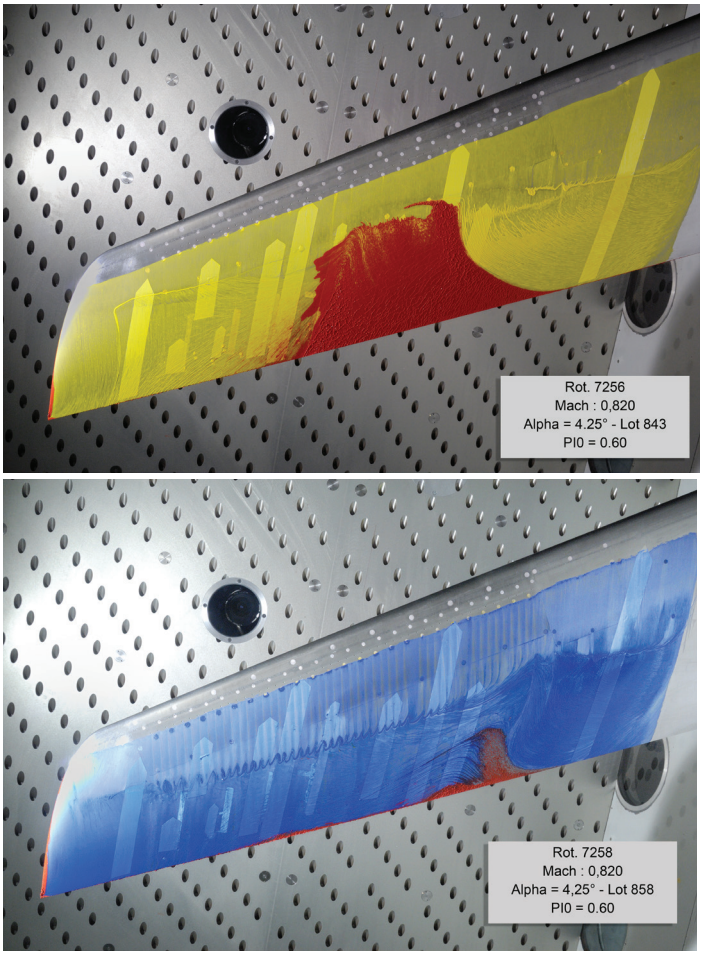

Figure 24 - Oil flow visualizations of the baseline (left) and the fluidic VGs case (C_μ=5.8 10-4) at $\alpha = 4.25°$

Fluidic VG (pulsed flow rate)

The wall pressure distributions for the baseline, the continuous blowing VGs and the pulsed fluidic VGs case at a mass flow rate of 4 g.s^{-1} are given in figure 26 for an angle-of-attack of 4.25° and $y/b = 72.5\%$. The actuator command varies between 0 and 100% of the fluidic VGs opening. As for the continuous blowing fluidic VGs, the effect of the pulsed fluidic VGs is to suppress the flow separation characterized by the Cp increase at the trailing edge, which occurs for $\alpha \geq 3^o$ for the baseline and to shift the shock downstream. The effect of the forcing frequency of the pulsed fluidic VGs is to modify the Cp gradient at the shock foot at around 50% of the chord: for $f = 65$ and 125 Hz, this gradient is smaller than in the continuous blowing case and than that for pulsed fluidic VGs with $f \geq 185$ Hz. This lower Cp gradient characterizes in 2D the shock motion on the suction of the airfoil so here, for a forcing frequency of 65 and 125 Hz, the shock motion amplitude is increased compared to the baseline.

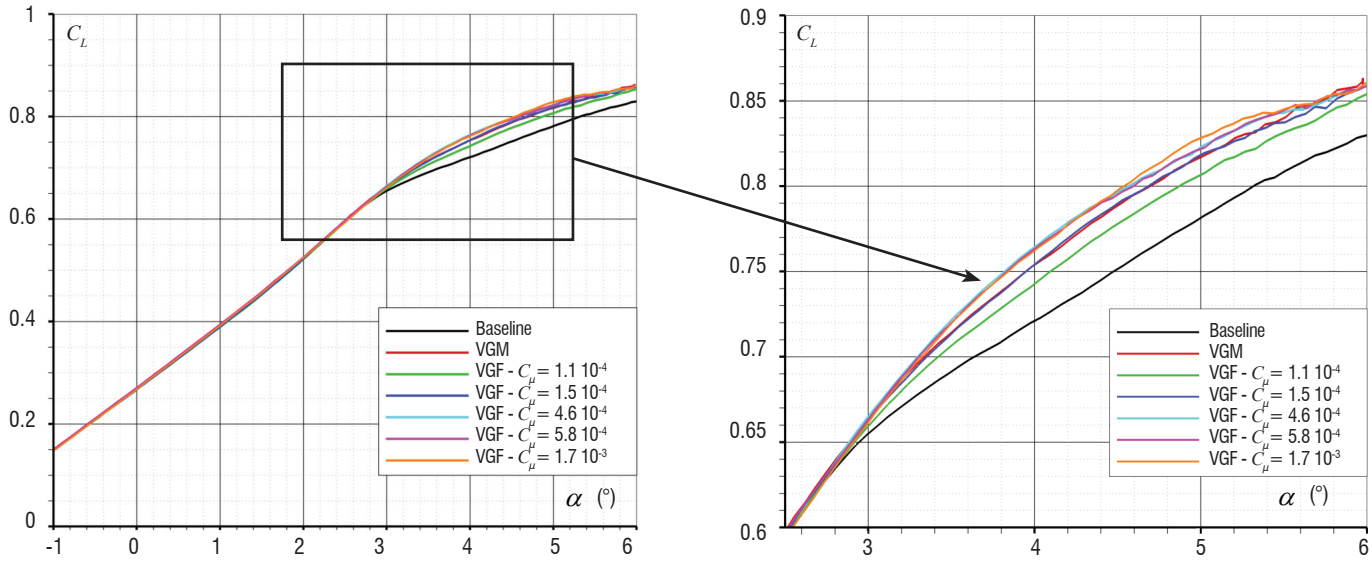

Figure 25 - Lift change with the angle of attack for the baseline, the mechanical VGs and some selected fluidic VGs cases

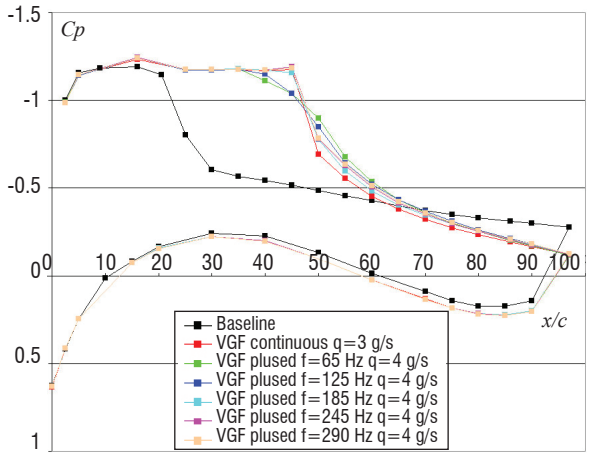

Figure 26 - Wall pressure distribution for the baseline, continuous blowing fluidic VGs and pulsed fluidic VGs at 4.25° and different frequencies at 4 g.s^{-1} and an actuator command between 0 and 100%.

Figure 27 gives the Frequency Response Function of the shock location versus the command signal. The amplitude of the FRF decreases strongly as the frequency increases. The global shape of the FRF amplitude is "smooth" without any "resonance peak". The analysis of the FRF phase is similar to a pure delay. Using the phase information over [10-100]Hz, the time lag can be estimated at 2.2 ms, which gives an estimation of the time delay in the whole system including all electric, mechanic, aerodynamic response times.

Synthetic Jet Actuator

A cover equipped with 14 synthetic jets has also been tested during the S2MA wind tunnel campaign. Seven of these have a hole exit diameter d of 0.5 mm and the seven others have a diameter of 1 mm. Their peak velocity without freestream has been measured at between 120 and 140 m.s^{-1} for d = 0.5 mm and between 110 and 150 m.s^{-1} for d = 1 mm. Figure 28 shows the static wall pressure distribution (left) and its fluctuation level on the upper side of the model (right) for the baseline and the controlled configuration with synthetic jets (two frequencies: purple and blue) and fluidic VGs at a very low mass flow rate of 0.5 g.s^{-1} (in cyan) for comparison. This figure shows that these synthetic jets have no effect on the static wall pressure distribution as well as on the pressure fluctuation level, since the curves are superimposed with the baseline ones. This is probably due to the too low peak velocity of these synthetic jets compared to the local one (around 420 m.s^{-1}).

Fluidic TED

The fluidic TED consists in a slot located on the lower side of the model at the trailing-edge. The blowing angle is normal to the lower surface (see figure 29). Its design is similar to that developed by LEA for the VZLU WT tests during the AVERT European project [19]. The slot is located at x/c = 95% and its width is equal to 0.5 mm. The spanwise length of the slot is 490 mm (between 45% and 85% of wing span). The design of the plenum that supplies the slot with air is based on the TED design for VZLU tests: 4 transverse sections can be feed separately, the maximum mass flow being equal to 180 g.s^{-1} (4×45 g.s^{-1}).

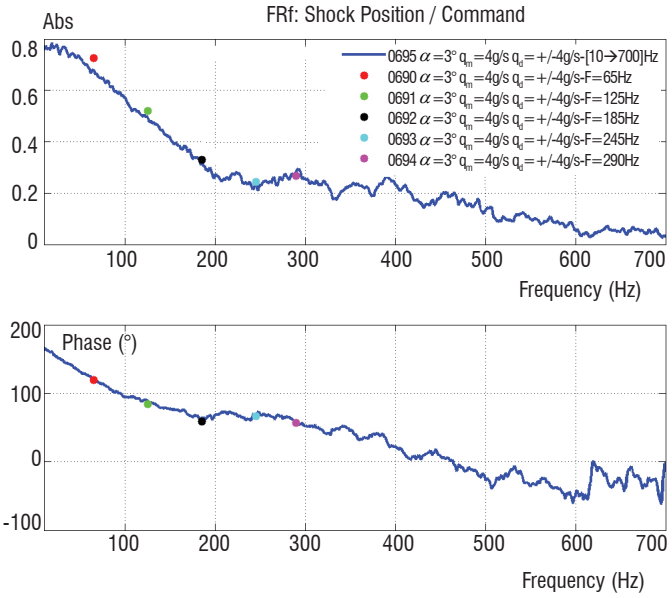

Figure 27 - Frequency Response Function: Shock Location vs. Command Signal

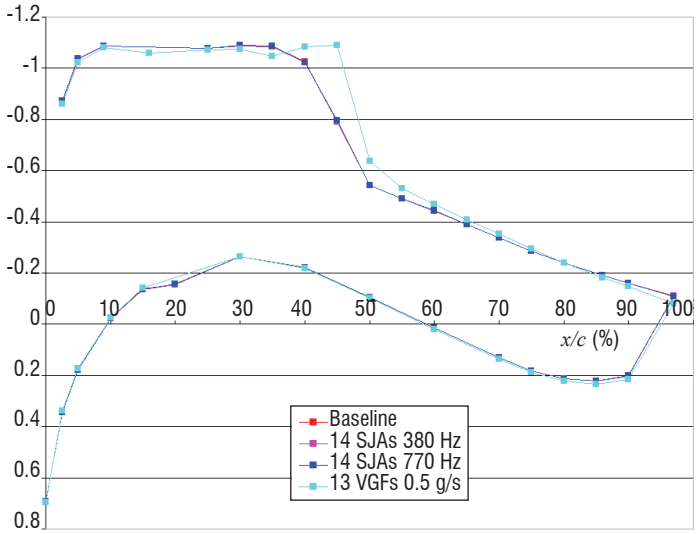

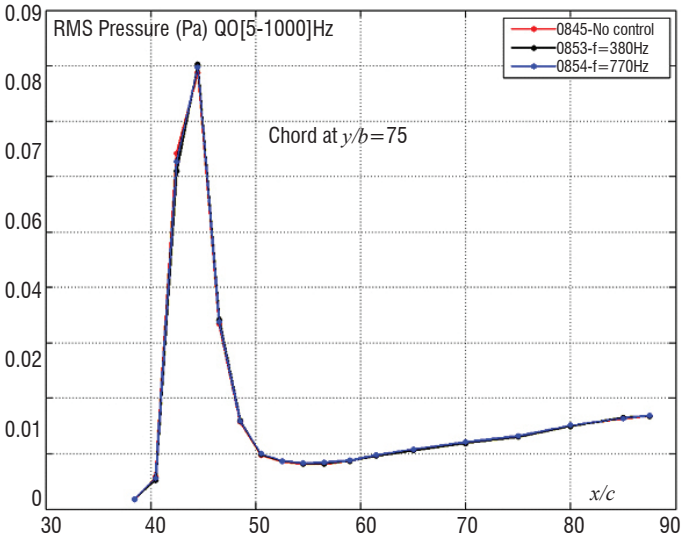

Figure 28 - Wall pressure distribution (top) and RMS pressure level as a function of x/c (down)

The lift change with the angle-of-attack is given in figure 30. The effect of the fluidic TED is a constant increase in its value over the entire angle-of-attack range. This global variation on C_L is progressive with the increase of the C_μ. Up to the maximal value of C_μ (0.0090), corresponding to the maximal mass flow rate of the test device, the observed effects vary linearly with C_μ: the effect for $C_\mu = 0.0090$ is approximately three times that for $C_\mu = 0.0027$.

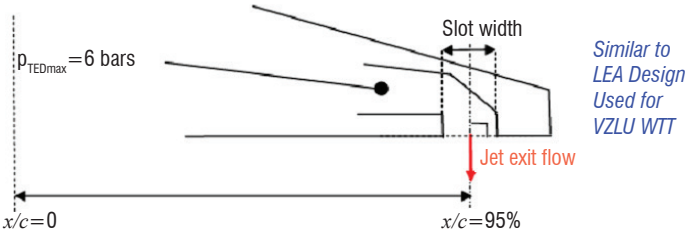

Figure 29 - Sketch showing the definitions of the main parameters of the fluidic TED

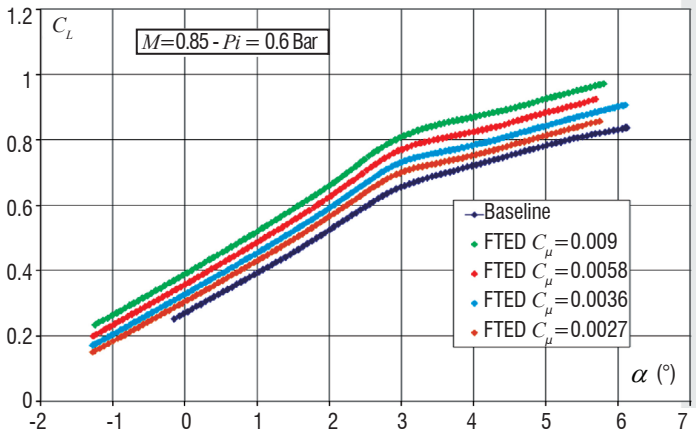

Figure 30 - Fluidic TED action (up to the maximal value of the blowing mass flow rate) on the lift versus α (M=0.82, Pi=0.6 bar)

The static wall pressure distributions for the baseline and the fluidic TED are given in figure 31 for two different spanwise sections and different C_μ values at the same lift coefficient value. This constant lift coefficient value 0.66 corresponds to the "starting" buffet for the baseline configuration ($\alpha \sim 3°$). For the fluidic TED cases, the buffet level is lower and close to the buffet onset limit, which can be estimated at $\alpha = 2.75°$, as well as for baseline than for FTED cases. When the fluidic TED slot is not blowing (slot open - dashed line) there are only slight differences in the pressure distributions compared to the baseline configuration case. For section $y/b = 55\%$, the strong upper side shock wave moves downstream (about 5% of the chord), while the wide supersonic plateau upstream of it becomes lower. On the aft part of the wing, the pressure distribution is "opening", both on the upper and lower side. For section $y/b = 72.5\%$, the effect is the same as in the 55% section, but the downstream displacement of the strong shock wave is more important (10% to 15% of the chord) and the opening of the distribution on the rear aft of the wing is stronger.

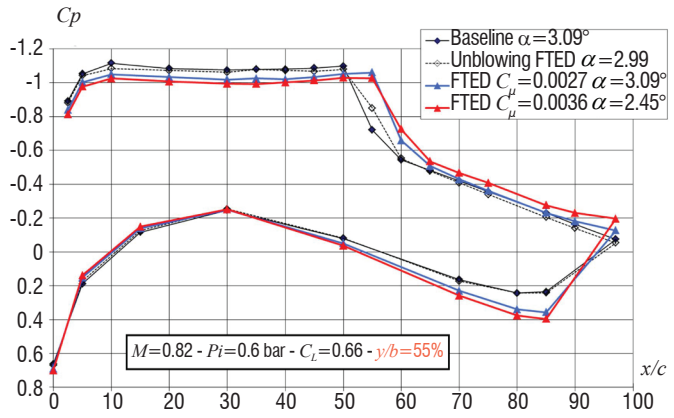

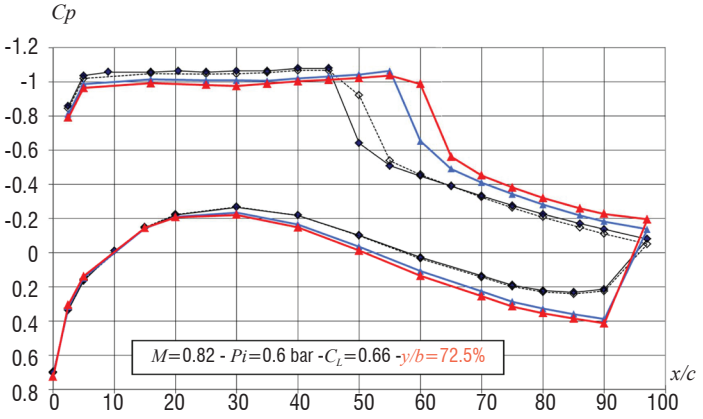

Figure 31 - Wall pressure distributions (M=0.82, Pi=0.6 bar): increasing fluidic TED effect at a constant value of the lift coefficient C_L=0.66 corresponding to buffet onset

Open Loop Result Summary

Figure 32 summarizes the behavior concerning buffet onset and development for the mechanical and fluidic VG configurations at different C_μ levels, in comparison with the baseline configuration at M= 0.82 and Pi=0.6 bar. The RMS fluctuations values are plotted versus the angle-of-attack and versus the lift coefficient for the upper side Kulite pressure transducer named K2, located near the trailing edge at x/c=85% on the spanwise section y/b=75%.

At low values of α or lift coefficient, fluidic or mechanical VGs do not produce any increase of the mechanical vibration level. For mechanical VGs, the strong increase in the pressure fluctuation and mechanical vibration corresponding to buffet is clearly postponed to higher angle-of-attack and lift values. Moreover, the increase in the pressure fluctuation seems to be reduced when buffet becomes stronger. The buffet onset limit is estimated at α = 3° (instead of 2.75° for baseline).

For fluidic VGs, the effects are similar, but stronger. At C_μ = 0.0006, the buffet onset limit can be estimated at α = 3.25° and the increase in the pressure fluctuation when buffet develops is lower, as for the baseline or even the mechanical VGs configuration.

Concerning the control by the fluidic TED, it is important to note that this flow control device does not delay the buffet onset at higher angles-of-attack (see figure 32 (left)) but only at higher lift values (see figure 32 (right)), since, as was shown in figure 30, the effect is a constant lift increase over the entire angle-of-attack range and the kink visible on the lift curve at around 3° is not delayed by the fluidic TED.

Buffet Control: closed loop approach

Different closed-loop control architectures were tested in the S3Ch wind tunnel for M = 0.82, Pi = 1 bar and an angle-of-attack of 3°. The main control parameters are described in table 1 depending on the signal and the objective function used in the closed loop.

Sensor \ Criterion	RMS value	Time-averaged value
Trailing edge Kulite (x/c = 90% & y/b = 60%)	Minimization	Maximization
Shock location signal	Minimization	Maximization

Table 1- Control configurations tested in S3Ch

The first schematic closed loop control architecture is shown in figure 33. The objective is to minimize the RMS value of an unsteady pressure transducer located at the 90% of the chord. The feedback law can be associated to a disturbance rejection strategy. In this case, no reference input is applied to the system, the control architecture is aimed at minimizing its response to a specific perturbation. This part deals only with a quasi-steady approach of a feedback control. The quasi-steadiness property results from the fact that the system output is passed into an integrator block, in order to estimate a specific criterion over a "long" time (RMS value, averaged value).

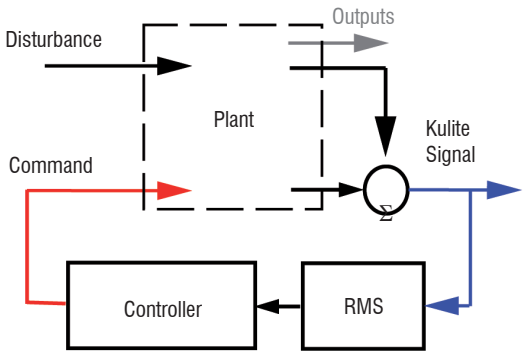

Figure 33 - Block diagram of the first control approach

The main results are plotted in figure 34. Starting from the uncontrolled configuration, the pressure fluctuations level (estimated through the RMS value) is very high. The command of the pulsed fluidic VGs is proportional to the RMS value. After a rise time and settling time, the control command converged to a fixed value.

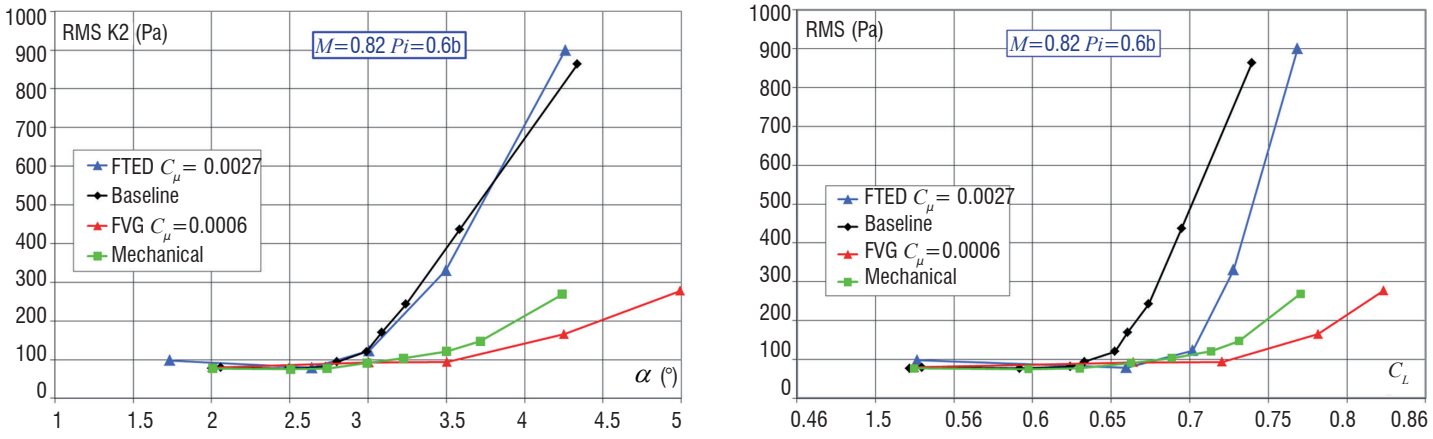

Figure 32 - Buffet entrance with fluidic and mechanical VGs; comparison with the baseline configuration at M=0.82 and Pi=0.6 bar: unsteady wall pressure measurements

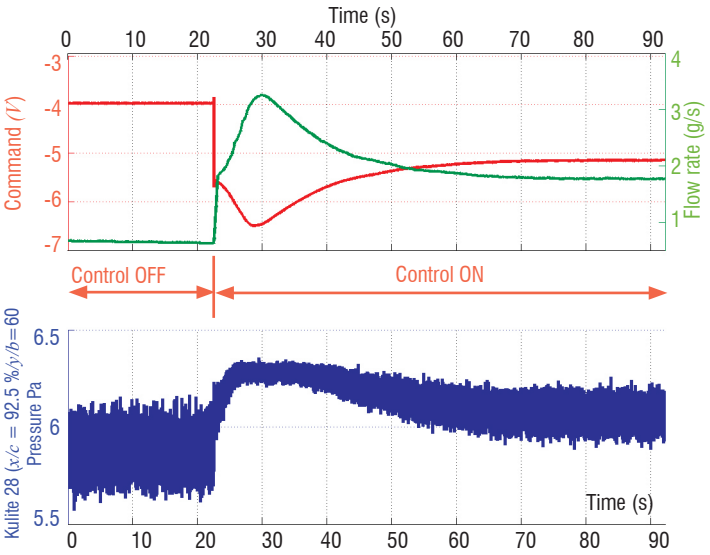

Figure 34 - Time evolutions of command, flow and pressure signals

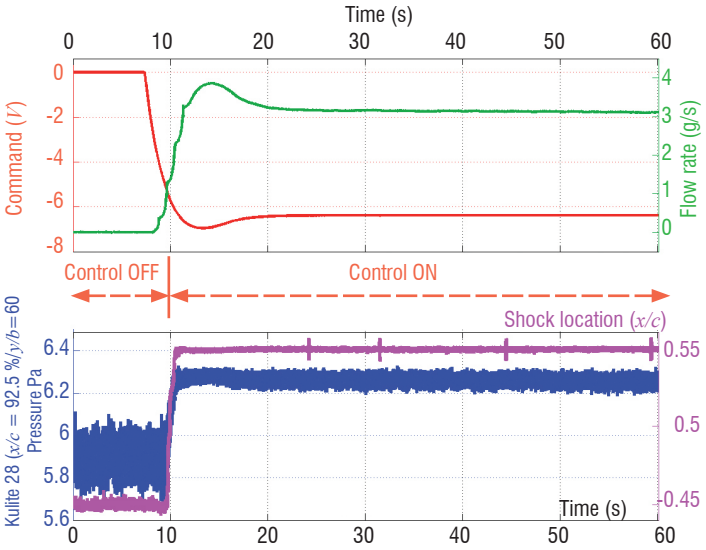

Figure 36 - Time evolutions of command, flow, pressure and shock location signals

A different closed-loop algorithm, consisting in maximizing the shock location, has also been tested. The schematic control architecture is shown in figure 35. In this closed loop approach, 10 unsteady pressure sensors were monitored continuously, in order to estimate the shock location in real time. The estimated signal was used as controller input.

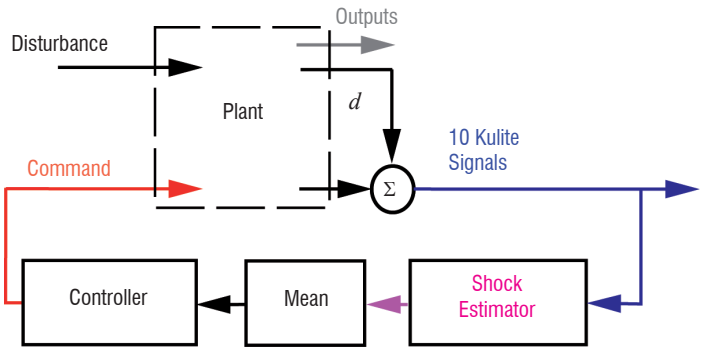

Figure 35 - Block diagram of the second control approach

The main results are plotted in figure 36. As for the previous case, the evolution of the VG command is clearly proportional to the chosen signal. With a small gain value, the actual command may result in an inefficient VG command, or may converge to the desirable output slowly. However, with a large control gain, the actual output may reach the (maximum) saturation value or may never converge (i.e., the controller-plant system oscillates). At the end of the test point shown in figure 36, the control efficiency shows that the shock location occurs more downstream, at about 10% in chord, than for the corresponding uncontrolled case. The RMS fluctuations of shock location (but also of the unsteady pressure at the trailing edge) were clearly decreased.

Conclusions

The aim of this paper was to summarize the work performed at Onera over the last decade within the framework of several European and self-funded projects.

Sections “2D Turbulent Airfoil” and “3D Turbulence Wings” have shown that the appearance of buffet under transonic conditions leads to some common features, for example on the change in the wall pressure distribution with the angle-of-attack (pressure plateau, shock location, trailing edge pressure divergence), but also has some fundamental differences. For example, it is important to mention that the signature of the 3D buffet phenomenon on the wall pressure spectra at the shock foot (a bump) is completely different from the 2D buffet, which is characterized by well-marked peaks.

Then, the efficiency of flow control devices has been evaluated in two wind tunnels under transonic flow conditions, at Mach numbers between 0.80 and 0.84 and at different Reynolds numbers, from 2.83 10^6 to 8.49 10^6. These results, recorded in an industrial-type environment, have allowed the behavior of such active technologies to be assessed and them to be brought to TRL "Technology Readiness Level" values of 3-4.

Each model instrumentation was very detailed and comprised steady pressure taps, unsteady transducers and accelerometers, which complement the flow visualizations (oil-film and mini-tufts) and global force measurements. This allows a perfect description of the turbulent flow, the wall streamlines, the flow unsteadiness, the mechanical vibrations and the buffet onset, for each of the tested configurations:
baseline or reference configuration ;

- mechanical VGs;
- fluidic VGs in continuous and pulsed blowing mode;
- fluidic TED “Trailing Edge Device” at a continuous flow rate.

The effect of both passive and active devices is to:

- postpone buffet onset at a higher angles of attack (mechanical/fluidic VGs), or at higher lift values (all);
- decrease the extent of separated areas (from oil-flow visualizations and mini-tufts);
- decrease the unsteadiness (records provided by Kulite transducers and accelerometers);
- increase the lift coefficient for high angles of attack (from force measurements).

Many parametric investigations were performed (not shown here) for different fluidic VG spacings, spanwise locations and also mass flow rates, and thus momentum coefficients.

The effect of the fluidic VGs is similar to that of the mechanical VGs, with a saturation reached for momentum coefficient C_μ above 9 10^{-5}, corresponding to a flow rate of 0.12 $g.s^{-1}$ per hole. Fluidic VGs at C_μ of 6 10^{-5} have very similar aerodynamic performances to those of the mechanical VGs case. The effect on unsteady components is very similar.

Concerning the fluidic TED, a linear-type behavior has been noted on the lift coefficient. It should be pointed out that the efficiency of a fluidic TED with C_μ=0.0027 corresponds to that of a mechanical TED or mini-flap deflected at ~30° when comparing to former results obtained by Onera.

Concerning the closed-loop control, the objective of this work was to demonstrate the feasibility of controlling the buffet using a closed loop based on a quasi-steady approach. Under transonic flow conditions, the buffet phenomenon is characterized by a strong interaction between the shock wave and the boundary layer inducing a massive flow separation on the upper side of the wing. Since all of the phenomena are coupled and dependent, the closed loop strategy based on the time-averaged shock location (respectively on the pressure level at the trailing edge) provides the desired effects, but also some effects on the pressure level at the trailing edge (respectively on the shock location)■

Acknowledgements

The AVERT wind tunnel tests were conducted within the FP7 AVERT European project (Contract N°.: AST5-CT-2006-030914), funded by EC and project partners (Airbus Operations Ltd, Arbus Operations SL, Dassault Aviation, Alenia Aeronautica and Onera). The closed-loop buffet control tests in the S3Ch wind tunnel, as well as the synthetic jet tests in the S2MA wind tunnel, have received funding from the European Union's Seventh Framework Program (FP7/2007-2013) for the Clean Sky Joint Technology Initiative, under Grant Agreement CSJU-GAM-SFWA-2008-001. The authors are very grateful to the Onera S3Ch and S2MA wind tunnel teams, who contributed to the success of these tests. The authors would also like to acknowledge the colleagues from the Onera Model Shop Department who designed the two models and the pulsed blowing actuators; without them the buffet closed-loop control would not have been possible.

References

[1] V. BRUNET - *Computational Study of Buffet Phenomenon with Unsteady RANS Equations*. AIAA Paper 2003-3679, 21st AIAA Applied Aerodynamics Conference, Orlando, USA, 2003.

[2] V. BRUNET, P. NAUDIN - *Etude du tremblement autour d'une aile en flèche entre parois. Analyse de la troisième campagne d'essais au TsAGI et étude numérique.* Onera Technical Report N° 238/05096 DAAP, Juin 2004.

[3] V. BRUNET - *Numerical Investigation of Buffet Phenomenon with URANS Equation.* 1st European Conference for Aerospace Sciences (EUCASS). Moscow, Russia 4-7 of July, 2005.

[4] V. BRUNET, S. DECK, P. MOLTON and M. THIERY - *A Complete Experimental and Numerical Study of the Buffet Phenomenon over the OAT15A Airfoil*. 40th Colloque Aérodynamique Appliquée de l'AAAF, Toulouse, France, March 21-23, 2005.

[5] V. BRUNET, S. DECK - *Zonal-Detached Eddy Simulation of Transonic Buffet on a Civil Aircraft Type Configuration.* AIAA Paper 2008-4152, 2008.

[6] R. BUR, P. MOLTON - *PRF BUFET'N Co - Essais du contrôle en boucle ouverte du tremblement dans la soufflerie S3Ch.* Onera Technical Report 4/16607 DAAP/DAFE, Jan. 2011.

[7] D. CARUANA, A. MIGNOSI, C. ROBITAILLÉ and M. CORRÈGE - *Separated Flow and Buffeting Control*. In Flow, Turbulence and Combustion, 71(1-4), pp. 221-245, 2003.

[8] D. CARUANA, A. MIGNOSI, A. LE POURHIET, M. CORRÈGE and A-M. RODDE - *Buffet and Buffeting Control in Transonic Flows*. Aerospace Science and Technology, Vol. 9, pp. 605-616, 2005.

[9] E. COUSTOLS, V. BRUNET, R. BUR, D. CARUANA and D. SIPP - *BUFET'N Co: A Joint Onera Research Project devoted to Buffet Control on a Transonic 3D Wing using a Closed-Loop Approach.* CEAS/KATNET II Conference, Bremen, Germany, 12-14 May 2009.

[10] J. DANDOIS, J.-B. DOR, A. LEPAGE, V. BRUNET, E. EGLINGER, F. TERNOY, and E. COUSTOLS. AVERT - *Onera S2MA Wind Tunnel Test*. Report, Onera Technical Reports N° 8/11669 DAAP & 2/10966 DAAP.

[11] S. DECK - *Numerical Simulation of Transonic Buffet over Supercritical Airfoil*. AIAA Journal, Vol. 43, N°7, pp. 1556-1566, 2005.

[12] E. GARNIER and S. DECK - *Large-eddy Simulation of Transonic Buffet over a Supercritical Airfoil.* 45th AAAF Symposium of Applied Aerodynamics, 22-24 March 2010, Marseille, France.

[13] L. JACQUIN, P. MOLTON, S. DECK, B. MAURY & D. SOULEVANT - *Experimental Study of the 2D Oscillation on a Transonic Wing*. Proceedings 35th AIAA Fluid Dynamics Conference, Toronto, Canada, June 2005, AIAA Paper 2005-4902.

[14] P. MOLTON, J. DANDOIS, A. LEPAGE, V. BRUNET and R. BUR - *Control of Buffet Phenomenon on a Transonic Swept Wing.* AIAA Paper 2010-4595 and AIAA Journal, to appear.

[15] J. RENEAUX, V. BRUNET, D. CARUANA, S. DECK and P. NAUDIN - *A Combined Experimental and Numerical Investigation of the Buffet Phenomenon and its Control Through Passive and Active Devices*. Katnet Conference, Bremen, June 2005.

[16] M. THIERY and E. COUSTOLS - *URANS Computations of Shock-induced Oscillations over 2D Rigid Airfoils: Influence of Test Section Geometry.* Flow Turbulence and Combustion, 74 (4), pp. 331-354, 2005.

[17] M. THIERY and E. COUSTOLS - *Numerical Prediction of Shock Induced Oscillations over a 2D Airfoil: Influence of Turbulence Modelling and Test Section Walls*. Int. Journal of Heat and Fluid Flow, Vol. 27, N°. 4, pp. 661-670, 2006.

[18] J. DANDOIS, V. BRUNET, P. MOLTON, J.-C. ABART and A. LEPAGE - *Buffet Control by Means of Mechanical and Fluidic Vortex Generators*. AIAA Paper 2010-4975, 5th AIAA Flow Control Conference, Chicago, 28 juin-1 juillet 2010.

[19] J. DANDOIS, C. GLEYZES, J.-B. DOR, F. TERNOY and E. COUSTOLS - *Report on the VZLU Wind Tunnel Test Analysis & report on the 3D RANS and URANS Computations of Mechanical/Fluidic VGs and Fluidic TEDs*. AVERT deliverables D1.3-3 & D1.3-8, June 2010.
[20] R. BUR, B. CORBEL AND J. DÉLERY - *Study of Passive Control in a Transonic Shock Wave / Boundary Layer Interaction*. AIAA Journal, Vol. 36, N°. 3, pp. 394-400, 1998.
[21] A.N. SMITH, H.A. HOLDEN, H. BABINSKY, J.L. FULKER and P.R. ASHILL - *Normal Shock-Wave/Turbulent Boundary Layer Interactions in the Presence of Streamwise Slots and Grooves*. Aeronautical Journal, Vol. 106, pp. 493-500, 2003.
[22] H.A. HOLDEN and H. BABINSKY - *Separated Shock-Boundary-Layer Interaction Control Using Streamwise Slots*. Journal of Aircraft, Vol. 42, N°. 1, pp. 166-17, 2005.
[23] E. STANEWSKY, J. DÉLERY, J.L. FULKER AND W. GEISSLER - *Synopsis of the Project EUROSHOCK*. Notes on Numerical Fluid Mechanics: Drag Reduction by Passive Shock Control - Results of the Project EUROSHOCK, Vol. 56, Vieweg Ed., Wiesbaden (Germany), pp. 1-81, 1997.
[24] J. DÉLERY and R. BUR - *The Physics of Shock Wave / Boundary Layer Interaction Control: Last Lessons Learned*. Proceedings of the ECCOMAS 2000 Congress, Barcelona (Spain), Sept. 11-14, 2000.
[25] E. STANEWSKY, J. DÉLERY, J.L. FULKER and P. DE MATTEIS - *Synopsis of the Project EUROSHOCK II.* Notes on Numerical Fluid Mechanics and Multidisciplinary Design: Drag Reduction by Shock and Boundary Layer Control - Results of the Project EUROSHOCK II, Vol. 80, Springer Ed., Berlin (Germany), pp. 1-124, 2002.
[26] J. BIRKEMEYER, H. ROSEMANN and E. STANEWSKY - *Shock Control on a Swept Wing*. Aerospace Science and Technology, Vol. 4, pp. 147-156, 2000.
[27] W.S. WONG, N. QIN, N. SELLARS, H.A. HOLDEN and H. BABINSKY - *A Combined Experimental and Numerical Study of Flow Structures over Three-Dimensional Shock Control Bumps*. Aerospace Science and Technology, Vol. 12, pp. 436-447, 2008.
[28] H. OGAWA, H. BABINSKY, M. PÄTZOLD and T. LUTZ - *Shock-Wave / Boundary-Layer Interaction Control Using Three-Dimensional Bumps for Transonic Wings*. AIAA Journal, Vol. 46, N°. 6, pp. 1442-1452, 2008.
[29] S.P. COLLISS, H. BABINSKY, P.J.K. BRUCE, K. NÜBLER and T. LUTZ - *An Experimental Investigation of Three-Dimensional Shock Control Bumps Applied to Transonic Airfoils*. AIAA Paper 2012-0043, 50th Aerospace Sciences Meeting, Nashville, Tennessee, Jan. 9-12, 2012.
[30] J.C. LIN - *Exploratory Study of Vortex-generating Devices for Turbulent Flow Separation Control*. AIAA Paper 91-0042, 29th Aerospace Sciences Meeting and Exhibit, Reno, NV, Jan. 7-10, 1991.
[31] J.S. MOUNTS and T. J. BARBER - *Numerical Analysis of Shock-Induced Separation Alleviation Using Vortex Generators*. AIAA Paper 92-0751, 1992.
[32] D.C. McCORMICK - *Shock-Boundary Layer Interaction with Low Profile Vortex Generators and Passive Cavity*. AIAA Journal, Vol. 31, N°. 1, p. 96, 1993.
[33] G. GODARD and M. STANISLAS - *Control of a Decelerating Boundary Layer. Part 1: Optimization of Passive Vortex Generators*. Aerospace Science and Technology, Vol. 10, pp. 181-191, 2006.
[34] H.A. HOLDEN AND H. BABINSKY - *Effect of Microvortex Generators on Separated Normal Shock / Boundary Layer Interactions*. Journal of Aircraft, Vol. 44, N°. 1, pp. 170-174, 2007.
[35] R. BUR, D. COPONET and Y. CARPELS - *Separation Control by Vortex Generator Devices in a Transonic Channel Flow*. Shock Waves Journal, Vol. 19, N°. 6, pp. 521-530 - 2009.
[36] M. RYBALKO, H. BABINSKY and E. LOTH - *Vortex Generators for a Normal Shock / Boundary Layer Interaction with a Downstream Diffuser.* Journal of Propulsion and Power. Vol. 28, N°. 1, pp. 71-82, 2012.
[37] D. CARUANA, A. MIGNOSI, C. ROBITAILLE and M. CORREGE - *Separated Flow and Buffeting Control*. Flow, Turbulence and Combustion, Vol. 71, pp. 221-245, 2003.
[38] R.A. WALLIS and C.M. STUART - *On the Control of Shock-Induced Boundary-Layer Separation with Discrete Air Jets*. Aeronautical Research Council C.P. N°. 595, 1962.
[39] M.K. RAO - *An Experimental Investigation of the Use of Air Jet Vortex Generators to Control Shock Induced Boundary Layer Separation*. PhD Dissertation, City University, 1998.
[40] H.H. PEARCEY, K. RAO and D.M. SYKES - *Inclined Air-Jets Used as Vortex Generators to Suppress Shock-Induced Separation*. Paper N°. 40 in AGARD CP-534, Fluid Dynamics Panel Symposium on Computational and Experimental Assessment of Jets in Crossflow, Winchester (UK), 1993.
[41] R. SZWABA - *Comparison of the Influence of Different Air-Jet Vortex Generators on the Separation Region*. Aerospace Science & Technology, Vol. 15, N°. 1, pp. 45-52, 2011.
[42] A. SEIFERT and LaTUNIA G. PACK - *Oscillatory Control of Shock-Induced Separation*. Journal of Aircraft, Vol. 38, N°. 3, 2001.
[43] A.A. HASSAN, B. OSBORNE, S. SCHWIMLEY and G. BILLMAN - *Control of Shock-Boundary Layer Interactions (SBLIs) Using An Oscillatory Jet*. AIAA Paper 2007-0476, 45th Aerospace Sciences Meeting and Exhibit, Reno, NV, 2007.
[44] C.P. TILMANN - *Enhancement of Transonic Airfoil Performance Using Pulsed Jets for Separation Control*. AIAA Paper 2001-0731, 39th Aerospace Sciences Meeting and Exhibit, Reno, NV, 2001.

Nomenclature

x	streamwise coordinate (m)
y	spanwise coordinate (m)
z	vertical coordinate (m)
c	local chord (m)
Cp	wall pressure coefficient
M_0	freestream Mach number
α	angle of attack (°)
C_L	lift coefficient
Pi	freestream stagnation pressure (Pa)
St	Strouhal number
f	frequency (Hz)
c_m	mean aerodynamic chord length (m)
U_0	freestream velocity (m.s^{-1})
Re_c	Reynolds number based on mean aerodynamic chord
h	mechanical vortex generator height (m)
δ	boundary layer local thickness (m)
λ	mechanical vortex generator spanwise spacing (m)
β	mechanical or fluidic vortex generator skew angle (°)
d	fluidic vortex generator hole diameter (m)
C_μ	momentum coefficient

Acronyms

LDV 3C (Three Component Laser Doppler Anemometry)
VG (Vortex Generator)
TED (Trailing Edge Device/Deflector)
PSD (power spectral density, (Pa^2/Hz))
RMS (root mean squared value)
ZDES (Zonal Detached Eddy Simulation)
AVERT (Aviation Emission Reduction Technologies (FP6 EC funded project))

AUTHORS

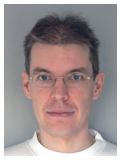

Julien Dandois graduated from the Ecole Nationale Supérieure d'Arts et Métiers (ENSAM) in 2003 and received a PhD in Fluid Mechanics from Paris 6 University in 2007. Since that time, he has worked in the Civil Aircraft Unit of the Applied Aerodynamics Department, in the fields of high-lift, separation control, buffet control, closed-loop control and aeroacoustics.

Pascal Molton received a DUT in Thermal Engineering and Energetics from the Ville d'Avray University in 1982. Since then, he has been a research engineer at Onera in the Fundamental and Experimental Aerodynamics Department. He works in the fields of subsonic/transonic/supersonic flows, jets, vortex flows and flow control.

Arnaud Lepage graduated from the National Engineering Institute in Mechanics (ENSMM) of Besançon in 1998 and received a PhD degree from the University of Franche-Comté for a thesis on experimental modal analysis in 2002. Then, he joined the aeroelasticity department of Onera as a research engineer, where he initially worked on the active vibration control. Since 2006, his fields of interest have been the experimental investigation and control of fixed wing aeroelasticity and unsteady aerodynamics.

Arnaud Geeraert graduated from the Ecole Nationale Supérieure d'Arts et Métiers (ENSAM) in 1999, and worked for 7 years in industry as a structural engineer. Finally, he joined the Onera aeroelasticity department in 2007, as an experimental research engineer, where most of his activities deal with fixed wing aeroelasticity and unsteady aerodynamics.

Vincent Brunet received his Master's Degree and Engineering Diploma from the CORIA / INSA Rouen School of Engineering in 2000. Then, he became a research engineer at Onera, first in the Numerical and Aeroacoustics Department (DSNA) and then in the Applied Aerodynamics Department (DAAP). In the Civil Aircraft team, he is in charge of unsteady and control fields.

Jean-Bernard Dor graduated in 1977 from the SupAéro Engineering School. He has been a research engineer at Onera since 1979. Since then, he has mainly been involved in experimental aerodynamics and wind tunnel testing, generally under transonic conditions and particularly on high Reynolds cryogenic flows (at the former T2 wind tunnel), buffet studies or drag reduction research.

Eric Coustols graduated from ENSEEIHT Toulouse in 1979. He received a Master of Sciences Degree from the University of California San Diego in 1980 and a PhD thesis from the ENSAE (Supaéro) in 1983. He has been working at Onera in the Department of Modelling for Aerodynamics and Energetics since 1983, in various research fields aimed at improving civil aircraft performances. For the last fifteen years or so, he has been coordinating the involvement of several Onera teams in EU-funded projects; more recently, he led the Onera research project BUFET'N Co related to Buffet Control on a 3D transonic wing.

Boundary Layer Transition Control using DBD Plasma Actuators

A. Kurz, S. Grundmann, C. Tropea
(Technische Universität Darmstadt)
M. Forte, A. Seraudie, O. Vermeersch, D. Arnal
(Onera)
N. Goldin, R. King
(Technische Universität Berlin)

E-mail: kurz@csi.tu-darmstadt.de, maxime.forte@onera.fr

This paper presents experimental and numerical investigations dealing with 2D boundary-layer transition control on an Onera-D airfoil using Dielectric Barrier Discharge actuators. These actuators generate a non-thermal surface discharge, which induces a momentum addition tangentially and close to the wall. In this case, the ability of this kind of plasma actuators to delay transition has been assessed using both steady and unsteady modes of actuation. On the one hand, wind tunnel investigations are conducted, as well as linear stability analyses, in order to study the effect of a steady operated DBD actuator on boundary-layer stabilization. The results show a maximum transition delay of about 35% of the chord for low free-stream velocity (U_∞ = 7 m/s). On the other hand, an experiment has been performed using the unsteady force produced by the DBD actuator, to achieve Active Wave Cancellation in a direct frequency mode. With the help of a closed loop control system, a significant transition delay has been achieved by damping artificially introduced TS waves for free-stream velocities up to U_∞ = 20 m/s. This work has been conducted within the framework of the PlasmAero project, funded by the European Commission.

Introduction

Plasma actuators for flow control applications have been studied for more than a decade now. Basically, these actuators can be sorted into two groups, depending on the kind of plasma that is generated: non-thermal plasma or thermal plasma. Thermal plasma actuators are based on the generation of an equilibrium discharge, in order to locally increase the pressure and the temperature of the surrounding gas. For example, Plasma Synthetic Jet (PSJ) actuators generate a spark discharge inside a small cavity having a pinhole exit at the wall. The pressure increase inside this cavity induces a wall-normal jet, which acts on the boundary layer as a vortex generator. These actuators have shown promising results in controlling several academic aerodynamic configurations, such as compressible jets or incompressible separated boundary layers [4], [12]. Non-thermal plasma actuators, like Dielectric Barrier Discharge (DBD) [19] or Corona Discharge [14], are based on the generation of a non-equilibrium surface discharge, which induces a body force parallel to the wall (called ionic wind) inside the boundary layer. This kind of actuator has been widely characterized in quiescent air for different ambient conditions. Moreover, many investigations have shown their ability to control airflows around different kinds of bodies: flat plates, cylinders and airfoils. Most of these studies are reported in detailed reviews [2], [5], [15]. The work presented in this paper has been performed within the framework of the PlasmAero project, funded by the European Commission, for which the main objective is to assess the ability of plasma actuators to control airflows, in order to reduce the environmental impact of air transport. One possible way to reduce aircraft fuel consumption is to delay boundary-layer transition on wing profiles, in order to reduce skin friction drag. Basically, two approaches are possible to achieve this goal on a 2D boundary-layer transition: on the one hand, steady actuation is used to modify the mean velocity profile, in order to make the boundary layer more stable. Different kinds of actuation have shown good results using this approach, like for instance steady suction. On the other hand, unsteady actuation is used to act (or counteract) directly on the instabilities growing within the boundary layer, the well-known Tollmien-Schlichting (TS) waves, which lead to turbulence for low disturbance level airflow. This approach is called Active Wave Cancellation (AWC). The goal of this study is to show the ability of a DBD plasma actuator to delay transition on an airfoil by means of either steady or unsteady actuation, as this actuator is able to induce either continuous or unsteady momentum addition to the boundary layer, depending on the electrical parameters of the high-voltage signal.

Experimental setup

These experiments have been conducted in the subsonic open-return "Juju" wind tunnel located at the research facilities of Onera Toulouse. It features a low turbulence level $0.5\text{x}10^{-3} < Tu < 0.5\text{x}10^{-2}$ depending on the free-stream velocity, which ranges from 5 to 75 m/s. This facility operates at ambient conditions and is well suited for transition experiments. As illustrated in figure 1, a two-dimensional model based on an Onera-D symmetric profile, having a chord length of $c = 0.35$ m, is mounted horizontally in the test-section of the wind tunnel.

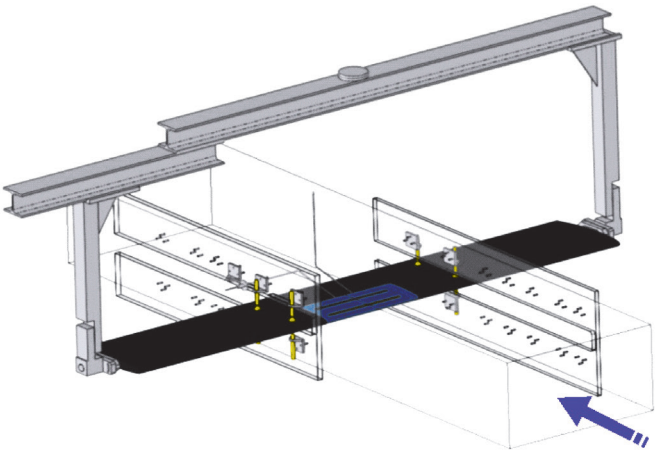

Figure 1 – Two-dimensional model of the Onera-D airfoil mounted inside the wind tunnel

The angle of attack can be adjusted between $\alpha = -8\,°$ and $\alpha = +3\,°$, in order to modify the pressure gradient and thus the natural transition location. Additionally, the model is equipped with 15 pressure taps on the upper side.

The DBD plasma actuator used during this experiment consists of a 5 mm-thick dielectric layer (blue insert in figures 1 and 2) made of Lab850 material, placed at the leading edge region and matching the model shape. This insert allows the model to be outfitted with the desired number of DBD actuators, adhering electrodes asymmetrically on both sides of the dielectric material. For example, figure 2 shows one single DBD actuator located at $x/c = 10$ % (the downstream edge of the air-exposed electrode is taken as the location reference).

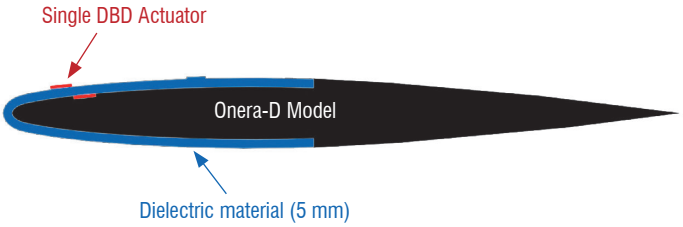

Figure 2 – Cross-sectional view of the Onera-D wing model equipped with one DBD actuator

The electrodes are 30 cm-long in spanwise direction and made of copper tape. The air-exposed electrodes are connected to a TREK power amplifier (model 30/20, ±30 kV, 20 mA peak) and supplied with AC high voltage, while other electrodes are grounded. Moreover, these air-exposed electrodes have been polished, in order to reduce their thickness down to 0.05 mm to prevent them from promoting transition. This value is one order of magnitude lower than the displacement thickness of the boundary layer measured at $x/c = 10$ % in the two following experiments. Hot wire anemometry (Dantec Streamline, 90C10 CTA modules, 55P15 probes) has been employed for boundary-layer explorations.

Transition delay using steady DBD actuation

The study presented in this section is related to 2D boundary-layer stabilization using the plasma actuator in a continuous mode of operation. In this way, a quasi-steady momentum is added to the flow, directly acting on the mean velocity profile of the boundary layer, in such a way that the amplification of the disturbances is impeded and transition can be delayed. For example, this approach has been successfully applied on a flat plate with artificially excited disturbances [9]. In fact, the actuator induces unsteady momentum at the same frequency than the high-voltage signal. This feature is used in the second part of this paper (unsteady actuation). Nevertheless, the effect of the actuator can be considered as quasi-steady in this first experiment, because the operating frequency of the actuator is high compared to the most unstable frequencies of the boundary layer.

Wind tunnel investigations

In a first step, boundary-layer transition delay is investigated experimentally using one single DBD actuator located at $x/c = 10$ % and operated continuously. The angle of attack of the model is set to $\alpha = 2.5\,°$ and the experiment has been performed for two different free-stream velocities $U_\infty = 7$ & 12 m/s. The plasma actuator is supplied with AC high voltage having three different amplitudes $V_{DBD} = 8.5$; 12 and 17 kV and an operating frequency set to $f_{DBD} = 2$ kHz. The maximum velocity of the ionic wind induced by the actuator in quiescent air is about 4.5 m/s at the highest voltage amplitude. Figures 3a and 3b present typical results for $U_\infty = 7$ & 12 m/s. Velocity fluctuations are computed from boundary-layer explorations along the chord, moving the hot-wire probe at a constant distance from the wall, with and without control. The location of the transition is deducted from the fluctuation increase. The natural transition is located at $x/c \approx 40$ % for $U_\infty = 7$ m/s and at $x/c = 26$ % for $U_\infty = 12$ m/s. In all cases, the ignition of the plasma actuator leads to a transition delay. As expected, the transition is shifted progressively downstream when the amplitude of the voltage is increased, since the mechanical effect of the actuator (ionic wind) increases. The maximum transition delays recorded during this experiment are 35 % of the chord for $U_\infty = 7$ m/s and 20 % of the chord for $U_\infty = 12$ m/s.

a)

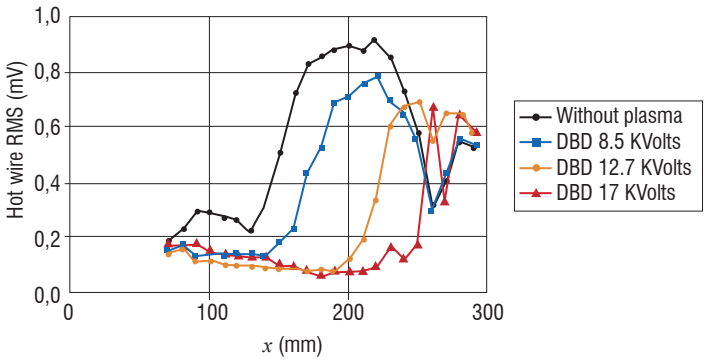

b)

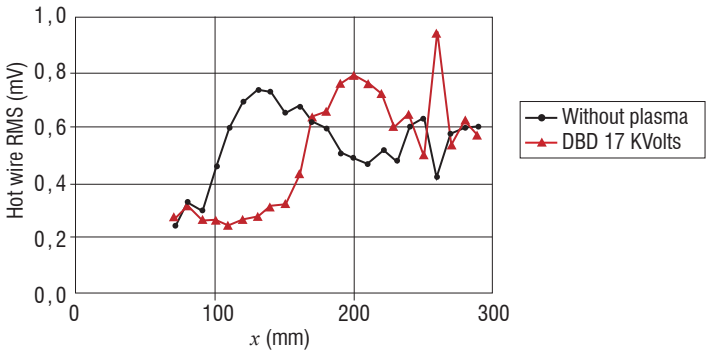

Figure 3 – Transition delay with steady DBD actuation
a) U_∞ = 7 m/s and b) U_∞ = 12 m/s (α = 2.5°)

Numerical investigations

In order to confirm that this transition delay is due to the modification of the mean velocity profile, the control of the boundary layer with steady actuation has been investigated from a numerical point of view. First, boundary-layer computations have been performed for the baseline cases (without plasma) using an Onera code (3C3D, [17]). Then, an artificial ionic wind profile with a simple model (previously described in [20]) has been numerically added at the location of the actuator (x/c=10 %) to the mean velocity profiles obtained from these base flow computations, in such a way that the resulting profiles fit the experimental ones. Finally, exact stability computations have been conducted on these modified profiles, using the envelope strategy so as to compute the amplification N-factor with an Onera code (Castet, [16]).

To describe the laminar-turbulent transition, it is common practice to distinguish three successive processes. The first, taking place close to the leading edge, is the receptivity. It describes the means by which external disturbances (such as free-stream turbulence or noise, as well as wall surface imperfections) excite the eigenmodes of the boundary layer. In the following amplification phase, these eigenmodes develop into periodic waves, which are convected in the streamwise direction. Some of them are exponentially amplified and will trigger transition further downstream. Their evolution is well described by the linear stability theory. When the amplitude of the waves is large, non-linear interactions occur and rapidly lead to turbulence (third step). Within the framework of classical linear stability theory, disturbances are introduced as:

$$q'(x,y,z) = \hat{q}(y).\exp(-\alpha_i x).\exp\left(i(\alpha_r x + \beta z - \omega t)\right) \qquad (1)$$

where q' is a fluctuation (velocity, pressure or temperature) and $\hat{q}$ its amplitude function (here x is perpendicular to the leading edge and y is normal to the wall). Considering the spatial theory, $\alpha = \alpha_i + i\alpha_i$ is the complex wave-number in the x direction. The spanwise wave-number β and frequency ω are real. Introducing expression (1) in the Navier-Stokes equations leads to a system of ordinary differential equations for the amplitude functions. The stability of the flow depends on the value of the imaginary part of the longitudinal component of the amplification vector α_i. When positive, the flow will be stable; when negative, the perturbation will be amplified until the transition is triggered. To quantify the amplification of disturbances, it is common practice to introduce the so-called N-factor given by relation (2), where A is the amplitude of the disturbance at a streamwise position x. Physically, the N-factor describes the total amplification rate of small disturbances along the propagation path. Considering a low velocity two-dimensional flow, only two-dimensional waves (β=0) need to be considered (the N-factor is simply computed by integrating $-\alpha_i$ in the streamwise direction), since Squire's theorem states that they are the most relevant ones.

$$N = \ln\left(A/A_0\right) = \int_{x_0}^{x} -\alpha_i(\xi)d\xi \qquad (2)$$

As explained previously, an artificial ionic wind profile with a simple model is added to the mean velocity profile of the base flow boundary layer, at the location of the actuator (x/c = 10 %). Downstream, the boundary layer is solved by the code with the usual equations. As illustrated in figure 4, three parameters define the ionic wind model:

- u_{plasma} is the maximum amplitude of the ionic wind profile;
- y_{max} is the height of this maximum amplitude;
- y_2 is the height at which the ionic profile returns to zero.

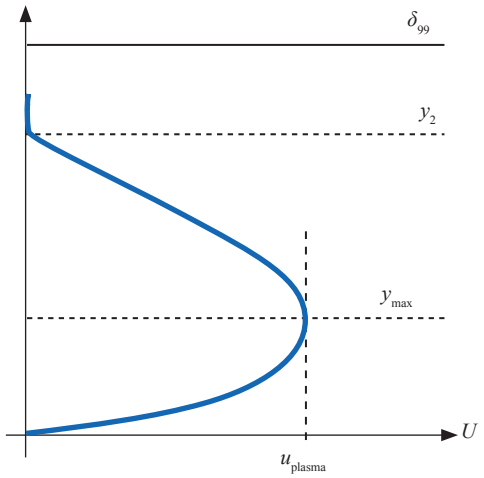

Figure 4 – Simple ionic wind model used to compute the mean velocity profiles of the boundary layer controlled by steady plasma actuation

Typical results of the linear stability analysis are given in figure 5, which presents the evolutions of the N-factor along the chord of the model for several instability frequencies in the baseline case (a) and for the controlled case (b). The aerodynamic configuration is the same as that for the case presented in figure 3b) with U_∞ = 12 m/s. Since the natural transition location is known from the experiment ($xt/c \sim$ 26 % or xt = 0.09 m), we can deduce the corresponding transition N-factor Nt = 5.8. Then, using this value in the controlled case plot, we can observe that the transition location is shifted downstream (xt = 0.22 m), not far from what has been observed experimentally (xt = 0.16 m). This stability analysis for the controlled case has been performed using ionic wind model parameters that are very close to the experimental values (u_{plasma} = 4m/s, y_{max} = 1.2 mm). The difference between measured

and predicted transition locations could be explained by the relative simplicity of the ionic wind model used here. A new model that takes into account the real spatial force distribution induced by the actuator would provide a better consistency in the results. In conclusion, stability computations as well as experiments show that DBD plasma actuators used in a steady mode have a stabilizing effect on the boundary layer. The modification of the mean velocity profiles is such that the amplification of the disturbances is impeded and transition can be delayed.

a)

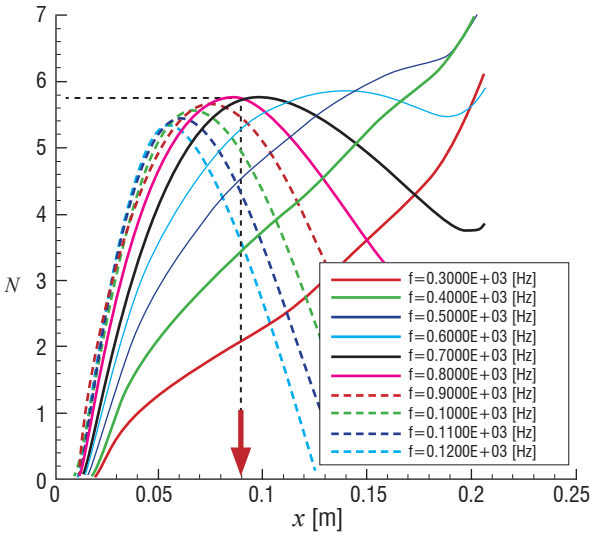

b)

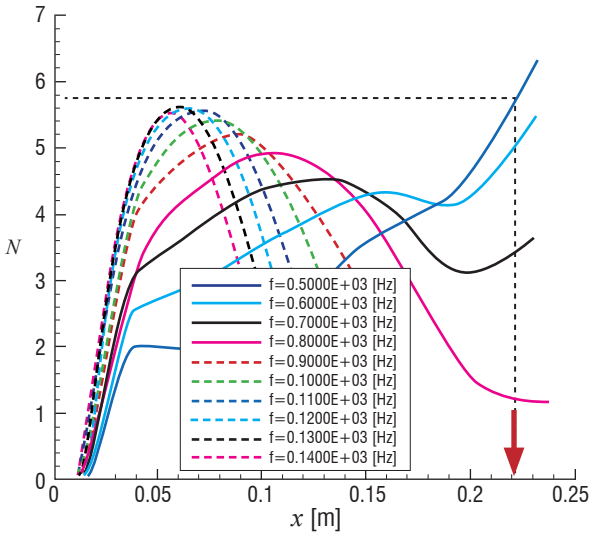

Figure 5 – Evolution of the N-factor along the chord of the model ($\alpha = 2.5°$, $U_\infty = 12$ m/s) without control a) and with control b) where $u_{\text{plasma}} = 4$ m/s and $y_{\max} = 1.2$ mm

Transition delay using unsteady DBD actuation

Another way to delay 2D transition is to use unsteadily operated actuators to act (or counteract) directly on the Tollmien-Schlichting waves growing inside the boundary layer and triggering transition. This approach is called Active Wave Cancellation: the goal is to generate an artificial perturbation with an unsteady force production, so as to damp natural TS waves by destructive interference. Transition is delayed because the TS wave amplitude has been reduced locally. Grundmann and Tropea [10] have conducted experiments using this approach on a flat plate. They used a single high-frequency driven DBD actuator with square wave modulation to generate artificially introduced waves. A sufficiently large difference between the TS wave frequency (modulation frequency) and the operating frequency of the plasma actuator is essential for this operation mode. However, with increasing flow speed, the unstable frequency band will shift to a higher range correspondingly, until a sufficient difference between the carrier frequency and TS wave frequency cannot be maintained anymore. Another possible solution, as suggested by Grundmann in [11], is to make use of the DBD plasma actuator unsteady force production during one cycle of the operating frequency and to directly operate the cancellation actuator at the TS wave frequency. In fact, several experimental [7] [8] and numerical [3] [21] studies have shown that a DBD actuator produces a local unsteady force, mainly due to the different discharge regimes between the positive and the negative half cycles. This phenomenon became clear by analyzing the plasma actuator response electrically [18], or by using optical measurement techniques in the direct vicinity of the plasma region [6]. This asymmetric behavior allows the use of DBD actuators in direct frequency mode. A careful adjustment of the phase relation between the TS waves and the actuator excitation signal can thereby potentially cancel the waves. Thus, the use of an active control system with a closed-loop, which detects the waves and optimizes the actuation, will be necessary.

The experimental set-up used for this study is quite the same as the one presented in the previous section, except that the angle of attack is set to $\alpha = 2$ ° and that the model is outfitted with two DBD actuators, as illustrated in figure 6. The upstream actuator DBD1 ($x/c = 10$ %) serves as a disturbance source to artificially excite a single frequency TS wave train, while DBD2 ($x/c = 30$ %) is utilized as the transition control device.

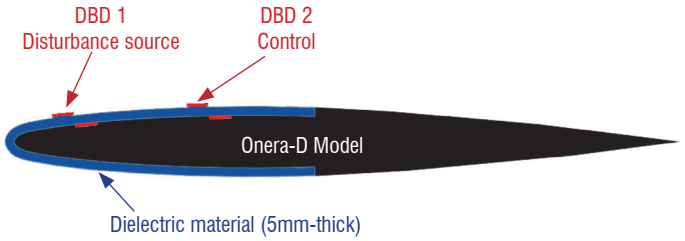

Figure 6 – Experimental set-up for the Active Wave Cancellation study

The experiments have been split into two phases. During an initial testing phase, the feasibility of the direct frequency mode for active wave cancellation had to be verified. In order to do so, a set-up employing a beat frequency approach without the use of a closed-loop controller was chosen, reproducing the experiments of Grundmann and Tropea. This allows for time efficient parameter studies to find appropriate settings and the corresponding attenuation rates. In the second testing phase, transition delay on the wing model has been shown with closed-loop control applied.

AWC without closed-loop control

For this set of measurements, the excitation frequency at the upstream actuator DBD 1 has been set to a value close to the naturally occurring TS frequencies ($f_{DBD1} = 250$ Hz). As the artificially excited waves travel downstream, they reach the control actuator (DBD2), which was operated at a slightly shifted frequency ($f_{DBD2} = 251$ Hz) in order to create a beat frequency with the two signals due to the continuously changing phase relation. Some typical results from these experiments are presented in figure 7 for a free-stream velocity of $U_\infty = 7$ m/s.

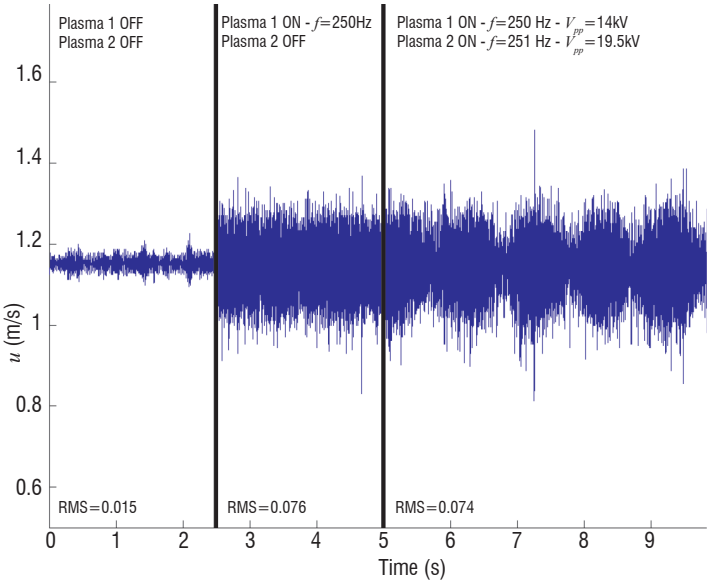

Figure 7 – Time trace of u velocity component given by a hot-wire probe located inside the boundary layer at $x/c = 40\%$ for the base flow (left), with excitation (center) and with excitation and control (right)

The hot wire measurements shown were taken at $x/c = 40$ % inside the boundary layer, at a wall-normal distance of $y = 0.4$ mm. The base flow case (left part of the plot) shows a low fluctuation level within the hot-wire signal of 0.015 m/s. With excitation (middle part of the plot), this disturbance level is raised to 0.076 m/s. Applying the control (right part of the plot), a slow oscillation of the amplitude of the TS waves develops farther downstream from the second actuator, with a maximum amplitude above that of the unaffected waves (amplification) and minimum amplitude below the unaffected wave (damping), resulting in an almost unchanged RMS-value of 0.074 m/s in this case. Figure 8 shows a time trace of the excited TS wave signal with smaller time scale (dashed line) compared to the base flow case (solid line), revealing that a clean TS wave train has been produced by DBD1. Two important results emerge from these experiments. First of all, the unsteady momentum production of the plasma actuator can be utilized to excite TS waves, if applied at the appropriate position, amplitude and a frequency that the flow is susceptible to. Secondly and most importantly, the direct frequency approach for flow control proved to be applicable and can be utilized for active wave cancellation.

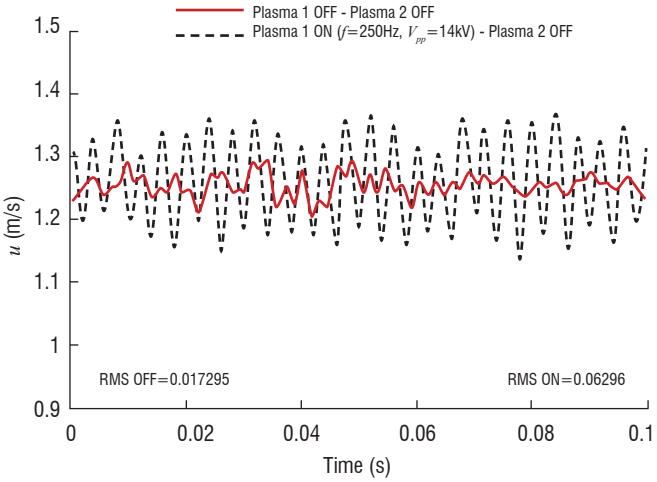

Figure 8 – Time trace of the u velocity component given by a hot-wire probe located inside the boundary layer at $x/c = 40$ % for the base flow (solid line) and with DBD1 turned on (dashed line)

AWC using closed-loop control

In order to have a permanent optimized phase shift between the TS waves generated by DBD1 and the controlling unsteady force induced by DBD2, a robust extremum-seeking control algorithm has been used. This algorithm, which has previously been successfully applied for flow control purposes [1], was supplied by the TU Berlin. The system utilizes the signal of a stationary hot wire probe ($x/c = 40$ %, $y = 0.2$ mm) as an error sensor to automatically optimize the control function. This control algorithm runs on a dSPACE real-time processing unit. Due to its robustness this algorithm is well suited to control artificially excited, single-frequency TS waves. By slowly and periodically deflecting the system out of its current operating point (perturbation), the gradient f' of the error signal is determined according to a change of the controlled variable, which in this case is the phase shift. The phase relation between the TS wave train and the flow structures created by the plasma actuator is then continuously adapted along this gradient, which drives the system into a minimum.

Following the promising beat frequency experiments, closed-loop control has been applied in order to show the transition delay using the direct frequency approach. The free-stream velocity and the angle of attack remain at $U_\infty = 7$ m/s and $\alpha = 2$ ° respectively. A spectral analysis of the stationary hot-wire signal reveals the frequency content of the flow, as shown in figure 9. The power spectral density is plotted in dB/Hz over frequency at a wall-normal position of $y = 0.2$ mm. In the base flow case (DBD1 off, DBD2 off) two frequency peaks, one at 250 Hz and a wider peak around 340 Hz, are prominent. These frequencies represent the naturally occurring TS waves present in the boundary layer for the given flow situation. However, as has been shown with linear stability analysis, well described in [13], frequencies around 340 Hz are damped downstream of DBD2, with the limit for the unstable frequency band being about 300 Hz. A frequency sweep in the unstable range revealed that an excitation at 280 Hz leads to the cleanest TS wave signal at the location of the error sensor. Consequently it was decided to use this frequency for the subsequent AWC experiments. Figure 9 shows that introducing the excitation at 10 % of the chord (DBD1 on, DBD2 off) produces the expected peak around 280 Hz, as well as an overall increase in the turbulence level as transition is being promoted. This increase is visible at the error sensor, since its location is close to the point of transition for the excited case ($\sim$ 47 % of the chord). Applying the control (DBD1 on, DBD2 on) the TS peak at 280 Hz can be reduced by about one order of magnitude. This effect is accompanied by a decreased overall turbulence level.

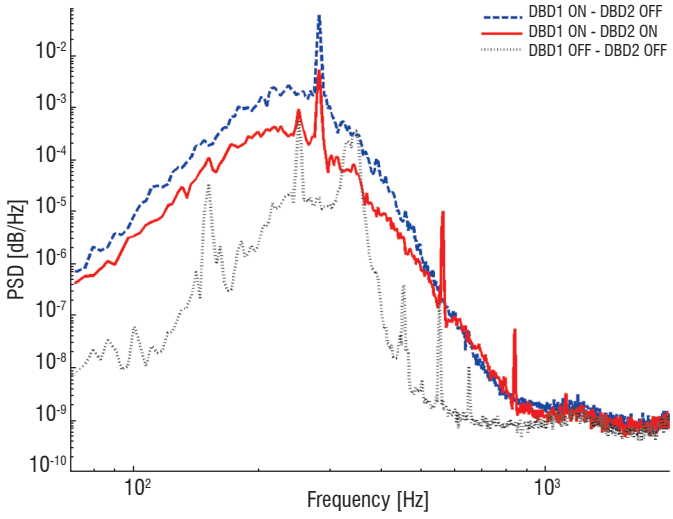

Figure 9 – Spectral analysis of the error sensor signal ($x/c = 40\%$, $U_\infty = 7$ m/s) for the base flow (DBD1 off, DBD2 off), with excitation (DBD1 on, DBD2 off) and with closed-loop control (DBD1 on, DBD2 on)

Figure 10 depicts a typical result of the transition delay studies. The RMS-value of the longitudinal velocity fluctuations recorded at various downstream locations at a constant distance above the wall within the boundary layer is plotted. The dark blue curve (◊) represents the natural transition case with the onset of transition at about 60% of the chord, *i.e.*, neither the disturbance source nor the control actuator is operating. Turning on the disturbance source, the TS wave amplitude is significantly increased at $f = 280$ Hz, which moves the transition region upstream to about 40% of the chord (□). Then, with the control system active, the transition region can be shifted downstream significantly by about 10% of the chord length (○).

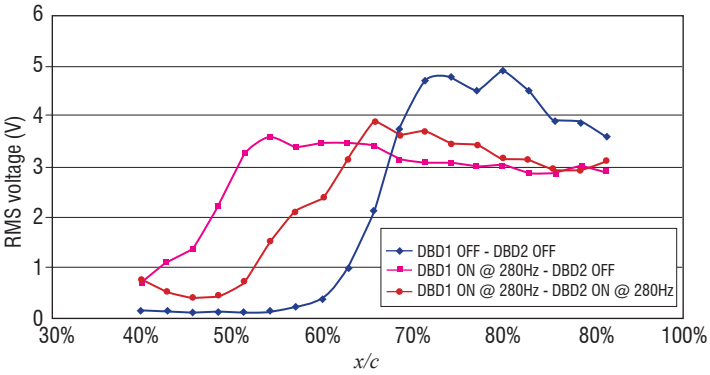

Figure 10 – RMS value of a hot-wire signal along the chord of the airfoil for the base flow, with excitation and with closed-loop control ($\alpha = 2°$, $U_\infty = 7$ m/s)

Even though the unsteadiness of the force production of DBD plasma actuators is used in this work to conduct active wave cancellation, it cannot be neglected that a net force is produced, which modifies the mean flow, *i.e.*, the boundary-layer velocity profile. This modification can by itself lead to a stabilization of the boundary layer, as presented in the previous text section, hence the delay in the transition. Complementary measurements have been carried out in order to exclude possible boundary-layer stabilization due to continuous addition of momentum. To quantify this effect, the momentum generation of DBD2 has been measured in quiescent air, using Pitot-tube measurements. The maximum achievable velocity, 10 mm downstream of the active electrode, was determined to be ~ 0.6 m/s at the prescribed plasma frequency of 280 Hz using this electrode configuration, dielectric material and thickness. In order to deactivate the active wave cancellation and to quantify the effect of a pure momentum addition of this magnitude, the recorded average wall-jet velocity has been reproduced at a plasma frequency of 1 kHz using DBD2. This frequency is located well outside the unstable frequency range and is assumed not to have any destabilizing effect on the boundary layer. The transition delay due to continuous momentum addition is small compared to the effect of the active wave cancellation and is of the order of 1-2 % of the chord length. For higher Reynolds numbers, it can be assumed that this effect will be reduced even further. This experiment proves that the achieved results can clearly be attributed to the unsteady force production of the DBD plasma actuator and are not the result of a modified mean flow.

The same experiment has been conducted with a higher free-stream velocity $U_\infty = 20$ m/s. The angle of attack has been slightly reduced to $\alpha = 1.5°$, in order to have the natural transition location near $x/c = 60$ %, as for the previous case. This time the frequency of the disturbance source is set to fDBD1 = 1 kHz, which is close to the frequency of the most unstable perturbations for this aerodynamic configuration. The changes in the velocity fluctuation along the chord, shown in figure 11, prove that transition delay has been achieved (4% of the chord) using a DBD plasma actuator with a closed-loop control system.

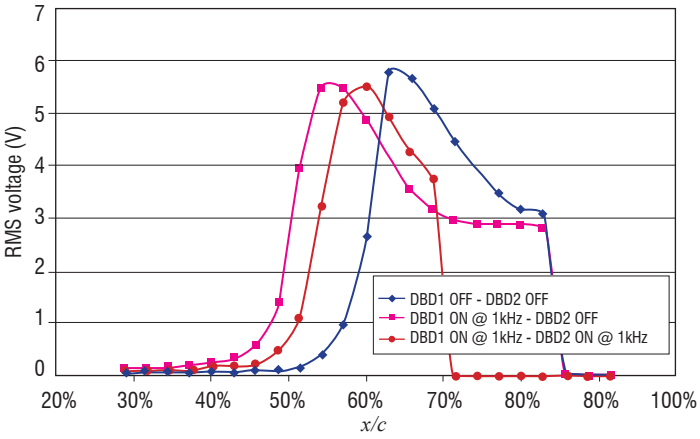

Figure 11 – RMS value of a hot-wire signal along the chord of the airfoil for the base flow, with excitation and with closed-loop control ($\alpha = 1.5°$, $U_\infty = 20$ m/s)

Conclusion

In this study, the ability of DBD plasma actuators to delay 2D boundary-layer transition has been assessed, by means of either steady or unsteady actuation. On the one hand, wind tunnel investigations together with linear stability analysis have shown that a DBD actuator used in a steady mode has a stabilizing effect on the boundary layer. The modification of the mean velocity profiles is such that the amplification of the disturbances is impeded and transition can be delayed. A maximum transition delay of about 35 % of the chord has been achieved for low free-stream velocity ($U_\infty = 7$ m/s). On the other hand, an experiment has been performed using the unsteady force produced by the DBD actuator to achieve Active Wave Cancellation in direct frequency mode. With the help of a closed loop control system, a significant transition delay has been achieved, by damping artificial TS waves for free-stream velocities up to $U_\infty = 20$ m/s ■

References

[1] R. BECKER, R. KING, R. PETZ and W. NITSCHE – *Adaptive Closed-Loop Separation Control on a High-Lift Configuration using Extremum Seeking*. AIAA Journal, vol. 45, pp. 1382-1392, 2007.

[2] N. BENARD and E. MOREAU – *EHD Force and Electric Wind Produced by Plasma Actuators Used for Airflow Control*. Proc. of the 6th AIAA Flow Control Conference, AIAA Paper 2012-3136, 2012.

[3] J.P. BOEUF, Y. LAGMICH and L. C. PITCHFORD – *Contribution of Positive and Negative Ions to the Electrohydrodynamic Force in a Dielectric Barrier Discharge Operating in Air.* Journal of Applied Physics, vol. 106-023115, 2009.

[4] D. CARUANA, P. BARRICAU, P. HARDY, J.P. CAMBRONNE and A. BELINGER – *The Plasma Synthetic Jet Actuator. Aero-Thermodynamic Characterization and First Flow Control Applications*. Proc. of the 47th AIAA Aerospace Sciences Meeting, AIAA Paper 2009-1307, 2009.

[5] T.C. CORKE, C.L. ENLOE and S.P. WILKINSON – *Dielectric Barrier Discharge Plasma Actuators for Flow Control.* Annu Rev Fluid Mech, vol. 42, pp. 505-529, 2010.

[6] C.L. ENLOE, T.E. McLAUGHLIN, R.D. VANDYKEN, K.D. KACHNER, E.J. JUMPER and T.C. CORKE – *Mechanisms and Responses of a Single Dielectric Barrier Plasma Actuator: Plasma Morphology.* AIAA Journal, vol. 42, n°. 3, pp. 595-605, 2004.

[7] M. FORTE, L. LEGER, J. PONS, E. MOREAU and G. TOUCHARD – *Plasma Actuators for Airflow Control: Measurement of the Non-Stationary Induced Flow Velocity*. Journal of Electrostatics, vol. 63, n° 6-10, pp. 929-936, 2005.

[8] M. FORTE, J. JOLIBOIS, J. PONS, E. MOREAU, G. TOUCHARD and M. CAZALENS – *Optimization of a Dielectric Barrier Discharge Actuator by Stationary and Non-Stationary Measurements of the Induced Flow Velocity: Application to Airflow Control.* Experiments in Fluids, vol. 43, pp. 917-928, 2007.

[9] S. GRUNDMANN and C. TROPEA – *Experimental Transition Delay Using Glow-Discharge Plasma Actuators*. Experiments in Fluids, vol. 42, n° 4, pp. 653-657, 2007.

[10] S. GRUNDMANN and C. TROPEA – *Active Cancellation of Artificially Introduced Tollmien-Schlichting Waves Using Plasma Actuators*. Experiments in Fluids, vol. 44, n° 5, pp. 795-806, 2008.

[11] S. GRUNDMANN – *Transition Control Using Dielectric Barrier Discharge Actuators*. Ph.D. Dissertation, Institute for Fluid Mechanics and Aerodynamics, Technische Universität Darmstadt, 2008.

[12] P. HARDY, P. BARRICAU, D. CARUANA, C. GLEYZES, A. BELINGER and J.P. CAMBRONNE – *Plasma Synthetic Jet for Flow Control.* Proceedings of the 40th AIAA Fluid Dynamics Conference and Exhibit, AIAA Paper 2010-5103, 2010.

[13] A. KURZ, C. TROPEA, S. GRUNDMANN, M. FORTE, O. VERMEERSCH, A. SERAUDIE, D. ARNAL, N. GOLDIN and R. KING – *Transition Delay Using DBD Plasma Actuators in Direct Frequency Mode*. Proceedings of the 6th AIAA Flow Control Conference, AIAA Paper 2012-2945, 2012.

[14] L. LEGER, E. MOREAU and G. TOUCHARD – *Electrohydrodynamic Airflow Control Along a Flat Plate by a DC Surface Corona Discharge – Velocity Profile and Wall Pressure Measurements*. Proceedings of the 1st AIAA Flow Control Conference, AIAA Paper 2002-2833, 2002.

[15] E. MOREAU – *Airflow Control by Non-Thermal Plasma Actuators*. Journal of Physics D: Applied Physics, vol. 40, pp. 605-636, 2007.

[16] J. PERRAUD – *Description et mode d'emploi du code CASTET*. Technical Report Onera/DERAT RT n° 124/5118.32, 1997.

[17] J. PERRAUD, O. VERMEERSCH and R. HOUDEVILLE – *Descriptif et mode d'emploi du code 3C3D.* Technical Report Onera RT 1/18325 DMAE, 2011.

[18] J. PONS, E. MOREAU and G. TOUCHARD – *Asymmetric Surface Dielectric Barrier Discharge in Air at Atmospheric Pressure: Electrical Properties and Induced Airflow Characteristics*. Journal of Physics D: Applied Physics, vol. 38, pp. 3635-3642, 2005.

[19] J. R. ROTH, D. M. SHERMAN and S. P. WILKINSON – *Boundary Layer Flow Control with a One Atmosphere Uniform Glow Discharge Surface Plasma*. Proceedings of the 36th AIAA Aerospace Sciences Meeting and Exhibit, AIAA Paper 98-0328, 1998.

[20] A. SERAUDIE, O. VERMEERSCH and D. ARNAL – *DBD Plasma Actuator Effect on a 2D Model Laminar Boundary Layer. Transition Delay under Ionic Wind Effect.* Proc. of the 29th AIAA Applied Aerodynamics Conference, AIAA Paper 2011-3515, 2011.

[21] T. UNFER and J. P. BOEUF – *Modeling and Comparison of Sinusoidal and Nanosecond Pulsed Surface Dielectric Barrier Discharges for Flow Control.* Plasma Physics and Controlled Fusion, vol. 52, n° 12-124019, 2010.

Acronyms

Active Wave Cancellation (AWC)
Dielectric Barrier Discharge (DBD)
Plasma Synthetic Jet (PSJ)
Root Mean Square (RMS)
Tollmien Schlichting (TS)

Armin Kurz graduated in 2003 from the University of Arizona where he obtained his Masters degree in Aeropace Engineering. Since 2008, he works as a doctoral student in the Drag and Circulation Control (DCC) Group of the Center of Smart Interfaces in Darmstadt. His current activities involve boundary-layer transition control with the use of plasma actuators.

Sven Grundmann obtained his Degree in Mechanical Engineering from the Technische Universität Darmstadt in 2003 and received his PhD in 2008 from the same institution. After a postdoctoral position in 2009 at the Stanford University in the Department of Flow Physics and Computational Engineering, he finally joined the Center of Smart Interfaces (CSI) and the Technische Universität Darmstadt in 2010. As a young research group leader, his research interests include drag and circulation control and magnetic resonance imaging for fluid mechanics.

Cameron Tropea graduated from the University of Toronto in Engineering Sciences, followed by a Masters degree in Mechanical Engineering (1977). He completed his Dr.-Ing. in Civil Engineering at the Technical University of Karlsruhe (1982) and his Habilitation in Fluid Mechanics at the University of Erlangen-Nürnberg (1991) where he was appointed as Professor of Fluid Mechanics until 1997. This was followed by an appointement to his current chair of Fluid Mechanics and Aerodynamics at the Technische Universität Darmstadt. Currently Editor-in-Chief of the Springer journal Experiments in Fluids, he is also the Director of Center of Smart Interfaces (CSI) since 2007. His research interests include Optical Measurement Techniques in Fluid Mechanics, Interfacial Transport Phenomena, Atomization and Spray Processes and Instationary Aerodynamics.

Maxime Forte graduated from École Nationale Supérieure de Mécanique et d'Aérotechnique (ENSMA - French engineering school specialized in space and aeronautics) in 2004 and received his PhD in Fluid Mechanics from the University of Poitiers in 2007. He joined Onera in 2010 and works as a research scientist in the Aerodynamics and Energetics Modeling Department in Toulouse. His research interests include experimental investigations on boundary-layer transition (flow control, tripping criteria and new devices for transition detection).

Alain Seraudie joined Onera in 1972 and worked as a research assistant specialized in experimental investigations on transonic flows. Graduated from Conservatoire National des Arts et Métiers (CNAM) in 1982, he then worked as a research scientist in one of the first cryogenic, pressurized and transonic wind tunnel in Europe. In the early 2000's, he joined the research unit "Transition and Instability" led by D. Arnal and started working experimentally on boundary-layer transition issues until he retired in 2011.

Olivier Vermeersch graduated from École Nationale Supérieure de Mécanique et d'Aérotechnique (ENSMA - French engineering school specialized in space and aeronautics) in 2006 and received his PhD in Fluid Mechanics from the University of Toulouse in 2009. Since then, he has worked as a research scientist in the Aerodynamics and Energetics Modeling Department of Onera. His research interests include boundary-layer stability computations and control of the laminar/turbulent transition with different kinds of actuation (micro-sized roughnesses, plasma actuators).

Daniel Arnal is a graduate from of Ecole Nationale Supérieure de Mécanique et Aérotechnique (ENSMA) in Poitiers, France. He received his PhD in 1976 from Onera Toulouse. He is working for more than 30 years on the topics related to laminar-turbulent transition (hydrodynamic instability, transition prediction, laminar flow control). In 1998, he became the Head of the research unit "Transition and Instability" in the Aerodynamics and Energetics Modeling Department at Onera Toulouse. He published approximately 150 archival journals or meeting papers.

Nikolas Goldin obtained his degree in Applied Mathematics from the Technische Universität Berlin in 2006. He completed his Dr.-Ing. in Control Engineering at the same institution in 2013. He is currently with DFG SFB 1029 at Technische Universität Berlin as a postdoctoral researcher. His research interests include drag reduction by flow control, biomimetics and flow control in gas turbines.

Rudibert King received his Dr.-Ing. from University of Stuttgart in 1988 and completed his habilitation in 1993. In 1993, he joined the University of Siegen as a Professor for Simulation Techniques. He moved to Berlin where he was appointed to Professor for Measurement and Control at the Technische Universität Berlin in 1995. His research interests include process control of chemical and biological systems, flow control, automatic modelling of reaction systems and control in uncertain systems.

F. Ternoy, J. Dandois, F. David, M. Pruvost
(Onera)

E-mail: frederic.ternoy@onera.fr

Overview of Onera Actuators for Active Flow Control

The purpose of this paper is to present an overview of existing actuators at Onera for active flow control. These actuators are used for various applications in wind tunnel tests, from 2D models to half-wing and helicopter models, for external or internal aerodynamics subjects.

Depending on the available volume in the models and on the aerodynamic requirements in terms of actuation magnitude and bandwidth from subsonic to transonic conditions, various technical solutions have been retained.

There are many ways to classify actuators between mechanical/fluidic, zero-net-mass-flux/nonzero mass flux/plasma, etc. The first part of this paper is devoted to mechanical actuators (moving aileron, mini trailing edge devices and deployable vortex generators). Fluidic actuators are presented in the second part, which deals with pulsed fluidic vortex generators, pulsed blowing slots and synthetic jets. The third part is focused on the characterization of the fluidic actuators.

Introduction

The field of flow control has witnessed an explosive growth of the number of publications over the last twenty years. It is now a well-accepted fact that flow control is a key technology to improve aerodynamic performance beyond actual aerodynamic design. To actively control the flow around an aircraft or a rotorcraft, one necessarily needs efficient actuators compact enough to be integrated inside the vehicle, taking into account the structural aspects. There are numerous types of actuators in the active flow control literature, but the most popular ones, and this is not an exhaustive list, are the pulsed blowing actuators [1], the zero-net-mass flux actuators [2], the plasma [3,4], the combustion driven device [5], the sparkjets [6-8], the vibrating flaps [9-11], the Hartman tube [12-15] and the fluidic oscillators also called sweeping jets [16]. A review of existing actuators for active flow control can be found in ref. [17] and [18]. The purpose of this paper is to present an overview of existing actuators at Onera for active flow control.

Tools for flow control …

Studies dealing with load control or flow control carried out by the actors of aeronautical research has led for many years to experiments on scaled wind tunnel models. By definition, these demonstrators are in general equipped with integrated actuators, controllable remotely and whose characteristics depend on the physical phenomenon to be controlled. There is a tremendous amount of types of actuators in the active flow control literature, and they can be classified in various ways. One possible classification is to organize them as mechanical and fluidic actuators.

Mechanical actuators are aimed at modifying the shape of a vehicle, so as to act directly on its aerodynamic coefficients. They can be devices allowing the control of components, such as an aileron or a mechanical vortex generator, or systems able to deform the wing locally in an elastic way, for example to modify the twist of a wing.

Fluidic actuators modify the main flow around the vehicle by injecting a secondary flow on its surface. It is, in this case, the interaction of this secondary flow with the main flow that leads to a modification of the aerodynamic performance of the vehicle.

… and simulation devices

For simple cases, commercial off-the-shelf devices are directly usable in the wind tunnel models, without modification, or after minor adaptations. However, it is clear that many studies require complex solutions to be implemented, often starting from existing technological bricks, in terms of control, motorization or regarding the kinematics of the devices. A strong constraint in the specifications of such actuators is the compatibility with the volume available in the model, taking into account, not only the vehicle shape, of course, but also

the constraints related to safety criteria, in terms of mechanical resistance or of the integrated services and the problems of accessibility to these elements. When the physical principle to be simulated by the actuator already led to the realization of “large scale” actuators, the passage on the small scale model, with the respect of the similarity rules, generally means the review of the existing design from zero.

Today, in most cases, numerical simulations allow the evolution of all flow variables to be followed, including those inside the fluidic actuators. Nevertheless, it is necessary to validate these unsteady numerical simulations with flow and load control, with the experimental approach using such advanced actuators. These tests allow the phenomena to be investigated taking into account all of the fluid physics parameters.

The aim of these studies being the fine characterization of the phenomena, precision on the actuators (geometry, position, output velocity, signal shape, etc.) remains essential.

Mechanical actuators

Largely used on commercial aircraft, this type of actuator is naturally the subject of many developments within the framework of industrial model projects for wind tunnel tests. In most cases, their only purpose is to increase the test productivity, by avoiding any human operation on the models at each configuration change. However, some studies on aerodynamic control are interested in an unusual operation of known control surfaces, or in the integration of completely innovative control surfaces. It is in this case requested to design, manufacture and develop adapted motorizations.

Remote controlled aileron by hydraulic system

Context

Within the framework of the French program “DTP Modèles 3” (see ref. [19] for more details), which is aimed at validating numerical methods for aircraft configurations featuring control surfaces, the goal is to design, manufacture and operate an actuator that allows a remotely controlled aileron to be integrated into a modern half-wing model, to be tested under transonic conditions (figure 1). The actuator must be compatible with high loads at high frequencies.

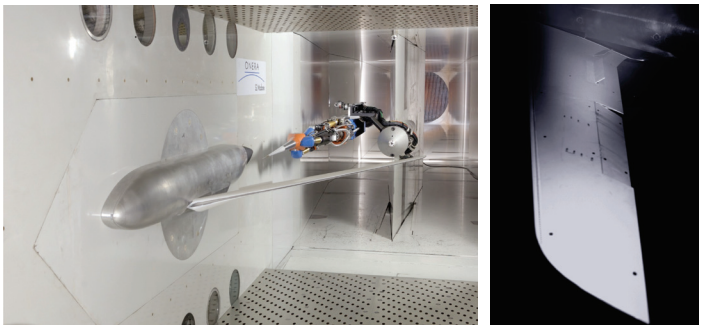

Figure 1 - DTP Modèles 3 – half-model in the S2MA wind tunnel (left) and detailed view of the R/C aileron (right)

The approximate dimensions of the aileron are 47 mm mean chord and 256 mm span, and the requirements in terms of displacements and efforts to sustain are:

- Static characteristics:
  - Positioning to static positions in the range [-15°; +15°];
  - Operational over the whole total pressure range [0.5; 1.9 bars];
  - Operational over the whole Mach number range [0.70; 0.89];
  - Operational up to the maximum lift coefficient;
- Dynamic characteristics:
  - Total pressure 0.5 bar (for pure aerodynamic purposes);
  - Unsteady aileron setting around an aileron average setting (sinusoidal type or step);
  - Average aileron setting in the range [-12°; +12°];
  - Dynamic movements up to 200 Hz;
  - Movement amplitude from ±1° (200 Hz) to ±3° (lower frequencies).

Technical solution

Due to the magnitude of the loads on the aileron (12 Nm maximum hinge moment), a hydraulic servo valve is used to provide the necessary power. The hydraulic pressure is driven to the aileron through the wing span in a cavity shared with the instrumentation wires (figure 2).

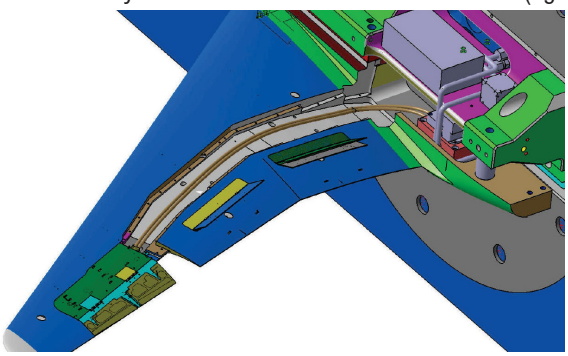

Figure 2 - Hydraulic pipes inside the wing main cavity

An innovative mechanical system is developed to transmit the movement to the aileron in the limited volume available in the aileron region. The solution is based on a multi-cylinder hydraulic system. Each cylinder pushes a stinger attached to the aileron at a certain distance from the aileron hinge, to allow for rotation. One stinger is equipped with a LVDT (Linear Variable Differential Transformer) sensor used as control sensor in the closed loop system. A second LVDT sensor is installed in the root area of the aileron and allows the surface deflection to be measured directly on the part. The aileron motorization is designed as a separate device, so that it is possible to test it first on a bench before integration into the wing.

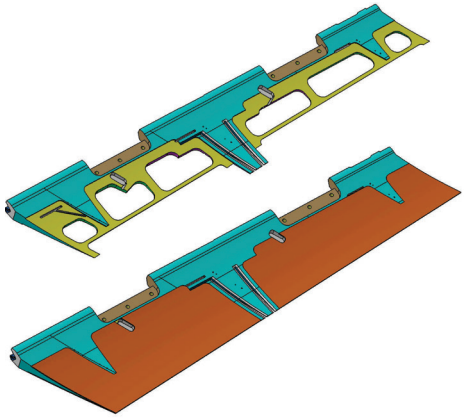

Figure 3 - CAD view of the aileron structure (above: without external composite skin)

The design takes into account the wing's deflection under aerodynamic loads, which is estimated by FEM analysis so that the behavior of the actuator is not modified because of the bending of the model. The aileron structure (steel structure and carbon skins) is a compromise between robustness, moment of inertia and internal stress, resulting in a surface with low deformation distortion over its span. To reduce its stiffness, the structure of the aileron is partially split over its chord following a « V » shape slots filled with adhesive silicon (figure 3).

Characterization

During the design phase, the response of the system is estimated analytically. Since the functioning with several cylinders in parallel is innovative and challenging, several tests are performed on the system to identify and adjust its response over the complete amplitude and frequency domain. The closed loop control is tuned by the analysis of successive Black diagrams, obtained with frequency sweeps between 10 Hz and 200 Hz. The response of the system is improved by using two electronic correctors.

Tests are first performed on a bench. For these tests, the aileron is replaced by a simple part, identical in terms of inertia. Three frequency cases are tested (figure 4). The system response to a step is also tested (figure 4d). The aileron position accuracy is improved by using an additional high frequency signal on the main input, which reduces the threshold effect of the servo valve. A loading test is also performed to check the stiffness of the system.

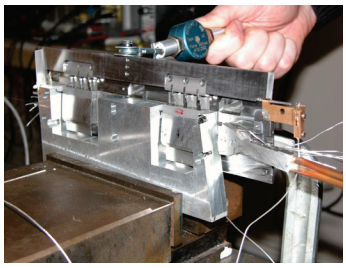

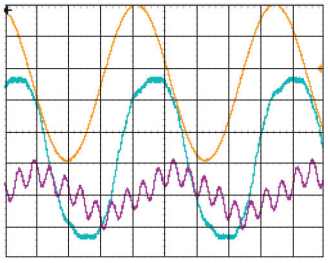

a) 45Hz ±2.5°

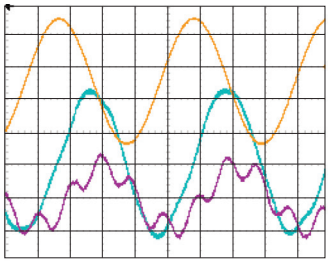

b) 95Hz ±2°

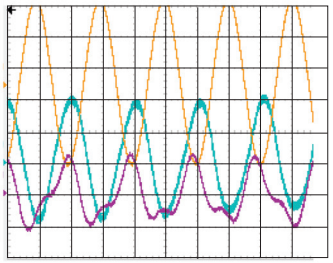

c) 195Hz ±1°

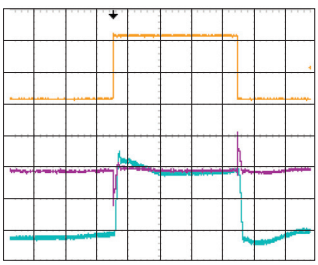

d) step of 2°

Figure 4 - Test bench (top) and response measurement for 4 cases (yellow: input signal - purple: input corrected with additional high frequency signal - blue: control sensor)

A second run of tests is performed after actuator integration into the wing and before the wind tunnel entry. The position of the aileron is recorded through the inner sensor and 2 Keyence systems located at the inner and outer part of the aileron (figure 5).

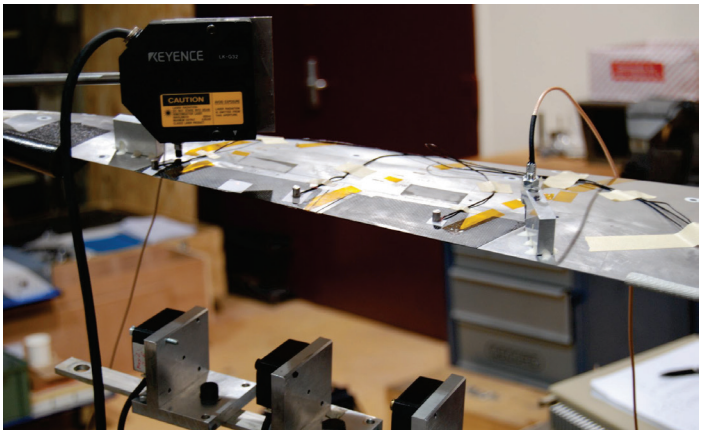

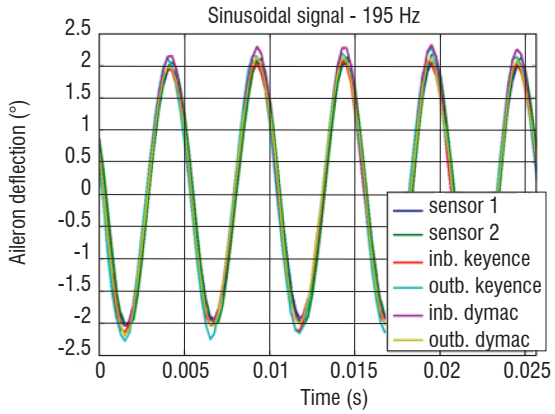

Figure 5 - Integrated actuator and final response analysis

Remote controlled piezoelectric mini trailing edgede vices

Context

This study was performed within the EC funded AWIATOR project managed by Airbus (see ref. [20] for more details). The aim is to test technologies applicable to future airliners and to study new control surfaces that could improve the wing performances during takeoff and landing operations.

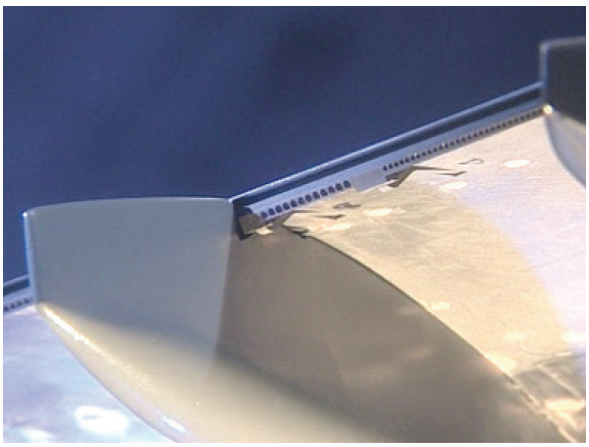

Figure 6 - Detailed view of the RC mini-TEDs (close-up view of the trailing edge on the lower side)

The work carried out by Onera consists in integrating a trailing edge equipped with mini-deflectors into the wing of an existing A340 1/19th scaled model. These mini-deflectors, called “minis-TEDs” (mini Trailing Edge Devices), whose chord is equal to 5mm, are controlled in frequency and amplitude. The bandwidth is 180 Hz for an amplitude of 10°. Electronic control allows piloting the deflectors using sinusoidal or step laws.

Technical solution

Contrary to the previous hydraulic actuator, the lower aerodynamic loads allow the use of a piezoelectric motorization. The model has 2 movable surfaces (mini trailing edge devices with a chord length equal to 2% of the profile) actuated by the piezoelectric actuator via a kinematics based on a lever and rod devices. The actuator is an amplified piezoelectric actuator designed especially for this model (dimensions: 10*49*141mm – max displacement: 0.5mm – max force: 700N).

This piezoelectric actuator has very short displacement amplitude, so it is necessary to amplify it to obtain a significant movement of the TED by using lever and rods integrated inside of the model. The kinematics converts the translation into a rotation of about 60° for the TED. The proposed design allows the relative angle of the 2 mini-TEDs to be adjusted accurately.

All of the articulations of the mechanism are obtained with “joint blades” to avoid any gaps that would lead to problem for the dynamical response of the system. Each part of this mechanism is optimized, in terms of mass and mechanical resistance, in order to obtain the specified bandwidth.

The joints, between mini-TEDs and rods on the one hand and between mini-TEDs and wing on the other hand, are obtained with very accurate shafts and bores, in order to decrease the mechanism gaps as much as possible.

Characterization

The mechanism is driven by an electronic control system. There are 4 position sensors installed in the mechanism: the first one measures the lever displacement, two sensors on outboard TED measure the angular position of the outboard TED via specific measurement rods and the last one directly measures the angular position of the inboard TED.

As for the dynamic aileron case, the response of the system is estimated analytically. The closed loop control is tuned by analysis of successive Black diagrams obtained with frequency sweeps between 10 Hz and 200 Hz. To make this actuator compatible with the specifications, the response of the system is improved by using two electronic correctors and adjustments are done following the results of lab tests performed first on bench.

Deployable mechanical VGs

Context

Helicopter rotor blades encounter a wide range of aerodynamic conditions during cruise flight, varying from transonic flow, with moderate angles of attack on the advancing blade side, to low subsonic flow with large angles of attack on the retreating blade side. With increasing cruise speed, angles of attack above static stall are reached on the retreating blade side. The cyclic pitching motion of the blade then leads to dynamic stall that induces large unsteady loads. In particular, large negative (nosedown) pitching moments are observed during dynamic stall and induce large impulsive pitch-link loads that can damage the control command of the helicopter. Dynamic stall may appear under several flight conditions, such as high-speed forward flight or maneuvers, and it strongly limits the flight envelope of the rotorcraft. The pitching moment alleviation of the dynamic stall will lead to an extension of the flight envelope, by reducing the unsteady loads on the blade, limiting the blade aeroelastic response and decreasing the vibratory loads for high-speed forward flight. Therefore, dynamic stall-related topics have been studied, in order to improve the understanding of the complex physical phenomena involved when the flow separates during the pitching motion of the blade. Dynamic stall control using dedicated actuated devices has also been studied. This was the main goal of the Onera-DLR "SIMCOS" research project (see ref. [21] for more details). In this project, the pitching moment is reduced by generating vortices with numerous (120) small blades located at the very leading-edge of a bi-dimensional “OA209” airfoil model.

Technical solution

Theses blades are spaced by 11.5 mm and oriented on an angle of 18 degrees with respect to the freestream (figure 7 and figure 8). With this orientation, each blade produces a vortex that will expand along the upper surface of the airfoil.

In order to reduce the pitching moment while avoiding drag and lift penalties outside the aerodynamic stall conditions, an active device is designed and, at the same time, the blades fit the airfoil leading-edge shape so that, when retracted, the airfoil is clean. The blades, named "DVGs" (Deployable Vortex Generators) are displaced with a forward-backward translation motion.

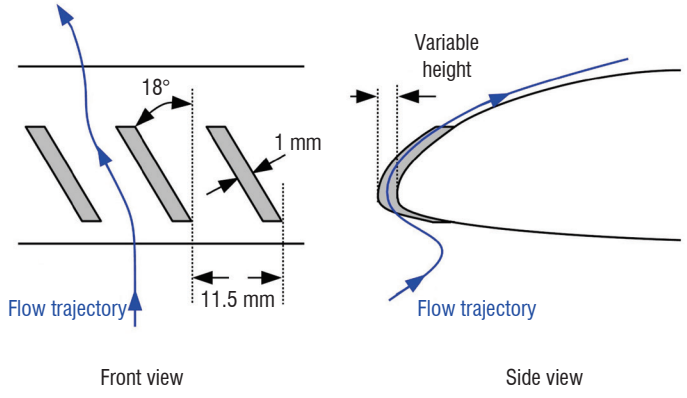

Figure 7 - Sketch of the vortex generator system

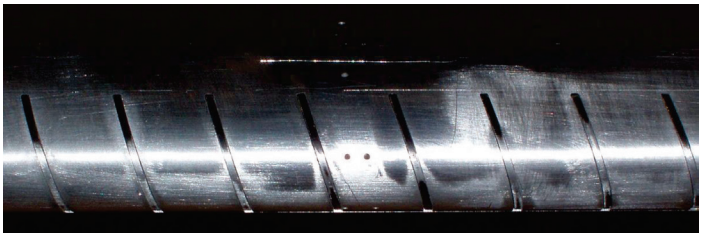

Figure 8 - Leading edge of the wind tunnel model

Facing the required amplitude (up to 3 mm), the control motion system makes use of two hydraulic jacks located in the airfoil body. The blades are fitted to the control system with the aid of a transverse carbon fiber bar, which goes through each blade heel (figure 9).

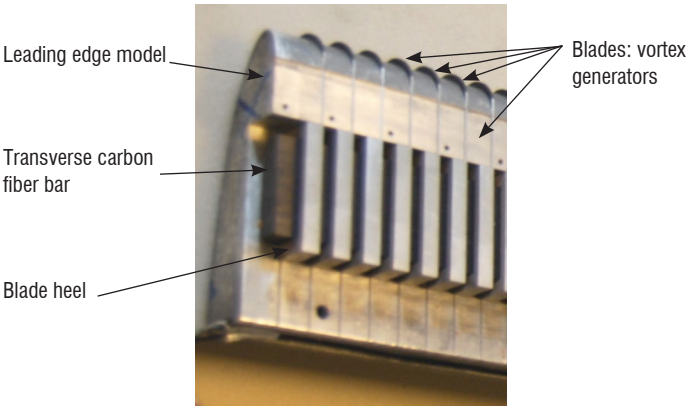

Figure 9 - Bottom view of the leading edge without its lower surface

A Teflon treatment is applied on each DVG, in order to limit frictions during the deployment. The clearance between the DVG, the model and the bar, is judiciously applied in order to insure the functioning and the control even with the model distortion caused by aerodynamic loads.

The test campaign has shown the efficiency of such a device and also shown that the size, the density and the maximum displacement of the blades should be reduced, with up to 55% reduction of the negative pitching-moment peak for height displacements between 1.5mm and 1.7mm [21], offering the possibility of using a more compact motion control system, like a piezo-hydraulic system, for example.

The effect of VGs was also evaluated numerically, showing that thinner blades could be more efficient (see ref. [22] for more details).

Actuator Characterization

Lab tests were performed and showed that the DVGs can be actuated at operational frequencies from 1-per-rev (approx. 3.5 Hz) to 10-per-rev (approx. 35Hz) for the full range of height deployment (3 mm), with a mean accuracy of 0.05mm (figure 10).

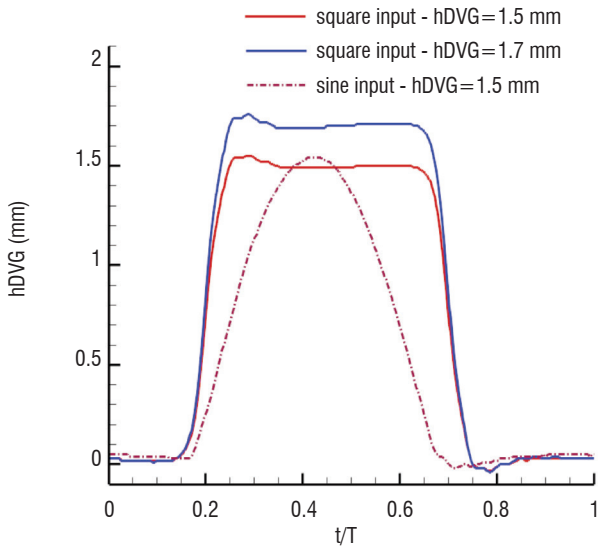

Figure 10 - Displacement response under square and sine excitations at 1 per-rev

The reliability of this simple device has been proven by a huge number of functioning hours (up to 150 functioning hours without control accuracy loss).

Fluidic actuators

In addition to the studies conducted on the mechanical actuators, the main current axis of research in the active flow control actuator community is the development of fluidic actuators. The goal is to address several external aerodynamics subjects (lift increase, drag reduction, buffet control) and internal aerodynamics ones (advanced air intakes). The development of these techniques and corresponding methods of CFD analysis requires wind tunnel tests. Two types of fluidic actuators are developed at Onera.

Pulsed blowing actuators are valves controlling the mass flow rate from an air feed whose characteristics (temperature and pressure) are generally fixed. These actuators can be used at various frequencies and duty cycles, the continuous blowing case being only a particular case where the forcing frequency is null. Today, many developments are made, not only by industrials specialized in the field of valves, but also by research institutes, to develop devices able to generate pulsed jets; however, the characteristics of these actuators remain limited. The main interests of the developed devices, compared with state of the art devices, are that they offer in a very small volume a high mass flow with the possibility to adjust it progressively for a large frequency bandwidth.

Synthetic jet actuators are different from the previous ones, due to the fact that they do not require any external air feeding. They work in the manner of syringes: the piston movement is alternate and a small quantity of fluid is successively sucked and expelled through an orifice, or a slot, in the main flow. Spark-jets which are not presented in this paper are a particular case of synthetic jets, for which the alternate fluid motion is obtained by a discharge from the cathode to the anode. The rapid gas heating generates an increase of the chamber pressure. Then, the high-pressure gas exhausts through the chamber orifice at high velocity. In the next stage, the initial conditions are recovered through the sucking of fresh air from the outside. For the synthetic jets actuator a brief analysis of the state of the art is given hereafter.

Such studies are at a very low Technology Readiness Level and also require the development of a suitable methodology, in order to characterize the gas jets in a fine way, and to make the wind tunnel test measurements exploitable.

Pulsed fluidic vortex generators

Context

Within the framework of the Onera internal project PRF BUFET'N CO [23,24], wind tunnel tests with fluidic actuators were carried out under transonic conditions. The objective of the project is the closed loop control of the buffet phenomenon to delay its onset on a wing. The reader interested in a summary of the results can refer to ref. [24] in the same volume of Aerospace Lab. One of the solutions tested is based on the use of pulsed fluidic vortex generators (VGs), requiring the development of specific actuators whose characteristics are the following:

- Orifice shape: circular section with diameter equal to 1mm;
- Fluidic VGs locations, spacing and blowing angles: located at 25% of chord, spacing equal to 10 diameters, pitch angle between the jets and the local wall tangent equal to 30° and skew angle between the jets and the freesteam direction equal to 90°;
- Maximum Mach number (nozzles): Mach 2;
- Frequency bandwidth: 1 kHz;
- Maximum mass flow: 1 $g.s^{-1}$ per hole.

The wing in which these devices are integrated has a span equal to 1.2 m. It is based on the OAT15A profile with a chord length equal to 300 mm in the equipped area.

Technical solution

The actuator is composed of a tight case in which the active devices are placed. The jet exit holes are located in the inner top face. The external face receives an interchangeable cover (in green on figure 11) in which the nozzles are milled, making it possible to create the desired jets (form, speed, direction). The general principle consists in controlling a valve actuated by an actuator. The generator is composed of a series of cells, each comprising one actuator (figure 12). The active elements are piezoelectric stacks amplified mechanically. These actuators lengthen proportionally with the tension applied to them. With such active elements, the frequencies can be higher than 1,000 Hz and the ratio between the volume and the product force by displacement is particularly interesting (volume=500mm^3 – max force*max displacement = 0.4N*mm). The stroke of the valve, which remains limited, is compensated by the length of the exit section, which is at its periphery.

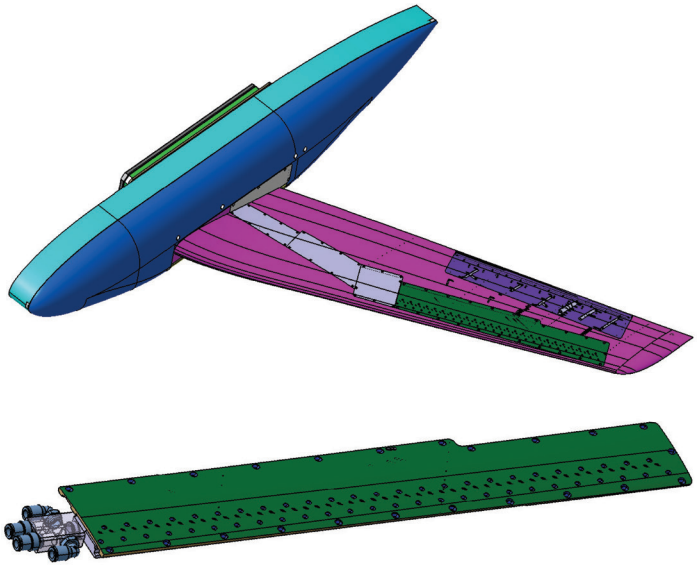

Figure 11 - CAD views of the model and the actuator clamped on its cover

To obtain a supersonic jet at the exit, it is necessary to have a high relative pressure. The maximum force that can be delivered by the piezoelectric actuator limits the diameter of the valve. Indeed, the latter is pressed on its seat when the valve is closed. The mechanical amplification system allows sufficient force to be kept available to move the valve under these conditions.

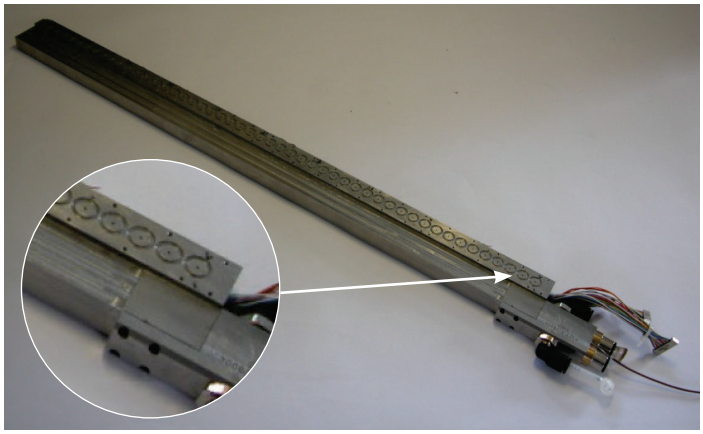

Figure 12 - Pulsed jet actuator (global view, leftt: detailed view of the orifices)

Actuator command and characterization

The actuator can be either controlled in an all-or-nothing way, or in a proportional way. In the case of a proportional valve opening, the command requires the use of an off-the-shelf commercial amplifier. If the actuator is used in an all-or-nothing way, the device having only two states (open or closed), a binary command of the actuators is sufficient and specific electronics are developed for the power supply. The actuators are either electrically fed or short-circuited. Since the electric behavior of these actuators is similar to a capacitance, the current becomes very important at high frequencies. Since the supply voltage is high also, the power needed can become very high. Depending on the operating time and the commutation frequency of the electronics, the protection resistances, as well as the cooling system, are dimensioned to limit the electronic temperature.

Visualizations by Schlieren photography are performed to check whether the jets are supersonic (figure 13). The mass flow measurements also allow the capacities of these actuators to be validated, to fulfill the specifications.

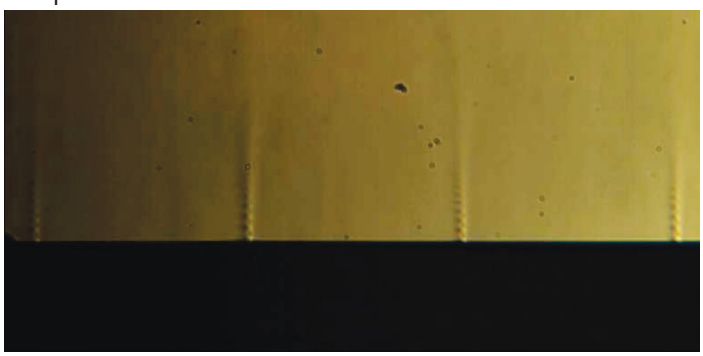

Figure 13 - Schlieren photography of the supersonic jets

Figure 14 shows the mean mass-flow for the 50 actuators with a sinusoidal excitation signal at various frequencies from 10 Hz to 700 Hz. It points out that the mean mass flow is rather uniform over the 50 actuators (~0.15g.s-1 +/- 0.03$g.s^{-1}$ except for actuator number 8) and that the actuator response is rather flat over the entire frequency range [10 Hz; 700 Hz] (delta max = 0.04$g.s^{-1}$).

Figure 15 shows the excitation signal (in black) and the measured velocity by hot-wire for various frequencies between 100 Hz and 700 Hz at a supply pressure of 2.7 bars. The peak velocity decreases

from 320 m.s-1 to 250 m.s^{-1} when the forcing frequency increases but the shape of signal is well preserved and there is no leak at high frequencies as it is often observed for other actuators.

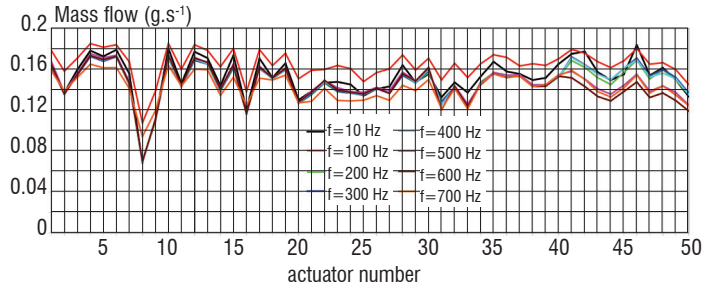

Figure 14 - Mean mass flow for the 50 actuators and a sinusoidal excitation signal at various frequencies

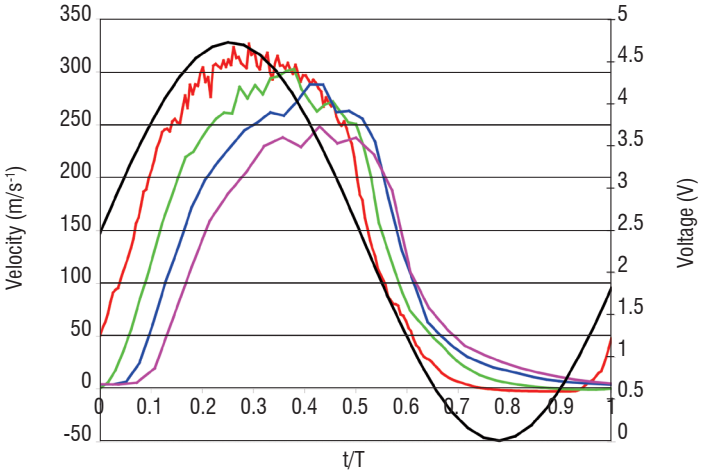

Figure 15 - Excitation voltage signal (in black) and hot-wire velocity signals for various frequencies at a supply pressure of 2.7 bars (red: 100 Hz, green: 300 Hz, blue: 500 Hz, purple: 700 Hz)

Pulsed blowing TED

Context

Within the project PRF BUFET'N CO, another kind of pulsed blowing actuator was integrated and tested on the wing described in the previous chapter. The reader interested in a summary of the results with this actuator can refer to ref. [24] in the same volume of Aerospace Lab. Specific tests were performed on fluidic TEDs (Trailing Edge Devices) whose characteristics are:

- Orifice dimensions: slot width equal to 0.2 mm and length equal to 490 mm in the spanwise direction (between 45% and 85% of the wing span);
- Slot location and orientation: located at 95% of the chord on the lower side of the model; normal blowing with respect to the local wall tangent;
- Frequency bandwidth: 200 Hz;
- Maximum mass flow: 140 g.s^{-1} per meter span in this configuration.

Technical solution

The actuator is based on the same principle as that used for the pulsed vortex generators, adapted for large mass flow or large scaled model applications. Indeed, it meets specifications that are less restricting in terms of bandwidth and volume availability, but more restricting concerning the high mass flow to produce. The actuator is installed in a large cavity in the model and feeds the slot via holes connected to a plenum integrated in the trailing edge of the model (figures 16 & 17).

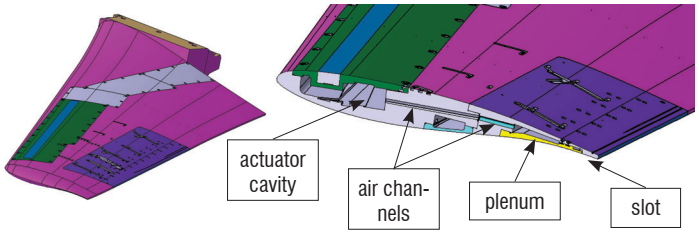

Figure 16 - CAD views of the model and section view of the air channel area

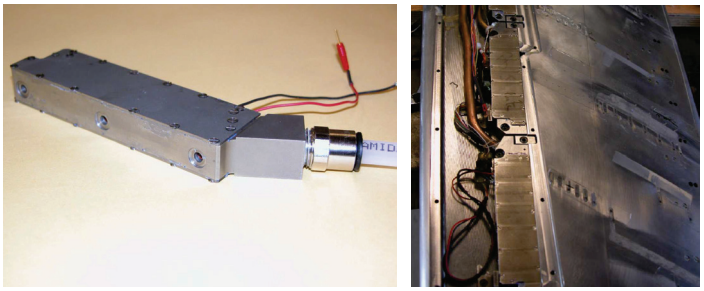

Figure 17 - actuator before integration (left) and integrated inside wing's main cavity (right)

The actuator employs piezoelectric stacks elements whose displacement is amplified mechanically by using kinematics based on steel joint blade articulations. The valve is made of aluminium to minimize its mass and reduce the response time of the system. To improve the behavior of the actuator at high frequencies, additional mechanical absorbers can be added between the valve and the tight case of the actuator. The air supply is connected directly onto the main body of the actuator. Its geometry is designed to ensure a good homogeneity between the 3 holes at the exit of the actuator.

Actuator command and characterization

As for the pulsed fluidic vortex generator, the actuator can be either controlled in an all or nothing way or in a proportional way, by using of a commercial amplifier or with a specific electronic developed for the power supply.

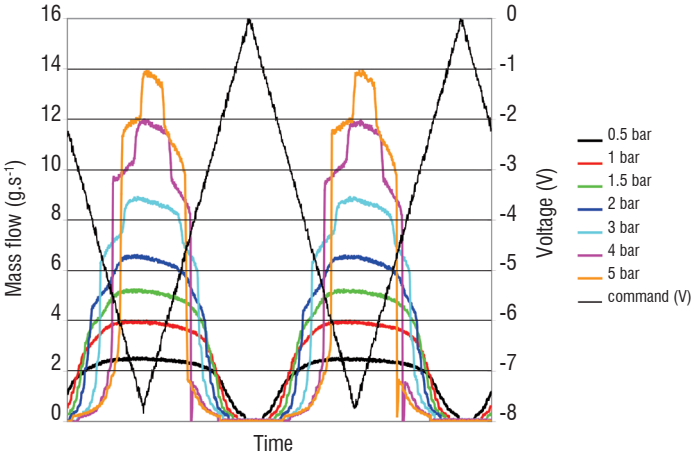

Figure 18 - Mass flow evolution vs. time for a triangular voltage signal and different air feeding pressure

Figure 18 shows the time evolution of the mass flow for a triangular voltage excitation and different air feeding relative pressure from 0.5

to 5 bars. It shows that it is possible to control the mass-flow in a proportional way and that the maximum mass flow is equal to 14 $g.s^{-1}$ for a relative pressure of 5 bars, for 10 cm slots length in the span wise direction.

Application of active flow control at the leading edge

Within JTI Clean Sky Smart Fixed Wing Aircraft Integrated Technology Demonstrator (SFWA-ITD) European project, a study was made in order to evaluate how compact a valve should be to be compatible with the equipment of a scaled 1 business jet wing tip. This actuator was proposed for integration and the outcome is a representative insert equipped with a large scale valve which blows through a tangential slot with a width of 0.5 mm located at 1% of the local chord (figure 19). In this configuration, the actuator is able to generate a pulsed blowing of 200 $g.s^{-1}$ per meter span at 200 Hz.

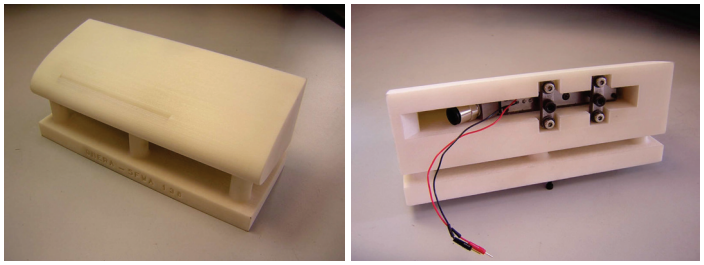

Figure 19 - Picture of the actuator integrated in a part representative of a scaled 1 wing tip

Synthetic jets by piezoelectric actuators

Context

Within the framework of the JTI Cleansky Smart Fixed Wing Aircraft (SFWA-ITD) and Green Rotorcraft Integrated Technology Demonstrator (GRC-ITD) European projects, many developments are carried out on the synthetic jet actuators. One of the objectives of SFWA-ITD is to increase Technology Readiness Level of this kind of devices. Onera is involved in this work and develops actuators which could be integrated and tested in wind tunnel models for both SFWA-ITD and GRC-ITD projects.

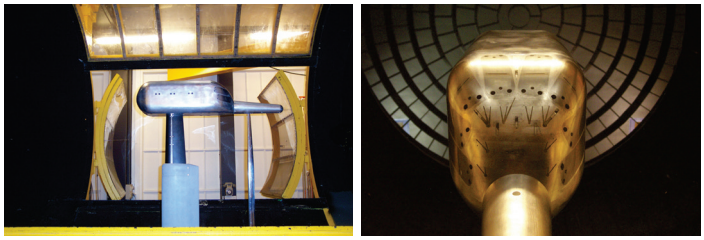

Figure 20 - GRC helicopter fuselage in the Onera L1 wind tunnel (left) and detailed view of the rear fuselage equipped with actuators (right)

Within GRC-ITD project, it was asked to integrate eight synthetic jets in the fuselage of a helicopter's wind tunnel model (figure 20 and [25] for the results). The specifications are the following ones:

- orifice shape: slots with dimensions 0.67mm*30mm;
- blowing angle: 45° with respect to local wall tangent;
- Peak velocity: 80 $m.s^{-1}$;
- Frequency bandwidth: 200 Hz.

The object of the study was to propose an actuator for which the speed of jets remains relatively constant on a large frequency bandwidth and for which it is possible to modify speed for a given frequency.

Comparison with state of the art

Many studies are dealing with synthetic jets devices. There are 2 main developments which are the subject of patents or publications.

The first one is the generators of synthetic jets operating piezoelectric technologies via the use of membrane type actuators, as it is the case for the following patents: US 2010/0044459A1, US 2010/0045752A1, US 2010/0043900A1, US 2008/0197208A1, US 2008/0087771A1. Contrary to these devices, the solution described in this paper does not imply the deformation of a membrane but the displacement of one (or several) piston(s), increasing the force and stroke available for the compression of the gas in the chamber of ejection. On the other hand, because of the actuator characteristics, the use of the membrane synthetic jets is limited to an optimal frequency generally based on the resonance of the active part and the cavity where is compressed the gas before ejection.

A second development deals with piston technology, as described in [5]. The main difference compared with Onera's design is that this solution is based on the movement of a piston actuated by a cranck/rod system which does not allow the adjustment of the piston stroke, and, as a consequence, does not allow the regulation of the jets speed for a given frequency.

Technical solution

Figure 21 shows a picture of one synthetic jet actuator. The synthetic jet comprises a cavity delimited by a fixed wall and a mobile wall. The fixed wall contains a sleeve and a head provided with an orifice through which the fluid is sucked from and expelled to the main flow. The mobile wall is opposite to the head. The actuator comprises a rigid piston which slides into the sleeve.

Figure 21 - One synthetic jet before integration into the model

The synthetic jet is based on a piezoelectric stacks actuator, mechanically linked with the piston and able to drive it with an alternating movement having a variable amplitude and frequency. Once again, since the stroke of the piezoelectric actuators is very short, the system comprises a mechanism for the mechanical amplification of displacements up to 0.6 mm, based on steel joint blade articulations in order to have a significant variation of the cavity volume. The fact that this amplification is not obtained by forcing of the piezoelectric at the natural resonant frequency allows a constant output velocity to be obtained over the entire actuator frequency range.

The solution applied here does not imply the deformation of a membrane, thereby increasing the force and the stroke available for the fluid compression inside the chamber. To modify the output velocity of the synthetic jet, the stroke of the piston is simply varied. The frequency bandwidth of this actuator is approximately 200 Hz.

Figure 22 shows the hot-wire velocity signal at the synthetic jet exit for three voltages at a frequency of 200 Hz. For this measurement, the hot wire is located in front of the slot. As expected, the higher the voltage is, the higher the output velocity is. The maximum output velocity is about 80 m.s^{-1}. The highest peaks correspond to the blowing phase and the lowest ones to the suction phase. Since for a synthetic jet the velocity vector is straight during the blowing phase and the flow coming into the actuator chamber is sucked in from all directions, the hot-wire location slightly above the actuator exit rather into the slot induces a difference in the amplitude of the velocity peaks between blowing and suction.

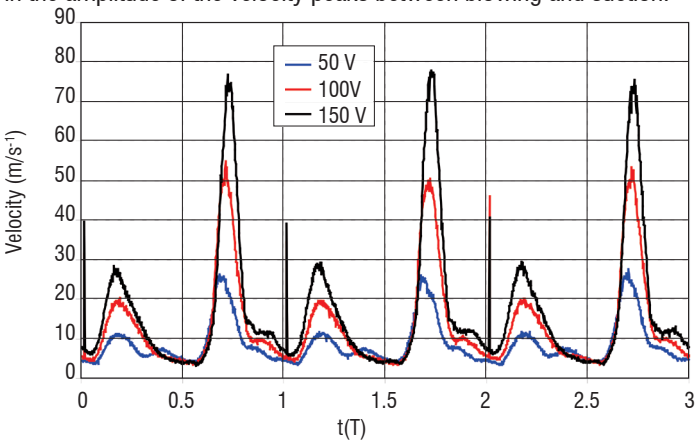

Figure 22 - Hot-wire velocity signal for three voltages at f=200 Hz

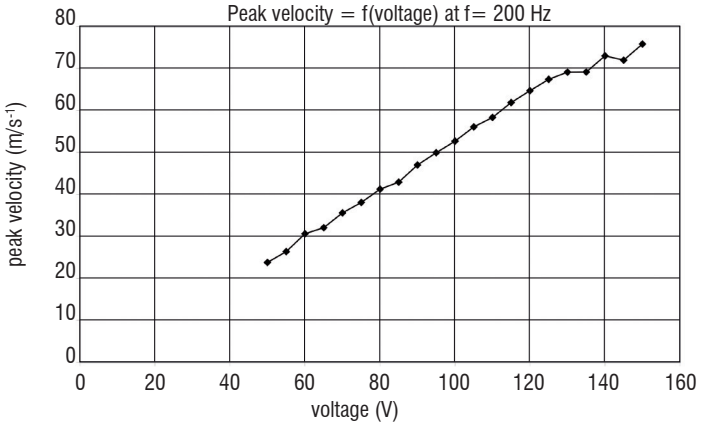

Figure 23 - Peak velocity as a function of voltage at f=200 Hz

The evolution of the peak velocity with the voltage applied to the actuator is plotted in figure 23 for a frequency of 200 Hz. As expected, since the piston stroke evolves linearly with the voltage, the peak velocity also evolves linearly with the voltage, since at the first-order (without viscous and compressibility effects), the peak velocity is given by:

$$U_{peak} = S_{piston}/S_{orifice}.A.\omega \quad (1)$$

where U_{peak} is the peak velocity, S_{piston} is the piston area, $S_{orifice}$ is the exit orifice area, A is the piston half stroke and ω is the pulsation.

The evolution of the peak velocity with the forcing frequency for a constant voltage equal to 150V is shown in figure 24. The peak velocity is nearly constant and equal to 80 m.s^{-1} between 170 and 240 Hz. Equation (1) shows that the peak velocity should increase linearly with the frequency but in fact, the rise time of the piston is constant and does not depend on the frequency. This is the reason why the peak velocity is constant between 170 and 240 Hz. In fact, in this case, it is the duty cycle, which varies with the frequency.

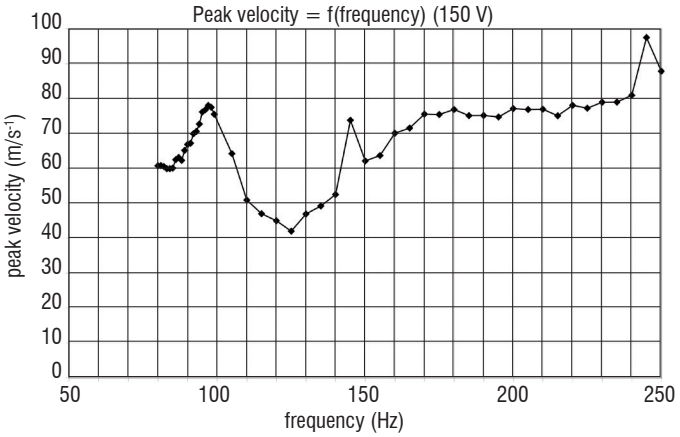

Figure 24 - Peak velocity as function of forcing frequency for 150 V

Actuator command

The input signal takes into account the mechanical behavior of the actuator and allows the piston displacement to be controlled according to the characteristics of the desired output velocity, by using gauge sensors installed on one steel joint blade of the kinematics. The input signal applied to the mechanically amplified piezoelectric actuator makes it possible to control the frequency and amplitude of the actuator. The difficulty with regard to the electric drive of such a device is how to take into account the mechanical response of the system to very short time pulses. To reduce the parasitic phenomena of oscillations, the input signal is adjusted (time-constant and duty cycle) according to the output signal. Sensors installed inside the actuator allow the piston displacement to be controlled by adapting it to the desired output velocity signal.

Application of active flow control at the leading edge

A study was carried out within the JTI Clean Sky Smart Fixed Wing Aircraft Integrated Technology Demonstrator (SFWA-ITD) European project, in order to evaluate the compatibility of this technology with the leading edge of a wing in a large scale model.

The outcome is a representative prototype equipped with a large scale synthetic jet actuator that blows through a tangential slot with a width of 0.2 mm and a span of 145 mm, located at 1% of the local chord (figure 25). In this configuration, the actuator is able to generate a jet whose velocity is equal to 110 m.s^{-1} [+/-10 m.s^{-1}] for a frequency range of [50 Hz; 200 Hz] (figure 26).

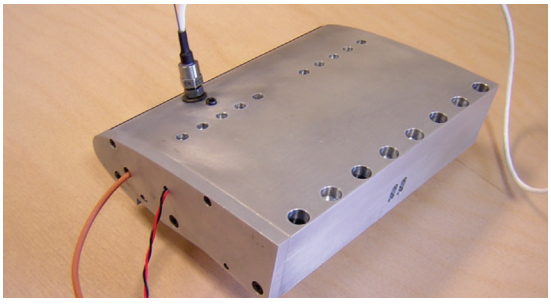

Figure 25 - Picture of synthetic jet actuator in a part representative of a large scale wing leading edge

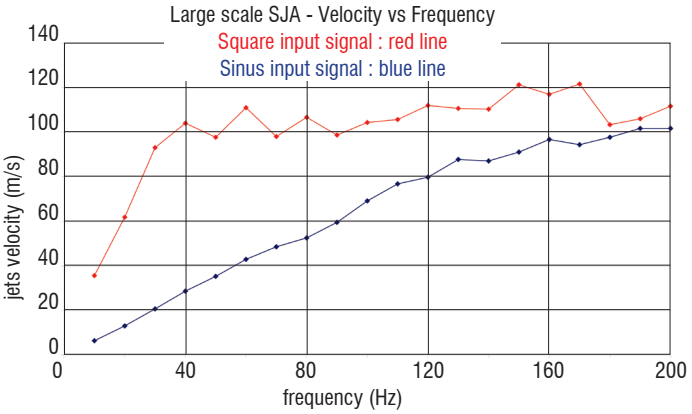

Figure 26 - Large scale SJA characterisation

Fluidic actuator characterization

The detailed knowledge of the performance of a fluidic actuator is a decisive input for its design and manufacturing process. The qualification of such an actuator is required, not only during the prototype optimization steps, but also for its reception as an isolated component of a wind tunnel model (figure 27) and once integrated into the model (figure 28). The qualification concerns all kinds of fluidic devices: continuous, pulsed and synthetic jets.

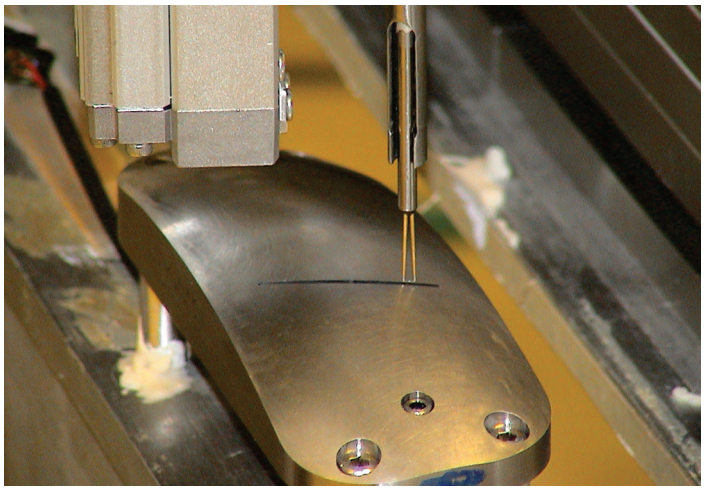

Figure 27 - Hot-wire qualification of an actuator as a wind tunnel model component

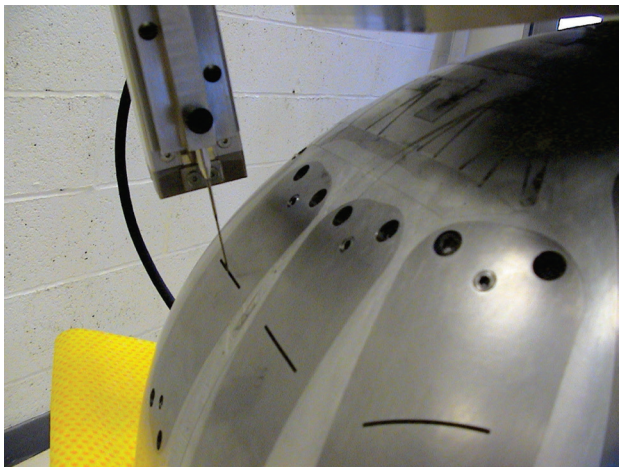

Figure 28 - Actuator qualification once integrated into the helicopter fuselage model

The objective of the qualification operations (referred to as "characterization") is to measure the performance of the actuator under quiescent air conditions, or exceptionally in interaction with an academic incoming flow, typically a turbulent boundary layer. Most often, the characterisation is performed on a specific bench, in quiet air. Thus, the characterization does not necessarily allow the identification of the actuator behavior under actual working conditions (wind tunnel tests once integrated in the model or flight conditions), which can be different from quiescent air conditions. However, it yields inputs for set parameters, such as input voltage or pressure, type of input signal shape, etc.

Generally, the characterisation consists first in determining the operational frequency domain in which the jet accurately responds to the desired input signal. Second, it consists in measuring the jet velocities (peaks or even entire shape of the velocity profile) in the operational frequency domain. Sometimes, it may include the assessment of the homogeneity of the exit velocities.

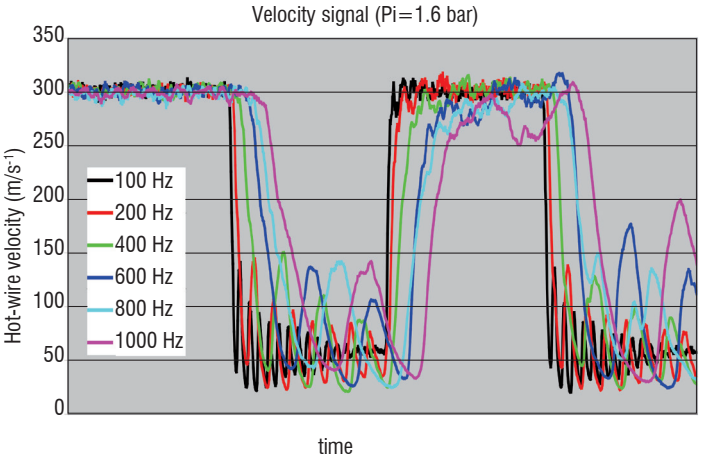

Figure 29 - Pulsed jet velocity obtained from hot-wire measurement with a square shaped input electrical signal – Specific in-situ calibration has been applied to HW before the measurement in order to catch an estimate of the instantaneous velocity (here 300 $m.s^{-1}$)

In practice, the excitation frequency ranges from ten hertz to one kilohertz and the jet velocity level can be low (incompressible flow) or high (supersonic compressible flow). For such conditions, the Hot-Wire Anemometry (HWA) is the preferred measurement technique: it is particularly well suited to derive (or at least get a good estimate of) the instantaneous velocity, or to identify velocity signal shapes (figure 29). For the latter, the velocity signal can be compared to other signals, such as electrical input, location of the moving component of the actuator or internal cavity unsteady pressure; this allows the transfer function, including amplitude and phase shift, to be derived. According to the results, the actuator will be (or not be) improved.

A key factor for the HWA is the calibration procedure. As a matter of fact, for most of the actuators, the classical calibration procedure in a calibrated, uniform flow does not apply. This is due to the diameter of the jet to be measured, which is of the order of magnitude of the hot wire length (figure 30). In such a case, the hot-wire active sensor sees the strong transverse gradient jet velocity profile, and is not uniformly cooled.

In order to take into account the jet velocity profile, a procedure has been developed to calibrate the hot-wire in-situ, i.e., without moving

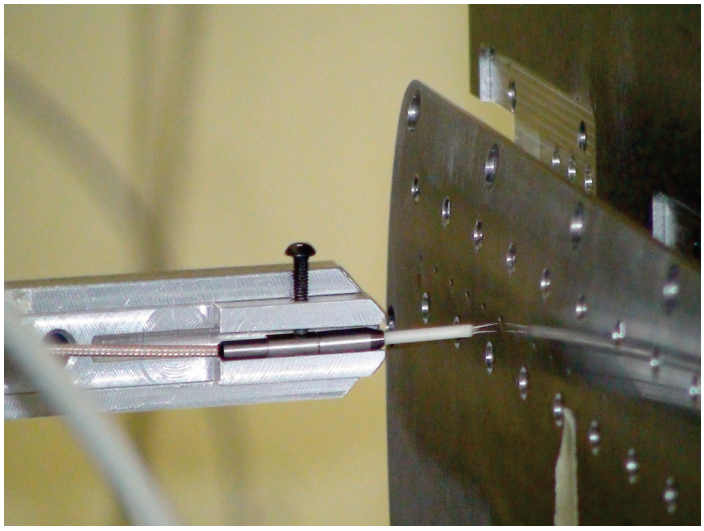

Figure 30 - Hot-wire in front of a supersonic jet actuator exit (here, a nozzle)

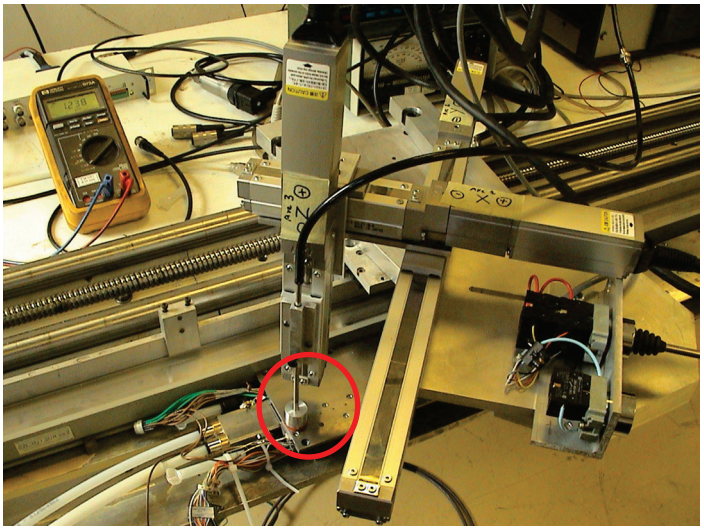

Figure 31 - Mass flow qualification of pulsed jet actuators using a specific air tight bell

the sensor for its calibration. This allows the hot wire to be calibrated with respect to well-known upstream conditions, either the total pressure of the air supply or the mass flow measured in the air supply circuit. In both cases, a theoretical velocity in the actuator exit section can be derived and thus, the relation between this theoretical velocity and the hot wire tension can be established for a range of upstream conditions. This procedure can directly be applied to continuous and pulsed jets, which require a pressurized air supply.

However, its application to synthetic jets is more challenging. For such devices, the notion of upstream conditions does not apply. In order to get such conditions, the actuation mechanism is temporarily replaced by a substitution nozzle, without any active mechanism, but with an upstream connection to the air supply. Once the relation between the hot-wire signal and the theoretical velocity has been established, the actuation mechanism of the synthetic jet is mounted again and its characterisation can be performed. Of course, this methodology is time consuming and delicate, especially when several actuators must be qualified simultaneously. Indeed, each new hot wire positioning requires a new specific calibration.

If the characterization of the velocity signal shape is not required, another method can be used for pulsed jets. The pulsed air can be collected at the actuator exit with an airtight bell (red circle in figure 31). Then, it is brought to a mass flow meter located downstream. This measures the average mass flow of the pulsed jet (figure 32).

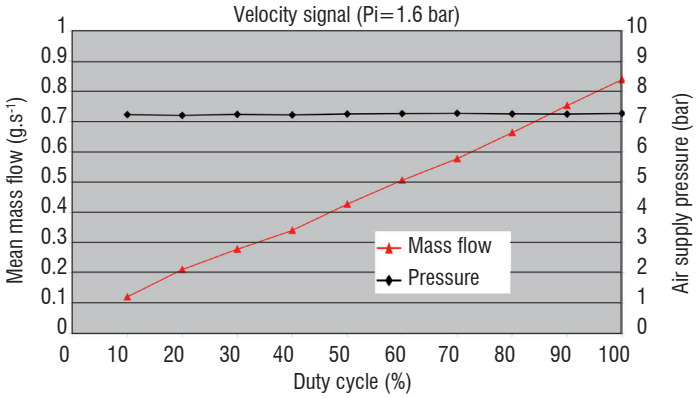

Figure 32 - Mean mass flow obtained with the bell method with respect to the duty cycle (square input signal)

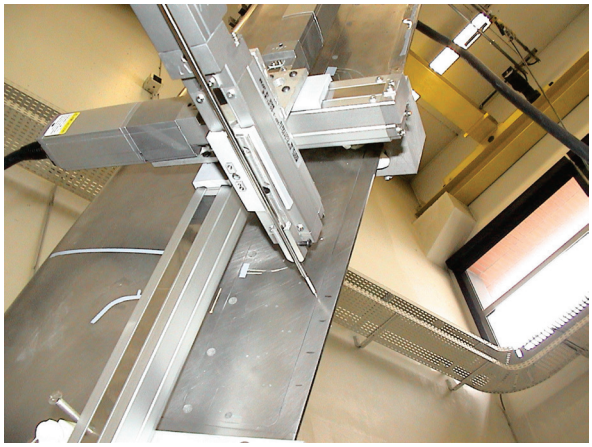

Figure 33 - In-situ hot-wire probing of a fluidic trailing edge device (TED). The probe is mounted on a high accuracy, motorized robot with 3 degrees of freedom

For cases where the hot wire length is much smaller than the jet exit section (limit arbitrarily fixed at 2 mm in next table), a classical calibration procedure can be used. A typical case is the high aspect ratio slot, for which the hot-wire can be moved in the slotwise direction. The velocity jet profile can be reconstructed from instantaneous measurements at different locations, using high accuracy robots and off-line post processing tools (figure 33 and figure 34).

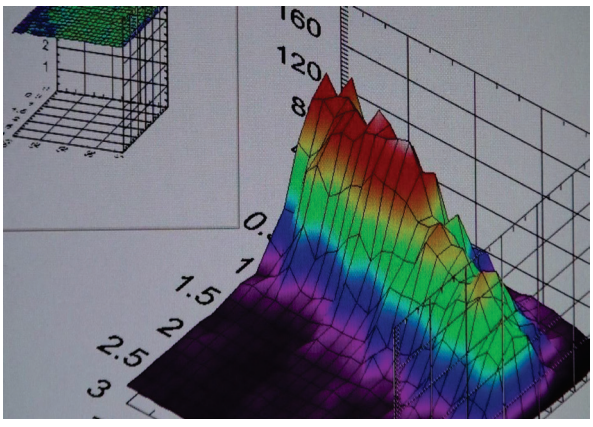

Figure 34 - Example of an instantaneous velocity profile at a slot exit (pulsed blowing TED)

Equipment	Actuator type➔	Pulsed		Synthetic	
Hot wire anemometry f_{max}>40 kHz	**Jet exit size➔ Measured data ↓**	**Lower than 2 mm**	**Longer than 2 mm**	**Lower than 2 mm**	**Longer than 2 mm**
Classical calibration	Instantaneous velocity, subsonic	no	yes	no	yes
In-situ calibration, from upstream total pressure and density	Max. instantaneous velocity, subsonic	yes	No interest	Substitution tip with air supply	No interest
In-situ calibration, from mass flow meter and density					
In-situ calibration, from airtight bell	Mean mass flow, subsonic and supersonic	yes	yes	homogeneity	homogeneity
Optical metrology					
LDV, max. frequency depending on the seeding quality	Instantaneous velocity of particles	yes	yes	yes	yes
PIV, fixed frequency	2D maps of instantaneous velocities	Depends on spatial resolution	yes	Depends on spatial resolution	yes

Table 1 - Summary of available methods for actuator qualifications

In addition, as an example of actuator qualification in an academic flow, a synthetic jet in a turbulent boundary layer has been studied in a boundary layer wind tunnel. In this case, the actuator exit was 0.5 mm wide and 30 mm long. The hot wire probe was located at 0.2 mm inside the slot. Similar results were obtained with the wind tunnel off and on (with and without wind) (not shown here). The velocity of the wind tunnel was fixed at 30 $m.s^{-1}$ and the actuator frequency at 200 Hz.

The various methods used for the actuator characterization are summarized in the following table. Although hot-wire anemometry has been used for most of the qualifications carried out up to now, optical methods like L.D.V. (Laser Doppler Velocity) or P.I.V. (Particle Velocity Imagery) are being considered and could bring significant improvements in a near future, since they are not intrusive. However, they require the seeding of the jet, which proves to be difficult, especially for high pressure upstream conditions. Temperature measurements to evaluate either generated momentum or flow rate should be also investigated in the future.

Conclusion and perspectives

Recent progress in the field of micro mechanics and micro sensors has made it possible to develop innovating flow control devices fulfilling the highly demanding specifications from aerodynamic engineers. The very ambitious wind tunnel tests performed using the actuators described in this article were carried out successfully and allow the accuracy of CFD codes developed by Onera to simulate this kind of devices to be assessed.

Since they are either mechanical or fluidic, the actuators developed have been designed to fulfill customer requirements. Moreover, in the case of fluidic actuators, these studies led to the development of specific measurement techniques dedicated to the characterization of micro jets.

Today, Onera still continues its efforts in actuator development, in order to be able to propose technical solutions for the upcoming studies. Thus, new mechanical actuators based on MEMS technologies are studied, with the purpose of making this kind of technology compatible with applications on wind tunnel models. Such solutions allow the flow control application to be considered as a tool for improving the quality of measurements made during wind tunnel tests, or for increasing the accuracy of numerical simulations with active flow control.

Regarding the fluidic actuators, not only within the framework of JTI Cleansky, but also in Onera self-funded projects, work is carried out to improve the performance, not only of the synthetic jets, but also of the pulsed jet actuators. For the latter, the final objective is today the application of these technologies at a larger scale to prepare flight tests.

To characterize such actuators, Onera explores new measurement methods, based on new micro sensors integrated into the mechanical actuators, or new velocity measurement techniques for fluidic actuators.

The actuator characterization benches adapt gradually to the requirements from the experimentalists, who require more and more information with an always greater precision ■

Acknowledgements

The studies performed on the remotely controlled aileron were conducted within the framework of a national program supported by French government agencies (DGAC – French Ministry of Transportation / DGA – French Ministry of Defense) in collaboration with Airbus and Dassault Aviation. The authors gratefully acknowledge Jean-Luc Hantrais-Gervois and Marc Deschamps.
The data related to TEDs actuator had been produced by the AWIATOR Consortium under the European Commission supported project G4RD-CT-2002-00836. The authors gratefully acknowledge Eric Coustols and Daniel Caruana.
Projects SIMCOS and BUFFET'N CO were conducted using Onera's own funding. The authors gratefully acknowledge Arnaud Le Pape, Eric Coustols, Jean-Bernard Dor, Emmanuel Eglinger, Arnaud Lepage and Jean-Marc Massonat.
The work related to the scaled 1 pulsed jet actuator, the synthetic jet actuator and the fluidic actuator characterization has been undertaken within the Joint Technology Initiative "JTI CleanSky", Smart Fixed Wing Aircraft Integrated Technology Demonstrator "SFWA-ITD" project (Contract N° CSJU-GAM-SFWA-2008-001) financed by the 7th Framework program of the European Commission. The authors gratefully acknowledge Eric Coustols, Annabelle Choffat, Jean-Luc De Coninck, Arnaud Le Pape, Christophe Verbeke and Bruno Mialon.

References

[1] R.PETZ, W. NITSCHE - *Active Separation Control on the Flap of a Two-Dimensional Generic High-Lift Configuration.* J. Aircraft, vol. 44, no. 3, pp. 865-874, 2007.
[2] A.GLEZER, M. AMITAY - *Synthetic Jets*. Annu. Rev. Fluid Mech., vol. 34, pp. 503-529, 2002.
[3] T.C. CORKE, C.L. ENLOE, S.P. WILKINSON - *Dielectric Barrier Discharge Plasma Actuators for Flow Control.* Annu. Rev. Fluid Mech, vol. 42, pp. 505-29, 2010.
[4] E. MOREAU - *Airflow Control by Non-Thermal Plasma Actuators.* J. Phys. D Appl. Phys., vol. 40, pp. 605-636, 2007.
[5] T.M. CRITTENDEN, S. RAGHU - *Combustion Powered Actuator with Integrated High Frequency Oscillator.* Int. J. Flow Control, vol. 1, pp. 87-97, 2009.
[6] B. CYBYK, K. GROSSMAN, J. WILKERSON - *Performance Characteristics of the Sparkjet Flow Control Actuator.* AIAA Paper 2004-2131, 2nd AIAA Flow Control Conf., Portland, 2004.
[7] V. NARAYANASWAMY, L.L. RAJA, N.T. CLEMENS - *Characterization of a High-Frequency Pulsed-Plasma Jet Actuator for Supersonic Flow Control.* AIAA J., vol. 48, pp. 297-305, 2010.
[8] A. BELINGER, P. HARDY, P. BARRICAU, J.P. CAMBRONNE, D. CARUANA - *Influence of the Energy Dissipation Rate in the Discharge of a Plasma Synthetic Jet Actuator.* J. Phys. D: Appl. Phys., vol. 44, 2011.
[9] L. CATTAFESTA, S. GARG, M. CHOUDHARI, F. LI - *Active Control of Flow-Induced Cavity Resonance.* AIAA Paper 1997-1804, 28th AIAA Fluid Dyn. Conf., Snowmass, 1997.
[10] A. SEIFERT, S. ELIAHU, D. GREENBLATT, I.J. WYGNANSKI - *Use of Piezoelectric Actuators for Airfoil Separation Control.* AIAA J., vol. 36, pp. 1535-1537, 1998.
[11] J.M. WILTSE, A. GLEZER - *Manipulation of Free Shear Flows Using Piezoelectric Actuators.* J. Fluid Mech., vol. 249, pp. 261–285, 1993.
[12] J. KASTNER, M. SAMIMY - *Development and Characterization of Hartmann Tube Fluidic Actuators for Highspeed Flow Control.* AIAA J., vol. 40, pp. 1926-1934, 2002.
[13] M.J. STANEK, R. SINHA, J. SEINER, B. PIERCE, M. JONES - *High Frequency Flow Control—Suppression of Aero-Optics in Tactical Directed Energy Beam Propagation and the Birth of a New Model (Part I).* AIAA Paper 2002-2272, 8th AIAA/CEAS Aeroacoust. Conf., Breckenridge, 2002.
[14] M.J. STANEK, G. RAMAN, J.A. ROSS, J. ODEDRA, J. PETO, et al. - *High Frequency Acoustic Suppression - the Role of Mass Flow, the Notion of Superposition, and the Role of Inviscid Instability - a New Model (Part II).* AIAA Paper 2002-2404, 8th AIAA/CEAS Aeroacoust. Conf., Breckenridge, 2002.
[15] G. RAMAN, S. KHANAFSEH, A.B. CAIN, F. KERCHEN - *Development of High Bandwidth Powered Resonance Tube Actuators with Feedback Control*. J. Sound Vib., vol. 269, pp. 1031–62, 2004.
[16] R. WOSZIDLO, H. NAWROTH, S. RAGHU, I.J. WYGNANSKI - *Parametric Study of Sweeping Jet Actuators for Separation Control.* AIAA Paper 2010-4247, 5th Flow Control Conference, Chicago, 2010.
[17] L.N. CATTAFESTA, M. SHEPLAK - *Actuators for Active Flow Control.* Annu. Rev. Fluid Mech., vol. 43, pp. 247-272, 2011.
[18] L. CATTAFESTA, M. SHEPLAK - *Actuators and Sensors.* Chapter 6 in "Fundamentals and Applications of Modern Flow Control", Miller D.N. and Joslin D. ed., Progress in Astronautics and Aeronautics, vol. 231, American Institute of Aeronautics and Astronautics, 2009.
[19] J.L. HANTRAIS-GERVOIS, A. LEPAGE, F. TERNOY, G. CARRAZ, G. JEANFAIVRE - *Assessment of Numerical Tools to Predict Control Surface Effectiveness.* AIAA Paper 2010-4816, 28th AIAA Applied Aerodynamics conference, Chicago, 2010.
[20] H. HANSEN - *Application of Mini-Trailing-Edge Devices in the AWIATOR Project.* ODAS Conference, Toulouse, June 2003.
[21] A.LE PAPE, M. COSTES, G. JOUBERT, F. DAVID, J.M. DELUC - *Dynamic Stall Control Using Deployable Leading-Edge Vortex Generators*. AIAA journal, vol. 50, no. 10, 2012.
[22] G. JOUBERT, A. LE PAPE, B. HEINE, S. HUBERSON - *Vortical Interactions Behind a Deployable Vortex Generator for Airfoil Static Stall Control.* AIAA Journal, Vol.51, n°1, pp240-252, January 2013, DOI: 10.2514/1.J051767
[23] E. COUSTOLS, V. BRUNET, R. BUR, D.CARUANA, D. SIPP - *BUFET'N Co: A Joint Onera Research Project devoted to Buffet Control on a Transonic 3D Wing using a Closed-Loop Approach.* CEAS/KATNET II Conference, Bremen, May 2009.
[24] J. DANDOIS, P. MOLTON, A. LEPAGE, A. GEERAERT, V. BRUNET, J.B. DOR, E. COUSTOLS - *Buffet Characterisation and Control for Turbulent Wings*. Aerospace Lab Issue 6, June 2013.
[25] C. LIENARD, A. LE PAPE, C. VERBEKE - *Numerical and Experimental Investigation of Helicopter Fuselage Drag Reduction Using Active Flow Control.* 68th AHS International Annual Forum, Fort Worth, May 2012.

AUTHORS

Frédéric Ternoy graduated as a mechanical engineer from the Ecole Nationale Supérieure d'Arts et Métiers (ENSAM) in 1999. He joined the Model Design and Manufacture Department of Onera as a design engineer and project manager. Since 2007, he has led this department and is involved in model design, especially dealing with flow control technologies.

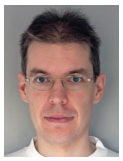

Julien Dandois graduated from the Ecole Nationale Supérieure d'Arts et Métiers (ENSAM) in 2003 and received a PhD in Fluid Mechanics from Paris 6 University in 2007. Since that time, he has worked in the Civil Aircraft Unit of the Applied Aerodynamics Department, in the fields of high-lift, separation control, buffet control, closed-loop control and aeroacoustics.

Frédéric David joined the Aeroelasticity and Structural Dynamics Department of Onera in 1983. Since 2011, he has worked as test engineer in the C19 facility of the Wind Tunnel Division.

Marc Pruvost received a DUT in Mechanics in 1975. He joined Onera in 1977 and he has been an engineer in the field of industry support since 1996. Since 2005, he has work on the characterization of the fluidic actuators developed at Onera, for which he has developed a test bench.

Active Flow Control for Helicopters

A. Le Pape, C. Lienard, J. Bailly
(Onera)

E-mail: alepape@onera.fr

Several active flow control helicopter applications aimed at improving aerodynamic performance have been studied at Onera and are presented in this paper. The distinction between applications for non-rotating or non-lifting parts and for rotating parts is presented. A first part deals with the application of steady/unsteady blowing to simplified rotor hub and fuselage shapes. The objective is to achieve significant drag reduction by suppressing the flow separation occurring in these areas. Numerical and experimental investigations are jointly performed to identify the best control strategies. The numerical efforts take into account the experimental constraints in the simulations. Significant work is done on the simplified fuselage drag reduction using various blowing actuations: synthetic jets, pulsed jets and steady blowing. The second part of the paper is dedicated to active flow control on rotor blades. A first application of deployable vortex generators for dynamic stall control is discussed. Then, more general active technologies aimed not only at improving the aerodynamic performance but also at reducing the vibratory loads or the noise radiation, are presented. Among the several active blade technologies that have been studied at Onera, both experimentally and numerically, this paper focuses on the active flap blade and the active twist blade concepts. The paper highlights the diversity of flow problems occurring on a rotorcraft and the various flow control strategies that must be considered to handle them. The numerical challenges to account for flow control in an unsteady environment are discussed for each flow control application.

Introduction

Flow control has been a very active area of research in recent years for the aerodynamic improvement of aerial vehicles [3], [24]. Based on simple and academic configurations [2], the significant first success of flow control led to more complex and realistic geometries being considered. Flow control techniques have since been applied to rotorcraft and in particular to helicopters. Helicopter aerodynamics is intrinsically highly unsteady, due to the main and tail rotor rotations. The non-rotating parts of helicopters may also have large separations, the design of the machine being generally more driven by the specified mission of the aircraft than by a quest for aerodynamic efficiency. The variety of helicopter missions fits in well with active devices that can be activated on-demand, on non-rotating or non-lifting parts. Separation control effectiveness has also been shown using active actuators [8], [15], [16]. Rotorcraft configuration applications are generally focused on separation control for drag reduction. It has been, for example, applied to hub fairing or hub pylon separation control [4], [49], [37] and this application will be discussed in the first part of the paper. Separation control for drag reduction has also been studied by several authors, on blunt fuselage using vortex generators [7], steady blowing [27], [40], synthetic jets [32], [50], [27], [40], combustion actuators [50] or plasma actuators used as vortex generators [13]. The Onera activities on this topic are discussed in the first part of the paper: different types of actuation (steady blowing, pulsed jets and synthetic jets) are used to reduce the drag of a simplified blunt fuselage.

On rotating parts, active flow control is well suited to the unsteady environment that the helicopter rotor experiences. The retreating and advancing blades are subjected to very different aerodynamic conditions: active flow control enables a particular phenomenon to be acted upon only in the needed azimuth range. For example, dynamic stall is a phenomenon that occurs on the retreating blade and that induces large penalties for high speed forward flight. Its control has been a topic of many studies and several devices have been proposed. Dynamic stall is linked to the shedding of a strong leading-edge dynamic stall vortex and therefore most authors have proposed devices acting at the airfoil leading-edge. For example, suction at the leading-edge [25], blowing [20][21] and plasma actuation using Dielectric Barrier Discharge (DBD) actuators [38] were shown to bring some benefits. Large modifications of the airfoil shape were also

investigated using a deforming leading-edge [11], a droop leading-edge airfoil [17] or leading-edge slats [9]. Vortex generators at the airfoil leading-edge were also successfully applied [31][30] to limit dynamic stall penalties and this idea has been extended at Onera by the addition of a deployable feature of the vortex generator device. Activities on dynamic stall control using Deployable Vortex Generators (DVGs) are presented in the second section of this paper.

A more global influence on the flow can be obtained using active blade technologies. The objectives of the actuation are generally not only to improve the aerodynamic performance of the rotor, but also to limit the noise radiations or the vibratory loads. The last part of the paper presents the Onera outcomes for two active blade technologies; the first is the active flap blade and the second is the active twist blade.

The objective, status and outcome of each application are discussed from both experimental and numerical aspects.

Active flow control for non-rotating components

Compared with fixed wing aircraft fuselage drag, the fuselage drag of a helicopter may be up to an order of magnitude larger. Due to the operational requirements for rotorcraft, the fuselages are typically not cleanly integrated with the engine, pylon, nacelle, hub, or landing gear. This may result in adverse flow interactions and excessive drag, due to the bluff body shape and separated flow. Suppressing the flow separation on non-rotating components of a helicopter can consequently lead to significant drag reduction and improve the overall performance of the machine. Massive separation occurs generally in two different regions of the fuselage: downstream from the rotor hub and downstream from the fuselage cabin (especially for rearward loading capability rotorcraft). The following sections present the application of active flow control on simplified geometries representing these two key-areas.

Pylon fairing separation control

Helicopter rotor hubs are characterized by a highly complex design ensuring the proper helicopter rotor control. If the rotor hub cannot be fully faired, the pylon that supports the rotor hub is generally faired using a streamlined shape. Usually, symmetric thick-airfoil shapes are used for pylon fairings [46]. Flow separation on those airfoils may appear at very low angles of attack, producing large drag penalties and unsteady vortex shedding that can impinge the rear lifting surfaces and lead to severe handling quality problems. Under the US/French Memorandum of Agreement on helicopter aeromechanics, a typical thick airfoil, a NACA0036 (figure 1), used for helicopter pylon fairing has numerically been investigated without and with flow control in a joint US Army/Onera effort [37]. Active flow control was ensured by zero-net mass-flux jets (or synthetic jets [19]) blowing and sucking air through slots located on the upper surface of the airfoil ([4], [37], [49]).

Wind-tunnel test measurements were available for both baseline and actuated configurations and the joint US/French work focused on computational work to assess the ability of computational fluid dynamics (CFD) tools to reproduce the experimental observations. The results of the computations are detailed and discussed, comparing with available experimental data in Ref. [37]. The baseline case is a very difficult one for CFD, with a large flow separation over the upper surface of the airfoil at a very low angle of attack. The flow is largely separated at the trailing-edge of the airfoil at a 0° angle of attack and separates totally over the upper surface at a 5° angle of attack, leading to a decrease in lift at low angles of attack. The numerical simulations performed with the Onera CFD solver *elsA* on this configuration in 2D and 3D show limited quantitative agreement with experimental measurements, in particular for lift and drag values. Some of the discrepancies could be linked to the experimental set-up (corner flow in the tunnel, roughness that triggers laminar-turbulent transition at the airfoil leading-edge) and were investigated using CFD, but the overall agreement was poor. It was however possible to investigate the modeling of the synthetic jet actuators in the simulation for actuated cases. The first significant conclusion identifies the required temporal resolution of the blowing and suction cycles in the simulation.

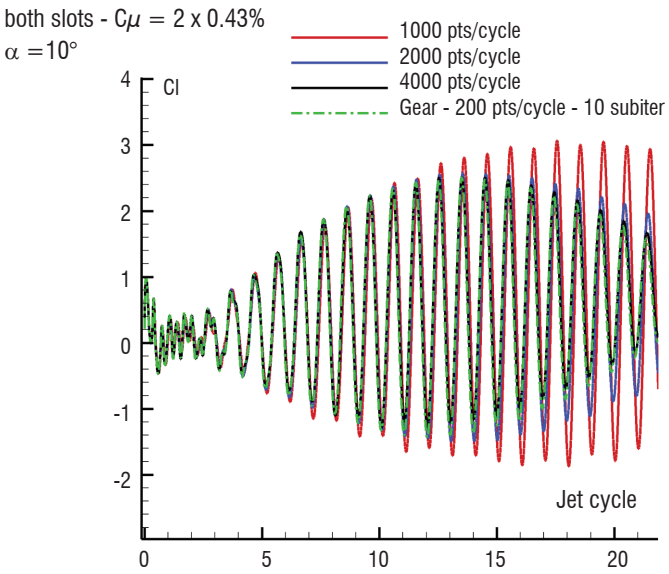

Figure 2 - Temporal convergence study of the synthetic jet cycle resolution in the simulation

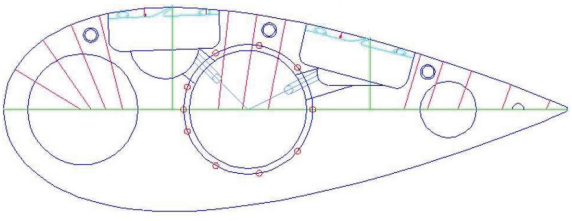

Figure 1 - Examples of rotorcraft with faired pylon (left), NACA0036 airfoil model (right) (from [37] and [4])

The results (figure 2) showed that a number of 2000 time steps per jet blowing/suction cycle (or 200 time steps with 10 sub-iterations per time step) were necessary to describe the synthetic jets effect correctly and consistently. This figure must be related to the typical separation timescales that can appear on a helicopter pylon; it should be also compared with the timescale of the rotor rotation, if active flow control is considered on the rotor. For example, for a rotor spinning at 200 rpm and a synthetic jet oscillating at f=120 Hz, a rotation corresponds to 400 synthetic jet cycles. Using a sub-iteration time scheme, 8.10^4 time steps per rotor revolution would be required, corresponding to a time step of 0.0045° of rotation, which is two orders of magnitude less than what is usually used in CFD, in the rotorcraft community.

Another important result is the identification of the influence of the active flow control phasing, in both the experimental and the numerical investigations. The different actuators implemented in the model can indeed be actuated to have the blowing/suction in phase or out-of-phase with each other. Here, the actuators located in the front part of the model are out of phase with the actuators on the aft part of the model. Wind-tunnel tests showed that phasing the jets improved the drag reduction and reduced the overall model vibration. CFD computations show similar trends and highlight the importance of the phase influence when using synthetic jets for flow separation control. The CFD investigations were performed for a limited number of phasing cases and no complete understanding of the phasing effect was drawn. A comprehensive understanding of the physics involved in jet phasing remains a topic for further research. This result has been important for the simplified blunt fuselage separation suppression [40] studied in the following section.

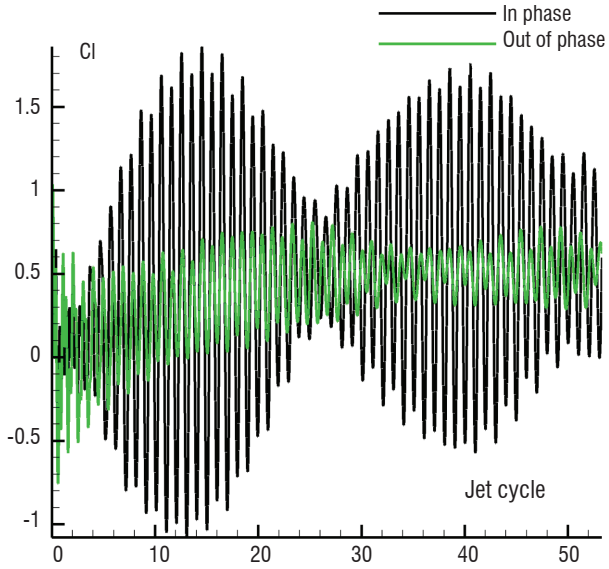

Figure 3 - Lift history for in-phase and out-of-phase synthetic jets

Helicopter blunt fuselage separation control

In high-speed forward flight, a major component of helicopter parasite drag is due to the fuselage and to the massive flow separation that occurs on its rear, especially for helicopters with a very pronounced aft loading ramp. A combined numerical and experimental investigation has been conducted within the Green Rotorcraft ITD of the CleanSky project, to obtain a better understanding of the flowfield around a helicopter generic fuselage and to investigate different flow control approaches to decrease this pressure drag. Many numerical and experimental baseline results are presented in ref. [27], as well as some active flow control computations, which helped in the designing of the actuators for the wind-tunnel tests. This research effort is applied on a generic fuselage, the ASF2, based on a fully open geometry. Already studied around 1985-1990 at Onera [18], this fuselage has a pronounced ramp, in order to produce a large area of separation (figure 4). Three promising flow control devices were chosen for study: steady blowing, pulsed jets and synthetic jets.

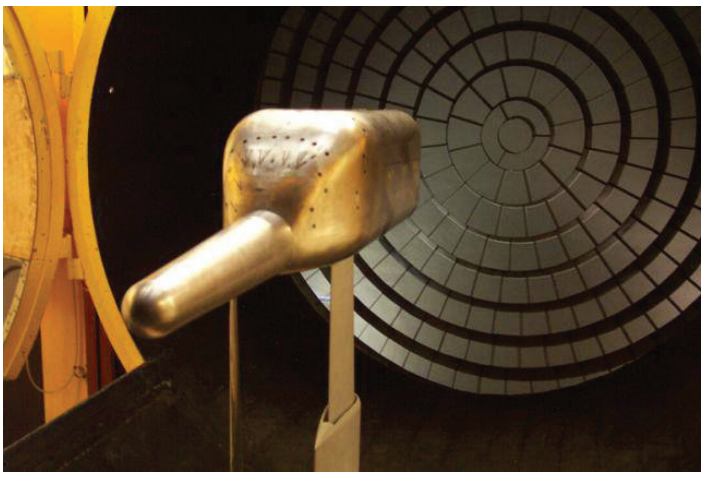

Figure 4 - ASF2 model mounted in Onera L1 wind-tunnel

Baseline case

The data presented in figure 5 shows a good correlation between numerical and experimental results for the baseline configuration, especially for angles of attack (AoA) higher than -2.5° (fuselage nose-down), considering the massive separation that occurs in the ramp region.

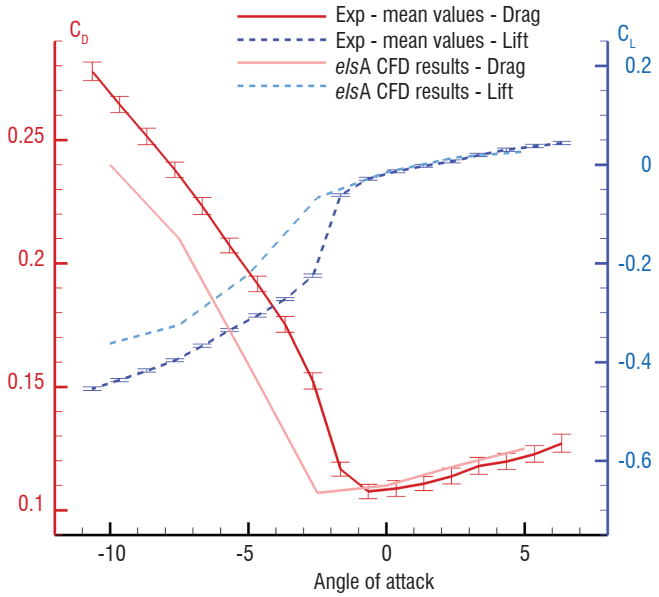

Figure 5 - Numerical/experimental comparison of the drag and lift coefficients for the baseline case

A detailed analysis of the flow allows two topologies to be identified, depending on the angle of attack, already established by Seddon [41]:

- an “eddy flow” for a nose-up angle of attack (AoA), which is the classic bluff-body flow consisting of cross-stream eddies and results in low drag but unsteady loads

• a “vortex flow” for a nose-down AoA, which is characterized by streamwise vortices and leads to high drag values.

However, the critical angle of attack is not well estimated by the numerical simulations. One possible explanation for this error could be the lack of the struts [39], and to a lesser extent of the wind-tunnel walls, in the simulations.

Flow control cases

Many simulations with flow control have been performed on this simplified blunt fuselage. In this investigation, simplified CFD simulations (half configuration with symmetry plane and coarse grids) with synthetic jets were used to get some idea of the effectiveness of active flow control on the ASF2 fuselage. Subsequently, numerical simulations have been performed to develop a flow control strategy and to identify actuator design parameters for the experiment, such as the slot location, width and angle.

Despite the approximations, those simulations resulted in a definition of the experimental flow control configuration to be tested in the wind-tunnel (0.67 mm-wide and 30 mm-long slots, slightly downstream from the separation line obtained for α=0°, 45° jet angle). They also helped to quantify the drag reduction that could be expected, these predicted around 15 - 20% in good agreement with state of the art drag reduction by active flow control on helicopter blunt fuselages [32], [40], [1], [34]. These also provided an initial idea of the flow control strategies to be applied, such as velocity ratios higher than 1 and phasing out of synthetic jets.

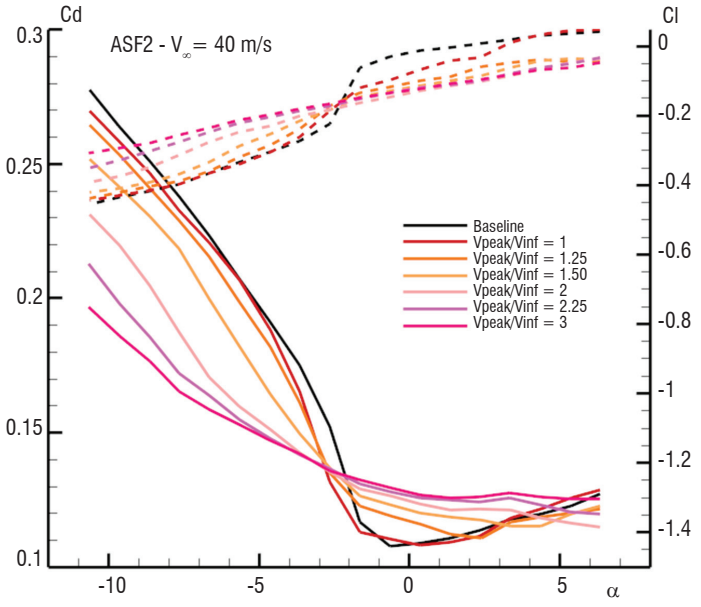

Figure 6 - Experimental drag (solid line) and lift (dashed line) for several steady blowing velocities

Confirmations of these potential benefits by wind-tunnel tests have been performed at Onera in the low-speed L1 facility. Specific attention was paid during the test preparation to actuator properties and performance. Laboratory tests were conducted on each individual actuator, to check the homogeneity of the actuators and to evaluate the output velocity peak and profile, frequency and voltage responses.

Then, an extensive parametric study including different velocity ratios, frequencies, duty cycles, phasing and slot schemes was successfully performed for the three chosen flow control devices. Experimental results are very promising, with significant drag reductions of 15 - 35% being observed. Higher drag reduction is achieved for negative AoA, which is favorable in the case of high speed flight of the helicopter. No drag reduction could be obtained for a narrow range of AoA around 0° (figure 6). Steady blowing configurations seem to be the most effective, but pulsed jets enable almost the same benefits at half of the required mass flow. The effect of synthetic jets is so far rather limited, with drag reduction only for a limited range of the fuselage angle of attack. These actuators have been slightly modified for another wind-tunnel entry expected in 2012, to achieve higher peak velocities.

Active flow control for helicopter main rotor

This second part is focused on the application of active flow control to rotating blades. Rotor blades encounter a wide range of aerodynamic conditions, from subsonic flow on the retreating blade to transonic flow on the advancing blade, leading to various aerodynamically penalizing phenomena. A first application focuses on dynamic stall. Dynamic stall occurs on the retreating blade for high speed forward flight or highly loaded rotors and it can be studied using the simplified configuration of an airfoil under pitching-oscillation motion. The following section presents the design and application of actively deployable vortex generators for dynamic stall penalty alleviation. Finally, two active blade technologies are discussed: active flap blade and active twist blade. The control principle is based on a more global action of the entire rotor. It not only enhances aerodynamic behavior, but also reduces the noise radiation and the vibratory loads.

Dynamic stall

Dynamic stall has been an intensive area of research over the last decades, to improve the understanding of the complex physics and it remains a very difficult problem in aerodynamics. The alleviation of dynamic stall on rotorcraft blades has also been an area of investigation for many researchers. Since structural problems associated with dynamic stall are due to the negative pitching-moment induced by the shedding of the strong leading-edge dynamic stall vortex, the objective of the dynamic stall control is primarily to reduce the negative pitching moment, while maintaining comparable mean and maximum achievable lift. The reduction of drag due to dynamic stall is generally considered as a secondary objective; any reduction of dynamic stall will lead to an extension of the flight envelope. Many devices have been proposed and experimental validation has been achieved on 2D wind–tunnel models for some of them. The technologies investigated include shape morphing (variable drooping leading-edge), active suction or blowing and passive control using vortex generators or Dielectric Barrier Discharge (DBD) plasma actuators (see for example the review of some devices in [10]).

The most promising studies concern the delay of dynamic stall, or its alleviation, using vortex generators. Significant dynamic stall reductions with leading-edge vortex generators were demonstrated experimentally by Martin et al. [31] and Mai et al.[30]. In the latter study, the devices are small flat cylinders attached to the airfoil leading-edge. However, even if the leading-edge-vortex generators are located near the stagnation point so that the flow is not affected at low and moderate angles of attack, the device may cause penalties for non-stalled flight conditions. Active flow control solves this problem; for example,

pulsed-jet vortex generators [29] [42] were successfully applied with one major drawback: the additional air supply required.

In this context, an innovative active device has been proposed and experimentally validated at Onera, in order to alleviate dynamic stall penalties, based on leading-edge vortex generation. The active device is intended to be used only during dynamic stall on the retreating blade; in order to avoid drag penalties on the advancing blade side, an actuation at a typical helicopter rotational frequency (1-per-rev, typically a few Hz) is thus foreseen. The actuator is a row of deployable vortex generators (DVGs) located at the nose of the airfoil (figure 7). The vortex-generators are small blades that conform to the airfoil leading-edge shape so that the airfoil is clean when retracted. The DVGs can be deployed at various heights (from 0.1 mm to 3 mm, with an accuracy of 0.05 mm) and with various deployment motions (sine, square) with respect to the airfoil pitching motion.

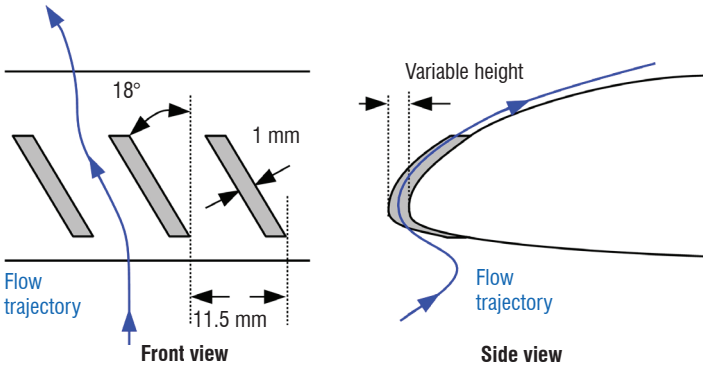

Figure 7 - Sketch of the designed Deployable Vortex Generator system.

The DVGs have been designed and implemented in an OA209 airfoil model and tested in the Onera F2 low-speed wind-tunnel for static and dynamic stall conditions [26]. A delay of up to 3° of the static stall angle of attack is achieved for static stall (figure 8). Results show that static stall delay is obtained for a small DVG height equal to 0.3 mm, but that more significant delays are obtained for hDVG∼1.5 mm. This delay is obtained by alleviating the leading-edge stall, while promoting the trailing-edge separation. Therefore, the static stall delay is achieved at the cost of reducing the maximum lift.

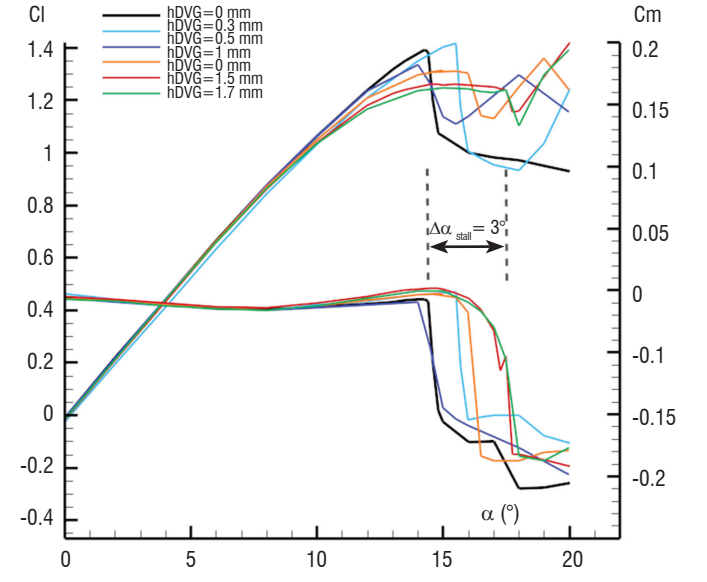

Figure 8 - Static stall delay obtained for various DVG heights

A large reduction in the negative pitching moment is shown for dynamic stall (figure 9). Up to 55% of the negative pitching-moment peak reduction is achieved when DVGs are deployed all over the airfoil oscillation cycle for an optimal DVG height equal to 1.5 mm. A loss of maximum lift of 10% is also observed. The analysis of various DVG deployment schemes shows that various compromises can be achieved between minimum negative pitching moment peak and maximum lift. When DVGs are deployed sufficiently soon before the occurrence of dynamic stall, a very large reduction of the negative pitching moment is achieved but there is also a loss of maximum lift. There is a good compromise for an actuation phase equal to 70°, for which a reduction of 30% of the negative pitching-moment is achieved with a limited loss of maximum lift of 2%. Duty-cycle (ratio of the duration of deployment during the oscillation cycle over the full oscillation cycle duration) optimization is performed and it is shown that these results can be obtained for a duty-cycle of down to 15%, ensuring limited drag penalties due to DVGs. Finally, it is shown that DVGs act primarily in the leading-edge region, where the dynamic stall is prevented from occurring by ensuring an attached flow at the leading-edge during the airfoil entire oscillation cycle.

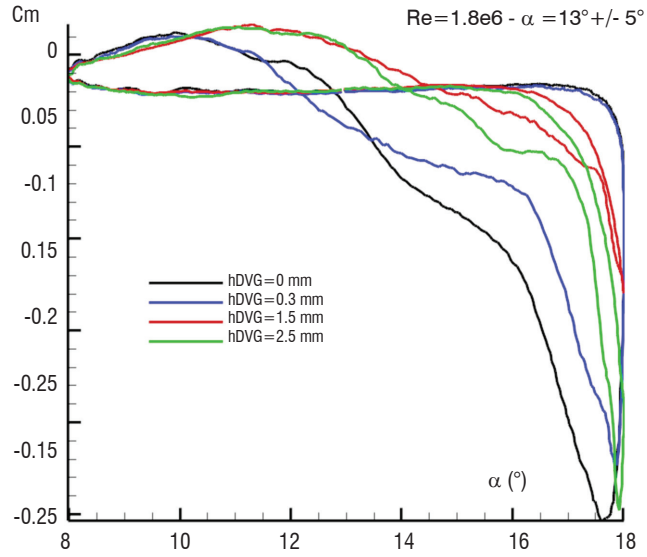

Figure 9 - Pitching-moment hysteresis obtained for various DVG heights

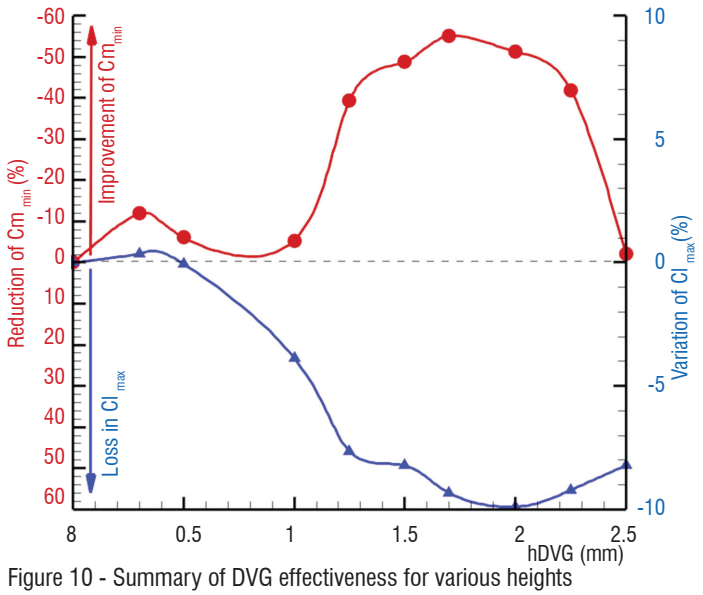

Figure 10 - Summary of DVG effectiveness for various heights

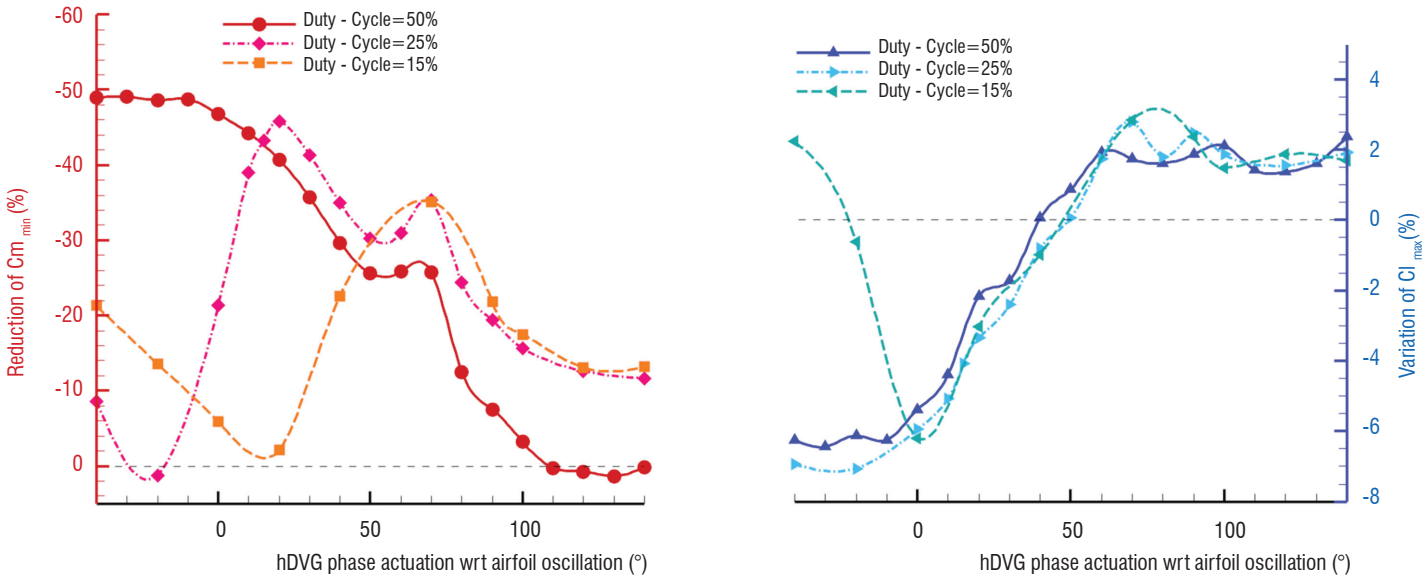

Figure 11 - Summary of DVG effectiveness for hDVG=1.5 mm and several duty-cycle wrt. DVG actuation phase, left: pitching-moment, right: lift

Along with the experimental demonstration of the effectiveness of DVGs for dynamic stall penalty reduction, significant effort has been made in the numerical investigations of this technology. The objective is to establish a computational model, which is validated using the experimental data used to investigate the physical mechanism of the interaction of the vortex emitted by the device and the flow separation at stall. On the other hand, the numerical simulation can also be used to improve the DVG design and optimize its effectiveness. These numerical investigations are presented in detail in [22] and [23]. It is shown that a good agreement with experimental data is obtained for static and dynamic stall, when the DVG device is included in the grid system for static deployment [22]. The analysis based on the numerical results also suggests that the specific aspect ratio of the DVGs is a primary parameter in the control effectiveness. The designed DVG is indeed thicker than the usual vortex generators, to allow mechanical deployment. Computations show that a thinner DVG could improve the static and dynamic stall control.

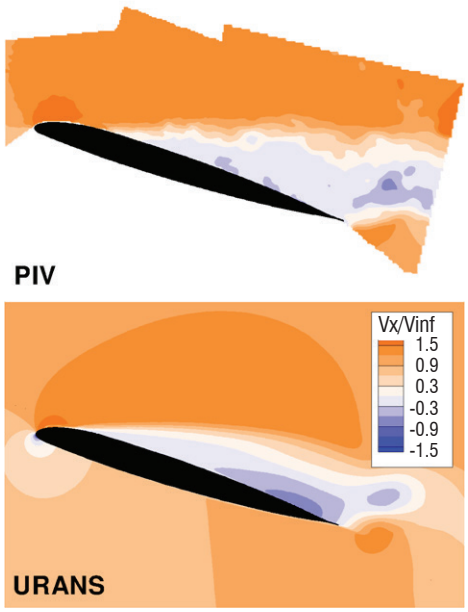

Figure 12 - Comparison of the computational result and the PIV data for dynamic stall control, using DVG

Since the ability of the DVGs to alleviate the dynamic stall penalties for 2D pitching airfoil has been shown, the effectiveness of this device on a helicopter rotor in high speed forward flight must still be estimated. However, including DVG on a rotor blade would require a very fine computational grid, since approximately 650 DVGs should be included to conserve the spacing used during the 2D wind-tunnel test. Time resolution of the single DVG computations is also one or two orders of magnitude higher than what is typically used for helicopter rotor simulations (usually 0.1°, here approx. 0.01°). Even if only a limited spanwise section of the blade is equipped with DVGs, computations of this magnitude remain out of reach with current computational resources and simpler evaluation methods are required. The following section describes active control investigations on rotor blades, based on comprehensive codes that use airfoil look-up tables and lifting-line methods with wake modeling that are simpler than (U)RANS computations.

Active blades

Active flow control on helicopter rotors has been a significant area of research over the last 20 years for active blade studies. The idea is not to add small disturbances in the flow using small actuators, but rather to apply technology that generates a general effect on the entire rotor system. The actuation can be on the rotor control or embedded in the blade to actively modify the blade shape. The expected effect on the flow can be obtained either from a direct local or global influence, or from an indirect influence through a specific aeroelastic response of the blade. Generally, the expected benefits are not only for improved aerodynamic performance, but also for noise and vibratory load reduction. Comprehensive aeromechanic tools are thus used to perform the benefit evaluation computations.

Active rotor studies were initiated at Onera through the HART (1994) and HARTII (2001) international (US Army, NASA, DLR, DNW, Onera) cooperative programs [47]. In these projects, the Higher Harmonic Control (HHC) technology was numerically and experimentally investigated in the continuation of a more industrial application of complex rotor command systems [36]. The objective of HHC is to replace the usual rotor swashplate that provides a 1-per-rev input to the blade motion by an advanced swashplate allowing higher harmonic inputs.

The wind tunnel tests on a 40% Mach-scaled hingeless model rotor showed a maximum reduction of 4dB in descent flight and a maximum vibratory load reduction of approximately 30% [45]. Numerical analysis performed at Onera using the Eurocopter aeromechanic comprehensive code HOST [5] provided good agreement on the trends, as well as other comprehensive codes [47]. Further computational studies focused on the aeroacoustics of the HARTII rotor and the ability of CFD/CSD [43] to accurately capture the rotor wake and the blade vortex interaction (BVI).

In the meantime, other active blade technologies have been studied at Onera, in particular the active flap blade and active twist blade, which are detailed in the following sections.

Active flap

The idea of active flap technology is to include a trailing-edge flap over a given spanwise extension of the blade. The trailing-edge flap can then be actively actuated at various frequencies (harmonic of the rotor rotation frequency are generally used, also noted n-per-rev frequencies) and for various angle of attack amplitude ranges. Preliminary computational studies were performed at Onera to design the trailing-edge flap spanwise extension and chordwise depth. In the comprehensive code used for these computations, the aerodynamic solution is based on a lifting line method and an airfoil property look-up table. To take into account the trailing-edge flap influence, dedicated airfoil polars for various flap deflections are used. The flap deflection airfoil polars are based on 2D wind-tunnel tests and analytical models. The results allowed the design of a model-scaled rotor equipped with trailing-edge flaps, with a spanwise extension equal to 10% of the total blade radius and a chord equal to 15% of the local blade chord. Several spanwise positions of between 70% and 90% of the blade radius were possible (figure 13).

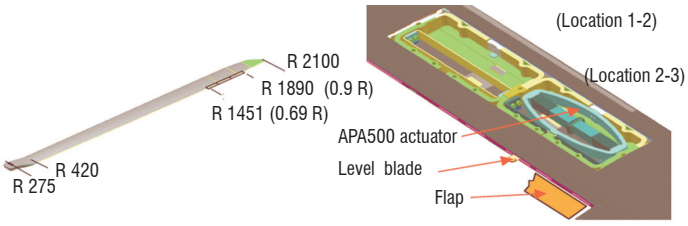

Figure 13 - Sketch of the active flap technology implemented in a helicopter rotor blade

Wind-tunnel tests were performed at Onera for several forward flight conditions [14]. Measurements included blade airloads computed from 168 unsteady pressure transducers, noise emission, blade deformation and rotor hub vibrations. The tests showed a significant reduction of the Blade Vortex Interaction (BVI) noise for a moderate level flight case with 1-per-rev and 4-per-rev actuations. Up to 2.8 dB reduction of the maximum noise measured could be obtained. Measurements of rotor hub vibratory loads were also performed and a closed-loop control of the flap deflection actuation allowed up to 20% of 4-per-rev hub vertical force to be reduced. However, no significant influence on the rotor power consumption was observed.

The wind-tunnel tests also showed that the flap deflection actuation acted in two distinct ways. The flap deflection can locally modify the blade section lift by changing the airfoil camber. In addition, the flap deflection at a given spanwise station and frequency actuation can modify the aeroelastic response of the entire blade and in particular the torsional response (servo-flap effect).

In parallel, Eurocopter Deutschland has developed a full-scaled demonstrator for this active flap rotor technology and has shown similar benefits during flight-tests [44]. Similar activities were also conducted in the US on a full-scale rotor demonstrator in wind-tunnel tests, with similar findings in terms of noise and vibration reduction [35], [28].

Active twist

The general purpose of active twist is to actively modify the rotor blade twist at various frequencies during the rotor rotation. As for the active flap, the flow control effect can be produced by a direct aerodynamic behavior variation with twist modification, or by inducing a modified aeroelastic response of the blade. Over this last decade, Onera developed a specific patented technology [33] based on the TWISCA concept (TWIstable Section Closed by Actuation), whose principle is an open blade section (figure 14) with a slot along the span direction, the two edges of this slot being connected by a Macro Fiber Composite (MFC) actuator located near the 25% of the chord line. Actuating this device induces a relative translation movement in the span direction of the upper and lower edges, resulting in a warping effect of the structure, leading to the twisting of the blade. One of the advantages of this structure is that the actuators, which are located close to the neutral axis, experience low bending stresses.

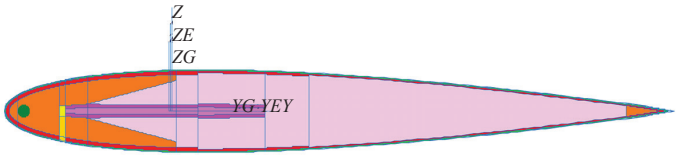

Figure 14 - Lift Demonstrator current section with actuation centered at 25% of the chord and slot at 10% (TWISCA concept)

Benefit evaluation computations, pre-design and wind-tunnel test preparation computations are performed using the comprehensive aeromechanic Eurocopter tools R85 and HOST, similarly to what was performed for active flap studies. Several models have been implemented to include twist modification in the aerodynamic lifting-line model. The first active twist model [6] is based on a direct modification of the local angle of attack of the blade, due to active twist. The active twist angle is included as an additive term of the total incidence angle, defined as the sum of the local pitch angle, the local twist angle and the elastic torsion.

All of the optimized control laws are defined using a harmonic decomposition with a maximum of 5 components, such as:

$$A(t) = A_0 + \sum_{i=1}^{5} A_{ic}\cos(i\omega t) + A_{is}\sin(i\omega t)$$

A_0, A_{ic}, and A_{is} being the fundamental, cosine and sine components of the active twist angle respectively.

Another way to model the active twist is to consider that the actuators create a torsion moment that can be added to the external forces and moments in the same way as the aerodynamic moments, as shown in figure 15. The elastic moment due to active twist must be provided using experimental data. This model implies that two point-sources of opposite sign are considered at each end of the active area of the blade.

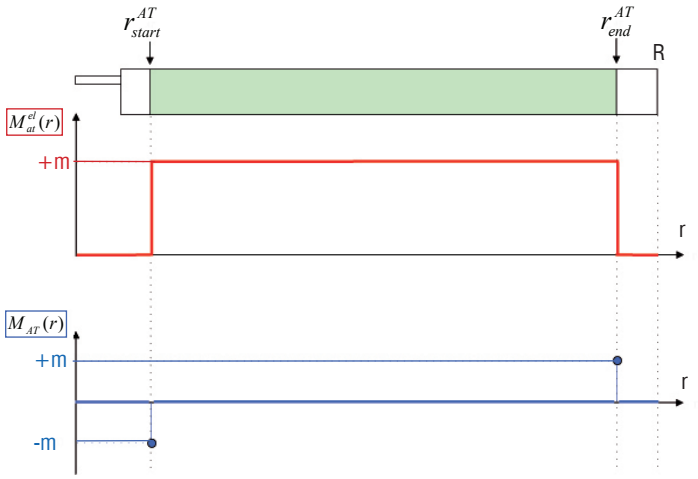

Figure 15 - Active twist model by moment

This model has the advantage of intrinsically containing the elastic response of the blade due to the twist actuation.

A comprehensive code and a genetic algorithm have been coupled to determine optimized active twist actuation laws for improved aerodynamic performance, noise and vibration reduction. The optimization variables are the 5 cosine (A_{ic}) and the 5 sine (A_{is}) components of the active twist angle. The computed configuration is a 4-bladed model-scaled helicopter rotor (2 meter radius). In this optimization process, active twist modeling by angle is applied with a maximum possible twist deflection (defined by technological constraints) of +/-2° at the blade tip. The results allowed the identification of achievable improvements for the various objectives and the useful actuation frequencies. An important result is that each individual objective requires a different type of actuation, as shown in figure 16. It was thus shown that rotor performance in forward flight could be improved using both 4-per-rev and 5-per-rev actuation, leading to up to 2.3% of consumed power reduction. This benefit comes from a reduction of the induced power, related to the modification of the geometric incidence, varying with the active twist angle.

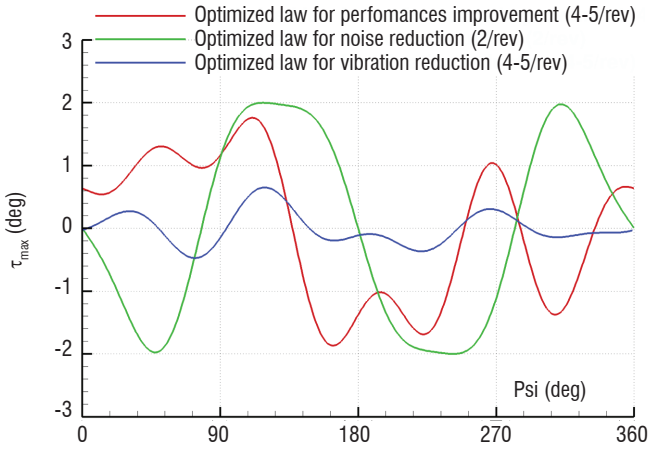

Figure 16 - Examples of active twist actuation laws for the various objectives

Noise reduction was investigated in descent flight for various descent angles. Active twist actuation is used to increase the local convection of the wake, so that interaction with the blade (responsible for BVI noise) is expected to be reduced or even eliminated. It was estimated that large BVI noise reduction could be achieved using 2-per-rev active twist actuations, leading to a noise abatement of up to 7.4 dB, as illustrated in figure 17.

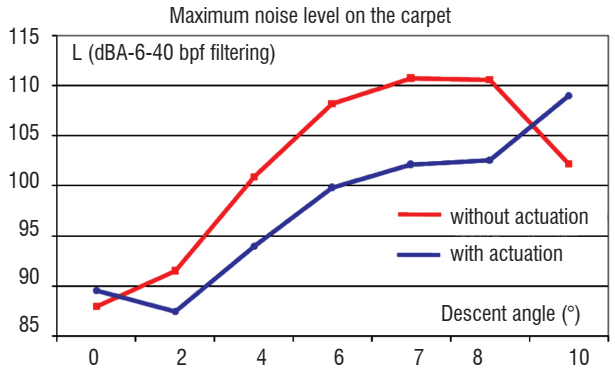

Figure 17 - Effect of actuated laws on maximum noise level

Vibration levels in forward flight estimated through the 3-per-rev in-plane moment and 4-per-rev vertical force (4-bladed rotor) were also be reduced using 3 to 5-per-rev actuations. Up to 100% reduction of the 4-per-rev vertical force was obtained.

These first benefit evaluations and twist actuation laws were demonstrated numerically, identifying the possible improvements achievable and identifying the proper actuation frequencies. The primary conclusion is that significant improvements can be obtained for noise and vibration, however only limited improvements of rotor power consumption can be expected. These improvements were obtained for different n-per-rev frequencies and, unfortunately, the actuation law for noise reduction was not of the same frequency as that required for vibration reduction.

Conclusion

Several applications of active flow control on helicopter airframes and on helicopter rotors have been presented. For non-rotating components, the objective is primarily the alleviation of flow separation region that can appear behind the rotor hub and in the fuselage back-door area, reducing the aircraft drag. This is achieved by applying unsteady blowing through slots. Numerical simulations show that a drag reduction benefit of approximately 15% can be expected. This figure has been confirmed by a wind-tunnel test on a simplified helicopter fuselage configuration. However, the dependence of the separation flow topology on the fuselage angle of attack has been identified, thus resulting in different control effectiveness. Very small time steps had to be used in the numerical simulations, in order to correctly account for the actuator influence. The typical time scales of the actuation are generally one or two orders of magnitude smaller than the time scale of the rotor rotation, which makes complete simulation challenging.

Applications on the main rotor were presented, considering the problem of dynamic stall control. A dedicated actuator based on deployable mechanical vortex generators was designed and tested on a pitching airfoil. Wind-tunnel tests show a very significant effectiveness of the device, with up to 40% of negative pitching-moment reduction. A 1-per-rev frequency actuation was applied to deploy the device on the retreating blade where dynamic stall occurs, while not affecting the flow on the advancing blade. Parametric investigations show that various compromises between maximum lift and minimum negative pitching moment peak can be obtained with a 1-per-rev actuation. Numerical simulations present good agreement with statically deployed VG, but only a small slice of the blade was considered. Taking into account numerous devices on a rotor blade in CFD simulations is

a very challenging computational problem, due to the small length scales of the actuators in comparison to the dimension of a helicopter rotor blade. Simpler aerodynamic modeling was thus considered for the evaluation of other active technologies applied to helicopter rotor blades. Active flap and active twist investigations performed at Onera were presented. In these cases, the objective was not only an improvement of the aerodynamic performance, but also noise and vibration reduction. The embedded actuators in the blade influenced the flow by a direct action or through a desired aeroelastic response of the blade. Such technologies are required to account for the aerodynamic properties of the blade, as well as the structural dynamics properties of the rotor. To date, aeromechanic comprehensive codes have been used. Computations show that significant reduction of BVI noise (between -5 and -7dB) and of vibratory loads (20-100%) can be expected. These improvements are obtained by specific n-per-rev actuations with dedicated actuation laws for noise and vibration. Only limited improvements on the rotor power consumption could be obtained. A deeper insight into active blade benefit evaluation will be performed through completed experimental data from the STAR project (international cooperation in continuation of the HART and HARTII programs). Validation of active twist models and CSD/CFD coupling simulations will be required to confirm these benefit evaluations and the rotor aero-elastic behavior.

The helicopter is a favorable platform for the application of active flow control, with significant areas of possible performance improvements. However, the application of active flow technologies on the rotor can be challenging due to the time scales involved and the coupling with the blade motion and elastic response. Long-term research projects are therefore mandatory to improve the active flow control technologies, in order to implement them in a flight demonstrator and verify their effectiveness for certification ■

Acknowledgments

The authors would like to thank all of the Onera teams that have been involved in the activities described and in particular the colleagues who participated in the model design and manufacturing, the wind-tunnel test preparation and execution, and the experimental post-processing. The following colleagues are specifically thanked for the active blade studies: Hugues Mercier des Rochettes for the blade and actuation technology design, Italo Cafarelli and Philippe Leconte for the vibration computations and Yves Delrieux for the acoustics computations.

Acronyms

AoA (Angle of Attack)
BVI (Blade Vortex Interaction)
CFD (Computational Fluid Dynamics)
CSD (Computational Structural Dynamics)
DBD (Dielectric Barrier Discharge)
DVG (Deployable Vortex Generators)
HART (Higher harmonic Aeroacoustic Rotor Test)
HHC (Higher Harmonic Control)
HOST (Helicopter Overall Simulation Tool)
MFC (Macro Fiber Composite)
STAR (Smart Twisting Active Rotor)
TWISCA (TWIstable Section Closed by Actuation)
(U)RANS ((Unsteady) Reynolds-Averaged Navier-Stokes)
VG (Vortex Generator)

References

[1] B. ALLAN, N. SCHAEFFLER - *Numerical Investigation of Rotorcraft Fuselage Drag Reduction using Active Flow Control*. 67th American Helicopter Society Forum, Virginia Beach(VA), USA, 3-5 May 2011
[2] M. AMITAY, A. HONOHAN, M. TRAUTMAN, A. GLEZER - *Modification of the Aerodynamic Characteristics of Bluff Bodies Using Fluidic Actuators*. AIAA paper 97-2004, 1997
[3] S. G. ANDERS, W. L. SELLERS, A. WASHBURN - *Active Flow Control Activities at NASA Langley*. AIAA-2004-2623, 2nd AIAA Flow Control Conference, Portland, OR, June 28 – July 1, 2004
[4] E. ARAD, P. B. MARTIN, J. WILSON, and C. TUNG - C*ontrol of Massive Separation on a Thick-airfoil Wing: A Computational and Experimental Study*. AIAA paper 2006-322, AIAA 44th Aerospace Sciences Meeting and Exhibit, Reno, NV, January 9-12, 2006
[5] J. BAILLY, Y. DELRIEUX, P. BEAUMIER - *HART II : Experimental Analysis and Validation of Onera methodology for the Prediction of Blade Vortex Interaction*. AHS International 61st Annual Forum, June 1-3 , 2005, Grapevine, Texas
[6] J. BAILLY, Y. DELRIEUX - *Improvement of Noise Reduction and Performance for a Helicopter Model Rotor Blade by Active Twist Actuation*. 35th European Rotorcraft Forum, September 22-25, 2009, Hamburg, Germany
[7] J. C. BONIFACE, G. JOUBERT, A. LE PAPE - *Passive Flow Control by Vortex Generators for some Internal and External Aerodynamics Configurations*. 48th International Symposium of Applied Aerodynamics, Saint Louis, France, March 25-27, 2013
[8] L. CATTAFESTA, M. SHEPLAK - *Actuators for Active Flow Control.* Annu. Rev. Fluid Mech., 2011, 43:247-272
[9] L. CARR, K. MCALISTER - *The Effects of Leading Edge Slaton the Dynamic Stall of an Oscillating Airfoil*. AIAA Paper 85-2533, Oct. 1983
[10] M. S. CHANDRASEKHARA - *A Review of Compressible Dynamic Stall Control Principles and Methods*. Proceedings of the Tenth Asian Congress of Fluid Mechanics May 17-21, 2004, Peradeniya, Sri Lanka
[11] M. CHANDRASEKHARA, M. WILDER, L. CARR - *Compressible Dynamic Stall Control Using Dynamic Shape Adaptation*. AIAA Journal, Vol. 39, No. 10, pp2021-2024, October 2001
[12] M. CHANDRASEKHARA, P. MARTIN, C. TUNG - *Compressible dynamic stall control using a variable droop leading-edge airfoil*. Journal of Aircraft, Vol.41, No4, pp 862-869, July-August 2004
[13] D. COLEMANN, F. THOMAS - *Rotorcraft Fuselage Flow Control Using Plasma Streamwise Vortex Generators*. 65th Annual Meeting on the APS Division of Fluid Dynamics, Volume 57, N°17, San Diego, CA, 18-20 November 2012
[14] Y. DELRIEUX, A. LE PAPE, P. LECONTE, P. CROZIER, B. GIMONET, H. MERCIER DES ROCHETTES - *Wind-Tunnel assessment of the concept of active flaps on a helicopter rotor model*. AHS International 63rd Annual Forum, Virginia Beach (VA), USA, 1-3 May 2007

[15] M. GAD-EL HAK - *Flow Control: Passive, Active, and Reactive Flow Management.* Cambridge, UK: Cambridge Univ. Press
[16] M. GAD-EL HAK - *Separation Control: Review*. J. Fluids Eng, Vol. 113, Issue 1,5, March 1991
[17] W. GEISSLER, G. DIETZ, H. MAI, J. JUNKER - *Dynamic Stall Control Investigations on a Full Size Chord Blade Section*. 30th European Rotorcraft Forum, Marseille, France, 14-16 September 2004
[18] C. GLEYZES, X. DE SAINT-VICTOR, G. FALEMPIN - *Experimental and Numerical Study of the Flow around an Helicopter Fuselage*. Determination of Drag Coefficient, 15th European Rotorcraft Forum Proceedings, Amsterdam, The Netherlands, September 12-15, 1989
[19] A. GLEZER, M. AMITAY - *Synthetic jets*. Annual Review of Fluid Mechanics, Vol. 34, pp503-529, 2002
[20] D. GREENBLATT, I. WYGNANSKI - *The Control of Flow Separation by Periodic Excitation*. Progress in Aerospace Sciences, Vol.36 (2000), pp487-545
[21] D. GREENBLATT, I. WYGNANSKI - *Effect of Leading-Edge Curvature and Slot Geometry on Dynamic Stall Control*. AIAA 1st Flow Control Conference, St. Louis, MO, June 24-26, 2002
[22] G. JOUBERT, A. LE PAPE, S. HUBERSON - *Numerical Study of Flow Separation Control Over a OA209 Airfoil Using Deployable Vortex Generator*. 49th AIAA Aerospace Sciences Meeting, Orlando, FL, USA, January 4-7, 2011
[23] G. JOUBERT, A. LE PAPE, B. HEINE, S. HUBERSON - *Investigation of Dynamic Stall Control by Deployable Vortex Generator Using Time-Resolved PIV Analysis and URANS Computations*. 37th European Rotorcraft Forum, Italy, 13-15 September 2011
[24] R. D. JOSLIN - *Aircraft Laminar Flow Control.* Annual Review of Fluid Mechanics, Vol30, pp1-29, January 1998
[25] M. KARIM, M. ACHARYA - *Suppression of Dynamic Stall Vortices over Pitching Airfoils by Leading-Edge Suction*. AIAA Journal, Vol.32, N°8, pp1647-1655, August 1994
[26] A. LE PAPE, M. COSTES, F. RICHEZ, G. JOUBERT, F. DAVID AND J. M. DELUC - *Dynamic Stall Control Using Deployable Leading-Edge Vortex Generators*. AIAA Journal, Vol. 50, N°10, pp2135-2145, October 2012
[27] C. LIENARD, A. LE PAPE, C. VERBEKE - *Numerical and Experimental Investigation of Helicopter Fuselage Drag Reduction Using Active Flow Control*. American Helicopter Society 68th Annual Forum, Fort Worth, TX, May 1-3, 2012
[28] P. LORBER, B. HEIN, J. WONG, B. WAKE - *Rotor aeromechanics Results From the Sikorsky Active Flap Demonstration Rotor*. American Helicopter Society 68th Annual Forum, Fort Worth, TX, May 1-3, 2012
[29] J. MAGILL, K. MCMANUS - *Control of Dynamic Stall Using Pulsed Vortex Generators Jets*. AIAA paper 98-0675, 1998
[30] H. MAI, G. DIETZ, W. GEISSLER, K. RICHTER, J. BOSBACH, H. RICHARD, K. DE GROOT - *Dynamic Stall Control by Leading-Edge Vortex Generators*. Journal of the American Helicopter Society, Vol. 53, No1, January 2008, doi:10.4050/JAHS.53.26
[31] P. MARTIN, J. WILSON, J. BERRY, T. C. WONG, M. MOULTON, M. MC VEIGH - *Passive Control of Dynamic Stall*. 26th AIAA Applied Aerodynamics Conference, Honolulu, Hawaii, 18-21 August 2008
[32] P. MARTIN, C. TUNG, A. HASSAN, D. CERCHIE, J. ROTH - *Active Flow Control Measurements and CFD on a Transport Helicopter Fuselage.* 61st American Helicopter Society Forum, Grapevine, TX, June 1-3, 2005
[33] H. MERCIER DES ROCHETTES, D. JOLY, L. BUCHANIEK, P. LECONTE - *A New Concept of Active Twist Blade Applied to Main Rotor of Helicopter.* RTO-MP-AVT-168 Symposium, Paper 25, Evora, Portugal, April 20-24, 2009
[34] M. MC VEIGH, H. NAGIB, T. WOOD, I. WYGNANSKI - *Full-Scale Flight Tests of Active Flow Control to Reduce Tiltrotor Aircraft download*. Journal of Aircraft, Vol.48, N°3, May-June 2011, pp786-795
[35] T. NORMAN, C. THEODORE, P. SHINODA, D. FUERST, U. ARNOLD, S. MAKINEN, P. LORBER, J. O'NEILL - *Full-Scale Wind Tunnel Test of A UH-60 Individual Blade Control System for Performance Improvement and Vibration, Loads, And Noise Control*. American Helicopter Society 65th Annual Forum, Grapevine TX, May 27-29, 2009
[36] M. POLYCHRONIADIS, M. ACHACHE - *Higher Harmonic Control: Flight Tests of an Experimental System on SA 349 Research Gazelle*. American Helicopter Society 42nd Annual Forum, Washington, DC, USA, 2-4 June 1986
[37] M. POTSDAM, A. LE PAPE - *CFD investigations on a NACA0036 airfoil with active flow control*. AIAA 4th Flow Control Conference, AIAA-2008-3869, Seattle, WA, 23-26 June 2008
[38] M. POST, T. CORKE - *Separation Control Using Plasma Actuators: Dynamic Stall Vortex Control on Oscillating Airfoil*. AIAA Journal, Vol.44, No12, pp3125-3135, December 2006
[39] T. RENAUD, D. O'BRIEN, M. SMITH, M. POSDAM – *Evaluation of Isolated Rotor-Fuselage Interaction Using CFD*. AHS International 60th Annual Forum, Baltimore, Maryland, 7-10 June 2004
[40] N. SCHAEFFLER, B. ALLAN, C. LIENARD, A. LE PAPE - *Progress towards Fuselage Drag Reduction via Active Flow Control: a Combined CFD and Experimental Effort*. 36th European Rotorcraft Forum, Paris, France, 7-9 September 2010
[41] J. SEDDON - *Basic Helicopter Aerodynamics*. BSP Professional Books, 1990, p. 78
[42] C. SINGH, D. J. PEAKE, A. KOKKALIS, V. KHODAGOLIAN, F. COTON, R. GALBRAITH - *Control of Rotorcraft Retreating Blade Stall Using Air-Jet Vortex Generators.*Journal of Aircraft, 43(4):pp1169-1176, 2006, doi:10.2514/1.18333
[43] M. SMITH, J. LIM, B. VAN DER WALL, J. BAEDER, R. BIEDRON, D. BOYD, B. JAYARAMAN, S. JUNG, B.Y. MIN - A*n Assessment of CFD/CSD Prediction State-of-the-Art using the HARTII International Workshop Data*. American Helicopter Society 68th Annual Forum, Fort Worth, TX, May 1-3, 2012
[44] D. ROTH, B. ENENKL, O. DIETERICH - *Active Rotor Control by Flaps for Vibration Reduction - Full Scale Demonstrator and First Flight Test Results*. 32nd European Rotorcraft Forum, Maastricht, the Netherlands, September 2006
[45] W. SPLETTSTOESSER, R. KUBE, U. SEELHORST, W. WAGNER, A. BOUTIER, F. MICHELI, E. MERCKER, K. PENGEL - *Key Results from a Harmonic Control Aeroacoustic Rotor Test (HART), in the German-Dutch Wind Tunnel*. 21st European Rotorcraft Forum, St Petersburg, Russia, 30 August – 1st September 1995
[46] R. STROUB, L. YOUNG, R. GRAHAM, A. LOUIE - *Investigation of Generic Hub Fairing and Pylon Shapes to Reduce Hub Drag.* NASA-TM-100008, September 1987
[47] B. VAN DER WALL, C. BURLEY, Y. YU, K. PENGEL, P. BEAUMIER - *The HART II Test - Measurement of Helicopter Rotor Wakes"*. Aerospace Science and Technology, Vol.8 (4), June 2004, pp. 273-284
[48] B. VAN DER WALL, J. LIM , M. SMITH, S. JUNG, J. BAILLY, J. BAEDER, D. BOYD - *An Assessment of Comprehensive Code Prediction State-of-the-Art using the HARTII International Workshop Data.* American Helicopter Society 68th Annual Forum, Fort Worth, TX, May 1-3, 2012
[49] J. S. WILSON - *Turbulence Measurements on a 2D NACA0036 with Synthetic Jet Flow Control*. 62nd American Helicopter Society Forum, Phoenix, AZ, May 9-11, 2006
[50] G. WOO, A. GLEZER, J. BAIN, L. SANKAR - *Rotorcraft Fuselage Drag Reduction Using Combustion Power Actuators*. 49th AIAA Aerospace Sciences Meeting, AIAA-2011-34, Orlando, FL, 4-7 January 2011

Authors

Arnaud Le Pape graduated from the "Ecole Centrale de Nantes" in 2001 and has been working since then in the Applied Aerodynamics Department at Onera on helicopter and wind-turbine aerodynamics. His research includes experimental and numerical activities. Recently he has been leading the Onera/DLR SIMCOS project dynamic stall studies and its control.

Caroline Lienard graduated from the "Ecole Nationale Supérieure de Mécanique et d'Aérotechnique" in 2008. She joined Onera in the Applied Aerodynamics Department to work on helicopter drag reduction using active flow control.

Joelle Bailly graduated from the "Ecole Nationale Supérieure de Techniques Avancées" in 1991. She joined Onera in the Applied Aerodynamics Department and has been working in the helicopter field since then. Her research is focused in particular on numerical optimization methodology and active blade technology evaluation.

V. Brunet, J. Dandois, C. Verbeke
(Onera)

E-mail: vincent.brunet@onera.fr

Recent Onera Flow Control Research on High-Lift Configurations

This paper concerns the recent and most representative work performed at Onera on the application of flow control technologies to high-lift systems of aircraft wings. Two different objectives are considered. First, keeping present architecture, flow control could either enhance the aerodynamic performance (mainly mean and stall lift coefficients) or simplify the mechanisms (flap gap or size). Secondly, a drastic geometry simplification, very attractive for aircraft manufacturers, like slot or even slat suppression, leads to a strong depletion of aerodynamic performance. In that case, the objective of flow control is to retrieve as much as possible the reference airfoil performance. Various flow control devices, from simple mechanical or fluidic vortex generators to pulsed blowing, are considered. Combined numerical and experimental studies are presented and the efficiency of the control is discussed.

Introduction

Aircraft high-lift systems are essential in low speed conditions for take-off and landing phases to reach the necessary high-lift coefficients (flap efficiency) and delay stalling (slat efficiency), as presented in figure 1. To do so, such complex mechanisms have been optimized throughout the aviation history, leading mostly to a single extended slat and one or more extended flap(s). Nonetheless, these optimized extended elements are still complex, heavy and expensive to manufacture. To overcome these issues, the coupling of flow control technologies and high-lift systems allows either an enhancement of actual high-lift device efficiency, or a simplification of the high-lift mechanisms. Hence, applying flow control directly at the design phase of the aircraft could lead to simpler and less expensive systems (from the manufacturing and maintenance point of view). Furthermore, some reduction of drag and acoustic emissions could be expected too.

The interest in flow control for high-lift elements is rather old, as presented in 1961 in an interesting book [11] that summarizes worldwide research on that topic. More recently, in a 1999 NASA/Boeing report from McLean et al. [12], a full integration study of flow control, both with steady or unsteady technologies, was carried out for the full aircraft development, including manufacturing, systems, costs and maintenance. Among all of the aircraft elements, high-lift systems were identified for flow control as the most promising in terms of potential and benefits. It was also highlighted that an accurate aerodynamic performance study of the flow control efficiency was the first mandatory input to perform the accurate full design.

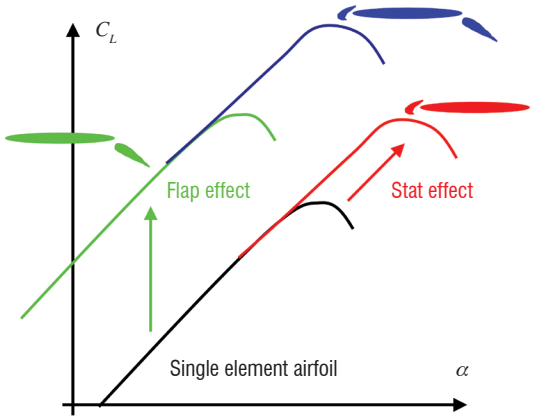

Figure 1 - High-lift slat and flap effects on the lift polar

To simplify high-lift systems of wings using the flow control application, two main separate topics can be considered. The first concerns the flap efficiency. Some studies evaluated its improvement based on present architecture, while others were aimed at eliminating the flap slot. The second topic concerns the leading edge region. Basically, it is aimed at delaying stall directly on a retracted slat configuration, which is difficult because of the very high suction peak in that region. Some people consider that such a configuration is too difficult to be controlled (see [12]) and prefer working on a droop nose configuration [16].

Many means of control exist; from simple passive mechanical vortex generators, to active fluidic, pulsed or synthetic actuators. Many stu-

dies in the literature (See [7], [12], [17], [21] and [23] among many) demonstrate the efficiency of these control devices and the potential of fluidic pulsed/synthetic technologies to reach affordable mass flow and/or energy provided by the aircraft systems. Indeed, pulsed or synthetic blowing allows for almost the same specific conditions and flow control characteristics and even better maximum lift coefficient to be achieved with a limited injected energy. In 2000, Greenblatt and Wygnanski [8] published a reference review of flow control by periodic excitation. Most of the efficiency parameters for unsteady flow control are presented for two-dimensional configurations and the results presented in this paper confirm its conclusions.

A very large amount of studies on this topic exist in the literature, both from the experimental and numerical points of view. Due to the appropriate field of flow control presented in this paper, it is rather difficult to present and make reference to the most representative studies performed worldwide. Hence, some authors cited in the references performed rather complete reviews of some of the most representative studies. Some of them were performed at an academic level, mostly on two dimensional configurations at rather small Reynolds numbers ($< 10^6$). In these cases (see [8] and [21] for example), accurate studies are performed in almost incompressible flows and the fluidic response of the flow to an unsteady excitation is significant. At more realistic Reynolds numbers ($> 10^6$) and Mach number ($M = 0.2$), the control efficiency is generally strongly reduced, but still promising (See [6], [18] and [24] as examples). Hence, to help aircraft manufacturers to apply flow control technologies to their airplanes under low speed conditions, Onera has carried out most of its studies on this topic at Reynolds numbers higher than 1 million, with Mach numbers most of time equal to 0.2.

The objective of flow control applied to the high-lift flap system could be either to improve current high-lift system performance, or simplify the high-lift mechanism. First, the most important dimensionless parameters used in the flow control community are presented. Then, the second section of this paper is dedicated to flow control applied to the flap system; the third is aimed at delaying stall using flow control near the leading edge.

Definition of dimensionless parameters

In the flow control community, some classical dimensionless variables are used to define the control parameters. Among these, the most important ones for this paper are the following:

- The velocity ratio (VR) defines the ratio between the jet exit velocity and the local flow velocity in the vicinity of the actuator.
- The momentum coefficient (C_μ) defines the fluidic momentum injected versus a "global" reference effort on the studied configuration.

  - for steady blowing:

$$C_\mu = \frac{q_m . U_j}{Q_{\inf} . S_{ref}} \quad (1)$$

  - for pulsed blowing (squared signal):

$$C_\mu = \frac{\rho_j S_j < U_j^2 >_t}{Q_{\inf} . S_{ref}} = \frac{1}{DC} . \frac{< q_m >_t . < U_j >_t}{Q_{\inf} . S_{ref}} \quad (2)$$

For a squared signal: $< U_j^2 >_t = DC \times U_{peak}^2$ and $< U_j >_t = DC \times U_{peak}$, where U_{peak} is the amplitude of the squared signal, ρ_j is the jet density, S_j is the blowing orifice area, $< q_m >_t = \rho_j S_j < U_j >_t$ is the time-averaged mass flow rate, $< U_j >_t$ is the time-averaged output velocity, DC is the duty cycle and S_{ref} is the reference surface (flap or entire wing). Since there is a factor $1/DC$ in the pulsed blowing definition, it can be noted that to obtain the same C_μ coefficient between steady and unsteady blowing, the mean mass flow rate $< q_m >_t$ in the unsteady blowing case must be decreased by a factor $\sqrt{DC}$, which means a $1 - \sqrt{DC} \approx 30\%$ mean mass flow rate reduction for $DC = 0.5$.

F^+ is the reduced frequency for unsteady blowing:

$F^+ = \frac{F_{injection} . x_{te}}{V_\infty}$, where $F_{injection}$ is the forcing frequency and x_{te} is the distance between the actuator and the trailing edge.

Flow Control on the Flap

According to McLean et al. [12], flow control applied to the flap system is of major interest. Two different strategies can be considered. First, keeping the same architecture, the flow control could lead to a higher performance or to a limited simplification of mechanisms (reduce flap size and/or gap). Some experimental studies were successful [17] in this objective, as well as detailed numerical work [9][10]. A more "aggressive" strategy is to strongly modify present architecture. Thus, the flap slot suppression leads to a strong separation and thus to a significant loss of lift. Applying flow control in the shoulder region of the flap could lead to an efficiently controlled flap, as presented by Seifert et al. [21].

"Classical" flap architecture

A well-known application of flow control to the flap consists in using mechanical vortex generators in its leading edge region, in order to delay the separation that may occur in the landing phase. This strategy, used nowadays on some commercial aircraft, is very attractive since these actuators, whose height is almost the same as the local boundary layer thickness, are hidden under cruising conditions. Accurate numerical restitutions of these actuators in a 2.5D configuration on the flap were carried out at Onera during the AWIATOR [2], [4] program and successfully compared to experiments. Despite this accurate numerical study, it appears that this expensive strategy was not feasible for complex three dimensional configurations and in a design process. Indeed, the actuators were fully meshed, leading to a prohibitive grid size on more realistic configurations and each actuator characteristic (location, sizes, orientation, etc.) leads to a dedicated grid. An example of this simulation is presented in figure 2, showing the vortices generated on the upper flap side. Optimal parameters where defined for the mechanical vortex generators and they were located upstream of the separation. The advected vortices increase the mixing between the boundary layer and the outer flow and consequently increase the boundary layer momentum, leading to a boundary layer that is more resistant to the adverse pressure gradient, thereby delaying the separation close to the flap trailing edge.

Since the design of such mechanism is too expensive to be fully performed in a wind tunnel or flight tests because of the multiplicity of physical scales involved (actuator sizes << flap length), dedicated methods were developed to numerically perform this optimization at a rather low cost, especially concerning the grid generation and size. To do so, Bender et al. [1] introduced a very simple source model based on the lifting line theory, which is called the BAY model. The effect

of the vortex generator is directly introduced into the flow and thus a single grid can be used for the entire design process of the actuator. This model was successfully used by Jirasek [10] on a high-lift airfoil and Brunet et al. [4] on a flat plate and an airfoil under transonic flow conditions.

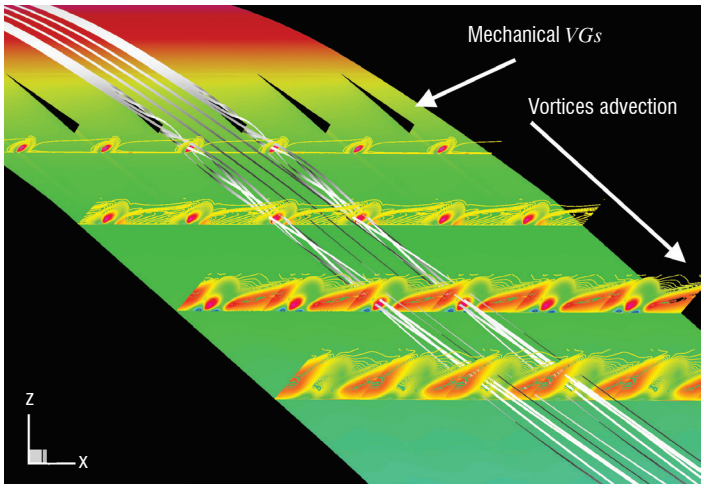

Figure 2 - Mechanical vortex generators on the flap (See [4])

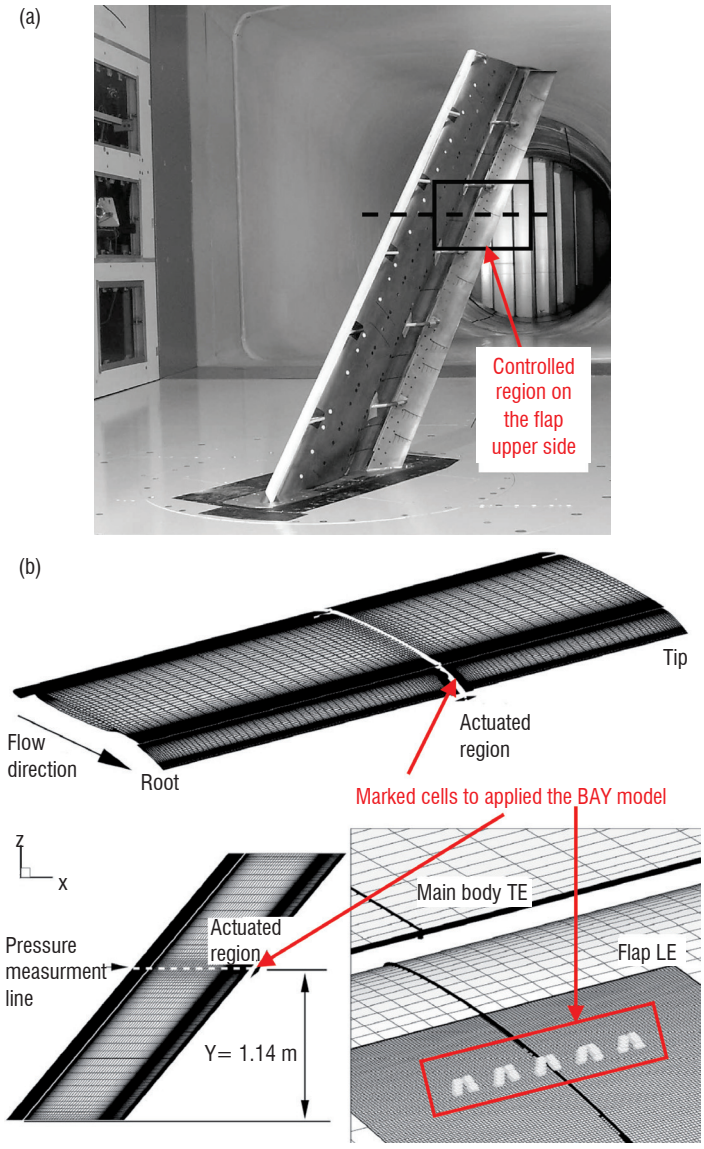

Figure 3 - Model installed in the F1 test section (a) – Skin grid of the AFV wing with cells marked to apply the BAY model (Bender et al. [1]) (b)

This BAY model was introduced into the Onera *elsA* software [4] and used to simulate the same 3D set-up as that tested during the AERO-MEMS II project [15],[23] in the F1 wind tunnel of Onera. The simulated case, including the refined area to capture the vortex generator effects, is presented in figure 3 and more details can be found in [15]. As presented, only a very limited region was controlled on the swept AFV wing, using these actuators located at $x/c_{flap} = 25$ %, which were counter-rotating vortex generators, their height being roughly equal to the boundary layer thickness. The flap angle was increased from 32.4° at its original setting to 40°, in order to reinforce the flap separation to be controlled and thus the flap gap was reduced, because of the flap rotation.

Tests were conducted in the F1 wind tunnel of Onera at a freestream Mach number equal to 0.22 and a Reynolds number of $Re_c = 6.27\,10^6$. Among all the tested angles of attack, the one equal to 12° is selected in this paper to compare simulations with experiments. Hence, pressure coefficient distributions, with or without the vanes, are presented in figure 4 for an equipped pressure chordline located in the vicinity of the actuators, as presented in figure 3. It appears that the simulation performed with the Spalart-Allmaras turbulence model, without control, does not agree well with measurements close to the trailing edge of the flap, because of a massive separation that extends over a large part of the flap. This modeling error is well known for such simulations. On the other hand, both simulations and experiments with vortex generators present a higher suction peak of the flap leading edge and a monotone pressure recovery at the trailing edge, showing only a limited separation. The beneficial control effect is not visible on all other parts of the airfoil, except at the trailing edge of the main element. Nevertheless, this rather limited global effect is mostly caused by the very limited spanwise extension of the controlled region. To enhance this effect, it is necessary to apply flow control to the entire flap. In the end, as presented in the details in [16], counter-rotating mechanical vortex generators, which are optimum for 2D flows, are not suitable for the 3D flows on a swept wing, since only one vane on each pair creates a vortex, the other being aligned with local streamlines.

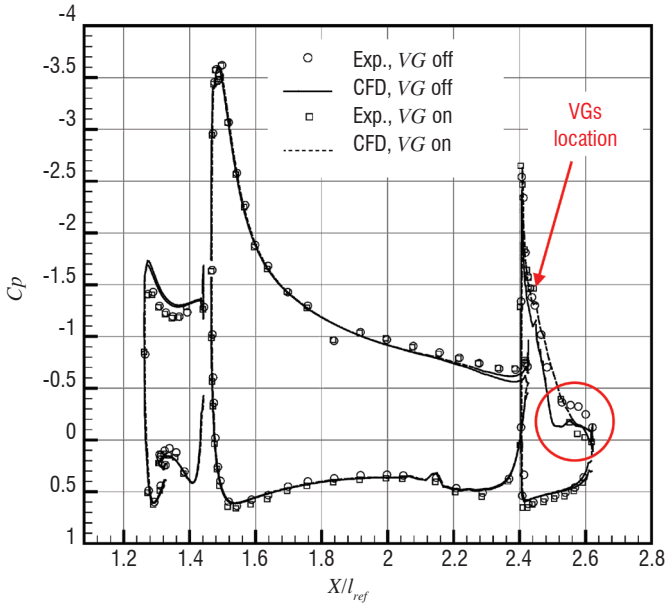

Figure 4 - Pressure distribution, with or without *VGs* on the flap

As presented above, flap efficiency can be increased using mechanical vortex generators installed near its leading edge, allowing a higher

lift or different flap installation characteristics. The drawback to this mechanism is its passive, permanent effect, even in flight domains like take-off, where it is useless. To solve this problem, adaptable and/or on-off vortices can be created using Air-Jet Vortex Generators (*AJVGs*). Many parametric studies exist for these *AJVGs* (For example, there is an interesting review on 2D cases by Greenblatt and Wygnanski [8] and a wing/body study by Crowther [7]) and they allow more or less the same effects as classical mechanical ones to be obtained. The same configuration as that previously presented in this paper has been studied with such *AJVGs*, both by experimental and numerical means. Conclusions are identical to those obtained for the mechanical vanes and the grid difficulties and sizes are also the same. Such grid complexity and size problems for numerical studies can be partially solved using a source term model, like the BAY model presented previously, or by using a chimera approach, as presented in the following sections.

Slotless flap installation

One major way to simplify this flap deployment is to completely suppress the flap slot, resulting in a "simple" hinged slotless flap, as presented in figure 5 (see [13] and [16] for more details). The reference airfoil is a GARTEUR high-lift configuration [22]. The lift loss is significant, as presented in the right side picture of figure 5, obtained with a numerical study. The objective of the flow control, mostly performed numerically, is to retrieve as much lift as possible with a control applied to the flap shoulder region, i.e., in the vicinity of the separation point (blue part of the picture on the left). Note that some tests (not presented and not published) have shown that the classical use of vortex generators (mechanical or fluidic) is inefficient to delay the separation and retrieve lift on such a configuration.

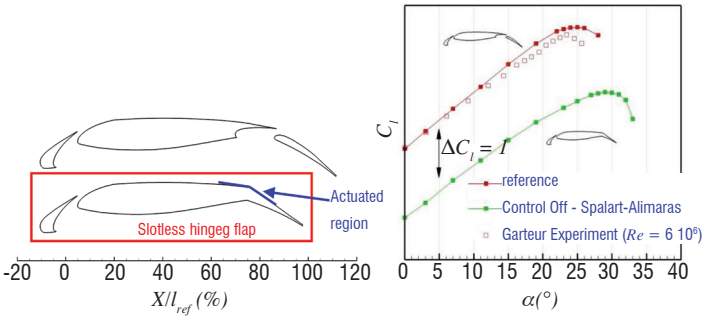

Figure 5 - Simplified slotless hinged flap configuration and resulting effect on the lift curve at $M = 0.2$ and $Re = 1.9\ 10^6$

A numerical optimization has been performed at Onera by Meunier [13],[14], to prepare experimental tests carried out in 2009 in the L1 wind tunnel of Onera Lille [3]. The optimization procedure is aimed at defining the optimum flow control parameters of a continuous blowing slot (location, mass flow, deflection angle) using a Kriging-based optimization method (see [13] and [14] for more details). The purpose of this optimization was to maximize the lift coefficient, which almost corresponds to the minimization of the separation size. Simulations were performed with the *elsA* software, using the chimera approach to simulate the slot and its surrounding flow. Automatic grid generation of the slot and its surrounding grid was performed to ensure the efficiency of the automatic optimization algorithm. The results are presented in the figure 6(a), which shows a Kriging mapping of the evaluations. Based on this study, a model was created and tested in the L1 wind tunnel of Onera Lille in 2009. Some comparisons between simulations and measurements, with and without steady blowing through the slot, are presented in figure 6(b). Note that the required mass flow to achieve this optimum is very high in terms of possible bleed-air drawn from the engine mass flow. Despite the fact that the wind tunnel data was uncorrected and the spanwise extension region of the control was limited to one third of the model, leading to a strong 3D behavior, simulations and experiments agree quite well and the control is very efficient, since it enables (according to simulations) the classical slotted flap performance to be retrieved (see figure 7(a)).

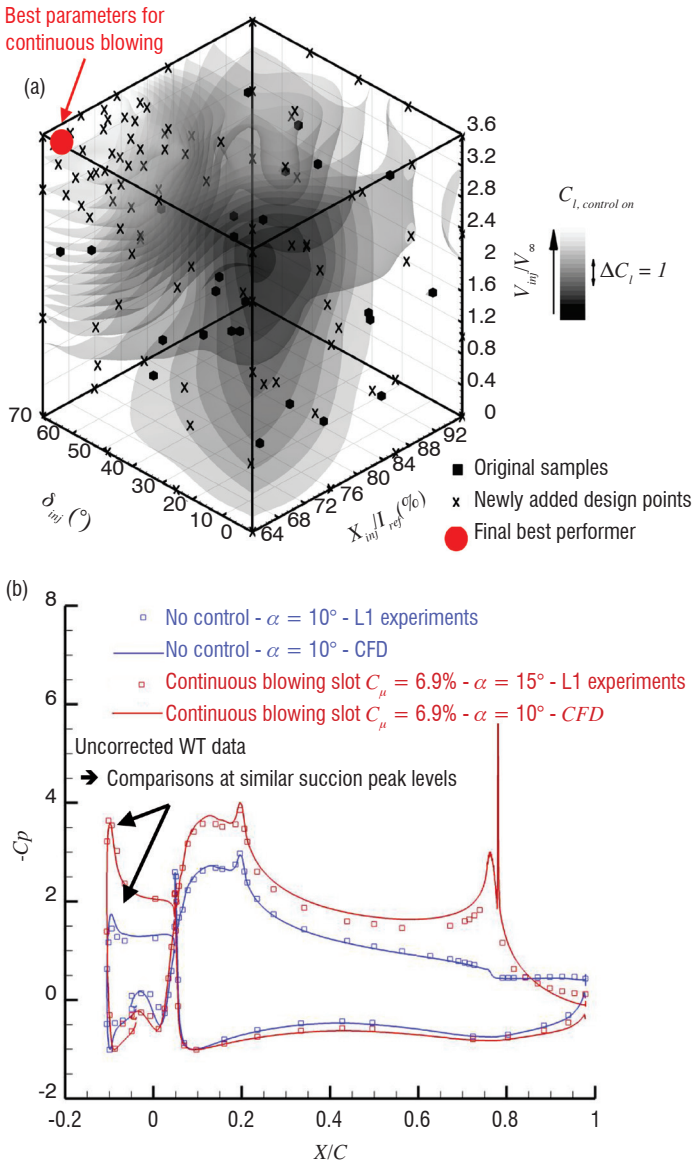

Figure 6 - (a) Sampling evolution and resulting Kriging interpolation for lift coefficient (*CFD*) – (b) Example of *CFD* / experiments obtained

In the literature (see [9] and [21] among many), many studies have shown that pulsed or synthetic blowing could allow a higher efficiency than the continuous one, thus limiting mass flow injection. One of the major drawbacks of such unsteady control is that the maximum control efficiency is often characterized by the generation of large structures, whose sizes are almost equal to half of the flap length. Hence, this maximum averaged lift frequently corresponds to a maximum lift unsteadiness. For 2D configurations, Meunier et al. [13],[14] and [16] show that this unsteadiness is of primary importance, but in recent 3D studies (Rudnik [18] and Ciobata [5]), the unsteadiness in lift levels caused by flow control is much more limited. Hence, though this unsteadiness is an important topic that must be taken into account, it is not obvious whether it could limit control efficiency or not.

Using a piezo-electric actuator, pulsed blowing was evaluated during the test in the L1 wind tunnel, in order to limit the injected mass flow and try to enhance the control efficiency using unsteady flow excitation. Despite a local efficiency being evidenced, the too limited spanwise extension of the actuated region does not allow an efficient control to be obtained and the following results are only based on unsteady simulations performed [14],[16] with the elsA software.

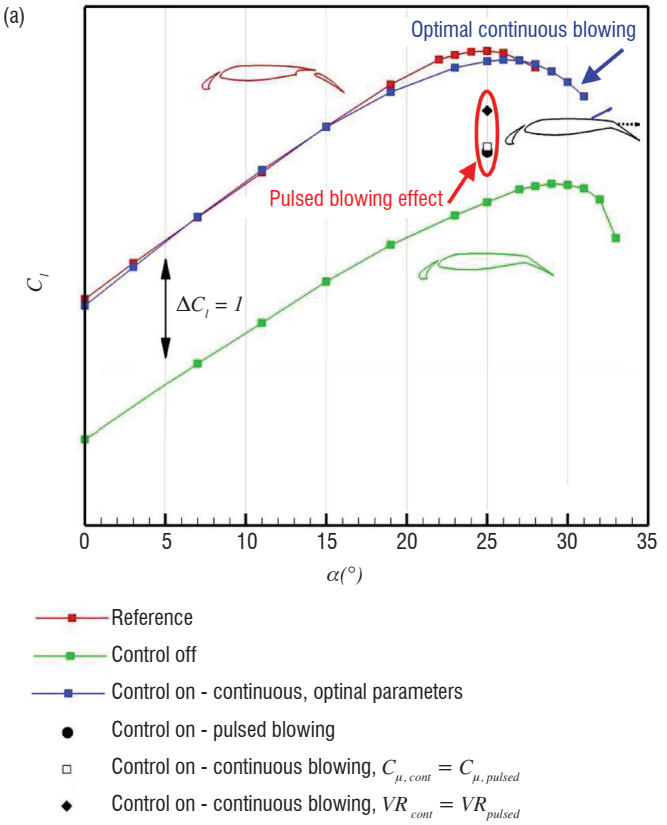

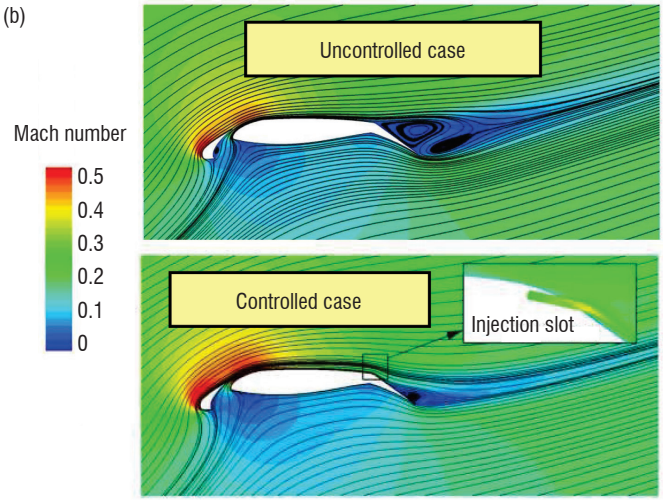

Figure 7 - (a) Efficiency of continuous and pulsed blowing on the lift curve – (b) Flow control effect on the flow field

A multi-objective optimization was carried out at Onera by Meunier [14],[16], for a single angle of attack close to stall, in order to both maximize the averaged lift coefficient and minimize lift fluctuations. To do so, unsteady RANS simulations were carried out and automatically post-processed during the optimization procedure. Based on a Kriging interpolation, two response surfaces were built and a single optimum point was selected for these two surrogate models. The results are presented in figure 7. In the left side picture presenting the lift versus the angle of attack, the great efficiency of the continuous blowing can be seen, with a high mass flow allowing more or less the performance of the classical configuration to be retrieved. The optimum, multi-objective optimization at a 25° of angle of attack presents a lower lift coefficient than steady blowing. The unsteady beneficial effect of the pulsed actuator is visible, since some steady blowing simulations carried out at the same velocity ratio (VR) or momentum coefficient C_μ present a lower efficiency. To better understand this beneficial effect, let us recall that for the same C_μ coefficient, the necessary mass flow is lower for the pulsed case than for the continuous one. Although the mass flow requirement is still too high to be installed on a real aircraft configuration, the required levels injected are in a correct order of magnitude. The figure 7(b) shows that the massive separation on the flap is mostly delayed, but a limited separation bubble still exists at the trailing edge.

In conclusion, the loss of efficiency of a slotless hinged flap can be entirely retrieved using a continuous blowing slot located in the vicinity of the flap shoulder, upstream of the massive separation. Nevertheless, the required mass flow is not realistic for aircraft. The use of pulsed blowing allows a reduction of the mass flow requirements and its efficiency is higher than steady blowing cases with the same mean mass flow injected. Hence, it has been shown that this kind of configuration can be envisaged, but the required mass flow to delay the separation is still too high and must be reduced. The exact necessary reduction is very difficult to quantify since it depends on the aircraft considered (business jets are different from classical civil aircraft), but it is roughly comprised between factors 2 to 5, compared with present studies at realistic Reynolds and Mach numbers. This could be considered with new actuators like synthetic jets which only require an electrical power.

Flow control at the leading edge

During the EUROLIFT II project [18], a high-lift slatless configuration (based on the AFV wing of Onera) was studied in the Airbus-UK F-LSWT wind tunnel. To delay the early stall of the simplified configuration, steady blowing at the leading edge through a slot was used. The control was efficient, even at realistic Reynolds and Mach numbers, but the required mass flow was again too high. It appears again that a strong effort must be made in order to drastically reduce the necessary mass flow for control, keeping efficiency acceptable. To do so, two main strategies can be considered. The first is to limit the physical complexity of the flow control using a suction peak reduction close to the leading edge. This idea was tested at Onera during the European AVERT project using a droop nose configuration. The second way is to the keep this leading edge unchanged and work on more efficient actuations, like pulsed or synthetic jets.

Droop nose configuration

First, the droop nose configuration studied during the European AVERT project is considered. The same basic GARTEUR high-lift configuration [22] used previously for a slotless flap is considered. As presented in figure 8, the slat replacement by a droop nose induces an earlier stall. A model was manufactured and tested in the L1 wind tunnel of Onera Lille to evaluate the control efficiency close to the shoulder in the blue region of the left side picture of figure 8. A first numerical analysis was carried out to optimize flow control parameters.

As presented in [16], control by mechanical and fluidic vortex generators was inefficient on this configuration, both in the numerical and experimental studies. Indeed, the generated vortices are convected away from the airfoil immediately downstream of the shoulder, because of the too strong geometry change. Hence, these vortices could not act on the separation, which occurs immediately after the slat shoulder and it appears that flow control based on blowing slots must be considered, to allow an efficient effect on the separation.

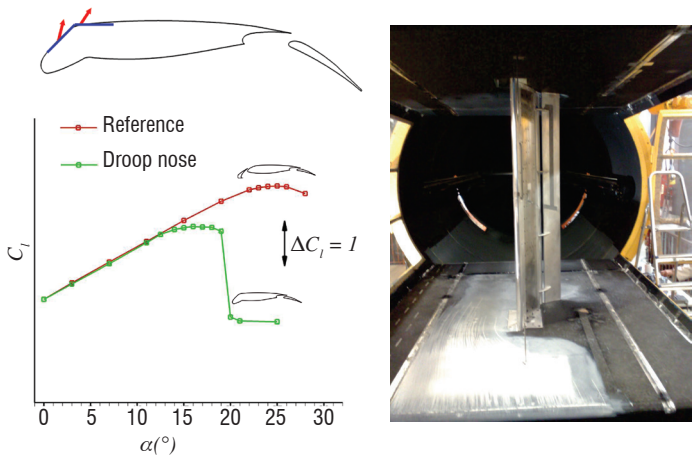

Figure 8 - Droop nose configuration, its effect on the lift curve (*CFD*) and corresponding model installed in the L1 wind tunnel

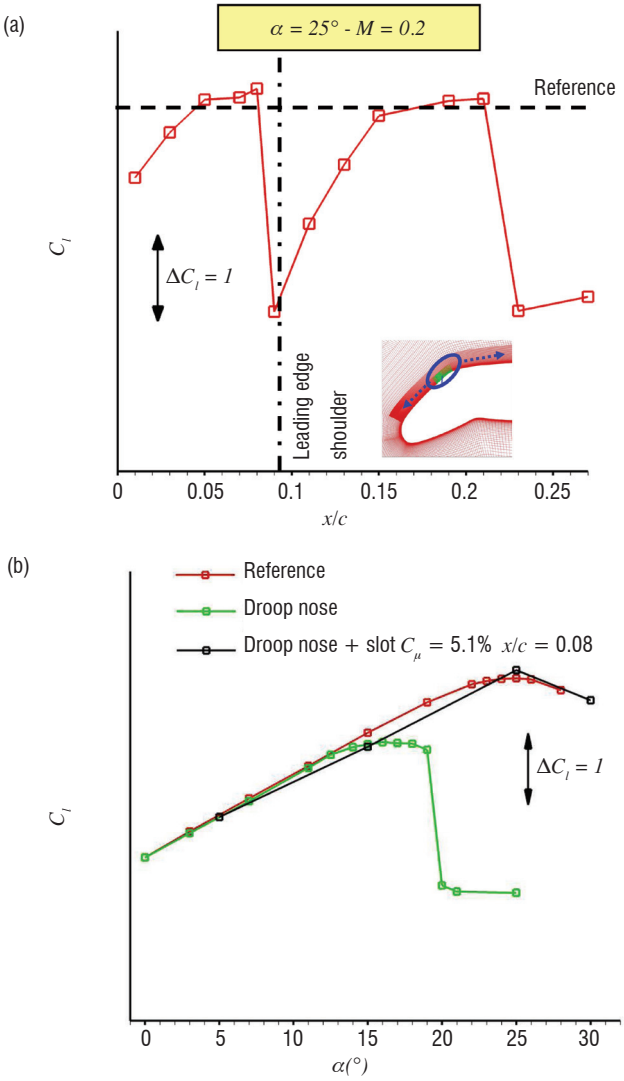

Figure 9 - (a) CFD simulations to optimize slot location - (b) Resulting lift curve with best continuous flow control parameters

Based on the chimera approach available in the elsA software, simulations were carried out to define the optimum slot location to be tested during the tests. Several flow control parameters (C_μ, slot location, injection angle) were studied [16], in order to find the optimum ones. Hence, the slot location effect at $C_\mu = 5.1\%$ and $\delta_{inj} = 70°$ is presented in figure 9(a), the resulting lift coefficient being presented figure 9(b). The optimum location is immediately upstream of the shoulder, or slightly downstream of it. The lift curve obtained with the location upstream of the shoulder shows that the original lift performance with a slotted slat can be retrieved. Once more, despite this remarkable efficiency, the required mass flow is far from being realistic for an aircraft and more work must be carried out to reduce it. To do so, pulsed jets or synthetic jets must be considered.

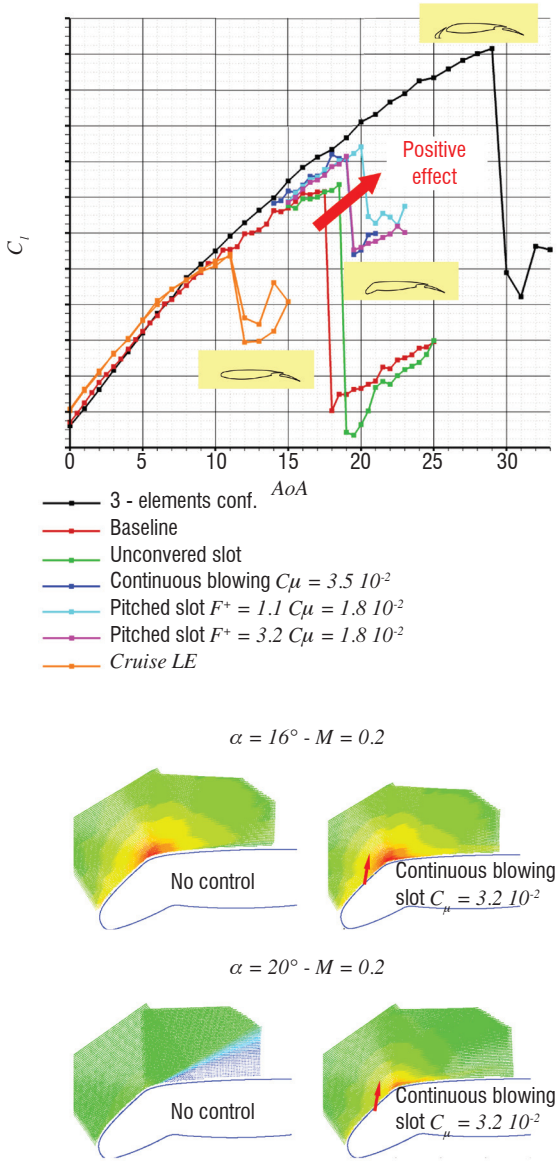

Figure 10 - Experimental lift coefficient of a continuous or pulsed slot and PIV fields for two different points ($M = 0.2 - Re = 2\ 10^6$)

During wind tunnel tests in the L1 wind tunnel of Onera Lille, a piezo-electric actuator was designed and manufactured by Onera, in order to perform pulsed blowing up to 1,000 Hz. Only one third of the spanwise extension of the model was controlled and the actuators were placed either upstream or downstream of the shoulder, as predicted by optimum steady simulations. The results on the lift curves are presented in figure 10. The reader can immediately see that the controlled cases exhibit only a slightly delayed stall, compared to the

baseline in black. This rather limited effect, strongly underestimated compared to the numerical studies, is probably mostly caused by the too limited spanwise controlled extension. Furthermore, the high momentum values ($C_\mu = 5.1\%$) for numerical steady blowing could not be fully reached with the installed actuator (maximum $C_\mu = 3.5\%$). Nevertheless, several interesting effects can be observed. First of all, pulsed blowing allows at least the same beneficial effect as continuous blowing for $F^+ = 3.2$, or even higher for $F^+ = 1.1$. Indeed, several frequency effects were evaluated and a maximum efficiency was observed at about $F^+ = 1$, which is fully consistent with the literature [8]. This beneficial unsteady effect allows a significant mass flow reduction, compared with steady blowing cases. To better evaluate this, it would have been necessary to pursue the tests and apply flow control to the full span of the model.

In figure 10(b), several PIV measurements are presented, just before and after the stall of the uncontrolled case. Before the stall, no flow control effect is clearly observable on the global flow, except a higher velocity value close to the wall in the shoulder region. In stalled conditions, a massive separation occurs after the shoulder for the uncontrolled case. The control suppresses this separation in the measured field showing the control efficiency, but the high velocity region is reduced compared to the case before stall.

In conclusion, for the droop nose configuration, it appears that the original performance of the reference slotted slat can be recovered using flow control. With a large mass flow rate value, this objective can be easily achieved, but a lot of work must still be performed with pulsed blowing to achieve the necessary efficiency. Indeed, an unsteady beneficial effect has been shown at about $F^+ = 1$, compared to steady blowing. A full spanwise control is necessary, to better evaluate the efficiency level.

Cruising slat configuration

Although the previously presented droop nose configuration seems to be "receptive" to flow control, it is clearly more interesting to work on a slatless leading edge, since this configuration presents no moving part and thus corresponds to the most simplified leading edge for high-lift configurations. Nevertheless, due to the very high suction peak characteristic of such a configuration, it is clearly a "challenging" case. Based on the same GARTEUR high-lift airfoil as the previous ones [22], a numerical and experimental study was carried out on the slatless configuration [3]. The conclusions of this study carried out at Onera (not presented in this paper, see [3]) were that once more the required mass flow rate is too high to delay separation and stall. Furthermore, the spanwise control extension was too limited and the slot located too far downstream. In the end, control by continuous or pulsed fluidic slot only allows a smoother stall to be obtained. To be more efficient, it is necessary to extend the actuation as much as possible all along the span and place it upstream of the separation point, very close to the leading edge.

Recently, in 2010, a new model with a laminar leading edge was designed and manufactured by Dassault-Aviation. This model, presented in figure 11, was studied in the L1 wind tunnel of Onera Lille and it has a reference chord length of 630 mm. The transition trip (bottom left picture) was carefully studied with a CADCUT technique, in order to properly distinguish control and transition effects. In the end, two Kruegers were installed at either side of the model (picture on the right), in order to limit corner separations arising from the interaction between wind tunnel walls and the model. These Kruegers were simply designed, based on the original airfoil shape, to limit the suction peak at the leading edge and thus postpone delay separation in a much more downstream location. Then, immediately downstream of the Kruegers, rather significant mechanical VGs are installed (The same ones as presented in a previous study [3]) and thanks to Kruegers they are efficient, since they are installed in an attached region. This combined wind tunnel set-up flow control methodology helped to limit the influence of corner flow separation and it ensured symmetrical flow on this limited span to chord ratio configuration.

Two means of control are presented in this paper. In both cases, the control was applied only on two thirds of the model span width, to reduce manufacturing costs for the actuators and also because of the limited mass blowing that could be provided. In the end, the spanwise blowing region corresponds to the region between Kruegers. First, continuous fluidic vortex generators (co-rotating or counter-rotating) are placed in the lower side, but very close to the leading edge, in order to allow the vortex convection towards the upper side. This lower side placement is defined in order to place them far enough upstream of the separation to allow a correct vortex development and increase the local velocity ratio. This efficient setting for fluidic VGs was originally proposed by Scholz et al. [19] and later further studies show that generated vortices survive the flow acceleration/deceleration around the leading edge (See Scholtz et al. [20] and Wild et al. [24]). The second means of control is tangential slots (pitched at 60°) placed at the upper side of the model, close to the separation point, i.e., $x/c = 1\%$. Three different slot widths were considered (0.25 mm / 0.37 mm / 0.5 mm) and a piezo-electric actuator allows either steady or pulsed blowing (up to 1,000 Hz) to be performed, with a maximum mass flow in continuous mode of up to 100 g.s-1 for a one meter span. The default duty cycle (DC) for pulsed jets is set to 50%, but some tests have been performed at 25% also.

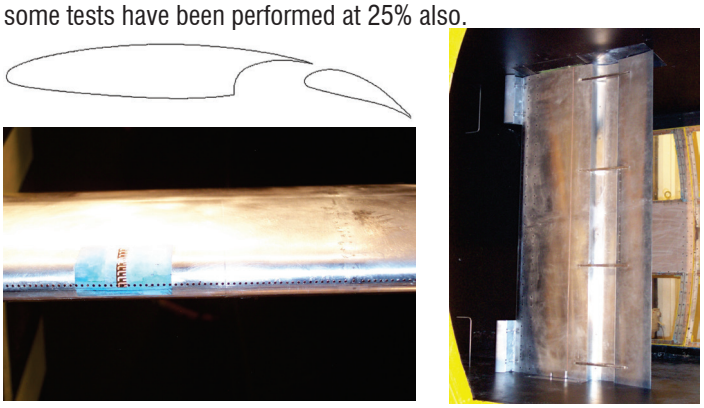

Figure 11 - The slatless model studied (top left), used transition trip (bottom left) and set-up in the test section (right)

A preliminary numerical study was carried out with the elsA software, to evaluate the control efficiency. These simulations were performed with the 0.25 mm slot width, in a continuous mode and at the maximum blowing mass flow rate. Control efficiency was observed, but strong compressibility effects and limitations were pointed out also. Hence, as presented in figure 12 (a), the control efficiency to delay stall strongly decreases when the freestream Mach number increases. One can say that it is linked to the flow control momentum coefficient, but a deeper analysis of the numerical solutions shows that the origin is linked to compressibility effects, as presented in the figure 12(b). Indeed, at high angles of attack and Mach numbers, a supersonic region appears with a shock recompression. This supersonic region is reinforced by the blowing slot and thus its beneficial

effect is compensated by this strong recompression, which leads to an earlier separation. Thus, during the tests, two different freestream Mach numbers were considered ($M = 0.115$ and $M = 0.175$), in order to better evaluate the control efficiency and the compressibility effects. In the future, special care for the slot design, location and mass flow must be taken in account, to limit these compressibility constraints.

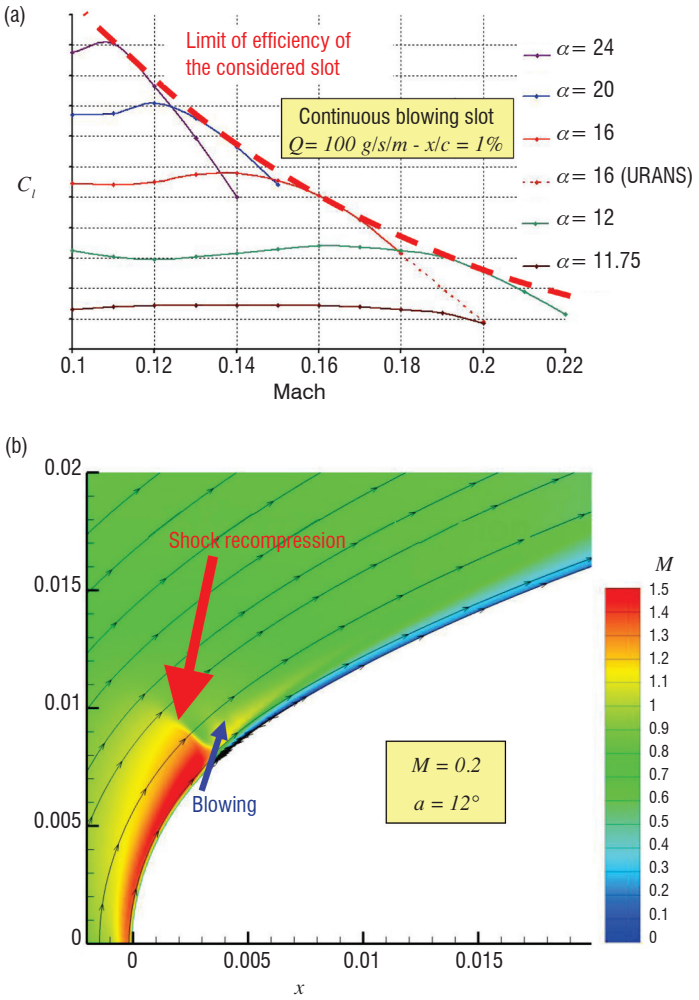

Figure 12 - CFD simulation - (a) Mach number effect on the control efficiency - (b) Detailed flowfield computed

All results obtained during the L1 tests cannot be presented in this paper. Only the most representative part is summarized. Thus, in figure 13, the normal force coefficient curves versus the angle of attack are presented, for the different tangential slots without pulsing. The two tested Mach numbers are shown. A clear beneficial effect is evidenced, especially at the lower Mach number. The increase in momentum coefficient highly delays the stall, but it can be noted that the mass flows presented are again very high, but pulsed blowing should strongly reduce them for the same aerodynamic effect. In regard to the slot width effect, it is strongly reduced compared to the momentum coefficient effect. Nevertheless, it can be seen that for the maximum mass flow injected, the efficiency is reduced for wider slots corresponding to limited velocity ratios and reduced momentum coefficient. As a conclusion, it is very interesting to reduce the slot width to enhance flow control efficiency through the velocity ratio and momentum coefficient increase. To better analyze the control efficiency, it is necessary to compare the maximum normal force coefficients. Despite the large spanwise actuated region, three dimensional effects were observed during the tests, caused by the low span to chord ratio. These complex effects have an influence on the normal force coefficient obtained by pressure tap integration. These effects are visible in figure 13, where the stall is sometimes difficult to determine. To partially solve this problem, the following comparisons are based on the minimum value of the wall pressure coefficient at the suction peak at the leading edge. This "solution" is not fully satisfactory, but it allows clearer conclusions to be obtained.

The changes in the minimum Cp values at the leading edge versus the momentum coefficient for the lower side fluidic vortex generators and upper side tangential blowing cases are presented in figure 14. On the one hand, fluidic vortex generators have only a limited effect and the momentum coefficient increase does not amplify this effect. On the other hand, the tangential blowing, continuous or pulsed, is clearly efficient and the reduced efficiency with increasing Mach number observed in numerical simulations is not retrieved here. Indeed, the control delayed stall seems almost proportional to the momentum coefficient and independent of the freestream Mach number. Strangely, the slot width effect has almost no influence on the control efficiency on these curves for pulsed blowing cases, but for continuous cases the efficiency decreases with the slot width. This could show that the control mechanisms are different between the continuous and pulsed cases. It can be noted that the momentum coefficient is the appropriate non-dimensionalized parameter to scale the control efficiency. The complete post-process of the various tests shows (no curves plotted in this paper) that a pulsed blowing, at a dimensionless coefficient F^+, equal to about 1, allows a higher efficiency compared to continuous blowing cases with the same mean mass flow rate. At higher or lower frequencies, the pulsed blowing is "only" as efficient as the continuous blowing at the same C_μ value. Nevertheless, considering the $C\mu$ formula for pulsed blowing presented at the beginning of this paper, it leads to a reduced mass flow by a factor of the square root of DC between pulsed and continuous blowing cases, whatever the actuator frequency is. Thus, even though the unsteady flow control is not always more effective than the continuous one, it could result in a significant mass flow reduction, provided that the forcing frequency is well chosen.

To summarize the results obtained during this wind tunnel test campaign, figure 15 shows the changes in the maximum normal force coefficient gain ΔC_{Nmax} with C_μ, for different freestream velocities, slot widths, duty cycles and forcing frequencies (optimal F^+ only). The results of the fluidic VGs are not plotted in this figure, since no maximum normal force coefficient gain is observed, contrary to figure 14, where there was a small decrease of the minimum pressure. Figure 15 (left) shows a linear increase in the maximum normal force with the momentum coefficient. Once again, this figure shows that, in this case, the momentum coefficient is the appropriate non-dimensionalized parameter to compare test cases with different freestream velocities, slot widths and duty cycles, but also to compare continuous and pulsed blowing, since all of the results fit rather well on a linear curve. For information, if a different definition of Cμ had been used (Eq. (2) without the factor $1/DC$), as is often found in the literature with pulsed blowing, the case with $DC = 0.25$ (orange triangle) would not have been on the linear curve. Figure 15 (right) shows the effect of F^+ on ΔC_{Nmax}. The lower the tested frequency is, the higher ΔC_{Nmax} is. The optimal reduced frequency among all those tested seems to be around $F^+ = 0.7$.

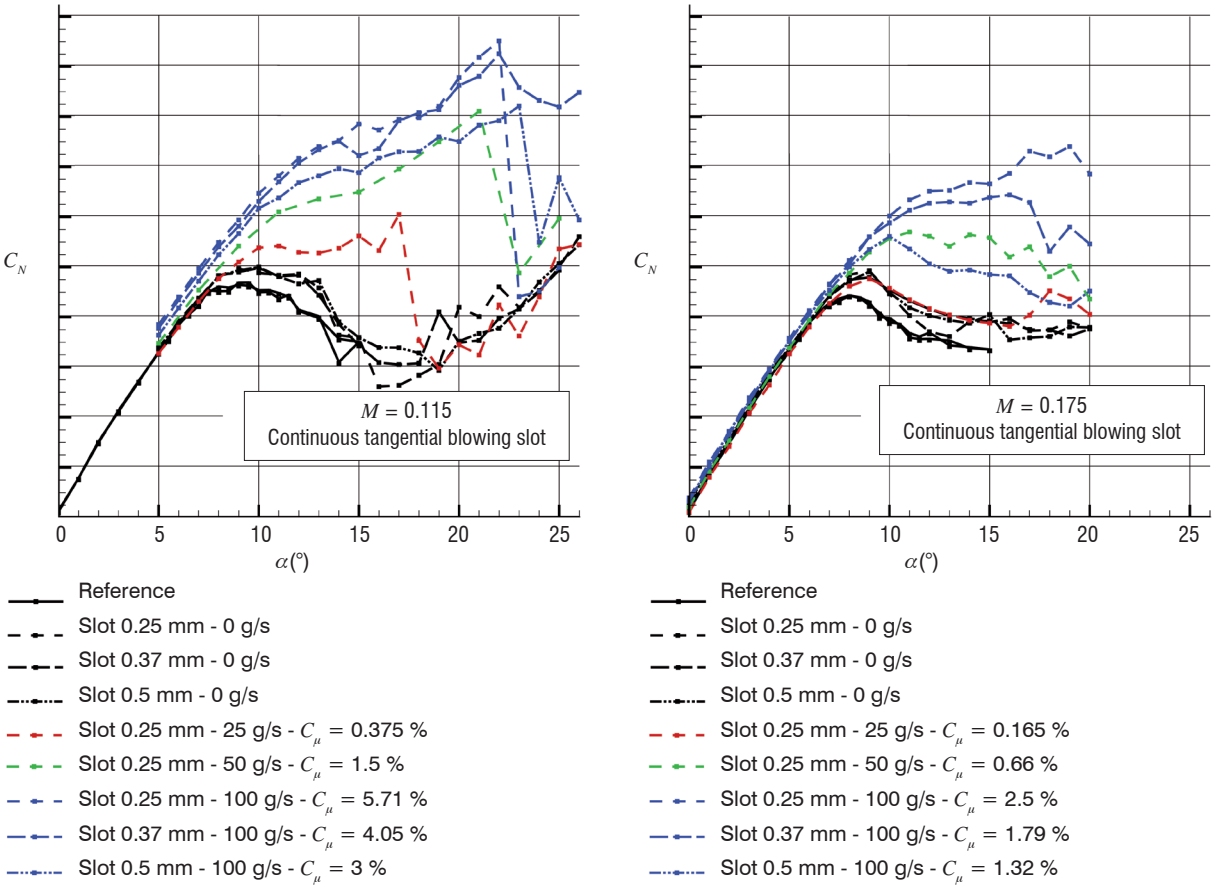

Figure 13 - Continuous control efficiency on the lift curves at M = 0.115 and M = 0.175

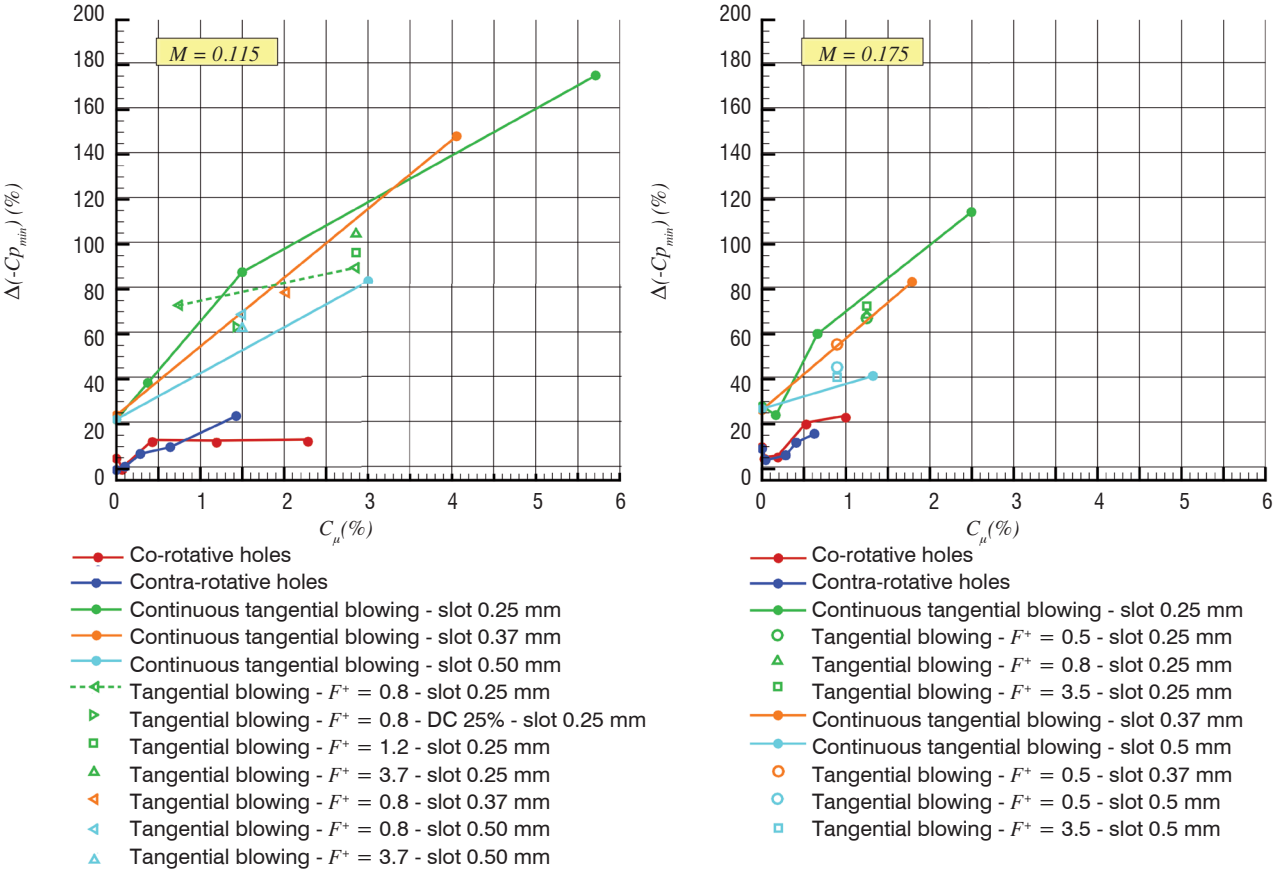

Figure 14 – Pulsed and continuous blowing effect on -Cp_{min} at M = 0.115 and M = 0.175

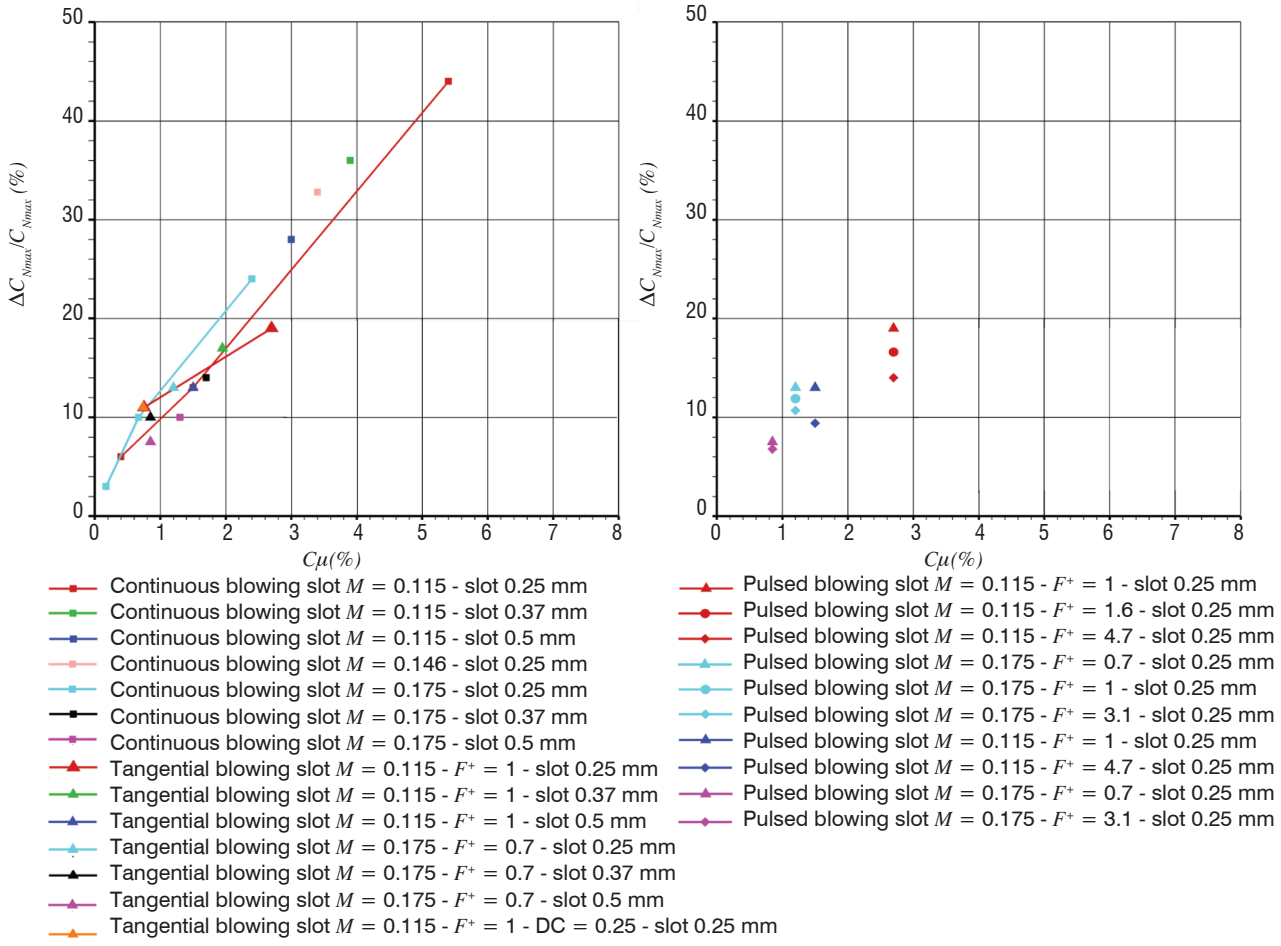

Figure 15 – Changes in ΔC_{Nmax} with $C\mu$ for different freestream velocities, slot widths, duty cycles and forcing frequencies

In the end, despite compressibility limitations on this configuration, a clear beneficial effect has been evidenced. Fluidic vortex generators placed on the lower side have a positive, but limited effect. Tangential blowing at the upper side seems to be more efficient and some additional beneficial effects were observed at a pulsed frequency of about $F^+ = 1$. Nevertheless, required mass flow is still too high to be considered on a realistic aircraft and a strong optimization of the slot width, shape, location and frequency must still be performed to enhance its efficiency, directly leading to a mass flow reduction. Additional pulsed or synthetic effects must be sought carefully, in order to limit the mass flow injected.

Conclusions and perspectives

The beneficial use of flow control technologies for high-lift configurations has been shown through various studies performed at Onera. For classical slotted slat and flap configurations, the use of mechanical or fluidic vortex generators at the flap leading edge is very efficient to delay the separation that may occur in a landing phase on its upper side. This simple means of control, already used under flight conditions, may be used to enhance the high-lift performance or simplify its mechanisms, such as a reduction of the flap size and gap. For more “aggressive” designs, the slot suppression is very interesting from the point of view of aircraft manufacturers. Nevertheless, this solution is much more complex to control and classical vortex generators seem to be inefficient to delay separation and stall for such configurations. Thus, tangential blowing is a promising approach and demonstrations performed at Onera, both numerically and experimentally, have shown that the original slotted configuration performance can be entirely recovered. Unfortunately, the most efficient cases are based on continuous blowing and the required mass flow is too high to be realistically considered. Thus, pulsed blowing has shown an additional efficiency at some frequency “exciting” the unsteadiness of the flow at a reduced required mass flow, but it is still a little too high. Thus, a lot of work must still be performed to upgrade actuator efficiency or use “advanced” actuators like synthetic jets, which do not use air blowing. Another interesting way to be considered, is to define new airfoil geometries more “receptive” to flow control, i.e., taking into account the flow control directly in their design phase.

The following table summarizes the conclusions obtained in our studies, which could be slightly different from those of the very broad literature. Note that only conclusions obtained here at "realistic" Mach (almost 0.2) and Reynolds numbers (almost 2 million) are considered. Many additional parameter studies carried out outside of Onera may lead to different conclusions.

	Mechanical of fluidic *VGs*	Continuous blowing slot	Pulsed blowing slot
Classical Flap	Efficient	Not tested yet at Onera	Not tested yet at Onera
Slotless Flap	Not efficient	Efficient but significant mass flow necessary	Efficient
Droop Nose Leading Edge	Not efficient	Efficient but significant mass flow necessary	Efficient
Slatless Leading Edge	Some limited efficiency at the lower side	Efficient but significant mass flow necessary	Efficient

Several studies are still in progress at Onera on this topic. The first main objective is to develop efficient and new actuators to show flight feasibility. Secondly, more realistic configurations, including swept wing, winglet and engine, will be studied to validate the efficiency and to control local separation also, which may cause earlier stall ■

Acknowledgements

These studies were partly conducted within the framework of a national program supported by French government agencies (DGAC – French Ministry of Transportation / DGA – French Ministry of Defense) in collaboration with Dassault-Aviation, and within the FP7 AVERT European project (Contract No.: AST5-CT-2006-030914), funded by EC and project partners. The authors gratefully acknowledge Jean-Luc De Coninck and Jean-Claude Monnier for the wind-tunnel tests in L1 and Frédéric Ternoy and his team for the actuators, model design and manufacturing, as well as Christophe François, Mickäel Meunier and Jean-Yves Andro for numerical simulations and Frédéric Moens for his knowledge and advice on high-lift aerodynamics.

References

[1] E. BENDER, B. ANDERSON, P. YAGLE - *Vortex Generator Modeling for Navier-Stokes Codes*. FEDSM99-6919. 3rd ASME/JSME join Fluids Engineering Conference, San Francisco, California, July 18-23 1999.
[2] K. BOHANNON - *Passive Flow Control on Civil Aircraft Flaps using Sub-Boundary Layer Generators in the AWIATOR Program*. AIAA 2006-2858, 3rd AIAA Flow Control Conference - San-Francisco (CA), 5-8 June 2006.
[3] V. BRUNET, J. DANDOIS, M. MEUNIER, J.-L. DE CONINCK, C. VERBEKE, F. TERNOY - *Flow Control for Simplified High-Lift Configurations*. CEAS/KATnet II Conference on Key Aerodynamic Technologies, 2009.
[4] V. BRUNET, C. FRANCOIS, E. GARNIER, M. PRUVOST - *Experimental and Numerical Investigations of Vortex Generators Effects*. AIAA2006-3027. 3rd AIAA Flow Control Conference - San Francisco, 5th - 8th, June 2006.
[5] V. CIOBACA, T. KÜHN, R. RUDNIK, M. BAUER, B. GÖLLING - *Active Flow Separation Control on a High-Lift Wing-Body Configuration. Part 2: The Pulsed Blowing Application.* AIAA2011-3169, Honolulu, Hawaii, 27-30 June 2011. 29th AIAA Applied Aerodynamics Conference.
[6] V. CIOBACA, T. KÜHN, R. RUDNIK, M. BAUER, B. GÖLLING, AND W. BREITENSTEIN - *Active Flow-Separation Control on a High-Lift Wing-Body Configuration*. Journal of Aircraft.
[7] W.J. CROWTHER - *Separation Control on a Trailing-Edge Flap Using Air Jet Vortex Generators*. Journal of Aircraft, 43(5):1589–1593, September-October 2006.
[8] D. GREENBLATT, I. WYGNANSKI - *The Control of Flow Separation by Periodic Excitation.* Progress in Aerospace Sciences, 36(7):487–545, 2000.
[9] B. GÜNTHER, F. THIELE, T. WEINKAUF, J. SAHNER, H.-C. HEGE - *Feature-Based Comparison of Flow Fields around a Three-Element High-Lift Configuration with Active Flow Control*. AIAA 2008-4079. 4th Flow Control Conference, Washington, 23-26 June 2008.
[10] A. JIRASEK - *Vortex-Generator Model and its Application to Flow Control.* Journal of Aircraft, 42(6):1486–1491, 2005.
[11] G.V. LACHMANN, editor - *Boundary Layer and Flow Control*. Its Principles and Application, volume 1. Pergamon Press, 1961.
[12] J.D. MCLEAN, J.D. CROUCH, R.C. STONER, S. SAKURAI, G. SEIDEL, W.M. FEIFEL, H.M. RUSH - *Study of the Application of Separation Control by Unsteady Excitation to Civil Transport Aircraft*. Technical Report NASA / CR-1999-209228, NASA, June 1999.
[13] M. MEUNIER - *Simulation and Optimization of Flow Control Strategies for Novel High-Lift Configurations*. AIAA J., 47:1145–1157, 2009.
[14] M. MEUNIER - *Simulation et optimisation de systèmes hypersustentés d'avions civils equipes de dispositifs de controle des decollements*. PhD thesis, Université Pierre et Marie Curie, Paris VI, 27 novembre 2009.
[15] M. MEUNIER AND V. BRUNET - *High-Lift Devices Performance Enhancement Using Mechanical and Air-Jet Vortex Generators*. Journal of Aircraft, 45(6):2049–2061, November-December 2008.
[16] M. MEUNIER, J. DANDOIS - *Simulations of Novel High-Lift Configurations Equiped with Passive and Active Means of Separation Control*. AIAA 2008-4080, Seatle, USA, 23-26 June 2008.
[17] A.J. RAE, S.A. GALPIN, J. FULKER - *Investigation into Scale Effects on the Performance of Sub Boundary-Layer Vortex Generators on Civil Aircraft High-Lift Devices*. AIAA 2002-3274, St. Louis, USA, 24-26 June 2002. 1st AIAA Flow Control Conference.
[18] R. RUDNIK, H. VON GEYR - *The European High Lift Project EUROLIFT II - Objectives, Approach, and Structure.* AIAA 2007-4296. 25th AIAA Applied Aerodynamics Conference, 25-28 June 2007.

[19] P. SCHOLZ, M. CASPER, J. ORTMANNS, C.J. KHALER, R. RADESPIEL - *Leading-Edge Separation Control by Means of Pulsed Vortex Generator Jets.* Journal of Aircraft, 46(4):837–846, 2008.
[20] P. SCHOLZ, C.J. KHALER, R. RADESPIEL, J. WILD, G. WICHMANN - *Active Control of Leading-Edge Separation within the German Flow Control Network*. AIAA 2009-529, 2009.
[21] A. SEIFERT, A. DARABI, AND I. WYGNANSKI - *Delay of Airfoil Stall by Periodic Excitation*. Journal of Aircraft, 33(4):691–696, August 1996.
[22] J.-J. THIBERT - *The Garteur High-Lift Research Program*. AGARD-CP515 "High Lift Aerodynamics", pages 16–1, 16–21, 1992.
[23] C. WARSOP - *Results and Lessons Learned from the European AEROMEMS 2 Project.* AIAA 2006-3503. 3rd AIAA Flow Control Conference, June 2006.
[24] J. WILD, G. WICHMANN, F. HAUCKE, I. PELTZER, P. SCHOLZ - *Large Scale Separation Flow Control Experiments with the German Flow Control Network*. AIAA 2009-530, 47th AIAA Aerospace Sciences Meeting Orlando, Florida, 5-8 January 2009.

AUTHORS

Vincent Brunet received his Master's Degree and Engineering Diploma from the CORIA / INSA Rouen School of Engineering in 2000. Then, he became a research engineer in Onera, first in the Numerical and Aeroacoustics Department (DSNA) and then in the Applied Aerodynamics Department (DAAP). In the Civil Aircraft team, he is in charge of unsteady and control fields.

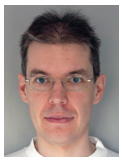

Julien Dandois graduated from the Ecole Nationale Supérieure d'Arts et Métiers (ENSAM) in 2003 and received a PhD in Fluid Mechanics from Paris 6 University in 2007. Since that time, he has worked in the Civil Aircraft Unit of the Applied Aerodynamics Department, in the fields of high-lift, separation control, buffet control, closed-loop control and aeroacoustics.

Christophe Verbeke obtained his engineering degree in 1986 at Polytech Lille (Lille University of Science and Techniques). He joined the Onera Lille center in 1987 as a research engineer. He is the scientific and technical manager of the L1 and L2 DAAP wind tunnels.

J. Dandois
(Onera)
P.-Y. Pamart
(Snecma)

E-mail: julien.dandois@onera.fr

NARX Modeling and Extremum-Seeking Control of a Separation

A numerical study concerning a SISO active closed-loop separation control on a rounded step is presented. A first study of the synthetic jet frequency effect on the separation shows that the mean separation bubble surface is minimized if the mean pressure of a single wall pressure sensor is maximized. With the aim of designing a closed-loop strategy for the control of the recirculation bubble, a NARX black-box model of the pressure signal is identified using a single unsteady RANS simulation. The basic extremum-seeking algorithm is improved with an adaptive gain, to guarantee algorithm performance and this modification is validated against the nonlinear black-box model of the forced flow. Then, the robust adaptive closed-loop is applied in real-time with an unsteady RANS simulation. Closed-loop results show the ability of the extremum-seeking control with adaptive gain to automatically control the separation, by minimizing the recirculation bubble surface using an unsteady RANS simulation.

Introduction

Separated flows occur in a variety of engineering applications and generally have a negative impact on performance. Recently, numerous attempts have been made to control turbulent separated flows, in order to improve aerodynamic performance. Even though open-loop control has been successful in suppressing separation, it often results in large requested mass flow rate values, which are not realistic for practical use on a real aircraft. More advanced closed-loop active flow control techniques are seen as a promising way to reduce the control cost, using a real-time adaptation of flow perturbations. The closed-loop control is generally performed on the mass flow rate for continuous or pulsed blowing and, in the case of separation control by synthetic jets, on the voltage amplitude. The relation between the aerodynamic gain and the mass flow rate or the voltage amplitude is generally monotonic, with some saturation (see for example [29]).

On the contrary, the relation between the aerodynamic gain and the forcing frequency sometimes exhibits an optimum frequency (see [30]), which allows the required energy input in the system to be reduced. The application of active flow control in a practical case requires a self-sustaining, autonomous control system to adapt the forcing frequency to the freestream velocity, for example.

When the actuator-sensor relationship is linear, the actuation and sensor signals can be linked by a transfer function and all of the linear controller theory of the automatics domain can be used, for instance: robust control, predictive control and adaptive control. On the contrary, when the actuator-sensor relationship is characterized by a steady-state map with an extremum, model-independent controllers based on gradient methods can be used. The extremum-seeking algorithm is especially well suited in this case. It is a non-model-based method for the control of non-linear plants, characterized by an output extremum in the steady state (Ariyur & Krstic [2] and Krstic & Wang [21]). This control technique has been used in different studies: Banaszuk et al. [3] and King et al. [20] used it to recover the pressure in a separated diffuser flow. Extremum-seeking and its variant, slope-seeking, were experimentally tested by Becker et al. [5-6] for separation control on a NACA 4412 flap. Pastoor et al. [26] applied it to control the separation behind a D-shaped body and Beaudoin et al. [4] to control the bluff-body drag. In order to improve the seeking algorithm, Henning et al. [18] added some slope estimators.

This short review shows the efficiency of the extremum-seeking strategy to control separation and underlines the fact that this strategy was only applied in experiments. A feature brought by our study is the fact that it is entirely numerical. It adds the challenge that the closed-loop convergence time must be lower than few seconds, in order to be compatible with actual computer capacities. Due to this computational cost, unsteady RANS (URANS) simulations are preferred to large-eddy simulations.

This study is devoted to the closed-loop control of a rounded step separation by synthetic jet, where the only real-time optimized

parameter is the frequency. The pressure of a single wall sensor in the separated zone is the output of the closed-loop. Since the steady-state map in the frequency domain exhibits an optimum frequency, the extremum-seeking algorithm is used with some improvements to increase convergence rate.

First, in order to tune the extremum-seeking parameters and validate the closed-loop strategy before applying it in a URANS computation, a reduced-order model is required to be able to quickly test the effect of all parameters. In order to have a model offering a good compromise between simplicity, cost and accuracy, a Nonlinear Auto-Regressive with eXogenous input (NARX model) has been selected.

This paper is divided into three main parts. In the first part, the NARX model is presented. In the second one, the model is identified and validated. Unsteady Reynolds-Averaged Navier-Stokes (URANS) computations are performed to obtain the unsteady flow response to the synthetic jet actuation. The location of the pressure sensor is justified and the relationship between the pressure information and the separation bubble geometry is evidenced. In a second step, the structure of the NARX model is chosen. A rigorous methodology is then developed to justify the choice of each of these model parameters and both the dynamic and the steady state responses of the model are assessed. The proposed methodology is inspired by the one developed by Box and Jenkins [7] for linear ARMAX models. The choice of the polynomial power, which introduces the nonlinearity, is specific to this study. In the third part, the extremum-seeking algorithm is presented, as well as its improvements: the adaptive gain and the use of Bessel filters. Then, the closed-loop is applied to the NARX model to check the convergence time before being applied in an URANS simulation.

Black-box modeling

Due to the nature of the governing equation, a nonlinear model is studied. Nevertheless, its accuracy will be compared to a linear model for each application, to justify the gain brought by the nonlinear modeling. The idea is not to capture the flow physics, but rather only to represent the pressure output as a function of the forcing signal. This is the reason why a black-box model is used. The NARMAX model [9] is a class of model that links inputs u and outputs y with nonlinear relationships. Its general formulation is written in equation (1), where G denotes a nonlinear function, k is the discrete time, n_u and n_y are the number of past inputs and past outputs, respectively, and ε and ξ stand for possible noise and residual error.

$$y(k) = G(y(k-1),...,y(k-n_y),u(k-1),...,u(k-n_u),\varepsilon(k-1),...,\varepsilon(k-n_y)) + \xi(x_k) \quad (1)$$

The nonlinear function G can be a polynomial, a neural network, a wavelet network, or any other nonlinear function.

In this study a polynomial NARX (a NARMAX with the noise terms excluded, see Section "Model identification and validation" below for the justification) is computed. The advantage of the polynomial NARX model is that the model is linear with respect to the coefficients of the model θ. The specific model structure used is described in equation (2).

$$\begin{aligned} y(k) = \theta_0 &+ \sum_{i=1}^{p}\sum_{j=1}^{n_y} \theta_{y|i,j}\, y(k-j)^i + \sum_{i=1}^{p}\sum_{j=1}^{n_u} \theta_{u|i,j}\, u(k-j-lag_u)^i \\ &+ \sum_{i=1}^{n_y}\sum_{j=1}^{n_y} \theta_{yy|i,j}\, y(k-i)y(k-j) \\ &+ \sum_{i=1}^{n_u}\sum_{j=1}^{n_u} \theta_{uu|i,j}\, u(k-i-lag_u)u(k-j-lag_u) \end{aligned} \quad (2)$$

where the θ_{ij} are the coefficients of the model, p is the polynomial power and lag_u is the delay between the output and the input, to take into account, for example, the convection time of the vortices between the actuator location and the sensor. The cross-terms $u(k\text{-}i)\times y(k\text{-}j)$, as well as the terms of order over 2 on the input u or the output y, are not taken into account in the model, in order to keep a reasonable total number of terms and avoid the problems of overfitting. Moreover, it must be noticed that the constant term θ_0 is particularly important, since it has been observed that it enables the mean output to be different from zero. Therefore, it allows the model to reproduce the static map $<P> = f(F^+)$, where $<P>$ is the time-averaged wall pressure, F^+ is the reduced frequency defined by $F+ = f L_{UC} / U_\infty$ and L_{UC} is the separation length of the uncontrolled case.

The total number of regressors is:

$$n_\theta = 1 + p(n_u + n_y) + n_y(n_y - 1)/2 + n_u(n_u - 1)/2 \quad (3)$$

and corresponds to the number of coefficients θ to be determined (see Section "Model identification and validation").

The identification phase consists in computing the NARX regressors θ. For this purpose, an identification signal u must be defined to explore the system response to an actuation. In this study, a periodic forcing is considered. In order to model the flow response, the identification signal must randomly explore the entire frequency range of interest. Then, the resulting model is not expected to be valid out of this frequency range.

Let Y_M be the URANS identification simulation pressure output vector, Θ be the regressor vector, M be the NARX relation matrix between Y_M and Θ so that $M\Theta = Y_M$, with the property that:

$$Y_M^T = (y(k), y(k-1),..., y(k-n_k)) \quad (4)$$

and

$$\Theta^T = (\theta_0, \theta_1,..., \theta_{n_\theta}) \quad (5)$$

where n_k is the number of samples, which must be larger than the number of regressors n_θ.

Since the number of measurements is larger than the number of regressors, the problem is overdetermined. The standard approach to solve an overdetermined system of linear equations given as $M\Theta = Y_M$ is known as linear least squares and seeks to minimize the residual $\|M\Theta - Y_M\|^2$, where $\|.\|$ is the Euclidean norm.

The matrix M is generally ill-conditioned. The Tikhonov regularization [32] is the most commonly used regularization method for ill-posed problems. In order to give preference to a particular solution

with desirable properties, the regularization term is included in this minimization: $\|M\Theta - Y_M\|^2 + \|\Gamma\Theta\|^2$ for some suitably chosen Tikhonov matrix Γ. In many cases, this matrix is chosen as the identity matrix $\Gamma = I$, giving preference to solutions with the smallest norm. In other cases, high-pass operators (e.g., a difference operator or a weighted Fourier operator) may be used to enforce smoothness, if the underlying vector is believed to be mostly continuous. This regularization improves the conditioning of the problem, thus enabling the existence of a numerical solution. An explicit solution, denoted by $\hat{\Theta}$, is given by:

$$\hat{\Theta} = (M^T M + \Gamma^T \Gamma)^{-1} M^T Y_M \quad (6)$$

The effect of regularization may be varied via the scale of matrix Γ (e.g. $\Gamma = \alpha I$). For $\alpha = 0$, this is reduced to the non-regularized least squares solution, provided that $(M^T M)^{-1}$ exists.

Separation control by a synthetic jet slot over a rounded ramp

Configuration

The geometry of the configuration is displayed in figure 1. The ramp height h is equal to 20 mm and the maximum slope is equal to 35°. The shape of the rounded backward-facing step is given by equation:

$$\frac{y}{h} = \frac{1}{2\pi}\left(\sin\left(\frac{a\pi x}{h}\right) - \frac{a\pi x}{h}\right)$$

where $\frac{x}{h} \in \left[0; \frac{2}{a}\right]$ and $\alpha = 0.703$.

The shape is the same as the one defined in Dandois et al. [11]. The Mach number M_∞ is set equal to 0.31 and the free-stream velocity U_∞ is equal to 104.0 m.s^{-1}.

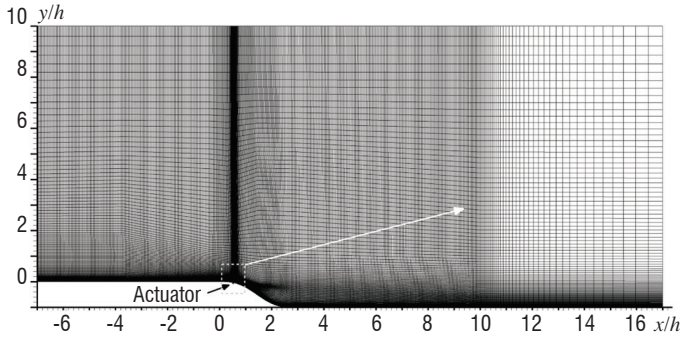

Figure 1- Flow configuration with the synthetic jet cavity and grid

The boundary layer thickness at $x/h = -1$ and its momentum thickness are equal to $0.5h$ and $0.05h$, respectively. The Reynolds number Re_θ based on the momentum thickness is equal to 1,460. The Reynolds number Re_h, based on the ramp height and freestream velocity, is equal to 29,200. The synthetic jet orifice consists in a two-dimensional slot. Its windward edge is located close to the mean separation point of the uncontrolled flow, following the methodology proposed by Neumann and Wengle [23].

The coordinate system is the following: x is oriented in the streamwise direction, y is vertical and z is in the spanwise direction. The origin is located at the beginning of the ramp.

Actuator

The actuator is composed of a slot cavity and described by four parameters: slot width d, slot height H_s, cavity width W_c and cavity height H_c. The actuator dimensions used in these computations are $d = 0.55$ mm, $H_s = d$, $W_c = 2d$ and $Hc = d/2$ (figure 2).

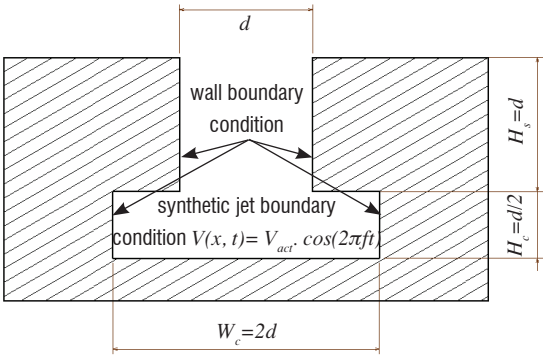

Figure 2 - Actuator geometry

The reduced frequency work range is chosen within the interval $F^+ \in [0.1;10]$. Quantitatively, $F^+ = 1$ corresponds to $f = 911$ Hz.

Actuator dimensions have been calculated with respect to classical synthetic jet designing criteria: the synthetic jet formation criterion and a minimal value of the Stokes number (Holman et al. [19] and Schuster et al. [28]). The resonance frequency definition of Gallas et al. [13,14] has been used to set up cavity design, with a resonance frequency chosen at $F^+_{resonance} \approx 59$, which is far enough from $F^+_{max} = 10$ to avoid resonance effects at high frequency. The synthetic jet forcing amplitude is characterized by its momentum coefficient, which is defined by:

$$C_\mu = \frac{\rho_j d V_{RMS}^2}{\rho_\infty L_{UC} U_\infty^2} \quad (7)$$

where ρ_j is the synthetic jet density, V_{RMS} is the root-mean-square value of the synthetic jet velocity at the orifice exit and ρ_∞ is the freestream density.

Numerical method

The geometry, the grid and the numerical method are the same as those used in [15] to compare the URANS and LES techniques.

The FLU3M code is a finite volume solver for the compressible Navier Stokes equations. The turbulence model used for URANS simulations is the Spalart-Allmaras one [31] with the rotation correction of Daclès-Mariani et al. [10]. The time integration is carried out by means of the second-order-accurate backward scheme of Gear [16]. The time step is equal to 5.10^{-7} s.

The spatial scheme is the one proposed by Mary and Sagaut [22] which is second-order-accurate. The accuracy of the solver has been assessed in various applications at Onera [11, 12, 25, 27, 33].

The streamwise length of the computation domain is $24h$ ($7.5h$ upstream of the separation point and $12h$ downstream from the reattachment point of the uncontrolled case), its height is $10h$ in the inflow plane. The grid is composed of 66,265 cells distributed as 515×127 for the ramp, 10×38 for the slot and 20×24 for the cavity.

Grid spacings in the streamwise and in the wall-normal directions are $\Delta x^+ = 50$ and $\Delta z^+_{min} = 0.5$, respectively. A view of the URANS grid in the x-z plane is displayed in figure 1.

Each controlled case is initialized with the same field. A transient time equivalent to 4.5 flow-through times was necessary to reach the permanent regime. Then, 11 flow-through times were found sufficient to obtain converged statistics.

To simulate the diaphragm displacement, a blowing/suction condition with a top-hat spatial distribution and sinusoidal temporal variation is implemented on the entire cavity bottom surface (figure 2): $V(x,t)=V_{act}.\ cos(2\pi ft)$. Previous studies have shown that the computation of the whole actuator cavity was mandatory for an accurate description of the synthetic jet effect on the separation.

Open-loop results

This section outlines some open-loop results regarding the forcing frequency effect, useful to determine a closed-loop strategy. It has two purposes. The first objective of this open-loop study is to find a criterion to quantify the control effect on the separation. The second one is to justify the use of a local measurement (which will be the model single output) by correlating it with the previous criterion.

Uncontrolled flow

The mean separation bubble contour results from the calculation at each abscissa of the integral of the mass flux in the wall normal direction. The zero-mass-flux line gives the separation bubble contour from which the bubble surface is deduced. This line and streamlines for the uncontrolled flow case are given in figure 3. From the skin friction distribution (not shown), it is found that the separation point is located at $x/h = 0.53$ and the reattachment point at $x/h = 6.26$, so the separation length is $L_{UC}/h = 5.73$.

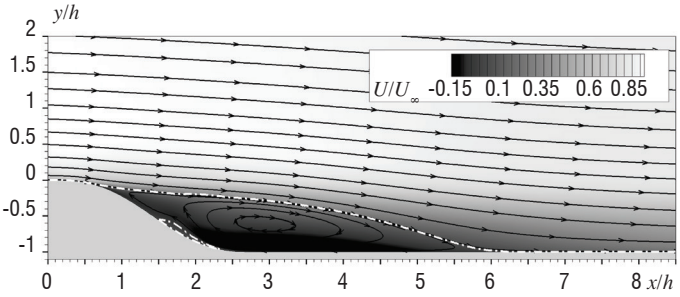

Figure 3 - Uncontrolled flow: streamwise non-dimensional velocity with streamlines and zero mass-flux line (dash-dot line)

Open-loop controlled cases

URANS computation series were performed in order to study the forcing frequency effect with V_{act} = 39.9 m.s^{-1}. This velocity corresponds to a theoretical momentum coefficient $C\mu$ equal to 0.28 %.

As a reminder, the reduced frequency is defined by $F^+ = f.L_{uc}/U_\infty$. The Strouhal number used in this paper is based on the ramp height: $St = f.h/U_\infty$.

The reduced frequency work range is chosen within the interval $F^+ \in [0.1;\ 10]$, in which 23 computations have been carried out. The set of reduced frequency forcing cases is: $F^+ = \{0.1;\ 0.3;\ 0.4;\ 0.5;\ 0.7;\ 0.9;\ 0.95;\ 1.0;\ 1.05;\ 1.055;\ 1.06;\ 1.065;\ 1.07;\ 1.075;\ 1.1;\ 1.2;\ 1.5;\ 2.0;\ 2.5;\ 3.0;\ 4.0;\ 6.0;\ 10.0\}$.

Forcing results on the mean bubble surface reduction

This study is based on URANS computations to make its computational cost acceptable. It is subject to classical RANS limitations; in particular, the results are not free from model sensitivity (see in particular the turbulence model study on this geometry in [15]). Nevertheless, we only need frequency sensitivity results to validate our closed-loop strategy. A previous LES study of synthetic jet frequency and amplitude effects in open-loop brings more physical meaning to the assessment of different control criteria (see Pamart et al. [24]).

For some frequencies, the forcing by the synthetic jet significantly modifies the entire flow. Consequently, some flow parameters are modified, such as pressure and viscous drag, mean separation and reattachment locations, mean recirculation bubble shape, turbulence level, etc. The mean recirculation bubble surface S, non-dimensionalized by the baseline separation bubble surface S_0, is plotted as a function of the forcing frequency in figure 4. The separation surface decreases with the reduced frequency for $0.1 \le F^+ \le 0.7$. The separation bubble surface is a minimum for F^+ around 0.7. For this reduced frequency, the bubble surface is reduced by 70 %. Then, for $0.7 \le F^+ \le 2$, the separation surface increases with the reduced frequency. For, $F^+ \ge 2$, there is no longer any effect of the control on the separation surface, since S/S_0 remains nearly equal to 1.

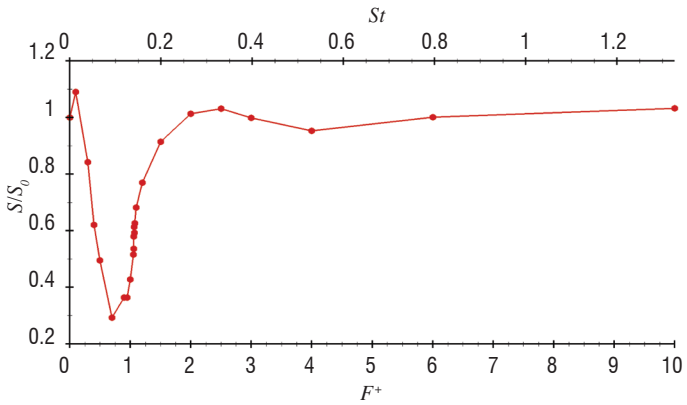

Figure 4 - Forcing frequency effect on the nondimensionalized mean separation bubble surface

Criterion and input choice for the closed-loop

In order to reduce the recirculation bubble surface, the closed-loop algorithm needs a measure of this criterion. The measurement of the bubble surface is not practically feasible, but the idea is to correlate this bubble surface with a wall pressure sensor. By comparing figures 4 and 5, one can observe that, in this case, a decrease of the separation bubble surface is concomitant with an increase of the wall pressure in the separated zone. Thus, the objective of the closed-loop could be to maximize the wall pressure at a given location.

The time-averaged wall pressure from the 23 URANS computations is plotted in figure 5, as a function of the forcing frequency and the x-coordinate. The mean pressure maximum corresponding to the optimal reduced frequency is extracted from this figure and the evolution of this optimal frequency is plotted in figure 6, as function of the x-coordinate. For $2.3 \le x/h \le 3.8$, the maximum mean pressure is obtained for a reduced frequency equal to 0.7, which exactly corresponds

to the reduced frequency for which the recirculation bubble surface is minimum in figure 4.

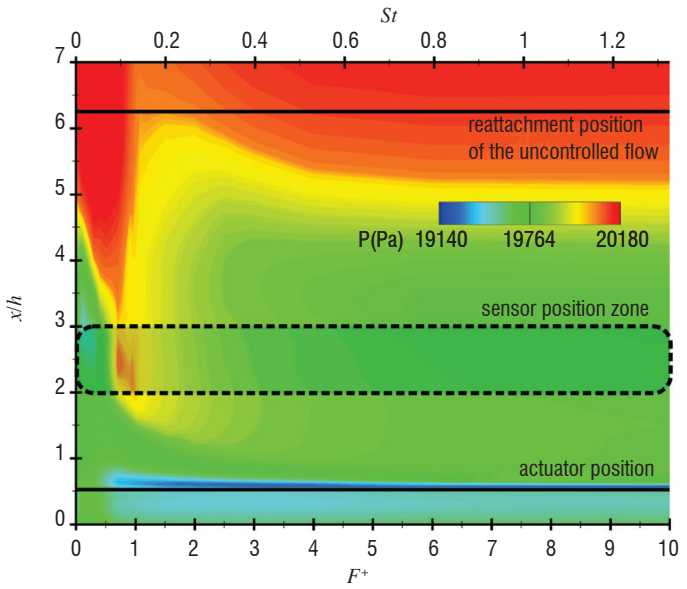

Figure 5 - Mean wall pressure as function of forcing frequency and x-coordinate

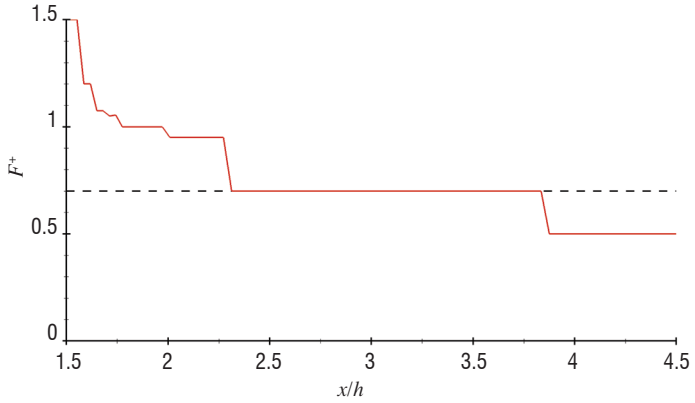

Figure 6 - Sensor position effect on the reduced frequency corresponding to the mean pressure maximum

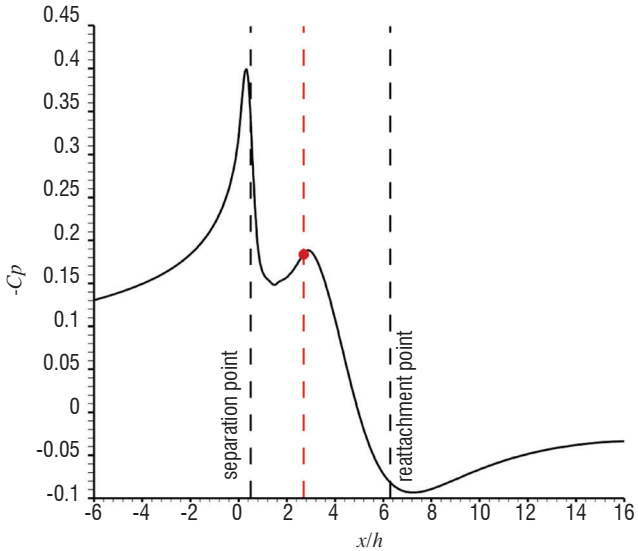

Figure 7 - Wall pressure distribution of the baseline (uncontrolled), showing the pressure sensor location (red dot)

Finally, the wall pressure sensor is chosen at $x/h = 2.71$, near the middle of the separated zone (figure 7). For example, the control objective could be to maximize the pressure at this location. A closed-loop algorithm, such as the extremum-seeking algorithm, is especially well suited for this purpose.

In the following, the objective will be to identify a model that links the actuator output velocity with the wall pressure sensor at $x/h = 2.71$.

Model identification

Identification signal

Due to the computational cost of URANS simulations, we cannot afford to collect a time signal of several seconds with a time step of 5.10^{-7} s. However, it is useful to consider that for $F^+ \geq 3$, the forcing effect on the flow is negligible (see figure 4 again). A NARX black-box model is then identified on a reduced frequency range $F^+ \in [0.1; 3]$, which is divided in 30 steps. Moreover, a good representation of the process steady-state map is made accessible if the signal is compounded of some command plateaus, which allow the flow to converge towards a steady state. With these two ingredients, the signal shape consists in a series of sinusoids of equal length. Each frequency is different and randomly distributed over the frequency range.

The duration of every command step is set equal to 29.4 ms (roughly twice the transient time), which results in a total signal duration of 0.9 s. In order to smooth the discontinuities generated by the steps, the signal is filtered by a first order transfer function, with a time constant equal to 0.35 ms. The reduced frequencies F^+ used for the identification are given in figure 8. The sinusoidal signal with the frequencies of figure 8 is then imposed as a boundary condition on the cavity bottom wall. The momentum coefficient C_μ is constant and equal to 0.28 %. The signal sampling is chosen such that the highest frequency is discretized by at least 12 samples. Consequently, the time step used for the NARX model is $2.5\ 10^{-5}$ s.

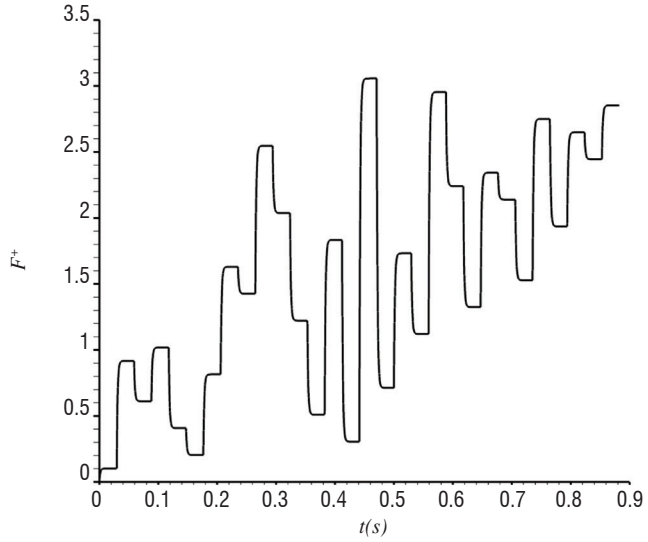

Figure 8 - Input sequence of reduced frequency for the NARX identification

Model identification and validation

A URANS simulation enables us to obtain the response of the considered pressure sensor to the identification signal. The model time

step being already fixed, the NARX parameters to set are the number of past elements for each NARX term (n_y, n_u), the polynomial power p and the lag lag_u. The lag lag_u and the number of past inputs n_u are found using the intercorrelation between the forcing u and the pressure y (figure 9). It can be seen that the intercorrelation is maximum for $lag = 46$. In this figure, the lag values for which the intercorrelation is higher than a predefined user threshold (±0.02) are picked up (red part of the curve with dots), since it means that these output terms are correlated with the input. lag_u is the first abscissa for which the intercorrelation is larger than the threshold ($lag_u = 2$). n_u is the difference between the abscissa above which the intercorrelation falls definitely below the threshold level (here $lag = 113$) and lag_u. Thus, in order to take into account the most correlated terms in the model, lag_u is chosen equal to 2 and $n_u = 111$.

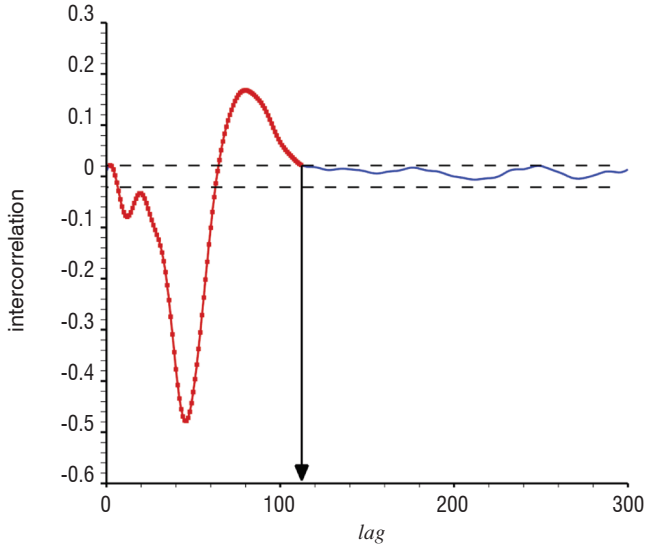

Figure 9 - Intercorrelation between the pressure y and the forcing u, for different lag values of u

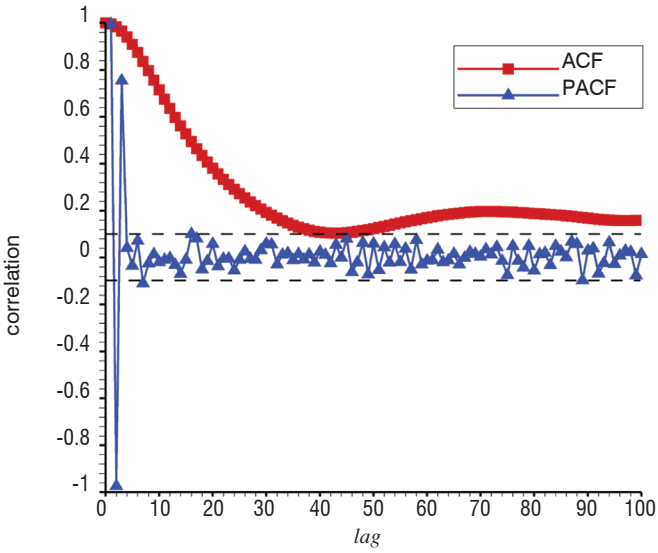

Figure 10 - Autocorrelation function (in red, square symbols) and partial autocorrelation function (in blue, triangle symbols) of the output y

Concerning the value of n_y, the partial autocorrelation function on the output y is computed (figure 10) as recommended by Box & Jenkins [7], to find the order m of an Auto-Regressive Model $AR(m)$. The partial autocorrelation of an $AR(m)$ process becomes zero at lag $m + 1$ and greater, so the partial autocorrelation function is examined to see if there is evidence of a departure from zero. This is usually determined by placing a 95 % confidence interval on the sample partial autocorrelation plot (black dashed line). Figure 10 shows that the autocorrelation function (ACF) decreases gradually, whereas the partial autocorrelation function (PACF) is close to zero for $n_y > 3$, which means that an $AR(2)$ model should be used. Consequently, n_y is chosen equal to 3.

The autocorrelation function of a $MA(q)$ process becomes zero at lag $q + 1$ and greater. Since the ACF tails off gradually and does not cut off after n_y lags, a Moving Average $MA(q)$ model should not be considered here (see Box & Jenkins [7]); thus, a NARX structure (without noise ε) is chosen, which justifies the fact that the noise terms were excluded in equation (2).

A parametric study of the effect of the model power p is then performed for a fixed value of the Tikhonov regularization coefficient $\alpha = 2$. This value of the regularization coefficient is chosen following the $L\text{-}curve$ rule (see figure 11 and Hansen [17]): the optimum value of α is obtained when the $L\text{-}curve$ is the closest to the axis origin.

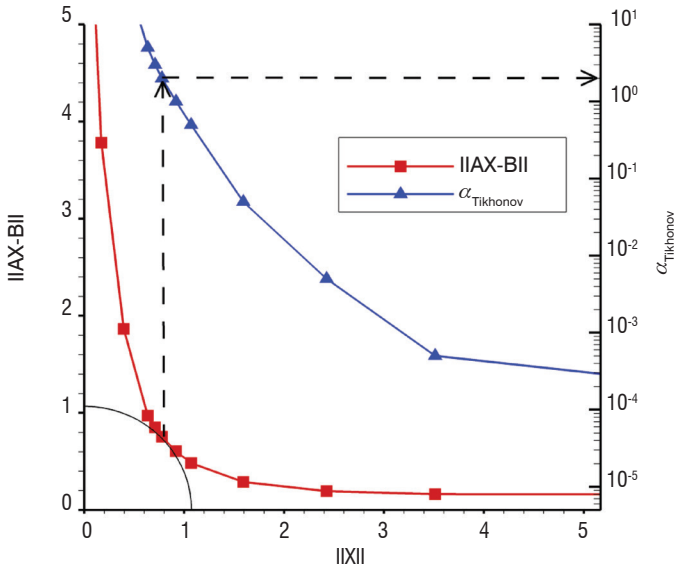

Figure 11 - $L\text{-}curve$ of the chosen NARX model

The range of the p parameter studied is $p \in [3; 7]$ (figure 12). The model power p is chosen to minimize the Akaike Information Criterion (AIC) (see [1]) and its modified definition ($AICc$), which increases the weight of the number of regressors n_θ when it becomes large which is the case here. They are defined by:

$$AIC = -2\ln(L) + 2n_\theta$$
$$AICc = AIC + \frac{2n_\theta(n_\theta + 1)}{n - n_\theta - 1} \quad (8)$$

where L is the likelihood function of the model, n_θ is the total number of regressors and n is the number of samples. If the error between the model output y_m and the learning data y is assumed to be zero-mean Gaussian (it has been checked that it is true here), the previous expression of the AIC criterion becomes (see [8]):

$$AIC = n\ln(RSS / n) + 2n_\theta \quad (9)$$

where RSS is the residual sum of squares:

$$RSS = \sum_{i=1}^{n_k} (y_m(i) - y(i))^2$$

This criterion is the sum of two terms: the first one depends on the error between the model and the true measurement and the second one includes a penalty, which increases with the number of regressors in the model. This prevents overfitting. The objective is to minimize one of these two criteria.

Figure 12 shows that the AIC of the model is minimized for $p = 6$ and that the $AICc$ is minimized for p $= 5$. Since AICc has a larger penalty on the number of regressors, we choose $p = 5$.

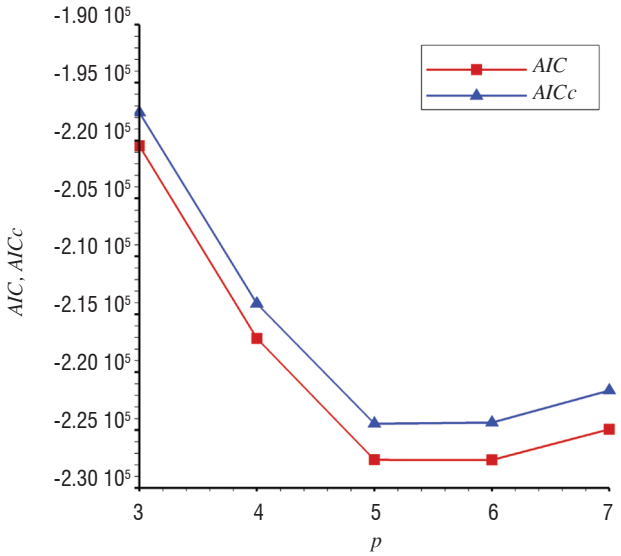

Figure 12 - AIC & $AICc$ criteria as a function of the NARX model power p.

To assess the performance of the NARX model, a fit coefficient (which must be maximized) is defined by equation (10). In this coefficient, the mean squared prediction error (MSPE) between the identification signal y and the NARX model y_m is computed

$$fit = 100 \times \left(1 - \sqrt{\frac{\sum_{i=1}^{n_k} (y_m(i) - y(i))^2}{\sum_{i=1}^{n_k} (y(i) - \bar{y}(i))^2}} \right) \quad (10)$$

where $\bar{y}$ is the mean value of y.

It must be noted that nothing prevents this fit coefficient from being negative.

For the previous set of NARX parameters ($lag_u = 2, n_y = 3, n_u = 111$ and $p = 5$), a very good fit equal to 84 % is obtained. In comparison, a fit of only 42.7 % is obtained with a linear ARX model with $lag_u = 18, n_y = 3, n_u = 111, p = 1$ and no cross terms giving a total of 115 regressors.

The representations of the response signal computed by the URANS simulation and the signal given by the NARX model for the same identification input command are given in figure 13. This figure shows the ability of the model to represent the temporal pressure evolution of the flow perturbed by the series of forcing frequencies shown in figure 8.

In addition, the black-box model is validated by comparing the model output with CFD results for different forcing frequencies. For each frequency, the measured pressure signal from the URANS simulations is compared with the output of the NARX model for the same input command. Some comparisons are displayed in figure 14. Figure 15 shows the relative error between the model and the CFD results:

$$error(\%)(i) = 100 \times \frac{y_m(i) - y(i)}{y(i)}$$

On the frequency interval covered by the identification command $F^+ \in [0.1; 3]$, the NARX model is in good agreement with the flow computed by URANS simulations. The fit coefficient varies between 48.6 % for the lowest frequency and 93.9 % for the highest. The error between the NARX model and the URANS decreases when the reduced frequency increases and is always lower than 2 % for $F^+ > 0.1$. Outside of this frequency interval (figure 16), the NARX model quickly diverges.

Another important point is to validate the steady state behavior of the NARX model, that is to say, to check whether the mean pressure given by the model is the same as that computed by time-averaging the URANS simulation. The evolution of the time-averaged pressure <P> with respect to the forcing frequency is given in figure 16. On the reduced forcing frequency interval $F^+ \in [0.1; 3]$, mean pressures are in good agreement. Nevertheless, for $F^+ > 3$, the NARX steady pressure estimations quickly diverge from those of the URANS simulation.

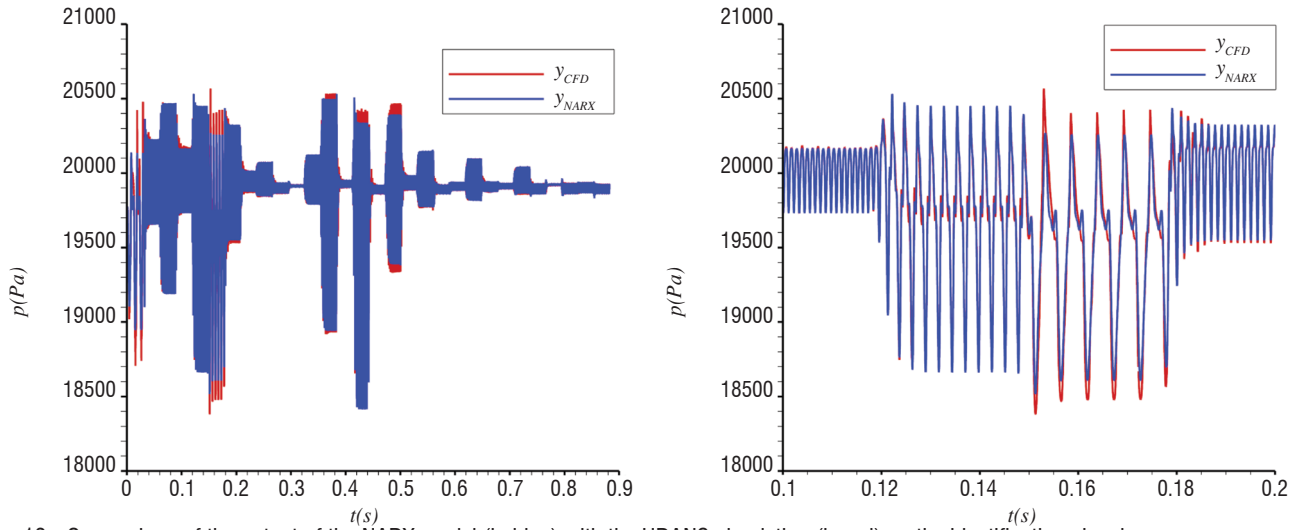

Figure 13 - Comparison of the output of the NARX model (in blue) with the URANS simulation (in red) on the identification signal (left: complete signal, right: zoom for 0.1<t<0.2)

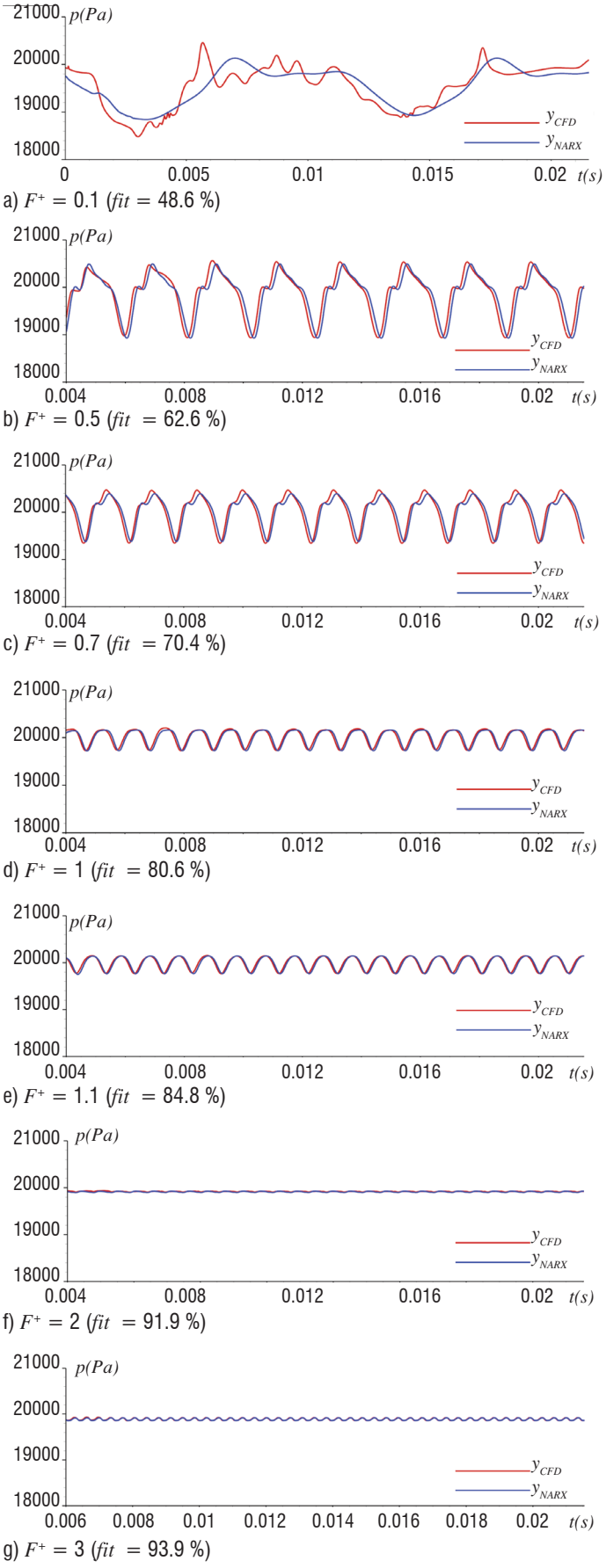

a) $F^+ = 0.1$ ($fit = 48.6$ %)

b) $F^+ = 0.5$ ($fit = 62.6$ %)

c) $F^+ = 0.7$ ($fit = 70.4$ %)

d) $F^+ = 1$ ($fit = 80.6$ %)

e) $F^+ = 1.1$ ($fit = 84.8$ %)

f) $F^+ = 2$ ($fit = 91.9$ %)

g) $F^+ = 3$ ($fit = 93.9$ %)

Figure 14 - NARX model validation with open-loop results for different reduced frequencies

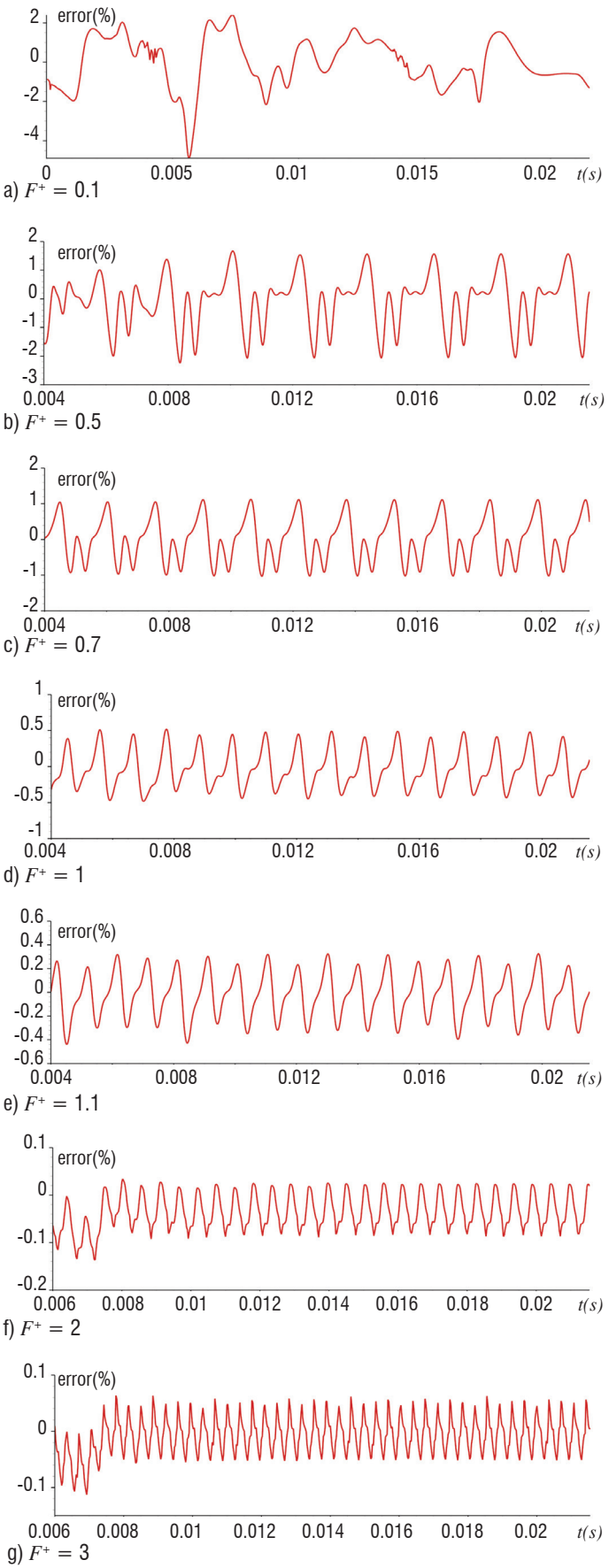

a) $F^+ = 0.1$

b) $F^+ = 0.5$

c) $F^+ = 0.7$

d) $F^+ = 1$

e) $F^+ = 1.1$

f) $F^+ = 2$

g) $F^+ = 3$

Figure 15 - Relative error between the NARX model and CFD results for different reduced frequencies

As expected, the model can be used for representing the steady pressure frequency response, but only on the frequency bandwidth of the identification signal.

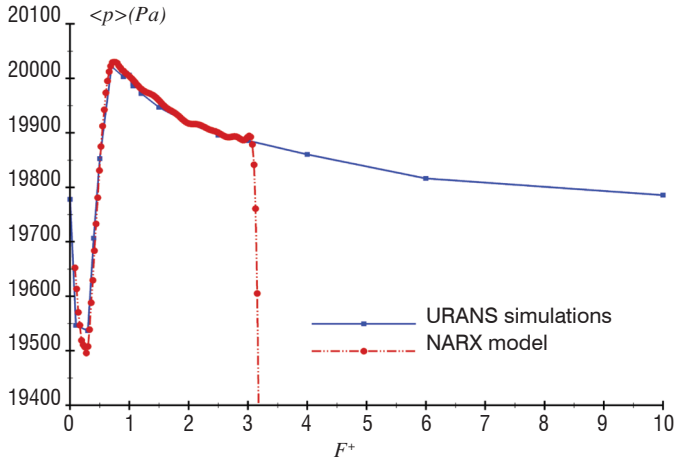

Figure 16 - Comparison of the evolutions of the time-averaged pressure with respect to the forcing frequency between the NARX model (in blue) and the CFD (in red).

Finally, this NARX model is able to accurately represent the steady component as well as the unsteady component of the pressure for $F^+ \in [0.1; 3]$ at the sensor location. The black-box model has its steady maximum at the same frequency as that given by URANS simulations. The NARX reduced-order model can then be used to design a closed-loop algorithm.

Closed-loop control by extremum seeking

Description of the extremum seeking algorithm

The extremum-seeking algorithm is a robust adaptive closed-loop algorithm without an internal model. It is appropriate for the control of nonlinear plants characterized by an output extremum in the steady state. Let a block with a command input u and an output y be a representation of the nonlinear system, with the static input-output-map $y=G(u)$. A typical SISO extremum-seeking structure is given in figure 17.

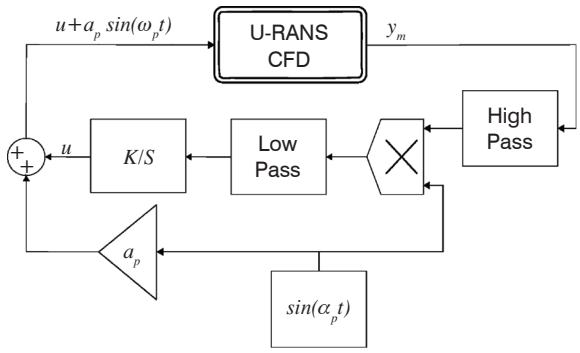

Figure 17 - Block diagram of the basic extremum-seeking feedback algorithm

The extremum-seeking control is based on a gradient online optimization. The aim is to adjust the control input u, in such a way that the maximal steady-state system output y^* is achieved without knowing the steady-state input-output map $y=G(u)$ and especially its extremum $y^* = max(G(u)) = G(u^*)$. The idea is to add a periodic perturbation to the command input u, in order to compute the static input-output slope and then modify the command u toward the optimal command u^*.

The perturbation addition is displayed in figure 18, as Step I. Typically, this perturbation is a sine signal $\alpha_p.sin(\omega_p.t)$ where α_p and ω_p denote the perturbation amplitude and pulsation, respectively. The perturbation period must be larger than the largest time constant of the dynamic plant, in order to obtain an approximate sinusoidal output y. If the static input-output slope is positive, then the sinusoidal output and the perturbation are in phase and vice versa (figure 18 Step II). The slope sign is obtained by filtering the system output with a high-pass filter (figure 17: High Pass box) and by demodulating this filtered signal with the perturbation (box with a cross in figure 17). The high-pass filter (Step III in figure 18) removes the mean value and keeps the unsteady component. The demodulation consists in doing the product of the latter with the perturbation signal. Indeed, the product of two signals in phase gives a signal with a positive mean and vice versa (Step IV in figure 18). This demodulation leads to a non-zero mean signal, as long as the maximum is not obtained. This output is passed through a low-pass filter (Low Pass box in figure 17), which gives a moving average value of the slope. The slope sign signal is multiplied by a gain K and integrated (K/s box in figure 17). As a result, the command u is shifted toward the optimal command u^*, which is displayed in figure 18 as Step V. For more details on the algorithm and in particular a demonstration of the algorithm stability, the reader should consult Ariyur and Krstić [2] and Krstić and Wang [21].

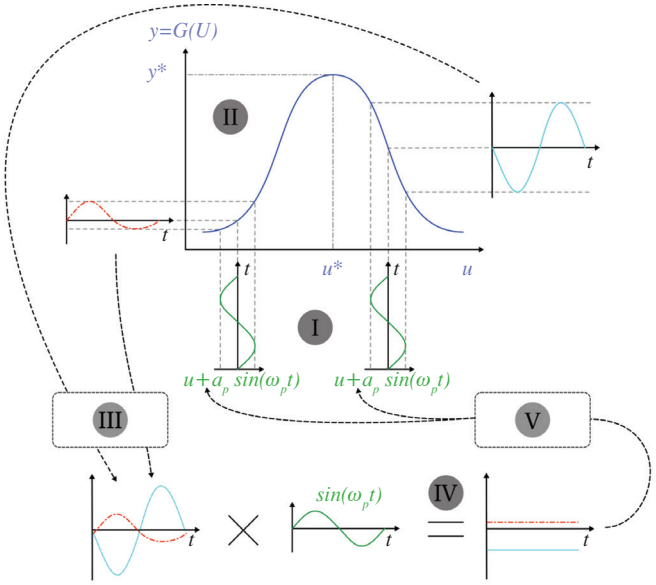

Figure 18 - Extremum-seeking algorithm in 5 steps

Since the extremum-seeking algorithm is based on the slope value estimation using a demodulation step, it is important to use high-pass and low-pass filters with ideal specifications. That is to say, a filter with the shortest possible time response and with a linear phase-shift. The last specification allows a minimum phase distortion, so that different frequencies in the band-pass have the same time delay and the shape of a signal remains unmodified by the filter.

This is the reason why the basic extremum-seeking feedback was improved by using Bessel filters. Bessel filters, also known as Thompson filters, are characterized by an almost constant group

delay across the entire pass-band, thus preserving the wave shape of filtered signals in the pass-band. The "Bessel" approximation aims to develop a normalized low-pass filter, with a maximal constant group delay at the origin. A Bessel low-pass filter is characterized by its transfer function:

$$H(s) = \frac{\theta_n(0)}{\theta_n(s/\omega_0)}$$

where $\theta_n(s)$ are reverse Bessel polynomials and ω_0 is a frequency chosen to give the desired cut-off frequency. The filter has a low-frequency group delay equal to $1/\omega_0$.

The reverse Bessel polynomials are given by:

$$\theta_n(s) = \sum_{k=0}^{n} a_{n|k} s^k \quad \text{with} \quad a_{n|k} = \frac{(2n-k)!}{2^{n-k}\, k!(n-k)!}$$

Extremum seeking tuning

First, the NARX previously identified in the first part of the paper in the case of flow separation over a ramp is used, with the aim of tuning the parameters of the extremum-seeking algorithm (pulsation ω_p and amplitude α_p of the perturbation, filter cut-off frequencies, loop gain K, etc.) and validating the closed-loop strategy. This NARX black-box model imitates the flow response to a periodic blowing and suction signal. Since the command input given by the extremum-seeking regulator is a frequency, an actuator signal converter is attached to the NARX model for converting the input command to an oscillatory signal. In order to ensure the signal continuity and to introduce actuator dynamics, a first-order transfer function is added to the system model. Its time constant τ allows the time response of the actuator, which is set equal to 0.35 ms here, to be managed.

To tune the extremum-seeking parameters, the U-RANS CFD box in figure 17 is replaced by the NARX model. Thus, the U-RANS CFD box in figure 17 is replaced by the blocks given in figure 19. The moving averaged pressure at the exit of the system block diagram is obtained by filtering the NARX model output with a low-pass filter. A correct mean pressure estimation requires a NARX pressure output averaged over at least two actuation periods. The lower bound of reduced forcing frequency interval is $F^+ = 0.1$, then the mean pressure estimator low-pass filter cut-off frequency ω_m is set equal to $F^+ = 0.05$. A representation of the entire system block diagram is given in figure 19.

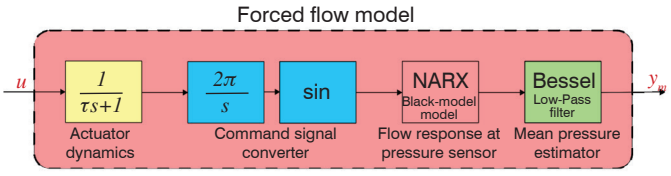

Figure 19 - System block diagram

Concerning the extremum-seeking algorithm itself, there are three pulsations to be chosen: the perturbation pulsation ω_p and the low-pass and high-pass filter ones, ω_{LPes} and ω_{HPes} respectively. The largest time constant of the system is given by the mean pressure estimator low-pass filter cut-off frequency ω_m. Then, it allows the sine perturbation pulsation ω_p to be adjusted. A pulsation ω_p equal to a quarter of ω_m is chosen. The extremum-seeking high-pass filter must remove frequencies larger than ω_p and the direct component. Bessel filters allow a constant group delay, but with a soft magnitude filtering, to be ensured. As a result, ω_{HPes} is set equal to ω_p. The extremum-seeking low-pass filter must be able to give a moving-average of the slope sign to the integrator. As a mean pressure estimator, the cut-off frequency is adjusted, so that the slope sign signal is averaged over two perturbation periods. Therefore, ω_{LPes} is chosen to be equal to $F^+ = 0.00625$.

Concerning the closed-loop gain K in figure 17, it is in principle a constant; however, here we propose an adaptive gain to increase the convergence rate of the closed-loop. When the steady state map slope is small (at the beginning of the closed-loop), K will be high to increase the convergence rate and, when the slope is large, K will be small to prevent the closed-loop from overshooting and oscillating around the extremum. The expression below has been chosen for the adaptive gain:

$$K(t) = \min\left(K_{\max}, \sigma \frac{2a_p\omega_p}{\pi y_{slope}(t)}\right)$$

where K_{max} is a user defined gain and σ is a safety margin with $0 \le \sigma \le 1$.

Validation of the extremum seeking parameter choice on the black-box model

Before applying this closed-loop algorithm in an unsteady RANS simulation, it is necessary to validate it on the NARX reduced-order model. The controller is tested in various cases listed in Table 1, where u_0 is an initial forcing frequency. The constant σ is set to be equal to 0.9. Simulations with the NARX model are plotted in figure 20, in which the closed-loop is initiated at $t = 0.1$ s.

Case	K_{max}	$\alpha_p(F^+)$	$f_p(F^+)$	$u_0(F^+)$
I	1000	0.01	0.0125	0.22
II	1000	0.03	0.0125	0.2
III	1500	0.02	0.0125	1.1

Table 1 - Closed-loop strategy validation cases

For each case, the command converges as expected toward F^+ equal to 0.78. The convergence time depends on the starting frequency point, the maximal gain chosen and the perturbation amplitude value. The representation of the mean pressure at the output of the model is given in figure 21. The extremum-seeking allows the mean pressure maximum that validates the closed-loop strategy to be found.

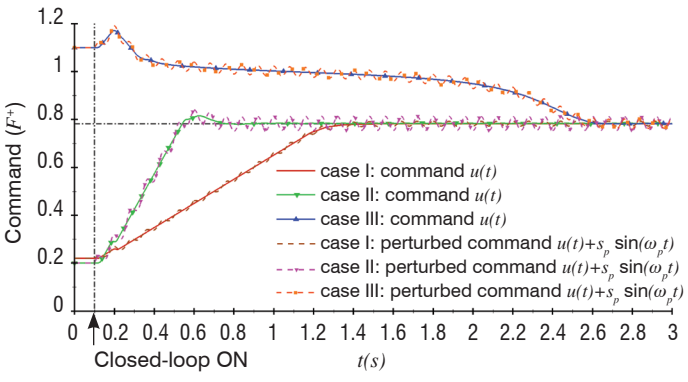

Figure 20 - Extremum-seeking with adaptive gain control of the NARX model

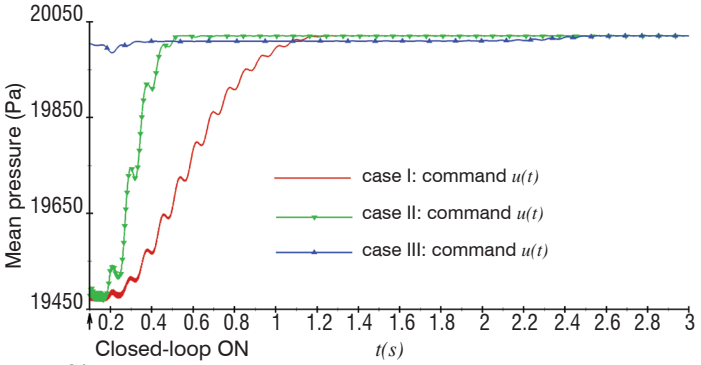

Figure 21 - Mean pressure given by the flow model for validation closed-loop

The closed-loop shows its ability to find in-line the maximum of a nonlinear model. The convergence time is small enough to allow the application of this closed-loop strategy in-line with an unsteady RANS simulation.

Application of the extremum seeking to an URANS computation

After having successfully applied and validated the extremum-seeking controller, the NARX model is replaced by unsteady RANS computations. The controller is tested in the different cases listed in Table 2. The command and mean pressure results are plotted in figure 22 and figure 23, respectively.

Case	K_{max}	$\alpha_p(F^+)$	$f_p(F^+)$	$u_0(F^+)$
I	1000	0.022	0.0125	0.11
II	1000	0.01	0.0125	0.22
III	900	0.03	0.0125	0.2

Table 2 - Closed-loop in unsteady RANS computation cases

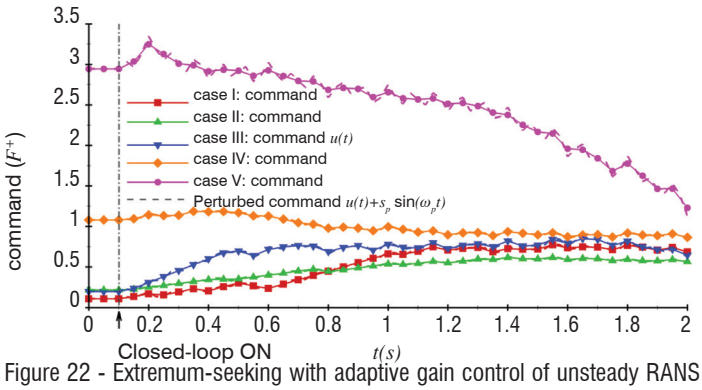

Figure 22 - Extremum-seeking with adaptive gain control of unsteady RANS computations

The convergence time is longer than with the black box model, due to the fact that the model does not perfectly reproduce the true CFD results. Thanks to the robustness of extremum-seeking, the closed-loop is still efficient and the pressure is well maximized. For Cases II, IV and V, simulation must be continued, in order to ensure the frequency command convergence. Cases I and II have converging commands, as expected in the vicinity of F^+ equal to 0.78.

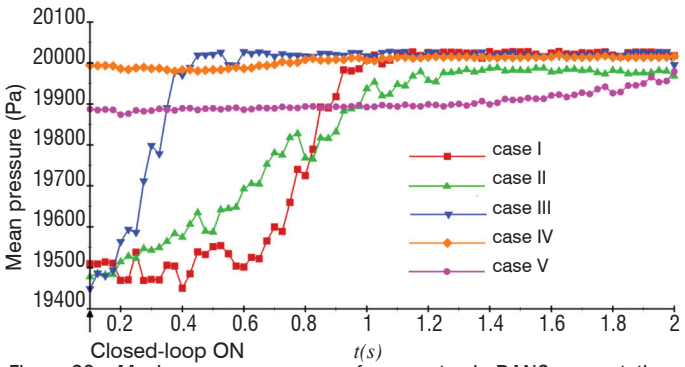

Figure 23 - Moving average pressure from unsteady RANS computations in closed-loop

Conclusion

This paper describes a successful approach of closed-loop separation control by synthetic jet on a generic rounded step configuration.

An open-loop study of the forcing frequency has allowed the verification of the system controllability. The chosen objective criterion to be optimized is the mean recirculation bubble surface. The mean wall pressure analysis has shown that maximizing the wall pressure sensor at x/h equal to 2.71 enables the recirculation bubble surface to be minimized.

Maximizing the mean pressure automatically at the sensor location implies the use of a closed-loop algorithm. In a first step, a single-input single-output black-box model was identified, in order to tune and validate the closed-loop strategy. A NARX model of the real time wall pressure signal response to the synthetic jet forcing was successfully designed and validated.

The selected control algorithm was the extremum-seeking, which is a robust adaptive command without internal model. It is appropriate for the control of non-linear plants, characterized by an output extremum in the steady state. The algorithm was improved with an adaptive gain, which guarantees optimal performance in terms of gradient estimation and, with the use of low-pass and high-pass Bessel filters, allows an accurate gradient estimation to be ensured.

The tuning of the control algorithm parameters was based on physical considerations and was validated using the black-box model. The results showed that it was possible to apply this closed-loop strategy in-line with an unsteady RANS simulation.

This control goal was to minimize the recirculation bubble surface. It is also possible, with the same methodology, to control some other criteria, such as the pressure drag or the turbulence level.

Extremum-seeking works with the steady state of the plant, which imposes an estimation of the moving-average state of the output. A simpler black-box model based on the steady state could have been used, but the system dynamics would have been lost.

A next step could be the automatic simultaneous adaptation of frequency and amplitude, using a multi-input multi-output regulator ■

Acknowledgements

The authors would like to acknowledge the DGA (the French Ministry of Defense) for the financial support granted for the PhD thesis of the second author.

References

[1] H. AKAIKE - *A New Look at the Statistical Model Identification*. IEEE Transactions on Automatic Control. 19(6):716–723 (1974).
[2] K.B. ARIYUR, M. KRSTIĆ - *Real-Time Optimization by Extremum-Seeking Control.* John Wiley & Sons (2003).
[3] A. BANASZUK, S. NARAYANAN, Y. ZHANG -*Adaptive Control of Flow Separation in a Planar Diffuser.* AIAA 41st Aerospace Sciences meeting and Exhibit, AIAA Paper 2003-0617 (2003).
[4] J.F. BEAUDOIN, O. CADOT, J.L. AIDER, J.E. WESFREID - *Bluff-Body Drag Reduction by Extremum-Seeking Control.* J. Fluid and Structure 22(7-8):973-978 (2006).
[5] R. BECKER, R. KING, R. PETZ, W. NITSCHE - *Adaptive Closed-Loop Separation Control on a High-Lift Configuration using Extremum Seeking*. AIAA 3rd Flow Control Conference, AIAA Paper 2006-3493 (2006).
[6] R. BECKER, R. KING, R. PETZ, W. NITSCHE - *Adaptive Closed-Loop Separation Control on a High-Lift Configuration Using Extremum Seeking*. AIAA Journal 45(6):1382-1392 (2007).
[7] G.E.P. BOX, G.M. JENKINS - *Time Series Analysis: Forecasting and Control.* Holden Day, San Francisco (1976).
[8] K.P. BURNHAM, D.R. ANDERSON - *Model Selection and Multimodel Inference: a Practical Information-Theoretic Approach*. 2nd ed. Springer-Verlag (2002).
[9] S. CHEN, S. BILLINGS - *Representation of Non-Linear Systems: the NARMAX Model.* International Journal of Control 49(3):1013-1029 (1989).
[10] J. DACLÈS-MARIANI, G.C. ZILLIAC, J.S. CHOW, P. BRADSHAW - *Numerical/Experimental Study of a Wingtip Vortex in the Near Field*. AIAA J. 33(9):1561-1568 (1995).
[11] J. DANDOIS, E. GARNIER, P. SAGAUT P - *Numerical Simulation of Active Separation Control by Synthetic Jet*. J Fluid Mech. 574:25-58 (2007).
[12] S. DECK - *Delayed Detached Eddy Simulation of Self-Sustained Unsteadiness and Side-Loads in an Overexpanded Nozzle Flow*. Shock Waves 19:239–249 (2009).
[13] Q. GALLAS, R. HOLMAN, T. NISHIDA, B. CARROLL, M. SHEPLAK, L. CATTAFESTA - *Lumped Element Modeling of Piezoelectric-Driven Synthetic Jet Actuators.* AIAA J 41(2):240-247 (2003).
[14] Q. GALLAS, G. WANG, M. PAPILA, M. SHELPLAK, L. CATTAFESTA - *Optimization of Synthetic Jet Actuators*. AIAA 41st Aerospace Sciences meeting and Exhibit, AIAA Paper 2003-0635 (2003).
[15] E. GARNIER, P.Y. PAMART, J. DANDOIS, P. SAGAUT - *Evaluation of the Unsteady RANS Capabilities for Separated Flows Control*. Computers & Fluids, 61:39-45 (2012).
[16] C.W. GEAR - *Algorithm 407-DIFSUB for the Solution of Ordinary Differential equations*. Commun. ACM, 14(3):185-190 (1971).
[17] P.C. HANSEN, D.P. O'LEARY - *The Use of the L-curve in the Regularisation of Discrete ill-Posed Problems*. SIAM J. Sci. Comput. 14(6):1487-1503 (1993).
[18] L. HENNING, R. BECKER, G. FEUERBACH, R. MIMINOVIC, R. KING, A. BRUNN, W. NITSCHE - *Extensions of Adaptive Slope-Seeking for Active Flow.* Proceedings of the Institution of Mechanical Engineers, Part I: Journal of Systems and control Engineering, 222:309-322 (2008).
[19] R. HOLMAN, Y. UTTURKAR, R. MITTAL, B.L. SMITH, L. CATTAFESTA - *Formation Oriterion for Synthetic Jets*. AIAA J 43(10):2110-2116 (2005).
[20] R. KING, R. BECKER, M. GARWON, L. HENNING - *Robust and Adaptive Closed-Loop Control of Separated Shear Flows*. AIAA 2nd Flow Control Conference, AIAA Paper 2004-2519 (2004).
[21] M. KRSTIĆ, H.H. WANG - *Stability of Extemum Seeking Feedback for General Nonlinear Dynamic Systems*. Automatica, 36:595-601 (2000).
[22] I. MARY, P. SAGAUT - *Large Eddy Simulation of a Flow Around an Airfoil Near Stall*. AIAA J 40(6):1139-1145 (2002).
[23] J. NEUMANN, H. WENGLE - *Coherent Structures in Controlled Separated Flow over Sharp-Edged and Rounded Steps*. J Turb 5:1-24 (2004).
[24] P.Y. PAMART, J. DANDOIS, E. GARNIER, P. SAGAUT - *Large Eddy Simulation study of Synthetic Jet Frequency and Amplitude Effects on a Rounded Step Separated Flow.* 5th AIAA Flow Control Conference, AIAA Paper 2010-5086 (2010).
[25] M. PAMIÈS, E. GARNIER, A. MERLEN, P. SAGAUT - *Response of a Spatially Developing Turbulent Boundary Layer to Active Control Strategies in the Framework of Opposition Control.* Phys. Fluids 19:108102 (2007).
[26] M. PASTOOR, L. HENNING, B.R. NOACK, R. KING, G. TADMOR - *Feedback Shear Layer Control for Bluff Body Drag Reduction*. J. Fluid Mech. 608:161-96 (2008).
[27] J. RIOU, E. GARNIER, C. BASDEVANT - *Compressibility Effects on the Vortical Flows Over a 65 deg Sweep Wing*. Phys. Fluids 22:035102 (2010).
28. J.M. SCHUSTER, D.R. SMITH - *A Study of the Formation and Scaling of a Synthetic Jet.* 42nd AIAA Aerospace Sciences Meeting and Exhibit. AIAA Paper 2004-90 (2004).
[29] A. SEIFERT, L.G. PACK - *Oscillatory Excitation of Unsteady Compressible Flows over Airfoils at Flight Reynolds Number*, AIAA Paper 99-0925 (1999).
[30] A. SEIFERT, T.BACHAR, D. KOSS, M. SHEPSHELOVICH, I. WYGNANSKI - *Oscillatory Blowing: a Tool to Delay Boundary-Layer Separation*. AIAA J. 31(11):2052-2060 (1993).
[31] P.R. SPALART, S.R. ALLMARAS - *A One Equation Turbulence Model for Aerodynamics Flows.* 30th AIAA Aerospace Sciences meeting and Exhibit, AIAA Paper 1992-0439 (1992).
[32] A.N. TIKHONOV, V.A. ARSENIN - *Solution of ill-Posed Problems*. Winston & Sons, Washington (1977).
[33] S. TRAPIER, S. DECK, P. DUVEAU - *Delayed Detached Eddy Simulation and Analysis of Supersonic Inlet Buzz*. AIAA J. 46(1):118–131 (2008).

Acronyms

SISO	(Single-Input Single-Output)
NARX	(Nonlinear Auto-Regressive with eXogenous input)
NARMAX	(Nonlinear Auto-Regressive Moving Average with eXogenous input)
RANS	(Reynolds Averaged Navier-Stokes)
LES	(Large-Eddy Simulation)
AR	(Auto-Regressive model)
MA	(Moving Average model)
ACF	(Auto-Correlation Function)
PACF	(Partial Auto-Correlation Function)
AIC	(Akaike Infomation Criterion)
RSS	(Residual Sum of Squares)
CFD	(Computational Fluid Dynamics)

AUTHORS

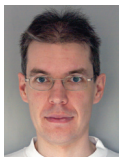

Julien Dandois graduated from the Ecole Nationale Supérieure d'Arts et Métiers (ENSAM) in 2003 and received a PhD in Fluid Mechanics from Paris 6 University in 2007. Since that time, he has worked in the Civil Aircraft Unit of the Applied Aerodynamics Department, in the fields of high-lift, separation control, buffet control, closed-loop control and aeroacoustics.

Pierre-Yves Pamart graduated from ISAE-ENSMA in 2007. He received a PhD in Fluid Mechanics from Paris 6 University in 2011. The subject of his thesis was the closed-loop control of a separation. Then, he became a research engineer in aerothermal methods and HVAC in the building field at CSTB. In 2012, he joined SAFRAN-Snecma, in the aerothermal and multi-physics methods department.

Closed-Loop Control of Fluid Flow: a Review of Linear Approaches and Tools for the Stabilization of Transitional Flows

D. Sipp
(Onera)
P. Schmid
(LadHyX Ecole Polytechnique)

E-mail: denis.sipp@onera.fr

Flow control is concerned with the targeted manipulation of intrinsic flow behavior to optimally satisfy prescribed objectives. This article will give an overview of the most common tools for the design of control strategies. We focus on linear control that is aimed at stabilizing fixed points of the Navier-Stokes equations, such as those existing in the case of transitional flows. Key steps to build a Galerkin-based and a data-based model will be presented and illustrated on two generic flow configurations: flow over an open cavity and over a backward-facing step. In the former case, a feedback configuration will result and particular attention will be paid to performance measures and robustness analyses. For the latter case, a feedforward setup has been chosen and a system-identification method will be employed to extract the fluid behavior from data sequences, via statistical learning techniques.

Introduction

The control of fluid flow is a central component of fluid mechanics, since it holds great promise in manipulating the inherent flow behavior of a fluid system. The suppression of instabilities, the exploration of previously inaccessible parameter ranges, efforts to increase stability margins and diminish sensitivity to external noise and attempts to improve efficiency and minimize environmental impact (less pollution, less unburnt gases, less NOx emission, less sound radiation, better and more homogeneous mixing) are just a few technological areas where active flow control could make an appreciable difference. Much effort has thus been concentrated on applying control-theoretic methods to fluid systems and on establishing a theoretical framework and foundation for the design of effective flow control strategies.

The design of flow control strategies relies on a model for the fluid system, but also on a model for the noise environment. For flows that are weakly sensitive to external noise - referred to as oscillator flows - it is difficult to design effective control strategies due to the inherent nonlinearities that drive the system; flow over a cavity at supercritical Reynolds numbers is a typical example of such a flow type. For flows that respond sensitively to environmental noise - known as amplifier flows - an additional difficulty lies in the design of an adequate model of the noise environment; a two-dimensional flow over a backward-facing step would fall into this category.

Past work in flow control has heavily relied on models using a projection of the Navier- Stokes equations onto a reduced basis, for example a POD basis. Both linear (see [1, 2, 3, 4, 5, 6]) and non-linear state-space models (see [7, 8]) can be designed. These models then form the foundation on which controllers can be built. Various control design approaches, from the simple PI (proportional integral) controller [9] to the more complex H_2 or H∞-control (see, for example, [10], [11], [12]) can be followed, each of which can be characterized by a Cavity flows as a source of unsteady loads and noise given performance - to what extent has the control objective been reached? - and a given robustness - how does the performance change as the reduced-order models are slightly perturbed?

A different approach to the design of control strategies consists in using data-based models, which are built from observing and evaluating sequences of system input and output signals. A discrete transfer function is extracted from a learning data-set, via system identification techniques [13]. This transfer function then forms the foundation for an optimal control design. First, attempts to design control schemes following this approach have been undertaken [14, 15], which showed that the underlying model - in particular the incorporation of unobservable noise sources - is of critical importance. The designed compensator showed a great amount of robustness to off-design noise environments and even to non-linear effects [15].

In this article, we will present and discuss the critical steps in the design of flow control schemes for both types of flow behavior (oscillators and amplifiers) and compare and contrast models derived from Galerkin projections and data-based models. We stress that this review focuses on the linear stabilization of equilibrium points existing in transitional flows. For more general approaches of closed-loop control - which aim, for example, at manipulating turbulent flows - the reader is referred to [16], [17], [18], [19], [20].

Description of a flow control problem

The motion of the fluid is assumed to be governed by an evolution equation of the general form

$$\dot{x} = f(x,u,w) \tag{1}$$

where x is the state vector containing all of the variables necessary to uniquely describe the state of the fluid system (such as velocities, pressure, density, temperature, mixture fractions, etc.), u is the control vector which contains input variables that are used to influence the flow, and w is the (stochastic) noise vector summarizing the influences of external noise sources or inaccuracies (freestream disturbances, acoustic noise sources, wall roughness distributions, etc.). The time rate of change $\dot{x}$ is related to these vectors by a (generally non-linear) function f. In this article, we assume that an equilibrium point x_0 of these equations exists, such that.

$$f(x_0, u=0, w=0) = 0 \tag{2}$$

The existence of such equilibrium points is assured in the case of transitional flows, as considered in this paper. In light of this, the control is thus aimed at maintaining the system as close as possible to these fixed points, where closeness is measured by a performance sensor $z = c_z\ (x\text{-}x_0)$. If the function c_z represents the deviation of the full state from the equilibrium solution, the perturbation kinetic energy can be targeted as a control objective and transition delay issues may be considered. However, c_z may also represent a local measure of the flow, for example the signal from a wall-shear stress sensor. The controller will minimize the following cost-functional

$$J = J(\mathrm{z},\mathrm{u}) \tag{3}$$

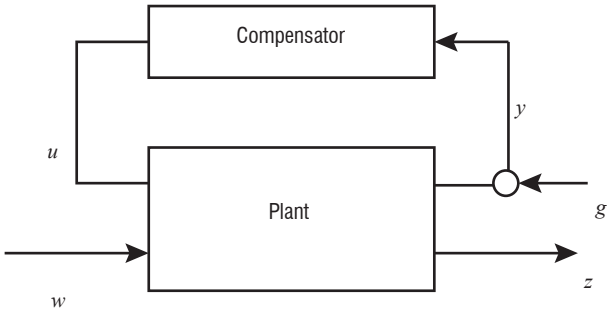

Figure 1 - Block diagram of a typical feedback control setup, including plant, compensator, external noise sources *(w, g)* and objective output z

which expresses the amount of gain from applying control strategies to the fluid system. It also contains the control vector u since, in most cases, we try to avoid excessive control input and thus wish to penalize the expended control energy. For example,

$J(z,u) = \int_0^\infty \left\| c_z\,(x\text{-}x_0) \right\|^2 + l^2 \left\| u \right\|_u^{\ 2}\, dt$ where $\|\cdot\|$ and $\|\cdot\|$

are suitable norms and l^2 is a user-specified parameter related to the cost of control. In a closed-loop set-up, the control input u depends via the controller on some measure y of the flow (the estimation measure) given by

$$y = c_y(x,g) \tag{4}$$

where y corresponds to a measurement vector, describing the information that we extract from the state vector x (for example, by shear sensors placed on the wall, by hot-wire probes placed in the wake of an obstacle, by microphones placed in the acoustic far-field, or by TR-PIV measurements in a two-dimensional slice). This measure is commonly different from the performance measure z. Realistically, the estimation measurements must be assumed to be contaminated by measurement noise g. The function c_y is thus a function that extracts exploitable (and measurable) information from the entire flow field.

The objective of our control problem is thus to find a mapping $y \rightarrow u$ (the compensator) that minimizes the cost functional (3) while observing the constraints given by the governing equation (1). Mathematically, we must solve a constrained optimization problem. The complete flow control setup is graphically illustrated in the form of a block diagram in figure 1. The flow system (labeled “plant”) is influenced by external noise w and driven by the control signal u from the compensator unit. The measurement signal y, contaminated by sensor noise g, is the output from the plant and is, in turn, used in the compensator unit to ultimately determine the optimal control signal u. The goal of the compensator is to force the plant in such a way that the performance measurement (z) is minimal, while at the same time excessive control input (u) is avoided.

For effective flow control, the placement of actuators and sensors plays a vital role, and two generic configurations can be distinguished, based on the inherent behavior of the fluid flow. The first category is referred to as oscillator flows, while the second category is known as amplifier flows.

Oscillator flows: the case of an open cavity

In the case of oscillator flows, the flow generally undergoes a supercritical Hopf bifurcation at a critical Reynolds number, becomes globally unstable and establishes limit-cycle behavior. The shedding of vortical structures in the wake of a cylinder above a critical Reynolds number of $R_{ec} = 47$ is a quintessential and much-studied example of an oscillator flow. This type of flow is characterized by a relative insensitivity to external perturbations and the dominant frequency of the flow is little influenced by noise sources. The control objective in this case can be two-fold. We can maintain the flow in the vicinity of the unstable equilibrium points using linear control theory. Alternatively, and more challenging, we can force the fluid system away from its natural limit-cycle behavior towards the equilibrium state; this effort requires a non-linear underlying model and a non-linear approach to flow control, especially if the Reynolds number is chosen well above its critical value. The scope of this article allows us to only concentrate on the first choice: a linear control effort near the critical Reynolds number. As a representative oscillator flow, we choose the flow over an open cavity at $R_e = 7500$ (see figure 2 (a) for a sketch of the geometry), with one actuator placed upstream of the cavity and one sensor located downstream of the cavity edge. In this setup, the upstream control u influences the downstream estimation sensor y, yielding a feedback configuration.

Amplifier flows: the case of a backward-facing step

Amplifier flows are globally stable flows that are characterized by a strong response to external forces. Their flow behavior is typically influenced and driven by upstream (unknown) noise sources and the

observed flow structures are the result of a frequency-selective amplification/damping of this noise environment. Even though globally stable, the flow is convectively unstable, and perturbations are amplified locally and convected downstream by the base flow. For sufficiently weak noise sources, the dynamics of amplifier flows can be suitably described by a linear model. In such a configuration, we can estimate the state downstream of the estimation sensor and manipulate the flow downstream of the actuator. A sensor-actuator setup (with a sensor upstream of the actuator) is thus appropriate for amplifier flows, whereas an actuator-sensor setup (with an actuator upstream of the sensor) is more suited for oscillator flows. A prototypical example of an amplifier flow is the flow over a backward-facing step at $R_e = 500$. Figure 2(b) illustrates the geometry of the flow and the appropriate control setup. The controller will be designed to cancel the perturbation field estimated by the sensor measurements. Due to the convective nature of the flow, the actuator signal u has no impact on the measurement y. This layout is known as a feedforward configuration.

Linear control

Even though techniques exist for designing effective control strategies for the above system of non-linear equations, it is often convenient and sufficient to apply control to a linear system describing the evolution of small perturbations around the equilibrium point x_0. In this case, the above equations simplify to

$$\dot{\hat{x}} = \bar{A}\hat{x} + \bar{B}_u u + L(y - \hat{y}) \quad (5)$$

$$y = C_y x + g \quad (6)$$

$$z = C_z x \quad (7)$$

Here $A = \partial f / \partial x \,|\, x_0$ and analogously for the other matrices $B_{u,w}$ and $C_{y,z}$. In what follows, we will work with the linearized set of equations (4)-(6).

A control strategy that minimizes our cost objective J (involving the quantity z) simply consists in finding a linear mapping between the measurement y and the control signal u. The design of this strategy depends on a representation of the governing equations (5)-(7) but cannot rely on explicit knowledge of the state vector x. The controller must operate in real-time mode and thus a reduced-order model (ROM) of the governing equations (5)-(7) with significantly lower degrees of freedom $\bar{x}$ is needed that still reproduces the input-output relation of the full system with sufficient fidelity. More precisely, for

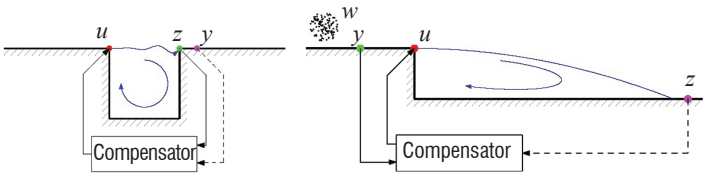

a) feedback configuration b) feedforward configuration

Figure 2 - Sketch of flow over an open cavity and a backward-facing step - two generic flow configurations representing an oscillator and noise-amplifier flow, respectively. The actuator (u), flow sensor (y) and performance sensor (z) are marked by colored symbols for each configuration. External upstream noise sources are indicated by w in the case of an amplifier flow. The cavity and backward-facing step configurations are defined in more detail in Barbagallo et al. [5] and Hervé et al. [15]

an effective controller design it is mandatory for the reduced-order model to recover the dynamic links between all inputs (w and u) and all outputs (y and z). When building this model, the state vector x can be thought of as an internal (hidden) variable describing the full state of the fluid system; typically, we do not have access to the state vector x.

Two approaches for the construction of a reduced-order representation emerge. First, a Galerkin-based approach can be taken that uses appropriately chosen flow structures to reduce the governing equations, via a Galerkin projection, followed by the design of an estimator that computes an approximate (reduced) state $\hat{x}$ by optimally processing any mismatch in the measurement vectors from the reduced-order system ($\bar{y}$) and a duplicate system ($\hat{y}$). Alternatively, we can eliminate the state vector $\bar{x}$ and postulate a direct relation between (u,w) and (y, z). The coefficients of this relation can be determined by observing and processing temporal sequences of control and measurement signals. The first approach yields the classical Kalman filter and LQG-compensator, while the second approach utilizes solely input-output information and produces disturbance-rejection control strategies. Both approaches - their underlying assumptions, strengths and shortcomings - will be discussed in more detail below.

Approach I : state-space model, observer and feedback control

The governing equations (5)-(7) constitute a mapping from a low-dimensional signal u via a high-dimensional state $\bar{x}$ to low-dimensional signals y and z. In the first approach, we follow a similar mapping and try to find a reduced-order model of the form

$$\dot{\bar{x}} = \bar{A}\bar{x} + \bar{B}_u u + \bar{B}_w w \quad (8)$$

$$y = \bar{C}_y \bar{x} + g \quad (9)$$

$$z = \bar{C}_z \bar{x} \quad (10)$$

The new state vector $\bar{x}$ represents a vector of coefficients in a linear combination of flow structure, i.e., $x = V\bar{x}$. The flow structures form the columns of the rectangular matrix V and are typically chosen from proper orthogonal decomposition (POD) modes or balanced POD (bPOD) modes. By selecting only a small number of modes, we arrive at the reduced-order system (8)-(10).

As mentioned previously, the reduced-order model must accurately match the unreduced dynamics from all input to all output variables. A quality measure for this match is based on transfer functions. The transfer functions can be derived by applying a Laplace transform to (8)-(10), which yields an algebraic expression between input and output variables. For example, the transfer function from u to y reads $\bar{T}_{yu}(s) = \bar{C}_y (s\bar{I} - \bar{A})^{-1} \bar{B}_u$, with s as the Laplace variable. Evaluating the transfer function $\bar{T}_{yu}(s)$ along the imaginary s-axis describes the frequency response of the input-output system. For control design purposes, a close match (in a norm to be specified) between the transfer function of the reduced system $\bar{T}_{yu}(s)$ and the transfer function of the original system $T_{yu}(s) = C_y (sI - A)^{-1} B_u$ is required. This quality measure, $\left\| T_{yu}(s) - \bar{T}_{yu}(s) \right\|$, can be applied to stable and unstable configurations; in the case of unstable systems, it requires that the unstable eigenvalues of the reduced and unreduced systems coincide and that a close match for the stable subspace-dynamics be attained. The quality of the match between the two transfer functions is influenced by the number and type of flow structures used in the reduction basis V.

In figure 3 (a), we have represented with a black dashed line the magnitude of the full-plant transfer function . This result can be obtained by directly evaluating the quantity $C_y(sI - A)^{-1}B_u$ for various frequencies $s = i\omega$, where A is the large-scale Jacobian matrix and appropriate numerical methods are required to perform the inversion. The peaks in the transfer function are linked to a series of global modes displaying Kelvin-Helmholtz type instabilities on the shear-layer : the first peak corresponds to a stable response, while the four subsequent peaks are linked to an unstable response.

How to build a reduced state-space model

Two approaches can be distinguished. The first approach is based on the reduction of the original system via a Petrov-Galerkin projection, as mentioned earlier. A bi-orthogonal basis for the state vector x consists of two rectangular matrices V, W satisfying $W^H V = \bar{I}$, with $\bar{I}$ as the identity matrix and ^{H} denoting the conjugate transpose. Expressing the state vector in this basis yields a reduced-order model for the coefficient vector $\bar{x} = W^H x$. The governing equations (5)-(7) can then be replaced by the reduced system (8)-(10) with $\bar{A} = W^H A V$. The expressions for the remaining matrices in (8)-(10) follow analogously. The critical question remains on how to choose the basis vectors in V to arrive at a meaningful reduced-order system that serves as a proper substitute for the original system, for the subsequent compensator design. A common approach of computing the bases V and W proceeds as follows: once a base-flow is computed, the direct and adjoint unstable global modes are extracted; this is followed by computing impulse responses for the various inputs (using the direct Navier-Stokes operator) and outputs (using the adjoint Navier-Stokes operator), each projected onto the stable subspaces. Processing of the snapshots with the balanced POD (bPOD) technique [2] straightforwardly yields the various matrices for the reduced-order system [5]. Alternatively, balanced modes can also be computed in the frequency domain [21], which directly produces the stable and unstable dynamics (without) having to compute the unstable global modes beforehand). The reduced state $\bar{x}$ then consists of the amplitudes of the unstable global modes and the amplitudes of the balanced modes.

In a second model-reduction approach, the same model can be obtained using system identification methods. Given the structure of the model, its unknown coefficients are identified from time-series of the input and output signals. Theoretically, this yields the same model as determined by the first (Petrov-Galerkin) approach. If the model is stable, the eigenvalue realization algorithm (ERA) technique directly yields the reduced system [22] without the need for a Jacobian matrix A and adjoint simulations; if the system is unstable, prior knowledge of a controller that maintains the dynamics of the system in the vicinity of the equilibrium point is required [23]. Then, the ERA technique is applied to identify the closed-loop dynamics, from which the open-loop dynamics can be deduced in a straightforward manner.

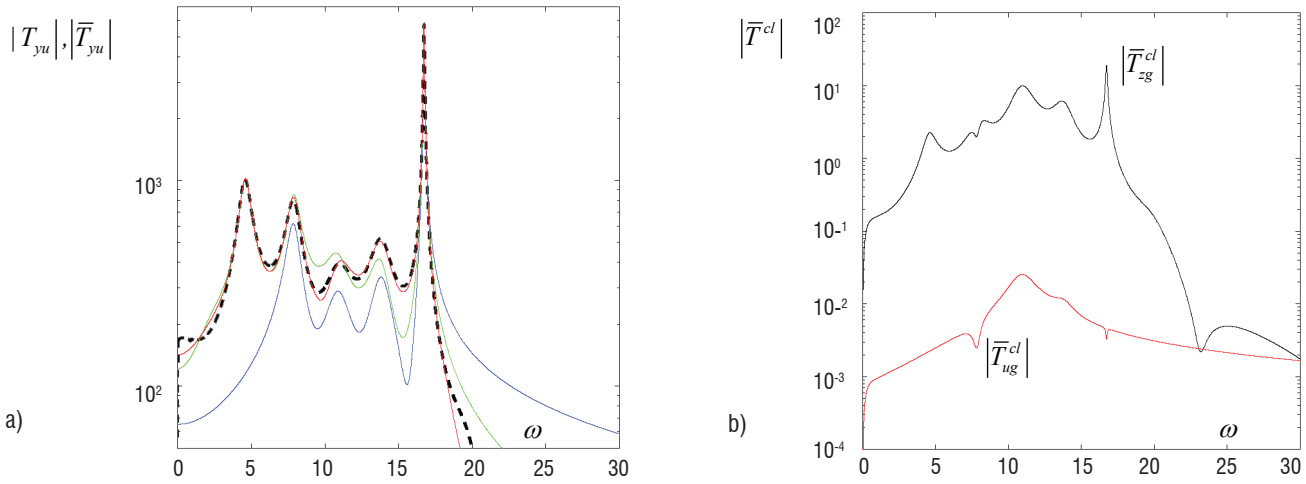

Figure 3 - a) Open-loop transfer function $|T_{yu}(\omega)|$ of the full plant (black dashed line) and of reduced- order models based on the four unstable global modes and no (blue), four (green) and eight (red) balanced POD modes to represent the stable subspace. b) Closed-loop transfer functions from the measurement noise g to the sensor output z (black) and from the measurement noise g to the control input u (red).

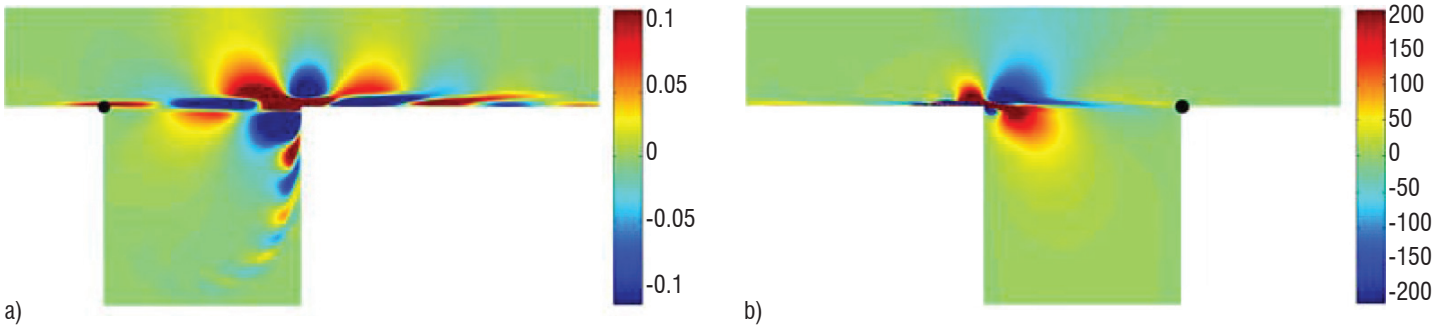

Figure 4 - Dominant balanced modes computed by the bPOD method for flow over an open cavity (visualized by streamwise velocity contours). a) The dominant direct mode, determined from the impulse responses of the actuator location (black symbol); b) the adjoint mode, determined from the adjoint impulse response of the sensor location (black symbol).

In figure 4 (a, b), we show the dominant direct and adjoint bPOD modes. These structures are respectively located near the downstream and upstream edges of the cavity, a consequence of the non-normality of the linearized Navier-Stokes operator. In figure 3 a, the magnitude of the transfer functions of models comprising the four unstable global modes plus zero (blue line), four (green line) and eight (red line) bPOD modes are displayed. A large error is observed if only the unstable global modes are considered in the model. This justifies the fact that additional modes must be considered in the model, to take into account features of the stable subspace. If more than eight bPOD modes are used, the reduced transfer function coincides with the full-plant transfer function.

Design of a compensator

In general, the reduced-order state $\bar{x}$ is not accessible to the controller; for this reason, an approximation to $\bar{x}$ must be determined directly from the available measurements y. The estimated state vector will be denoted by $\hat{x}$, which is governed by a Kalman filter written as

$$\dot{\hat{x}} = \bar{A}\hat{x}+\bar{B}_u u+L\left(y-\hat{y}\right) \tag{11}$$

$$\hat{y} = \bar{C}_y\hat{x} \tag{12}$$

This system of equations for the estimated state $\hat{x}$ resembles (7)-(8), except for the absence of noise terms and for the additional term $L\left(y-\hat{y}\right)$. This latter term represents a driving term based on the discrepancy between the true measurement y and the measurement from the proxy system (10)-(11). The manner in which this discrepancy is processed is given by the quantity L, which is determined by posing an optimization problem : we wish to minimize the covariance of the estimation error $\bar{x}-\hat{x}$, while observing the governing equations (10)- (11). Covariances appear due to the fact that y and thus $\hat{x}$ are stochastic variables and the statistical moments of $\hat{x}$ are the appropriate quantities to focus on. The optimization problem can be formulated variationally, yielding the following algebraic matrix Riccati equation for an auxiliary variable P, according to

$$\bar{A}P + P\bar{A}^H - P\bar{C}_y^H G^{-1}\bar{C}_y P + \bar{B}_w W\bar{B}_w^H = 0 \tag{13}$$

from which the Kalman gain L follows as

$$L = P\bar{C}_y^H G^{-1} \tag{14}$$

Note that equation (12) yields the steady-state Riccati-solution, which results when the objective functional to be minimized is given by the infinite-time integral of the covariance of the estimation error. In equation (12) information about the two noise sources (system noise w and measurement noise g) enters via their respective covariances $W = E(ww^H)$ and $G = E(gg^H)$, with $E(\bullet)$ denoting the expected value. The statement that the Kalman gain L, and consequently the quality of the estimated state $\hat{x}$, crucially depends on the fidelity of the noise covariances seems self-evident. In the limit of large ratios, $G/W \gg 1$, we have either highly contaminated measurement sensors or very weak external noise levels. In this limit, we can be particularly confident in our model which is reflected in very low Kalman gains L. For small ratios, $G/W \ll 1$, we deal with very accurate measurement

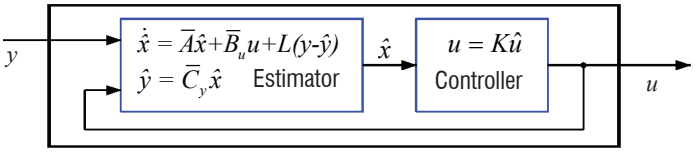

Figure 5 - Block diagram of a compensator consisting of an estimator and a controller module

sensors or a strong response of our system to external noise. In this case, frequent sensing is necessary to accurately estimate the state of the system and high Kalman gains L are common. In a final design step, the controller will be based on the state vector, given by a proportional law according to $u = K\bar{x}$. In this manner, it represents a mapping from the state vector $\bar{x}$ to the low-dimensional control signal u. The control gain K is again obtained from an optimization problem : we wish to minimize our cost objective, while observing the governing equations. When considering a cost objective involving an infinite-time integral, the solution of this optimization problem, as before, leads to the following algebraic matrix Riccati equation for an auxiliary variable Q, according to

$$\bar{A}^H Q + Q\bar{A} - Q\bar{B}_u R^{-1}\bar{B}_u^H Q + \bar{C}_z^H\bar{C}_z = 0 \tag{15}$$

from which the control gain K follows as

$$K = -R^{-1}\bar{B}_u^H Q \tag{16}$$

where R is a weight matrix appearing in the chosen quadratic form of the cost functional $J = \int_0^\infty \bar{x}^H\bar{C}_z^H\bar{C}_z\bar{x} + u^H R u\, dt$; it accounts for the cost associated with the expended control. If the cost of control is high and any control effort is heavily penalized ($R \gg 1$), the associated control gains K are very low and the control signal u is expended rather parsimoniously. In the Riccati equation (14) for the control problem, we notice the absence of noise-related terms. It thus appears that the controller is not concerned with noise sources; they are strictly dealt with by the estimator. Any performance degradation due to noise (or any failure to model noise sources accurately) must be ascribed to the estimator, not the controller. In the above analysis, we assumed a proportional control involving the true state vector $\bar{x}$; of course, under realistic conditions, this must be substituted by the estimated state $\hat{}$. The resulting control law thus reads $u = K\hat{x}$. The separation principle assures that the control gain K is still optimal, after this substitution has been made. The combination of estimator and controller, referred to as the compensator, is sketched as a block diagram in figure 5 : it processes the measurement vector y and produces the optimal control signal u. The noise sources enter into the Kalman gain L, the cost objective is accounted for in the control gain K and the estimated (reduced) state vector $\hat{x}$ appears as an internal (hidden) variable.

The full closed-loop control problem, including true and estimated states, is finally written (in matrix form) as:

$$\begin{pmatrix}\dot{\bar{x}}\\ \dot{\hat{x}}\end{pmatrix} = \underbrace{\begin{pmatrix}\bar{A} & \bar{B}_u K\\ L\bar{C}_y & \bar{A}-L\bar{C}_y+\bar{B}_u K\end{pmatrix}}_{\bar{A}^{cl}}\begin{pmatrix}\bar{x}\\ \hat{x}\end{pmatrix} + \begin{pmatrix}\bar{B}_w w\\ Lg\end{pmatrix} \tag{17}$$

The composite block-matrix $\overline{A}^{cl}$, describing the dynamics of the controlled and estimated system, is stable by design. The performance of the compensated system (16) can be measured by the norm of the transfer functions from the noise sources (w, g) to the performance measurement signal z.

Returning to the configuration of the open cavity flow, if the noise sources are negligibly small, only very few measurements y are required to fully capture the system dynamics. In this case, the Kalman gain L can be determined in the small-gain limit. If furthermore the cost of control is considerable, the control gain K can also be computed in the small-gain limit. The performance of the resulting controller is then given by the magnitude of the transfer function of the compensated $\overline{T}_{zg}^{cl}$ system, from the measurement noise g to the performance measure z (see the black line in figure 3 b). The magnitude of the resulting control signal is obtained by inspection of the transfer function $\overline{T}_{ug}^{cl}$ of the compensated system, from the measurement noise g to the control input u (see the red line in figure 3 b).

Robustness

It is important to realize that the design of the compensator, i.e., the estimator and the controller, is based on the reduced-order model (see figure 6 a). Ultimately, however, the compensator is applied to the full system on which it must prove its effectiveness (see figure 6 b). Owing to residual degrees of freedom that have not been included in the reduced-order model, it is conceivable that problems may arise when applying a compensator to a system that it was not exactly designed for. The issue of robustness thus naturally arises in this case.

If the compensator is applied to the full system, the closed-loop transfer function from the sensor noise g to the performance measure z is written as $T_{zg}^{cl} = T_{zu}K_{uy}\left/\left(1-T_{yu}K_{uy}\right.\right)$, where T_{zu} and T_{yu} are the full-plant transfer functions (see figure 3 a) and K_{uy} is the transfer function of the compensator, which is given by $K_{uy}(s) = K\left(sI - \overline{A} - \overline{B}_u K + L\overline{C}_y\right)^{-1} L$. By inspection of the transfer function T_{zg}^{cl}, the stability margins can be obtained by scrutinizing the appearance of unstable zeros in the denominator of $\mathrm{T}_{\mathrm{zg}}^{\mathrm{cl}}$, i.e, $1 \quad \mathrm{T}_{yu}(\mathrm{s})\mathrm{K}_{uy}(\ )$. If the full-plant transfer function coincides with the reduced transfer function T_{yu}, then by the design of K_{uy}, all zeros of $1-\overline{T}_{yu}(s)K_{uy}(s)$ are stable (these zeros correspond to the eigenvalues of $\overline{A}^{cl}$). However, since $\overline{T}_{yu}$ was based on an approximation procedure, deviations from the transfer function of the original system, T_{yu}, arise. This slight mismatch may cause instabilities in the feedback loop, in other words, unstable zeros of $1-T_{yu}(s)K_{uy}(s)$. A robustness analysis encompasses a modification of the reduced-plant transfer function $\overline{\ }_{yu}$, followed by an analysis of its influence on the stability of the compensated system. More specifically, we consider modified transfer functions $T_{yu} = g\overline{T}_{yu}$, with g as a complex constant and track the appearance of unstable zeros of $1-\overline{T}_{yu}(s)K_{uy}(s)$ as a function of g. In particular, we seek critical gain margins $g = a \in \mathbb{R}^+$ and phase margins $g = e^{i\varphi}$ that render the closed-loop system unstable. Physically, the gain margin a refers to an error in the estimation of the amplification rate of an instability in the system, while the phase margin φ describes an error in the estimation of the convection speed of the perturbations.

It is noteworthy that this issue is only relevant when $T_{yu} \neq 0$, that is, in the case of a feedback configuration where the control u affects the estimation measurement y. This is the case for oscillator flows, where a global structure is destabilized and, in turn, synchronizes the entire dynamics. In the case of convective (amplifier) flows, however, with the measurement y located upstream of the actuator u, the issue of robustness is inconsequential.

For orientation we first display the eigenvalues of the original reduced-order plant, i.e., the eigenvalues of $\overline{A}$, in figure 7a by blue symbols; only positive frequencies $\lambda_i > 0$ are shown. Four eigenvalues can be identified in the unstable (gray) half-plane. Applying the compensator, the originally unstable flow will be stabilized, which manifests itself in the reflection of the unstable eigenvalues around the neutral line ($\lambda_r = 0$) into the stable half-plane. The compensated eigenvalues are depicted by red symbols. In the small-gain limit (expensive control and $G/W \rangle\rangle 1$), control efforts focus only on the stabilization of the system, while leaving the stable sub-dynamics unaffected : the stable compensated eigenvalues therefore coincide with the uncontrolled eigenvalues.

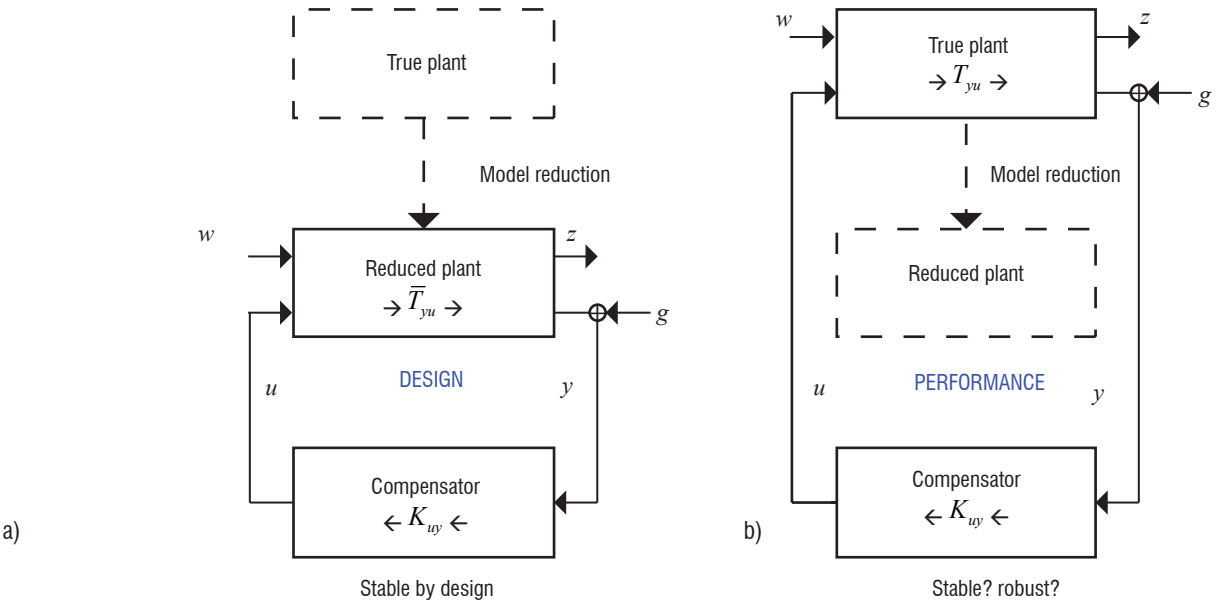

Figure 6 - a) Design of a compensator based on a reduced-order model of the true plant. b) Application of the designed compensator to the full model of the true plant

Following our robustness analysis, we will explore the movement of these eigenvalues as the parameter g is varied. We will concentrate on the gain margins of the compensated system and choose $g = a \in \mathbb{R}^+$, ranging from 0.75 to 1.5. For the case $a = 1$, we recover the true design configuration which, by construction, yields a stable compensated system (the case shown in figure 7a). The eigenvalues that yield the critical gain margins are indicated by the green box; we will focus on their trace through the complex plane for $0.75 \leq a \leq 1.5$. Figure 7b displays the locus of the two eigenvalues of the compensated system (i.e., the eigenvalues of $\overline{A}^{cl}$ from (3.13)) for the specified parameter range. We observe that for $a = 0.75$ the two eigenvalues start out in the unstable half-plane and gradually move into the stable one. At a critical value of $a^- = 0.931$ both eigenvalues are contained in the stable half-plane, indicating stability of the compensated system. The design-state is recovered for $a = 1$ (green box). By further increasing a, the two eigenvalues move in opposite direction: one eigenvalue tends to higher damping rates, while the other re-crosses into the unstable half-plane at a critical value of $a^+ = 1.05$, rendering the compensated system unstable again. We can thus conclude that the stability of the compensated system can be guaranteed only for $0.931 \leq a \leq 1.05$. Obviously, this interval contains the design point $a = 1$; however, it shows rather narrow margin values and thus rather poor robustness of the compensator.

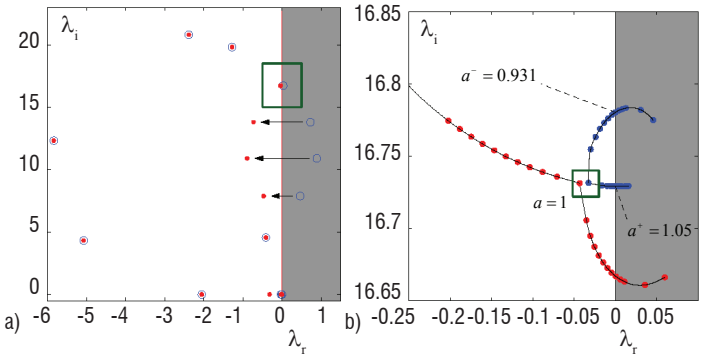

Figure 7 - a) Eigenvalues of the uncontrolled reduced-order model (blue symbols) and of the compensated system (red symbols), showing the reflection of the (four) unstable eigenvalues into the stable half-plane, as well as the invariance of the stable eigenvalues. (b) Robustness analysis: tracing the critical eigenvalues (indicated by the green box in (a)) as a function of $g = a \in \mathbb{R}^+$. The gain margins are given by $a^+ = 1.05$ and $a^- = 0.931$. For $0.931 \leq a \leq 1.05$ the compensated system is stable. The case $a = 1$ corresponds to the red eigenvalues inside the green box in Subfigure (a).

An analogous analysis can be conducted by choosing $g = \exp(i\varphi)$, thus exploring phase margins and robustness with respect to a mismatch in the estimated convection speed. The results are very similar and thus omitted here: only a small phase margin of $\varphi = \pm 3°$ can be tolerated before instabilities in $\overline{A}^{cl}$ are encountered.

Performance of the compensator in full-plant mode

The compensator is now evaluated in the direct numerical simulation code. Despite the narrow stability margins, we expect the compensator to perform well, since the error between the full-plant transfer function T_{yu} and the reduced-plant transfer function $\overline{T}_{yu}$, on which the compensator has been designed, is very small. The initial condition of the simulation consists of the base-flow and of the most unstable global mode with a low amplitude. The estimation sensor is contaminated by Gaussian white noise of variance $G = 1$. The simulation has been performed from time $t = 0$ to time $t = 16$. Results are shown in figures 8 a,b, where the performance measure z and the control input u are shown as a function of time t. After a short transient, the performance measure z decreases and oscillates erratically with a variance and spectrum in accordance with the performance predicted in figure 3 b. Similar comments can be made for the control input u and for the variance and spectrum of the resulting control input. At time $t = 16$, control is switched off : the signal u is set to and maintained at zero, and the performance measure z is seen to increase dramatically for some time before saturating, in agreement with the expected limit-cycle behavior.

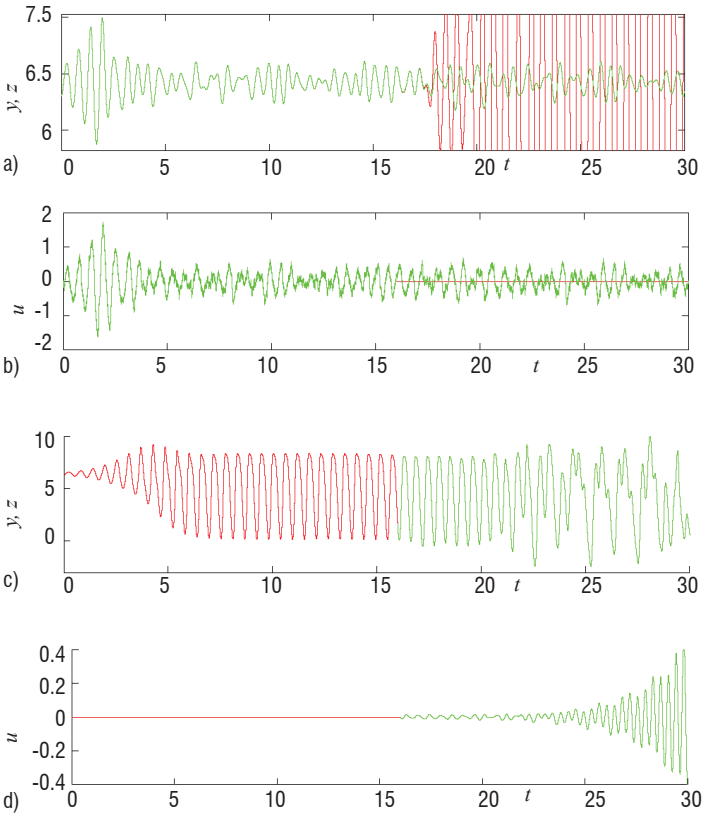

Figure 8 - Controller performance for flow over an open cavity. a) Applying control to the system dynamics near the base flow, with corresponding control signal b), c) Applying linear control to the saturated limit-cycle behavior, with corresponding control signal d).

We have shown that the designed compensator manages to maintain the flowfield in the vicinity of the equilibrium point. We will now test whether the same compensator is able to drive the system from the limit cycle towards the equilibrium point. For this, we have first performed (from $t = 0$ to $t = 16$) an uncontrolled simulation leading to the limit-cycling behavior; then, at $t = 16$, control has been switched on. Results are shown in figures 8 c,d, where the performance measure z and the control input u have been represented as a function of time t. We observe that both the performance measure and the control input display oscillations that continuously grow in amplitude, indicating that this compensator is ineffective once limit-cycle behavior is established. We note that a more robust compensator - one that may have been obtained, for example, using an $H\infty$-approach [10] - may have given better results.

The backward-facing step

As mentioned above, the configuration of the backward- facing step is a feedforward configuration, for which the control input u has only a weak influence on the estimation sensor y. Therefore, the feedback framework as described in the previous sections seems inappropriate here. It is thus futile to perform control based on a state- space model and to conduct a robustness analysis. More generally, this observation is typical of advection-dominated noise amplifiers with a sensor location upstream of the actuator. In addition, the prevalence of the noise input w and its inaccessibility in a real control experiment further rule out the use of a state-space model or Galerkin-framework, which would require precise knowledge of B_w and of the covariance W (see Bagheri et al. [4] for an example of a feedforward configuration that has been treated within a feedback framework). In essence, for any flow situations, in which noise amplification through the fluid system is the primary source of perturbation dynamics, the necessity of an accurate noise model constitutes a major design difficulty and often the weakest point of the first (state-space) approach. The next section will introduce techniques and tools to address this problem.

Approach II: input-output map and feedforward control

The first approach replicated the mapping of the system between low-dimensional signals (u and z), via a reduced state vector, by estimating the state. The alternative approach is to directly extract this mapping between the low-dimensional signals by eliminating the state. This approach is easily motivated by the formal solution to (4-5) for vanishing initial condition ($x(0) = 0$) and in the absence of noise ($w = 0$, $g = 0$). We have

$$z = \int_0^t \underbrace{C_z \exp\big((t-\tau)A\big)B_u}_{h_{zu}(t-\tau)} u(\tau)\,d\tau \qquad (18)$$

where we recognize the low-high-low-dimensional expression $\mathrm{C_z \exp\big((t-\tau)A\big)B_u}$ but replace it with the low-dimensional temporal convolution kernel $\mathrm{h_{zu}(t\quad)}$.This expression then suggests that the measurement z can be modeled by a time-history of control signals u, appropriately weighted by the kernel function $\mathrm{h_{zu}}$, which implicitly contains information about the system dynamics (given by A), the control (given by B_u) and the measurement (given by C_z). In the presence of noise sources ($\mathrm{w \neq 0}$, $g \neq 0$), modifications to the previous expression must be made; the general approach, however, persists. For convenience (but without loss of generality), we convert to a time-discrete version of (4-5) and further assume a scalar control signal u, a scalar measurement signal z and scalar noise signals w and g. We obtain

$$x_{n+1} = Ax_n + B_u u_n + B_w w_n \qquad (19)$$

$$z_n = C_z x_n \qquad (20)$$

where $x_n = x(n\Delta t)$ and similar for the other time-dependent variables. Note that the system, control and measurement matrices A, B, C are not identical (but related) to their continuous equivalents in (4-6). Pursuing the approach outlined above, we continue by expressing the discrete measurement vector z_n in general as a function of the control and noise sources, according to

$$z_n + \sum_{i=1} a_i z_{n-i} = \sum_{j=0} b_j u_{n-j} + \sum_{k=0} c_k w_{n-k} + R \qquad (21)$$

with (yet) unknown coefficients {b}, {c}. An additional dependence on the history of z has been included, in the form of an auto-regressive term with unknown coefficients {a}. By observing temporal sequences of measurement, control and noise signals, the above coefficients can be determined using linear regression techniques. Two problems arise: (i) measurements of the noise signal w are difficult to obtain and (ii) linear regression techniques assume a uniform (white) distribution for the residual error R. The first difficulty will be remedied by introducing additional sensor input upstream of the actuator that provides information about the incoming disturbance environment; this additional (scalar) sensor will be denoted by y and will be treated as a substitute for w. We thus have

$$z_n + \sum_{i=1} a_i z_{n-i} = \sum_{j=0} b_j u_{n-j} + \sum_{k=0} c_k y_{n-k} + R \qquad (22)$$

A sketch of the control configuration is shown in figure 9, together with the paths of information transfer in the flow. The influence of the control u on z is labeled by (1), while the influence of the upstream measurement y on z is indicated by (2). Even though the y-signal will capture most of the incoming noise (given by path (3) in figure 9), it is conceivable that part of the environmental noise w will not be detected by the y-sensor upstream, will pass through the fluid system and will affect the measurement z further downstream (see path (4) in figure 9). During this passage through the system, the (perhaps) white noise upstream will be modified by the system - some frequency components will be amplified, others will be damped - and will have a distinct color when it impacts the measurement z downstream. This component, at the moment represented by the residual error R, however, will be treated as white by any linear regression technique; instead, a colored noise model is needed to express R. This is accomplished by allowing a relation between time-instants of R. We thus postulate the revised model

$$z_n + \sum_{i=1} a_i z_{n-i} = \sum_{j=0} b_j u_{n-j} + \sum_{k=0} c_k y_{n-k} + \sum_{p=1} d_p R_{n-p} + R_n \qquad (23)$$

The newly introduced coefficients d_p capture a temporal correlation of the error term and thus model the color of the noise affecting the downstream sensor. The model above is known as an ARMAX model : consisting of an auto-regressive (AR) part for the measurement signal z, a moving-average (MA) part for R and two exogenous (X) inputs for u and y.

Model obtained by statistical learning

Once the structure of the model has been selected on physical grounds, time sequences of the various signals will be used as a learning data-set to determine the set of coefficients {a}, {b}, {c} and {d}. To this end, in addition to the excitations w arising from external noise sources, the system is forced by an input signal u, which is chosen as sufficiently rich in frequencies to excite the relevant time scales of the fluid system. The response to this forcing in the sensors y and z will be recorded, together with the input signal u, and will form the learning data-set. The coefficients will be determined using a least-squares technique, by matching the predicted response in z to the true measured response. Once the coefficients are known, the generality of the ARMAX- model must be verified by processing a testing data-set. This validation will ensure that input signals and/or noise environments that have not been part of the learning data-set will nevertheless yield accurate predictions of the output signal z. It is no trivial task to determine the proper complexity of the model, or the

length of the learning samples. Too short data-sequences or models displaying too high a complexity will result in rather small errors for the learning data-set, but often in large deviations for the testing data-set. This phenomenon is known as overlearning and must be avoided by striking a compromise between the error norm from the learning and testing data-set [24].

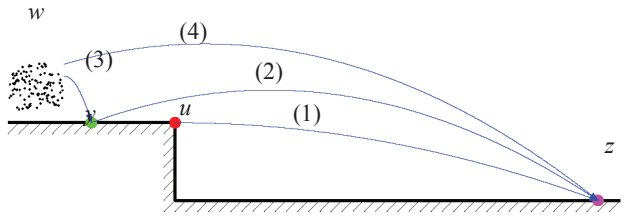

Figure 9 - Sketch indicating the transfer of information to be modeled by the ARMAX structure. Transfer of information (1) from the control u to the performance sensor z, (2) from the upstream sensor y to the performance sensor z, (3) the observable part of the disturbance environment w measured by y and (4) the part of w, unobservable by y but affecting the performance sensor z

For our case of the backward-facing step, the relevant signals y, u and z from the learning data-set are shown as a function of time in figures 10 a,b,c. We force the system in u by finite-width pulses from the actuator and record the upstream measurement y (note the rather stochastic nature of the signal), as well as the signal from the downstream sensor z. The identified model is then validated by subjecting it to a different forcing u and a different noise environment w and by comparing the model output in z to the true output from a direct numerical simulation. Comparison between true z_t and predicted z_p performance measures are shown in figure 10 d: after a transient, which corresponds to the time taken for a perturbation to travel from sensor y and actuator u to the performance sensor z, the two curves collapse indicating that the model is able to perfectly predict the performance measure z from knowledge of the estimation measure y and control input u.

Design of a compensator

Once the ARMAX model has been identified by determining the coefficients such that the predicted sensor output matches the actual one, a compensator can be designed. The underlying principle of this design is disturbance rejection, which is based on the relation $z = T_{zy}y + T_{zu}u$ linking the measurement from the upstream sensor y and the control input u to the downstream sensor z via two transfer functions. Our goal is to minimize the signal z, and, by postulating $z = 0$, we can derive the control law $u = -T_{zu}^{-1}uT_{zy}y$ based on the upstream sensor measurements y. It is conceivable, and often the case, that the transfer function T_{zu} is small or zero for certain frequencies; in this case, the inversion in the expression for the control law would fail, or lead to undesirable large control gains. To avoid this issue, a pseudo-inversion (rather than an exact inversion) is taken, where a lower threshold can be specified, below which no control action is taken. This regularization step is necessary to obtain effective control action.

The control design can also be performed in the time-domain, rather than frequency domain. In this case, a time-horizon must be specified, over which the measurement signal z is minimized. Also within this setting, a regularized inversion (via a pseudo-inverse) is required to produce an operative and practical control strategy.

Performance of the compensator in full-plant mode

Following its design, the compensator is now applied to the direct numerical simulations: measurements from the upstream sensor y are taken and processed by the compensator, which provides the input signal u. This signal has been designed to optimally reduce the downstream measurement signal z. Even though not explicitly stated in the control objective, the total perturbation energy of the fluid system is expected to be reduced as well by this action. This expectation is not assured, but rather depends on the specifics of the flow configuration and must be verified for each case. Figure 11 presents results from uncontrolled and controlled simulations. A significant reduction of the perturbation energy can be observed, where control efforts lead to a lowering by about two orders of magnitude (see figure 11(a)). The spatial extent of the perturbation energy is obtained by locally time-averaging the fluctuation energy. Figure 11(b,c) juxtaposes the controlled and uncontrolled case, using identical color maps for the displayed contours. In the uncontrolled case, a substantial concentration of high perturbation energy (about 25 step heights from the step) is observed downstream of the base-flow reattachment point, which eventually decays due to the global stability of the flow. This concentration could be drastically decreased by applying flow control, as illustrated in figure 11(c). Even though the location of the perturbation-energy peak has not changed significantly, the amplitude has been reduced by two orders of magnitude, as evidenced in figure 11(a). It is noteworthy that fluctuation energy is reduced throughout the

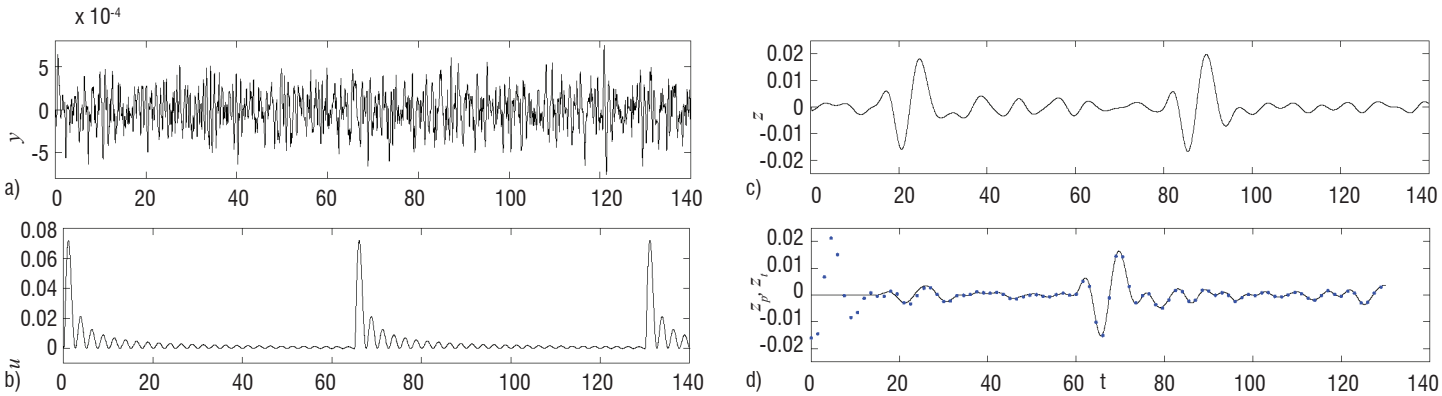

Figure 10 - Learning data-set consisting of the recorded measurements from the upstream estimation sensor y (a), input signal u (b) and downstream performance sensor z (c). Note that a pulse in u (b) yields a pulse in z (c) after a time-delay corresponding to the travelling time of a perturbation between the actuator and the performance sensor location. The validation of the model is shown in (d), where the predicted output (solid black line), for a forcing different from the learning set and for a different noise environment, is compared to the true signal (blue symbols) from the full system.

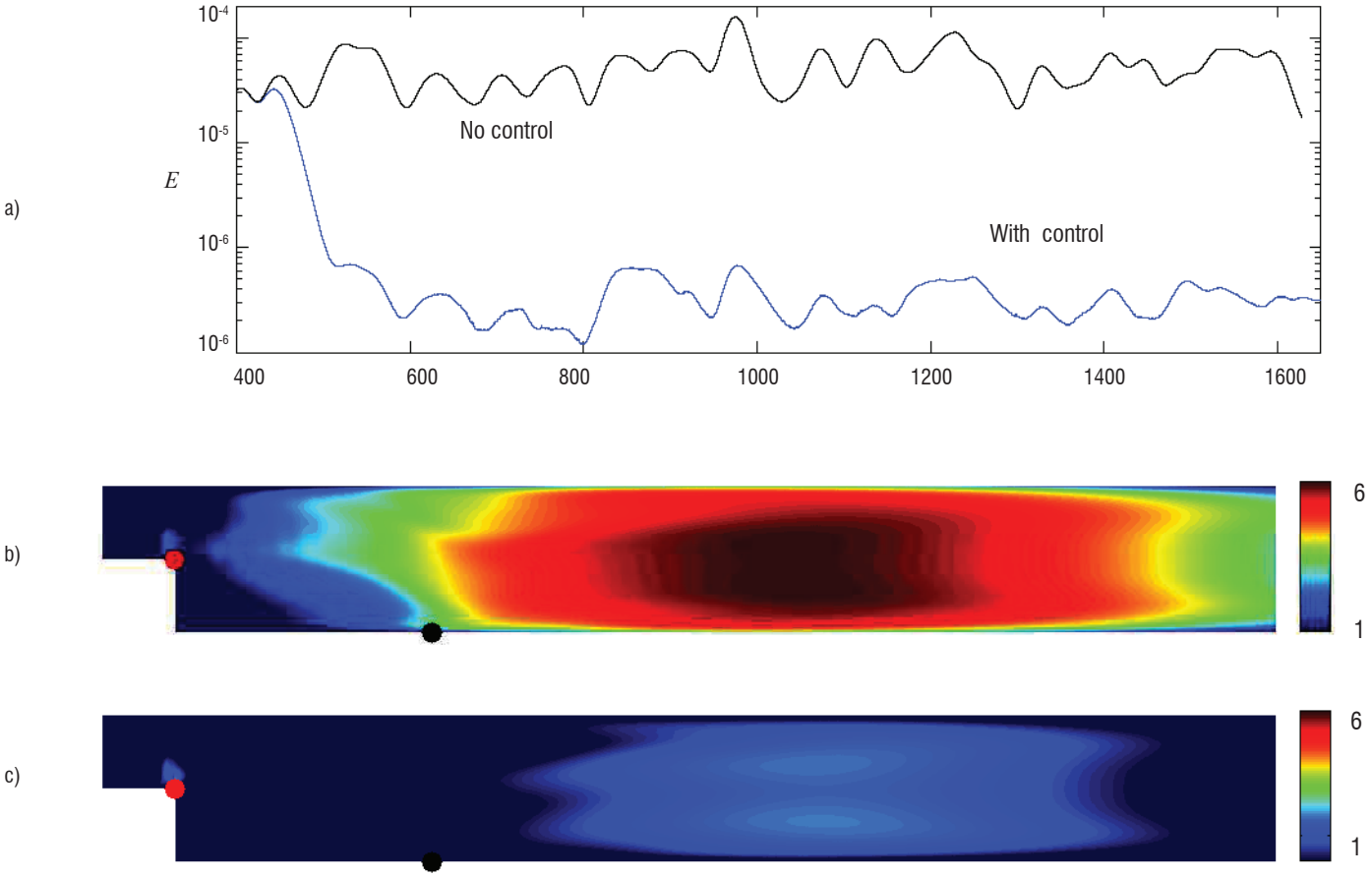

Figure 11 -(a) Global perturbation energy versus time for the uncontrolled (black) and controlled (blue) case; a reduction of two orders of magnitude is accomplished, by applying feedforward flow control. (b,c) Time-averaged local perturbation energy for the uncontrolled (b) and controlled (c) flow over a backward-facing step. The vertical coordinate has been scaled by a factor of three; the controller location (red symbol) and objective sensor location (black symbol) are also indicated. Logarithmic contour levels have been used, with identical color maps.

computational domain downstream of the reattachment point, even though only a reduction of the measurement signal from the downstream sensor (black symbol in figures 11(b,c)) has been included in the design of the compensator.

Summary and outlook

An overview of approaches and tools for the design of effective control strategies has been given. Two generic flow configurations have been used throughout this article: (i) the two-dimensional flow over an open cavity, which above a critical Reynolds number is globally unstable and thus acts as a flow-oscillator and (ii) the two-dimensional flow over a backward-facing step, which is globally stable but acts as an amplifier of ambient noise sources. Due to the prevailing global instability, the first case is rather insensitive to noise sources and can thus be accurately described by a Galerkin-based approach within a state- space formulation; in fact, the noise terms can safely be discarded in the analysis. An LQG (optimal control) approach for designing a feedback controller yields optimal performance for the compensated system, but does not guarantee robustness. Instead, a separate robustness analysis of the closed-loop transfer function must be performed, to establish stability margins. The second case, flow over a backward-facing step, responds sensitively to a noisy environment. It is thus less amenable to a Galerkin-based model, since a sufficiently accurate model of the environmental noise is difficult to come by. A data-based model is more suitable in this case and for amplifier flows in general. It involves the processing of noisy input and output signals, and the recovery of a discrete transfer function, which is subsequently used to design a feedforward controller.

In summary, a Galerkin-based approach is efficient for globally unstable flows, where an internal instability synchronizes the flow and makes it insensitive to external noise sources. Any control effort focuses on the suppression of this instability; performance is optimal, but robustness needs to be assessed a posteriori. A data-based model is suited for globally stable noise-amplifier flows. No user-supplied environmental noise model is required, since the upstream sensor acts as a substitute for the incoming noise background and a moving-average residual captures the remaining unobservable part of the upstream noise sources. This approach appears robust and efficient across a considerable range of off-design parameter values ■

Acknowledgments

The authors would like to thank Alexandre Barbagallo and Aurelien Hervé for their support and constructive criticism.

References

[1] A.C. ANTOULAS - *Approximation of Large-Scale Dynamical Systems*. Advances in Design and Control, SIAM (2005).
[2] C.W. ROWLEY - *Model Reduction for Fluids, Using Balanced Proper Orthogonal Decomposition.* Int. J. Bifur- cation Chaos, 15 (2005), 997.
[3] E. AKERVIK, J. HOEPPFNER, U. EHRENSTEIN and D.S. HENNINGSON - *Optimal Growth, Model Reduction and Control in a Separated Boundary-Layer Flow Using Global Eigenmodes*. J. Fluid Mech., 579 (2007), pp. 305–314.
[4] S. BAGHERI, L. BRANDT and D.S. HENNINGSON - *Input-Output Analysis, Model Reduction and Control of the Flat-Plate Boundary Layer.* J. Fluid Mech., 620 (2009), pp. 263–298.
[5] A. BARBAGALLO, D. SIPP, and P.J. SCHMID - *Closed-Loop Control of an Open Cavity Flow Using Reduced - Order Models*. J. Fluid Mech., 641 (2009), pp. 1-50.
[6] S. AHUJA and C.W. ROWLEY - *Feedback Control of Unstable Steady States of Flow Past a Flat Plate Using Reduced-Order Estimators*. J. Fluid Mech., 645 (2010), pp. 447-478.
[7] B.R. NOACK, K. AFANASIEV, M. MORZYN´SKI, G. TADMOR, and F. THIELE - *A Hierarchy of Low-Dimensional Models for the Transient and Post-Transient Cylinder Wake*. J. Fluid Mech., 497 (2003), pp. 335–363.
[8] E. CARABALLO, J. LITTLE, M. DEBIASI and M. SAMIMY - *Development and Implementation of an Experimental-Based Reduced-Order Model for Feedback Control of Subsonic Cavity Flows*. J. Fluids En- gin., 129 (2007), pp. 813–824.
[9] S.S. JOSHI, J.L. SPEYER and J. KIM - *A Systems Theory Approach to the Feedback Stabilization of in Finitesimal and Finite-Amplitude Disturbances in Plane Poiseuille Flow*. J. Fluid Mech., 332 (1997), pp. 157–184.
[10] J.C. DOYLE, K. GLOVER, P.P. KHARGONEKAR and B.A. FRANCIS - *State-Space Solutions to Standard H2 and H∞ Control Problems*. IEEE Trans. Automat. Control, 34(8) (1989), pp. 831–847.
[11] T.R. BEWLEY and S. LIU - *Optimal and Robust Control and Estimation of Linear Paths to Transition.* J. Fluid Mech., 365 (1998), pp. 305–349.
[12] J. KIM and T.R. BEWLEY - *A Linear Systems Approach to Flow Control*. Annu. Rev. Fluid Mech., 39 (2007), pp. 383–417.
[13] L. LJUNG - *System Identification: Theory for the User.* 2nd edition, Prentice Hall (1998).
[14] S.-C. HUANG and J. KIM - *Control and System Identification of a Separated Flow*. Phys. Fluids, 20(10) (2008), pp. 101509.
[15] A. HERVÉ, D. SIPP, and P.J. SCHMID - *A Physics-Based Approach to Flow Control Using System Identification.* J. Fluid Mech., 702 (2012), pp. 26–58.
[16] S.S. COLLIS, R.D. JOSLIN, A. SEIFERT and V. THEOFILIS - *Active Flow Control: Theory, Control, Simulation, and Experiment*. Prog. Aerosp. Sci., 40 (2004), pp. 237–289.
[17] M. PASTOOR, B.R. NOACK, R. KING and G. TADMOR - *Spatiotemporal Waveform Observers and Feedback in Shear Layer Control*. AIAA paper, 2006-1402 (2006).
[18] M. SAMIMY, J.H. KIM, J. KASTNER, I. ADAMOVICH and Y. UTKIN - *Active Control of High-Speed and High-Reynolds-Number Jets Using Plasma actuators*. J. Fluid Mech., 578 (2007), pp. 305–330.
[19] L.N. CATTAFESTA III, Q. SONG, D.R. WILLIAMS, C.W. ROWLEY, F.S. ALVI - *Active Control of Flow- Induced Cavity Oscillations*. Prog. Aerosp. Sci., 44 (2008), pp. 479-502.
[20] R. KING (Editor) - *Active Flow Control II*. Springer Berlin Heidelberg, (2010).
[21] G. DERGHAM, D. SIPP, J.-C. ROBINET, and A. BARBAGALLO - *Model Reduction for Fluids Using Frequential Snapshots*. Phys. Fluids, 23 (2011), 064101.
[22] Z. MA, S. AHUJA, and C.W. ROWLEY - *Reduced-Order Models for Control of Fluids Using the Eigensystem Realization Algorithm*. Theot. Comp. Fluid Dyn., 25, 1-4 (2011), pp. 233–247.
[23] S.J. ILLINGWORTH, A.S. MORGANS, and C.W. ROWLEY - *Feedback Control off Low Resonances Using Balanced Reduced-Order Models*. J. Sound Vib., 330 (2011), pp. 1567–1581.

[24] G. DREYFUS, J.-M. MARTINEZ, et M. SAMUELIDES - *Apprentissage statistique*. Editions Eyrolles, Paris (2011)

Acronyms

LQG	(Linear Quadradic Gaussian)
PI	(Proportional Integral)
POD	(Proper Orthogonal Decomposition)
ROM	(Reduced Order Model)
ARMAX	(Auto Regressive Moving Average with eXternal inputs)
bPOD	(Balanced Proper Orthogonal Decompostion)
ERA	(Eigenvalue Realization Algorithm)

AUTHORS

Denis Sipp has been a researcher at Onera since 2002. He is the head of the Fluid Mechanics unit in the Department of Fundamental and Experimental Aerodynamics. He obtained a PhD degree from Ecole Polytechnique in 1999, on the stability of vortex pairs. He obtained his Habilitation Degree in 2009 at the Pierre et Marie Curie University in Paris. He has been a Professor (PCC) in the Department of Mechanics at Ecole Polytechnique since 2003.

Peter Schmid is currently a research director with the French National Research Agency (Cnrs) and Professor (PCC) of Mechanics at the Ecole Polytechnique in Paris. Previously, he held a faculty position in Applied Mathematics at the University of Washington in Seattle. He received his Ph.D. in Math-

Passive Control of Cavity Flows

S. Yamouni, C. Mettot
D. Sipp, L. Jacquin
(Onera)

E-mail: denis.sipp@onera.fr

This paper deals with cavity flow physics and its passive control by means of a spanwise cylinder. Two configurations are considered. First, a laminar study of a flow over an unconfined square cavity at a low Reynolds number (7500) is presented. Global stability results are shown, allowing the identification of the driving mechanisms of the cavity flow: the aeroacoustic feedback mechanism ([18]) and the acoustic resonance mechanism [4]. When both mechanisms interact, the growth rate of the global modes is seen to display a local maximum. At low Mach numbers, we suggest that it is still the feedback aeroacoustic mechanism that selects the frequency mode, the acoustic resonance mechanism only enhancing the response. Second, we study the dynamics of a turbulent deep cavity flow in a transonic regime. Global modes and sensitivity results are shown and compared to experimental data, with and without control cylinder. Concerning the baseline (without control), RANS and URANS simulations, based on the k-ω model of Wilcox, display very good agreement with experiments. Also, the sensitivity map obtained numerically is extremely close to the experimental control map obtained by moving a small control cylinder in the usptream boundary layer and the shear-layer. Different interpretation elements are discussed.

Cavity flows as a source of unsteady loads and noise

Historical note

The flow that develops over an open cavity is a generic example of self-sustained fluidic oscillations. Other flows of this type are shock oscillations on the suction side of a wing profile at a high (subsonic) Mach number and high angles of attack, impinging jets, combustion instability phenomena, or bluff bodies. These self-sustained oscillating flows result from complex interactions between fundamental mechanisms comprising hydrodynamic instabilities, vortex dynamics, acoustic wave propagation and turbulence. In the compressible regime, the impingement of vortices induced by Kelvin-Helmholtz instabilities, which develop in the shear-layer over the cavity, generates acoustic pressure waves travelling upstream. These pressure waves excite the Kelvin-Helmholtz instabilities, which closes the feedback loop. As a result, specific frequencies are selected. This interaction can be the source of unsteady loads and noise, which can be detrimental to the obstacle surroundings. Indeed, even if the acoustic energy only represents a weak part of the total mechanical energy of the system ($E_{ac} \approx 10^{-5} E_{total}$), high acoustic levels can be reached. Cavity flows have been studied since the 1950s, motivated by aeroacoustics, aero-elasticity and aero-optics applications. In military applications [6], [8], weapon bays are subjected to oscillations that can enter in resonance with the modes of the aircraft structure. Image distortion due to cavity flow effects is a great concern for in-born observations. During the landing and take-off of transport aircraft, landing gears are important sources of noise [7]. Cavity flow phenomena also concern ground transportation. Car sun-roofs and windows, and the shallow cavities receiving the pantograph in trains are classical examples.

Driving mechanisms

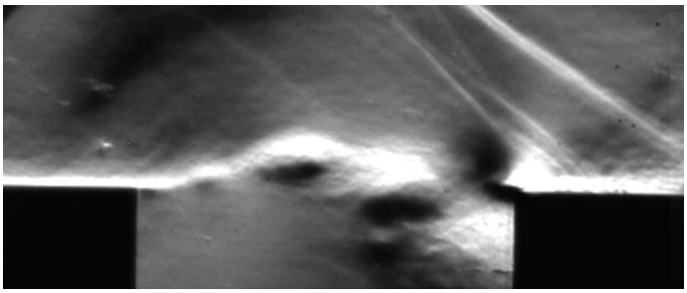

Figure 1 - Schlieren picture of an uncontrolled cavity flow at M=0.8

In a cavity flow, it is generally acknowledged that two physical mechanisms are at play. First, the feedback aeroacoustic mechanism, described by [18], induces self-sustained oscillations. Small disturbances are amplified along the shear layer by the Kelvin-Helmholtz instability and convected downstream. The impact of these structures upon the cavity trailing edge leads to the formation of acoustic waves traveling upstream up to the sensitive region located at the leading edge. This process is visible in figure 1, where the large vortical structures of the shear layer and the pressure waves are clearly

visible thanks to a Schlieren system. Second, [4] modeled empirically the resonant response of deep cavities, which is linked to the presence of acoustic standing-waves inside the cavity. Henceforth, this phenomenon is referred to as the acoustic resonance mechanism. This phenomenon occurs when the acoustic wavelength is of the same order as the length (or depth) of the cavity. The feedback aeroacoustic mechanism can be enhanced by acoustic standing-wave resonances [17]. However, [25] stated that a theory combining both mechanisms is still lacking.

Recent advances improving the understanding of cavity flow physics are described in the section "The physics of cavity flows: new results" [26], [27]. We will show that a global stability analysis is a relevant theory to, first, capture the two aforementioned mechanisms, the feedback aeroacoustic and the acoustic resonance mechanisms, and second, to show that a similar mechanism is at play in the incompressible and the compressible regimes.

Control of cavity noise

Many control techniques have been tested in order to reduce the cavity acoustic tones with variable results. Both active and passive control systems have been used (see article review of [2]). Passive control devices are the easiest to implement and a wide variety of systems were tested, in particular: spoilers, mass injection and modification of the cavity leading and/or trailing edge. These concepts sometimes proved to be very effective in reducing energetic tones but, in general, they did not succeed in suppressing multiple acoustic modes simultaneously. The effect of a spanwise cylinder in compressible crossflow parallel to the leading edge of the cavity is another passive device that proved to be very efficient, as shown first by [13]. This control system has been subsequently described by [22], [23], [9] and [15]. Some active control methods have been also tested, where small amplitude disturbances are introduced by means of unsteady flow injections or flapping actuator devices. Control by open-loop forcing or feedback control strategies have been also tested [19], [20].

In [28], an experiment was performed where the evolution of the pressure spectrum energy was measured as a function of the cylinder position within the upstream boundary layer and the shear layer of the cavity. This experiment will be described in the section "The passive control of cavity flows". From this experiment, a sensitivity map that favorably compares with the theory was deduced, showing that the regions where cavity tones are controlled are the regions where the global modes are stabilized.

The physics of cavity flows: new results

As mentioned above, cavity flow physics stems from a global mechanism that couples hydrodynamics (the shear layer) and acoustics (pressure waves). Note that a local approach for the hydrodynamic part is not recommended due to the global nature of this physics. A global approach based on a hydrodynamic global stability analysis also successfully described the dynamics of other flows, such as shock-induced transonic-buffet [3], shock wave/laminar boundary layer interaction [16], flow around a swept parabolic body [11] or axisymmetric wake flows [14].

In this section, we will present results using the global stability analysis for two cavity cases [27], [28].

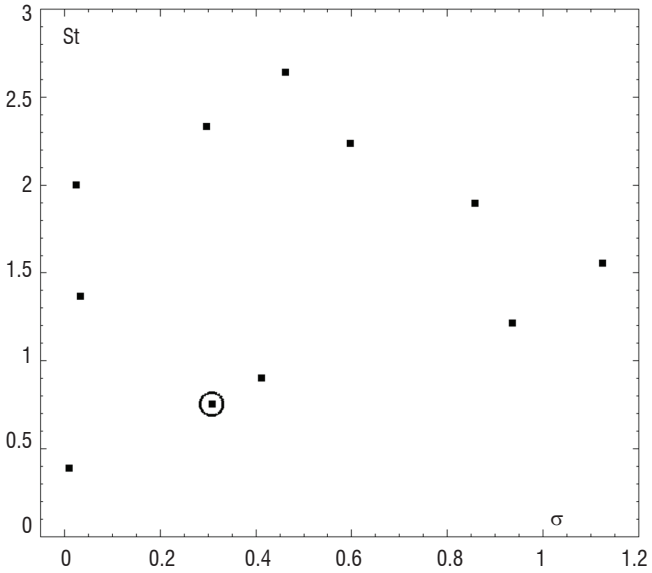

Figure 2 - Spectrum of the unstable global modes obtained at M=0.8 [27]

Global modes: principle

The equations governing the flow dynamics can be written in the form

$$\partial_t W = R(W) \qquad (1)$$

where W represents the aerodynamic field and $R(W)$ represents the residual. W denotes either the divergence-free velocity field in the case of the incompressible Navier-Stokes equations ($W = (\mathbf{U},\mathrm{p})^T$), or a set of variables containing the density, the velocity field and the energy in the compressible case ($W = (\rho,\mathbf{U},\mathrm{T})^T$).

The base flow W_0, an equilibrium point of eq. (1), is defined by:

$$R(W_0) = 0 \qquad (2)$$

The dynamics of the small perturbations w superimposed on this field are governed by $\partial_t w = A(w)$, where A is the Jacobian operator linked to the residuals $\boldsymbol{R}$ by the relation $A = \left.\frac{\partial R}{\partial W}\right|_{W_0}$.

The perturbation is then sought in the form of normal modes $w(x,y,t) = \hat{w}(x,y)e^{(\sigma+i\omega)t}$, where σ and ω represent the temporal growth rate and the frequency of the global mode $\hat{w}$, respectively. When $\sigma > 0$ (resp. < 0), the base flow is unstable (resp. stable). Substituting w leads to a generalized eigenvalue problem for $\lambda = \sigma + i\omega$ and $\hat{w}$:

$$A\hat{w} = \lambda\hat{w} \qquad (3)$$

In figure 2, an example of global spectrum obtained at M=0.8 is displayed in the (σ, St) plane. There are eleven unstable modes whose convergence has been checked by varying the mesh refinement [27].

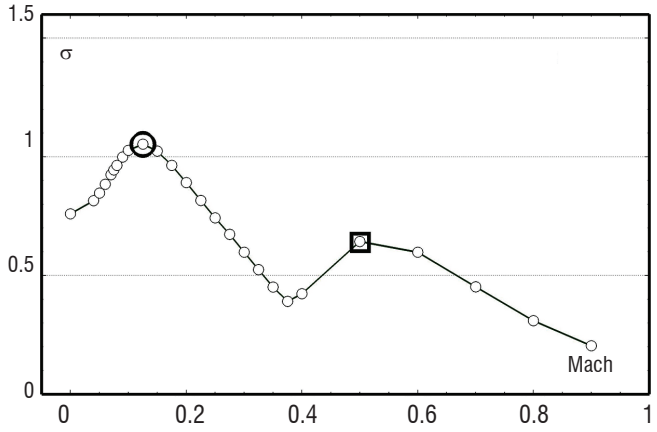

Figure 3 - Temporal growth rate evolution of the unstable global mode n=2 as a function of the Mach number [27].

Mach effects on the global modes

In this paragraph, new insights on the cavity dynamics are presented. They concern the dependency of the unstable global modes with the Mach number and the link between the incompressible and the compressible regimes. Results are extracted from [27] dealing with a laminar flow passing above an unconfined square cavity. The Reynolds number based on the cavity length is set at $Re_L=7500$, sufficient to be unstable [21], while the Mach number has been varied from the incompressible regime (M=0) to high subsonic compressible regime (M=0.9).

Interaction between feedback aeroacoustic mechanism and acoustic resonance mechanism

The interaction phenomenon between the feedback aeroacoustic and acoustic resonance mechanisms has already been observed in experiments and simulations by monitoring acoustic pressure levels. For example, in the case of a deep cavity of length-to-depth ratio equal to 0.66, [1] analyzed the pressure spectrum by varying the Mach number between low Mach numbers up to M=0.5. Block observed several peaks evolving as a function of the Mach number and noticed that the amplitude of these peaks is the greatest when the aeroacoustic feedback curves (n=1, 2) (see Eq. (4)) match with the first acoustic resonance curve of [4]. The aeroacoustic feedback mechanism has been formulated by [1] as,

$$St = \frac{n-\gamma}{\frac{1}{\kappa}+M} \tag{4}$$

where n is the mode number, κ is the ratio between the convection speed of the vortices and the free-stream velocity, M is the Mach number and γ is a delay time ($\gamma<1$).

[27] tracked the eigenvalues by varying the Mach number. In figure 3, one trajectory (n=2) has been represented in the (M; σ) plane. Note that the Strouhal number varies along such a curve. The authors observed that, for intermediate Mach numbers, the trajectory displays two local maxima in the growth rate, corresponding to the match between both mechanisms in accordance with experimental evidence.

Link between the incompressible and the compressible regimes

Initially, the feedback aeroacoustic model proposed by [18] was made to match the mode evolution as a function of the Mach number (see Eq. (4)), and was restricted to the compressible regime. In the incompressible regime, where the pressure feedback is instantaneous, its applicability remains controversial. However, in [27], the authors argue that the feedback aeroacoustic mechanism is also valid in the incompressible regime. They first showed that the frequency and the shape of the unstable global modes in the incompressible case are very similar to the ones observed at very low Mach numbers. Second, thanks to spatio-temporal (x-t) diagrams such as those displayed in figure 4, they showed that a common mechanism is at play throughout the entire range of subsonic Mach numbers, from M=0 to M=0.8. This figure displays the pressure of the global modes

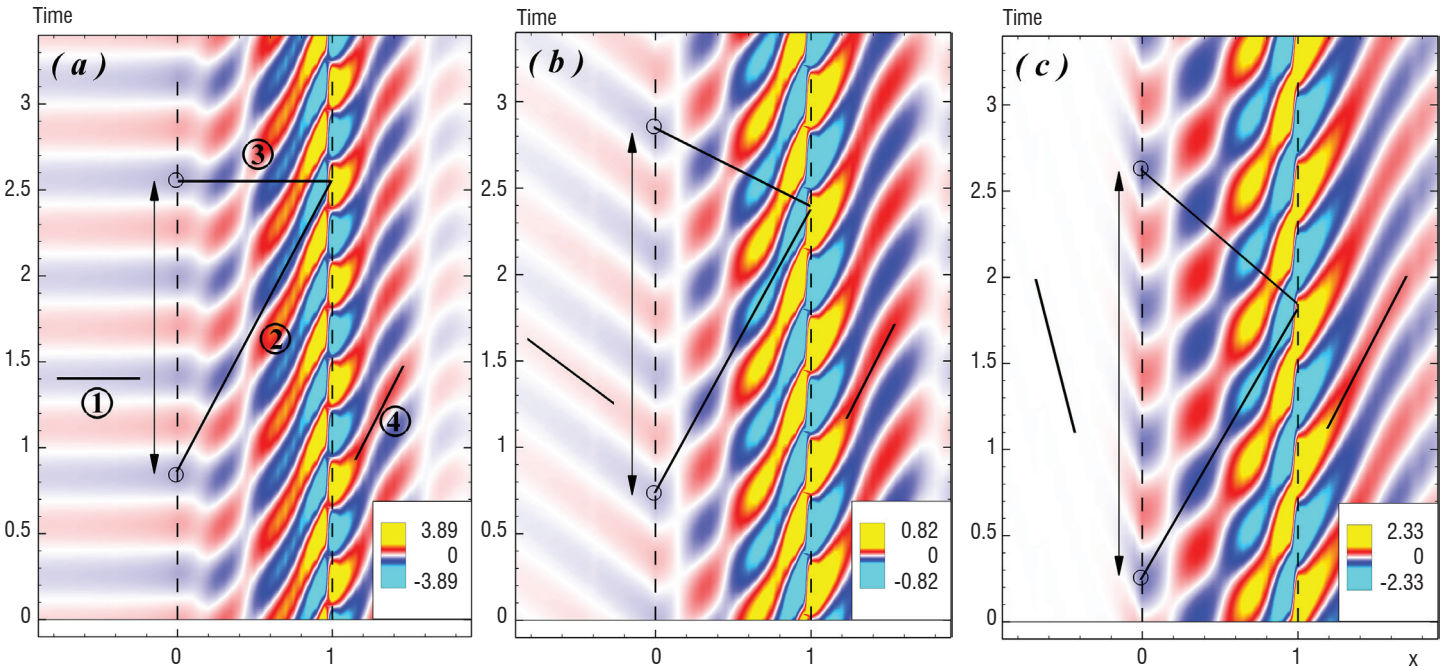

Figure 4 - Spatio-temporal diagrams of the modes belonging to branch n=3 showing the pressure extracted on a segment at y=0. Three Mach numbers are displayed: (a) M=0, (b) M=0.4, (c) M=0.8.

lying on branch n=3 (see Eq. (4)), extracted at the cavity mouth (y=0). The leading (x=0) and downstream (x=1) edges of the cavity are identified by the dashed lines. The slopes of the elongated blue line patterns denote the celerity of the pressure waves. For x in [0;1] and y=0, the pressure of the global modes is characterized by patterns that are pressure fluctuations associated with the vortical structures of the mixing layer. For $x \leq 0$, the patterns are uniquely due to acoustic pressure waves. For instance, considering the slope of the lines labeled ②, the convective velocity of the vortices inside the shear layer is nearly constant and independent of the Mach number value. Differences are only observed in the return speed of the feedback pressure wave (lines labeled ③), which is infinite for M=0 and finite for $M > 0$. This shows that the basic physics is the same for incompressible and compressible flows.

Turbulent regimes

The previous section dealt with laminar flows. Accounting for turbulence is necessary when dealing with an experiment such as the one that we are going to describe. Specific CFD tools are required.
For the latter, we use a RANS code (*elsA*, the Onera CFD suite) for the base flow and global mode calculation. The base flow is still a steady solution of the Navier-Stokes equations, obtained from the convergence of RANS simulations. The URANS version of the code is also used to check good agreement with the experiment.

In this section, stability calculations, unsteady simulations, both based on RANS equations using the k-ω model of Wilcox and comparison with experiment are shown. Sensitivity maps are established from both calculation and experiment. The results are extracted from [28].

Flow configuration

The cavity is that studied by [5], [10] and [28]. It is a deep cavity with a length-to-depth ratio of L/D=0.42. The Mach number is equal to 0.76 and the Reynolds number, based on the cavity length, is equal to Re_L = 815000. The boundary layer thickness at the cavity leading edge is $\delta_0 \approx$ 10 mm. Numerical simulations were also performed, using the same geometry, with a Mach number of 0.8, a Reynolds number equal to Re_L= 860000 and a turbulent upstream boundary layer thickness set at $\delta_0 \approx$ 2.3 mm. In both cases, the reference pressure signal is P_{Ref}, located at the downstream cavity edge (x=50; z=-0.5 mm).

Interpretation of the cavity dynamics with global modes

In figure 5(a), the unstable global modes obtained from the stability calculations (see the section "Global modes: Principle") are displayed. Within the framework of the RANS equations with the Wilcox k-ω model, a set of conservative variables is used ($W = (\rho, \rho\mathbf{U}, \rho E, \rho k, \rho\omega)^t$), where E represents the total energy, k, the turbulent kinetic energy, and ω represents the specific dissipation rate. Two types of global modes are obtained: the first type called the "Kelvin-Helmholtz branch" (red circled symbols) displays modes with shear layer instabilities; the second type comprises the acoustic modes, which exhibit lower but non-zero temporal growth rates σ, since they result from the interaction with hydrodynamic structures. These modes display an intense resonant structure inside the cavity and in the tunnel [26] and [28]. One notes the similarity between this global spectrum and the one displayed in figure 2, in the case of a laminar flow at the same Mach number M=0.8, despite the huge difference in the Reynolds numbers. The frequency of the modes lying on the "Kelvin-Helmholtz branch" is similar, while the general growth rate levels are weaker in the turbulent case, due to eddy viscosity effect. In figure 6, the spatial structure of two unstable global modes is shown through the density: the first is the lowest Strouhal mode (σ=0.13; St=0.40) (a) and the second is the most unstable mode (σ=0.62; St=1.5) (b). Both belong to the "Kelvin-Helmholtz branch". The mode structure is similar to the one presented in [27], displaying vortical structures in the shear layer and acoustic pressure waves with a resonance pattern inside the cavity.

Returning to figure 5(b), the spectrum of the downstream pressure sensor, P_{Ref}, obtained with unsteady RANS simulations, is compared with the experimental one. Good agreement is found for the peak frequencies up to the fifth harmonic, whereas the sound pressure level is overestimated in the numerical simulation, with a difference of nearly 10 dB regarding the fundamental peak ($St \approx$ 0.4). In the same figure, the dashed horizontal lines represent the frequencies of the unstable global modes lying on the "Kelvin-Helmholtz branch" displayed

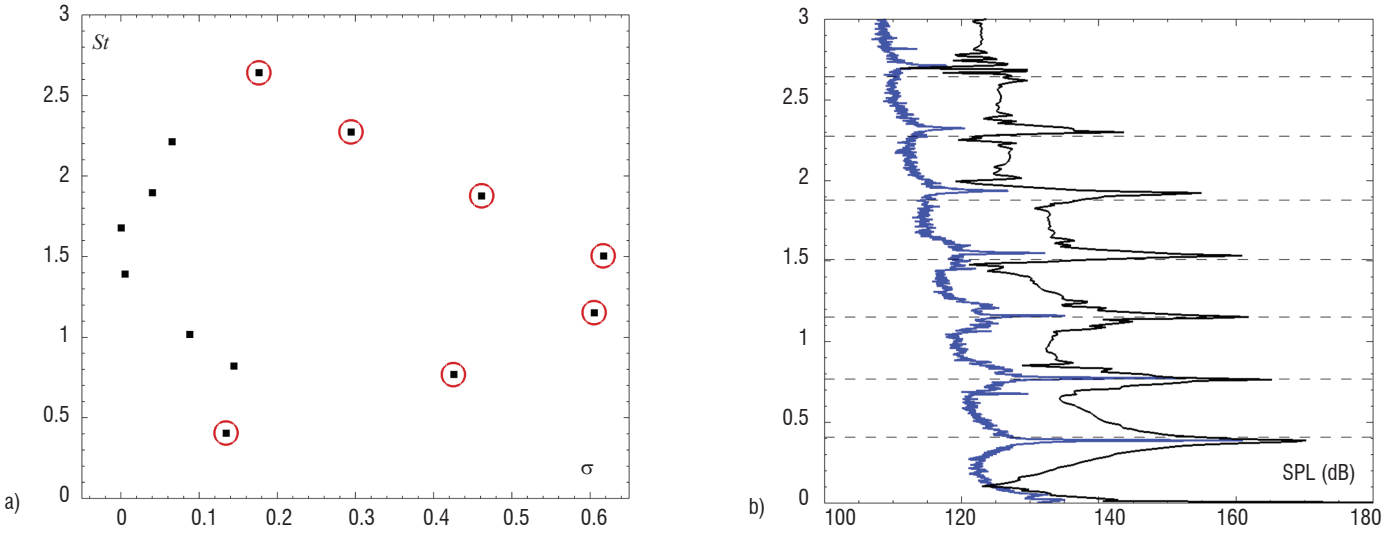

Figure 5 - Comparison between (a) the spectrum of the unstable global modes and (b), the spectra obtained from the URANS simulation (black solid lines) and experiments (blue solid lines). The red circled symbols in (a) are the modes lying on the "Kelvin-Helmholtz branch" and the dashed lines in (b) correspond to the frequencies of these modes.

in figure 5(a). Again, the agreement is very good, which proves that a global stability analysis is able to predict the frequency of the shear layer modes.

In conclusion, the main physics of the cavity, as described by the global mode approach, is very poorly dependent on turbulence. The latter only alters the growth rate of the global modes.

The passive control of cavity flows

In this last section, experimental and numerical results based on the same configuration as above are considered, with the presence of a passive control cylinder.

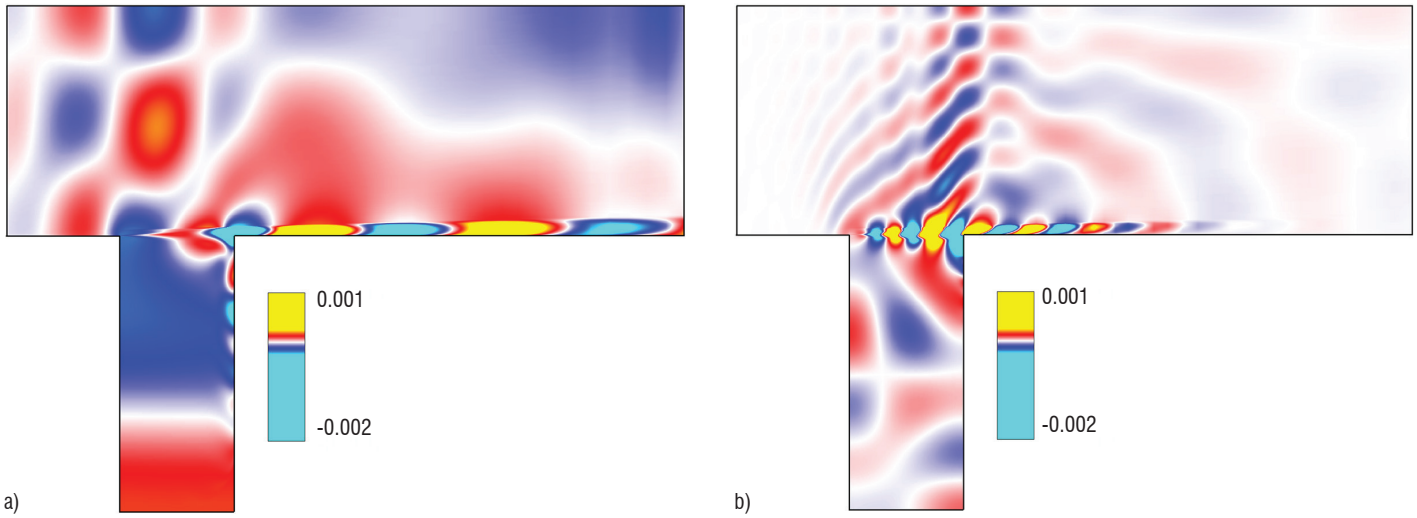

Figure 6 - Spatial distribution of density for the two unstable global modes (0.13; 0.40)(a) and (0.62;1.5)(b).

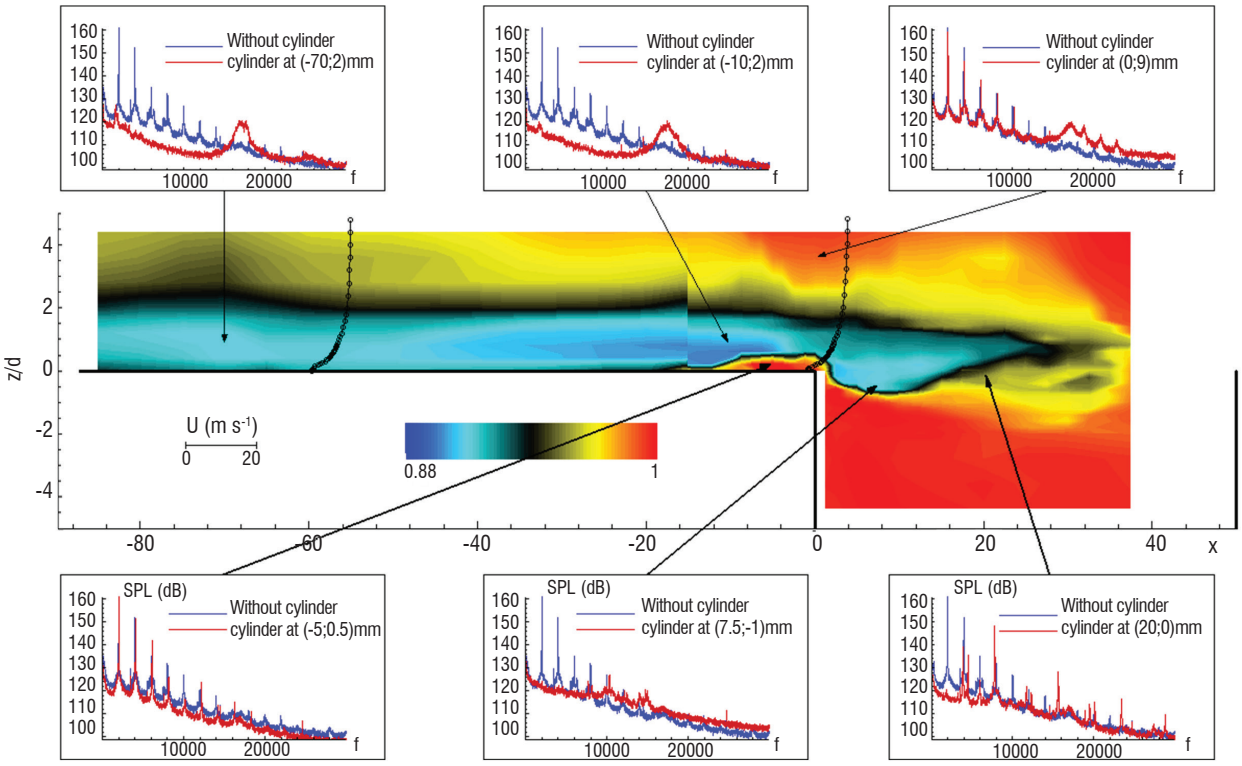

Figure 7 - Control map obtained by integrating the pressure spectrum of the reference sensor P_{Ref} located at the downstream cavity edge (50; -5) mm. All around the map, pressure spectra are displayed, comparing the reference case with the cylinder to controlled cases. The arrows indicate the cylinder position in the map for each spectrum.

Experimental control map

To make the cavity control map, the cylinder (d=2.5 mm) is moved within both the upstream boundary layer and the shear layer. The acoustic energy of the reference pressure sensor P_{Ref}, located at the downstream cavity edge ((50; -5) mm), is calculated for each position of the cylinder. It is then compared with the acoustic energy of the cavity without cylinder. In figure 7, the control map of the cylinder, i.e., the ratio of the acoustic energy between the controlled and the uncontrolled situation, is displayed. In the blue regions, the control cylinder is effective in reducing the acoustic energy, while it is not in the red regions. First, we observe that, for x< -10 mm, the control is effective in the entire upstream boundary layer for z_d/d < 2. Looking at the position x=-5 mm, we retrieve the results from [10]: the control fails if $z_d/d \leq$ 0.4 and $z_d/d \geq$ 2. Second, the control is also effective in the upstream part of the shear layer for z_d/d in [-0.7; 1.2] and x up to 25 mm.

Sound Pressure Level spectra (in dB), comparing the reference case to the controlled cases for different cylinder positions, are also displayed in figure 7. Control may lead to a reduction of the dominant cavity tones from 160 dB to 120 dB (see control location (-10;2) mm). The control efficiency seems to be related to the strength of the Von-Karman vortex shedding, which may be monitored at P_{Ref}. The cylinder Von-Karman frequency ($St=fd/U_\infty \approx 0.2$) is visible for the control locations (x,z)=(-70;2) mm and (-10;2) mm, for which the control is effective. Also, it is seen that the control is ineffective when the cylinder Von-Karman frequency is not seen (see location (x,z)=(-5;0.5) mm), or when the control cylinder wake does not directly interact with the mixing-layer (see location (x,z) = (0;9) mm). Hence, the control is effective when the turbulent stresses associated to the Von-Karman vortex street efficiently diffuse the mixing layer and thus change the mean-flow. However, this appears not to be true when the control cylinder is located at (x,z) = (7.5;-1) mm in the shear-layer. There it is seen that the flow may be efficiently manipulated while the cylinder Von-Karman frequency is only barely seen at P_{Ref}. These observations suggest that the addition of the small cylinder controls the flow by modifying the stability of the mean velocity field. To confirm this, in the following section we have performed a sensitivity study of the unstable eigenvalues to a steady forcing.

Comparison with numerical sensitivity

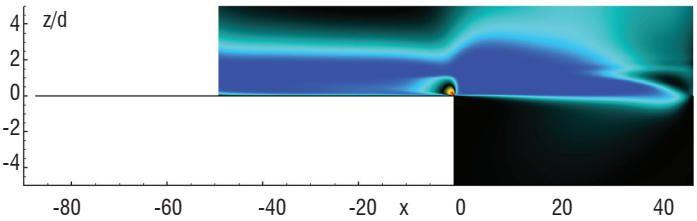

Figure 8 - Sensitivity map of the lowest Strouhal mode (0.13; 0.40) (see figure 6(a)), displaying the growth rate sensitivity ($\delta\sigma$) to a steady forcing δf, imitating the effect of a small cylinder on the flow.

In the case of the control of a cylinder wake by means of a small cylinder, [12] introduced a formalism able to predict the stabilizing regions identified by [24]. The idea is to consider the eigenvalue λ as a function of the base flow W_0, which is itself a function of the steady forcing **f**, simulating the effect of a small cylinder. We wonder to what extent the application of a small amplitude steady force (δF) on the base flow (W_0) could modify the eigenvalue spectrum (λ). The sensitivity can then be expressed using a gradient formulation:

$$\delta\lambda = < \nabla_f \lambda, \delta f > \quad (5)$$

where , to model the presence of a solid cylinder at the position . Substituting δf(x,y) in Eq. (5), the variation of the eigenvalue ($\delta\lambda(x_0,y_0)$) for a position of the control cylinder (x_0,y_0) is given by:

$$\delta f(x,y) = -U_0(x_0,y_0)\delta(x-x_0,y-y_0) \quad (6)$$

In figure 8, the sensitivity map of the lowest Strouhal mode ((0.13; 0.40) in figure 5(a)), showing where the control cylinder should be placed to stabilize the flow (real part of $\delta\lambda$), is displayed. It quantifies the modification induced by the steady forcing δf on this unstable global mode. The stabilization region, depicted in blue, contains the upstream boundary layer up to x=-50 mm (limit of the numerical domain), and one part of the shear layer. This control region is very similar to the experimental control region displayed in figure 7.

Conclusion

In this article, we first present results concerning a laminar case: the flow over an unconfined square cavity flow at a Reynolds number of 7500. Global stability results for Mach numbers ranging from M=0 to M=0.9. By analyzing the evolution of the growth rate (σ) and the frequency (ω) of the unstable global modes obtained, two main observations have been made. First, the unstable modes display a local growth rate maximum, where both driving mechanisms (the feedback aeroacoustic and the acoustic resonance mechanisms) intersect. Second, the applicability of the feedback aeroacoustic mechanism at very low Mach numbers, including the incompressible regime (M=0), has been exemplified at different Mach numbers thanks to spatio-temporal diagrams.

Then, results from numerical simulations, including global modes, unsteady simulations and sensitivity analysis, were compared to experimental data, with and without the passive control cylinder. It appears that the linear global stability analysis of RANS equations (k- ω model of Wilcox), is able to capture the unsteady non-linear cavity flow dynamics. Finally, the sensitivity analysis succeeded in predicting the stabilization region, where the flow is controlled by means of a small control cylinder ■

References

[1] P. J.W. BLOCK – *Noise Response of Cavities of Varying Dimensions at Subsonic Speeds.* Technical Report D-8351, N.A.S.A. Tech. Note, 1976

[2] L.N. CATTAFESTA III, Q. SONG, D.R. WILLIAMS, C.W. ROWLEY, F.S. ALVI - *Active Control of Flow-Induced Cavity Oscillations*. Progress in Aerospace Sciences, 44(7):479–502, 2008

[3] JD CROUCH, A. GARBARUK, and D. MAGIDOV - *Predicting the Onset of Flow Unsteadiness Based on Global Instability*. AIAA paper 97-2004, 1997

[4] L.F. EAST - *Aerodynamically Induced Resonance in Rectangular Cavities.* J. Sound Vib., 3:277–287, 1966.
[5] N. FORESTIER, L. JACQUIN, and P. GEFFROY - *The Mixing Layer over a Deep Cavity at High-Subsonic Speed*. Journal of Fluid Mechanics, 475:101–145, 2003
[6] J.S. GIBSON - *Non-Engine Aerodynamic Noise Investigation of a Large Aircraft*. volume 2378. National Aeronautics and Space Administration, 1974
[7] H.H. HELLER and W.M. DOBRZYNSKI - *Sound Radiation from Aircraft Wheel-Well/Landing-Gear Configurations*. J. Aircr, 14(8):768–774, 1977
[8] H.H. HUBBARD - *Aeroacoustics of Flight Vehicles: Theory and Practice*. Volume 1. noise sources. Technical report, DTIC Document, 1991
[9] H. ILLY - *Contrôle de l'écoulement au-dessus d'une cavité en régime transsonique*. PhD thesis, Université de Lyon, 2005.
[10] H. ILLY, L. JACQUIN, and P. GEFFROY - *Observations on the Passive Control of Flow Oscillations over a Cavity in a Transonic Regime by Means of a Spanwise Cylinder*. AIAA paper, 5th AIAA Theoretical Fluid Mechanics Conference, 23-26 June 2008, Seattle, Washington, AIAA 2008-3774, 2008.
[11] C.J. MACK, P.J. SCHMID, and J.L. SESTERHENN - *Global Stability of Swept Flow around a Parabolic Body: Connecting Attachment-Line and Crossflow Modes*. Journal of Fluid Mechanics, 611(1):205–214, 2008
[12] O. MARQUET, D. SIPP, and L. JACQUIN - *Sensitivity Analysis and Passive Control of Cylinder Flow.* Journal of Fluid Mechanics, 615:221–252, 2008
[13] S. MCGRATH and L. SHAW - *Active Control of Shallow Cavity Acoustic Resonance*. AIAA paper, 1996-1949, 1996
[14] P. MELIGA, D. SIPP, and J.M. CHOMAZ - *Effect of Compressibility on the Global Stability of Axisymmetric Wake Flows.* J. Fluid Mech., 660:499–526, 2010
[15] P. PANICKAR and G. RAMAN - *Understanding the Mechanism of Cavity Resonance Suppression using a Cylindrical Rod in Crossflow*. AIAA paper 2008-54, 2008
[16] J.C. ROBINET - *Bifurcations in Shock-Wave/Laminar-Boundary-Layer Interaction: Global Instability Approach*. Journal of Fluid Mechanics, 579(1):85–112, 2007
[17] D. ROCKWELL and E. NAUDASCHER - *Review - Self-Sustaining Oscillations of Flow Past Cavities*. Journal of Fluids Engineering, 100:152, 1978
[18] J.E. Rossiter - *Wind-Tunnel Experiments on the Flow over Rectangular Cavities at Subsonic and Transonic Speeds*. Technical report, Aero. Res. Counc. R. & M., 1964
[19] C.W. ROWLEY and D.R. WILLIAMS - *Dynamics and Control of High-Reynolds-Number Flow over Open Cavities*. Annu. Rev. Fluid Mech., 38:251–276, 2006
[20] M. SAMIMY, M. DEBIASI, E. CARABALLO, A. SERRANI, X. YUAN, J. LITTLE, and JH MYATT - *Feedback Control of Subsonic Cavity Flows using Reduced-order Models.* Journal of Fluid Mechanics, 579:315, 2007.
[21] D. SIPP AND A. LEBEDEV - *Global Stability of Base and Mean Flows: a General Approach and its Applications to Cylinder and Open Cavity Flows*. Journal of Fluid Mechanics, 593:333–358, 2007
[22] M.J. STANEK, G. RAMAN, V. KIBENS, J.A. ROSS, J. ODEDRA, AND J.W. PETO - *Control of Cavity Resonance Through very High Frequency Forcing.* AIAA 2000-1905, 2000
[23] M.J. STANEK, J.A. ROSS, J. ODEDRA, and J. PETO - *High Frequency Acoustic Suppression - the Mystery of the Rod-in-Crossflow Revealed*. In 41st AIAA Aerospace Sciences Meeting & Exhibit, Reno, NV, AIAA 2003-0007, 2003
[24] PJ STRYKOWSKI and KR SREENIVASAN - *On the Formation and Suppression of Vortex'Shedding' at Low Reynolds Numbers*. Journal of Fluid Mechanics, 218:71–107, 1990
[25] C.K.W. TAM and P.J.W. BLOCK - *Tones Induced by Flow over Cavities*. J. Fluid Mech., 89:373–399, 1978
[26] S. YAMOUNI – *Contrôle en boucle ouverte des instationnarités de cavité en régime transsonique*. PhD thesis, Ecole Polytechnique, Paris, 2013
[27] S. YAMOUNI, D. SIPP, AND L. JACQUIN - *Interaction between Feedback Aeroacoustic and Acoustic Resonance Mechanisms in a Cavity Flow: a Global Stability Analysis*. Journal of Fluid Mechanics, 717:134–165, 2013
[28] S. YAMOUNI, C. METTOT, D. SIPP, and L. JACQUIN - *Passive Control of a Transonic Deep Cavity Flow by Means of a Spanwise Cylinder*. In preparation for publication in Journal of Fluid Mechanics, 2013

Acronyms

RANS (Reynolds-Averaged Navier-Stokes)
uRANS (unsteady Reynolds-Averaged Navier-Stokes)
CFD (Computational Fluid Dynamics)

AUTHORS

Sami Yamouni graduated from "Supmeca Paris" in 2009. He joined Onera in the Fundamental/Experimental Aerodynamics Dept for his research internship regarding the control of cavity flow. He obtained his PhD in Fluid Mechanics from the Ecole Polytechnique in 2013. His research interests include Aeroacoustics, Hydrodynamic Stability, Compressible Flows, Aerodynamics and Experimental and Numerical activities.

Clément Mettot graduated from the Ecole Polytechnique and is currently doing his PhD in the Fundamental and Experimental Aerodynamics Department. His work concerns the passive control of turbulent flows, with the development of a numerical method to compute sensitivity gradients for turbulent flows.

Denis Sipp has been a researcher at Onera since 2002. He is the head of the Fluid Mechanics unit in the Fundamental and Experimental Aerodynamics Department. He obtained a PhD degree from the Ecole Polytechnique in 1999 on the stability of vortex pairs. He obtained his Habilitation Degree in 2009 at the Pierre et Marie Curie University in Paris. He has been a Professor (PCC) in the Mechanics Department of the Ecole Polytechnique since 2003.

Laurent Jacquin Research Director, Director of the Fundamental/Experimental Aerodynamics Dept of Onera. Associate Professor in Mechanical Engineering (from 1996 to 2007) and Professor in Fluid Mechanics at the Ecole Polytechnique. Background: Master's Degree in Mechanical Engineering from the University of Marseille. PhD from the University of Marseille in 1983. Research Habilitation Thesis (thèse d'état) from the University of Lyon in 1987. He joined Onera in 1987. His research topics include: Turbulence, Hydrodynamic Stability, Vortex Dynamics, Compressible Flows, Aerodynamics and Experimental Methods.

J. Marty, L. Castillon,
J.-C. Boniface,
(Onera)
S. Burguburu
(Snecma)
A. Godard
(Ecole Centrale de Lyon)

E-mail: julien.marty@onera.fr

Numerical and Experimental Investigations of Flow Control in Axial Compressors

The increase of the thrust-to-weight ratio of modern gas-turbine engines results in higher loads and a reduced number of blades and stages for the compressor. The designer must ensure the acceptable performance of each compressor stage (efficiency and stable operating range) and control the rising risk of blade boundary layer separation. This can be obtained using passive or active control devices which act on the behavior of the tip leakage flows or the endwall corner stall when the operating point gets closer to the stall or surge limit (compressor). This study focuses on casing treatments, with axisymmetrical and non-axisymmetrical slots, on injection or recirculating grooves, which are efficient approaches to extend the stable operating range, especially by increasing the stall margin of a compressor system while the efficiency penalty must remain as small as possible. The hub corner stall is controlled by aspirated compressor and vortex generators.

Introduction

The current trend in gas-turbine engine design is to increase the thrust-to-weight ratio. This leads to a compressor design with higher aerodynamic loads and a reduced number of blades and stages. The pressure rise per stage and the efficiency must be increased. Nevertheless, the increased blade loading tends to decrease the stall margin and therefore the stable operating range of compressors. Many passive or active control devices are used to increase the efficiency and/or the stable operating range of the compression system without any penalty on other performance parameters.

The aerodynamic stability of a compressor is limited by the behavior of the tip leakage flows or the hub corner stall when the operating point gets closer to the stall or surge limit. One approach to increase the compressor stability consists in the use of casing treatments, such as circumferential, non-axisymmetrical or axial skewed grooves to control the tip flow. Some authors focus on the extension of the operating range using casing treatments delaying stall limit ([13][16][43]). Nevertheless, the casing treatment can induce additional losses at peak efficiency condition. According to earlier research, the stall margin increase varies between 6 and 10% and the variation of efficiency is about $\pm 0.5\%$ compared to a smooth casing configuration. The efficiency of the casing treatment depends on the slot location. Rabe and Hah [40] show that grooves close to the trailing edge seemed ineffective. The influence of the groove position was also studied by Perrot et al. [39]. The configuration consists of five circumferential grooves. They reported that for this configuration only the first groove has a beneficial effect at near stall operating conditions and increases stall margin, while the second one improves the pressure ratio and efficiency. This influence of the groove position was also observed by Legras et al. [29].

Another approach to control the flow near the rotor blade tip is based on the injection of high momentum fluid and/or bleed of low momentum fluid. The combination of injection and bleed leads to recirculating flow: the compressor static pressure rise induces a recirculation of high pressure flow from the rear to the front of a rotor. This can be achieved by either a single bridge, which creates a natural flow from TE to LE, or experimentally by two separate devices: one for the suction and another for the blowing. Hathaway [23] investigates the influence of the injection, bleed and recirculation applications on the operating range. The latter can be increased up to 60% with bleed near the trailing edge, 38% with fluid injection upstream of the lower momentum region and 64% with recirculating flow where the massflow rate reaches 1.9% of the choke massflow rate. Suder et al. [48] found that the tip injection increases stability. The stalling flow coefficient can be reduced by 6% with an injected massflow which is equal to 2% of the annulus flow. The extension of the stable operating range was also investigated by Weigl and Spakovsky ([44][45][50]).

The hub or casing corner stall is also a source of important losses and can be the cause of stall or surge. The injection and bleed techniques can be used to control this kind of flow. Several authors found the beneficial effect of the boundary layer suction at the endwall and/or at the blade wall ([12][17][37][41]). Another approach is based on the vortex generators (VG). Their induced vortices mix high and low momentum flow near the wall, allowing the boundary layer to over-

come a strong adverse pressure gradient. Chima [11], Hergt et al. [25], Ortmanns et al. [36] applied VG to control the secondary flows, especially the hub or casing corner stall. In aircraft applications, they are usually employed to delay stall.

This paper does not deal with the technology involved in the control device but focuses only on the methodology to simulate the aerodynamic effect of the control device. It is also important to keep in mind that the purpose of this paper is not to give a deep and exhaustive physical analysis of turbomachinery flows subjected to control methods, nor to give advice concerning the best way to perform an efficient flow control. That would be a difficult challenge far beyond the scope of this paper. Our goal here is more to give a synthetic overview of handy numerical methods developed at Onera, which can be used by aero-engine designers in an industrial context in order to investigate control techniques and optimize control devices. Ongoing numerical activities carried out at the Applied Aerodynamics Department of Onera for passive or active flow control devices applied in turbomachinery are presented below. The methodology developed for flow control within a CFD analysis is described first. Investigations on flow control, especially on the compressor side, are reviewed: (i) tip leakage flow control considering axisymmetrical and non-axisymmetrical casing treatments, (ii) tip flow control with the help of suction, blowing or recirculating grooves, (iii) secondary flow and boundary layer flow control by using vortex generators or aspiration devices.

Methodology

The elsA solver, developed at Onera since 1997, is a multi-application aerodynamic code based on a cell-centered finite-volume discretization in structured meshes. From the solution of the compressible, three-dimensional Reynolds-averaged Navier-Stokes equations (RANS), the elsA solver has been developed to handle a wide range of aerospace configurations such as aircrafts, space launchers, missiles, helicopters and turbomachines ([7][8]). A large variety of turbulence models, ranging from algebraic to non-Boussinesq modeling, have been implemented.

The centered space-discretization scheme of Jameson or the upwind Roe-MUSCL solver are some of the classical second-order space-discretization schemes used for turbomachinery applications. A second-order accurate Roe scheme is used for the transport equations of turbulence models. Several time-integration schemes can be considered to perform steady and unsteady computations. Explicit or implicit schemes, such as a pseudo-time approach (Dual Time Stepping) or the Gear Method, are available. Time integration can be solved either by an implicit residual smoothing phase with a 4-step Runge-Kutta technique, or by an implicit LU scalar relaxation phase associated with a backward Euler scheme. In steady flow assumption, standard convergence acceleration techniques, such as local time stepping and multi-grid methods improve the convergence rate, thus reducing the global CPU time.

Suitable boundary conditions for turbomachinery configurations have also been implemented, in order to compute steady flows: coincident and non-coincident matching conditions have been developed for the treatment of the periodicity condition and a steady multi-stage condition using pitch-averaging for the treatment of the rotor-stator interface. Physical boundary conditions include different types of inlet, outlet and wall conditions.

For structured-grid flow solvers, a major issue is the difficulty in generating meshes around complex configurations. One way to alleviate this problem is to use the Chimera technique ([3][4]), which has been widely developed in the elsA software ([5][26]) and applied to turbomachinery configurations [9]. This overset grid approach operates as a matching condition between blocks that overlap and can be generated independently around each body. Any grid can overlap with an arbitrary number of other grids, which may overlap themselves. The RANS equations are solved on each grid system and transfers are then performed between overlapping grids by interpolation of the conservative and turbulent variables, first at overlapping boundaries and then around blanked mesh-cells lying inside solid bodies. A cell search procedure is performed using an alternating digital tree research algorithm (ADT) [6] which determines the donor cell and the interpolation coefficient for a given target cell. Multiply-defined walls are treated using the Schwarz algorithm [42] for interpolation coefficient calculations. Several hole-cutting techniques have been developed, including the Object X-Ray technique, originally developed by Meakin [31].

A major advantage of the Chimera method is that it significantly simplifies the process of mesh generation by using overlapping grids. Different parts of the grid can therefore be generated independently: for example, the blade channel can be constructed on one side with a family of coincident structured blocks, while and a second family of structured coincident domains can be generated on another side (eventually with a different grid generator) to mesh a technological component or a control device. This approach is also very well suited for parametric studies on the characteristics of the technological components or the control actuator, since there is no need the re-mesh the entire configuration. For example, while investigating the impact of the size or of the position of a technological effect on the flow field, it is only necessary to modify the grids associated with this geometrical component.

Tip Blade Flow Control

Axisymmetric Casing Treatment

The casing treatment consists of slots or grooves within the rotor casing and is used to extend the surge margin of the compressor ([22] [24]). Two sets of casing treatment are studied. The first one, called "HCT", is based on the work of Müller et al. [34] and the second one "SCT" is based on the work of Legras et al. [27]. The location of the first slot, the height, width and spacing of the slots are normalized by the axial chord C_{ax} at the blade tip. The HCT and SCT normalized values are summed up in table 1. The main discrepancy between the two casing treatments concerns the slot height h and the location of the leading edge of the first slot X_{LE}. The height, width and spacing of the slots, the leading edge of the first slot and the slot number are schematized in figure 1.

The considered test-case is the first rotor of the 3.5-stage research compressor CREATE. This compressor is representative of median or rear stages of a modern, highly loaded multi-stage compressor. For the CREATE facility, the number of blades of each rotor and stator is a multiple of 16. The rotational speed is 11500 rpm and the design massflow is 12.7 kg/s. Experimental data have been obtained through detailed instrumentation of the compressor, using both pneumatic measurements and laser Doppler anemometry techniques on several measurement planes. The measurements are performed in the circu-

Normalized values	Location of the slot leading edge	Width	Height	Spacing	Slot number
HCT	LE+15.25%C_{ax}	0.0976C_{ax}	0.2927C_{ax}	0.04878C_{ax}	6
SCT	LE-5%C_{ax}	0.109C_{ax}	0.0763C_{ax}	0.0545C_{ax}	6

Table 1: Casing treatment characteristics, extracted from [34] and [27]. LE and C_{ax} mean respectively rotor leading edge and rotor axial chord length

mferential direction at different constant radius locations downstream of each row. Since the spatial periodicity of the compressor is 22.5°, the azimuth measurements allow aerodynamic phenomena interacting over a complete spatial period to be represented. A detailed description of the compressor is provided by Touyeras and Villain [49] and by Arnaud et al. ([1][2]).

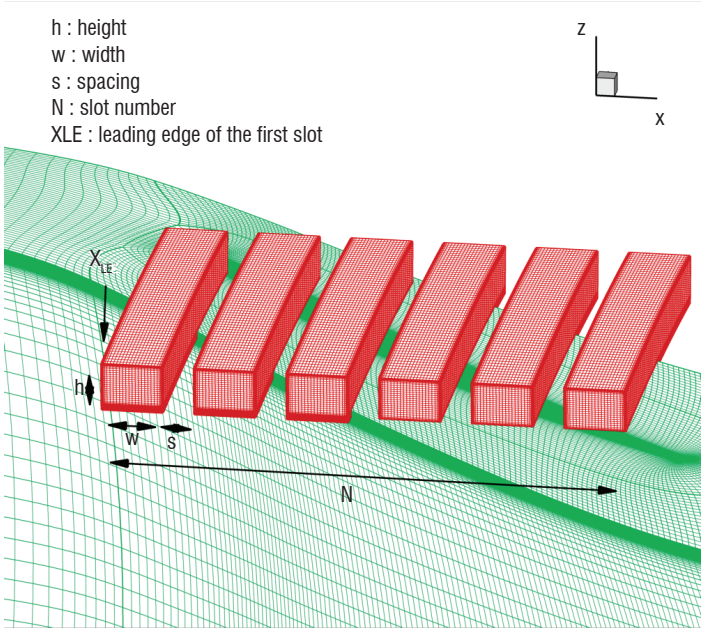

Figure 1 - Schematic view of casing treatment

Since the casing treatment is axisymmetric and the numerical domain is an isolated row, steady simulations are performed using the Chimera approach. A fully turbulent flow assumption is made and the Spalart-Allmaras turbulence model has been considered [46]. The computational domain consists of one rotor blade channel and six casing treatment slots. The mesh is composed of $5.5.10^6$ points. The values of y^+ at the blade wall are lower than 1 in the entire domain.

The radial velocity field is depicted in figure 2 at three given azimuths and one selected radius. The operating point is the nominal point for the three simulations. The tip leakage vortex can be identified by the alternation of negative (blue) and positive (red) radial velocity on the constant radius plane. The casing treatments strongly modify the flow and vortex development in the vicinity of the blade tip. Due to the grooves, the expansion of the tip leakage vortex is limited in the direction perpendicular to the blade chord. For both simulations with slots, the impingement point of the tip leakage vortex on the adjacent blade is located downstream of the reference point. This modification of the tip leakage vortex trajectory is one reason for the stall margin increase. It should be noticed that all casing treatments induce a slight reduction of the isentropic efficiency. The main discrepancy between the two slot configurations concerns the flow topology within the casing treatments. A large part of the HCT is useless as the radial velocity is close to zero and the two downstream grooves have a small influence as the casing treatment acts significantly in the vicinity of the tip leakage vortex appearance. Thus, the position and height of the casing treatments are important parameters for the slot design. As a general rule, the design of the casing treatment depends strongly on the configuration and should be designed simultaneously with the rotor blade tip.

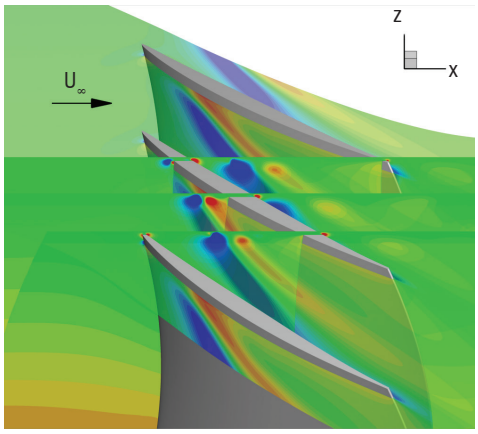

(a) Without casing treatment

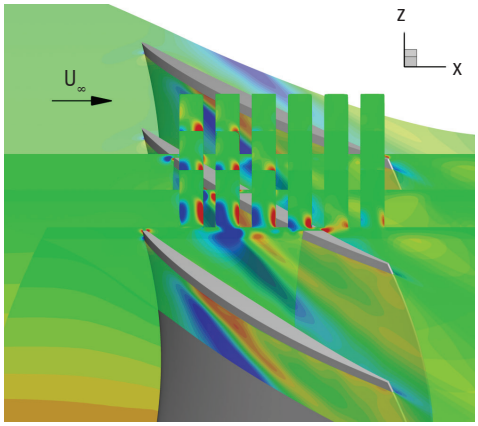

(b) With casing treatment (HCT)

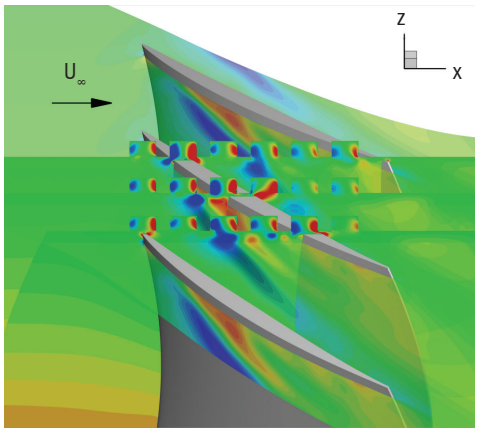

(c) With casing treatment (SCT)

Figure 2 - Radial velocity field. Negative and positive values are respectively in blue and red

Non-axisymmetric Casing Treatment

Many experimental and numerical works achieved in the past have shown the interest of using casing treatments on compressor configurations, in order to extend stall margins. Investigations on the impact of non-circumferential casing treatments have been performed at Onera ([10][28]). An unsteady Chimera approach combined with a phase-lag technique has been developed in the elsA code to simulate non-circumferential casing treatments and the unsteady interactions between rotors and slots. The configuration is the experimental transonic rotor tested at the School of Jet Propulsion, Beijing University of Aeronautics and Astronautics (BUAA), composed of 17 rotor blades with 9 slots per blade passage ([30][35]) as represented in figure 3. A view of the grid is presented in figure 4 (left), the two families of blocks (channel and casing treatment) overlap in the meridian plane in order to ensure continuity of the flow field at their interface. The computational domain, composed of one rotor blade channel and one casing treatment slot, is meshed with a 13 block structured grid including 3.10^6 points. The values of y^+ at the blade wall range from 1 to 2.

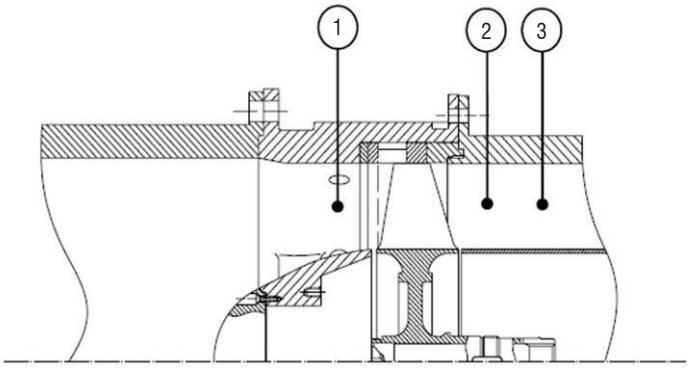

1 - Inlet plane: one total pressure comb
2 - Outlet plane I: one fast response pressure probe, monitoring the onset of rotating stall
3 - Outlet plane II: two total pressure combs

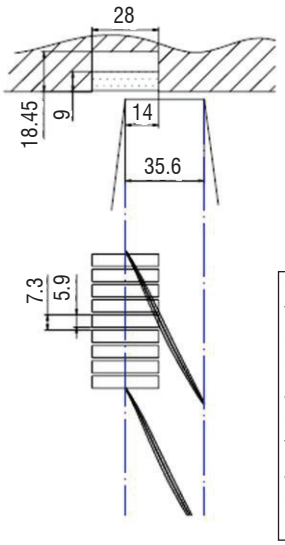

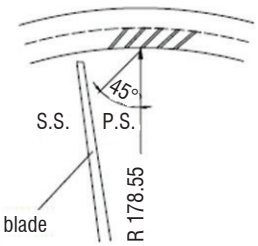

Blade number	17
Tip diameter	355.8 mm
Design speed	22 000 rpm
Hub-to-tip ratio	0.565
Aspect ratio	0.956
Mass flow at design point	13.4 kg/sec
Total pressure ratio at design point	1.6 (stage)
Adiabatic efficiency at design point	0.88 (stage)
Relative Mach number of inflow at rotor up	1.404
Nominal tip clearence at 100% speed	0.25 mm

Figure 3 - Cross-section view of the test section (top) and sketch of the slot type casing treatment (Lin et al. [30])

The Chimera method developed enables the capturing of the unsteady flow migrations between the slots and the rotor channel, as can be seen in figure 4 (right), which represents a snapshot of the radial velocity distribution near the casing. Two zones can be distinguished: the zones of positive radial velocity in the downstream part of the slot, corresponding to the flow entering into the casing treatment, and the zones of negative radial velocity, where the flow is reinjected into the rotor channel.

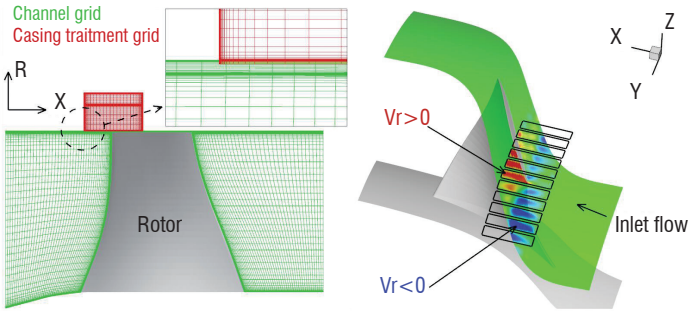

Figure 4 - Left: BUAA overset grids. Right: snapshot of the radial velocity distribution near the casing

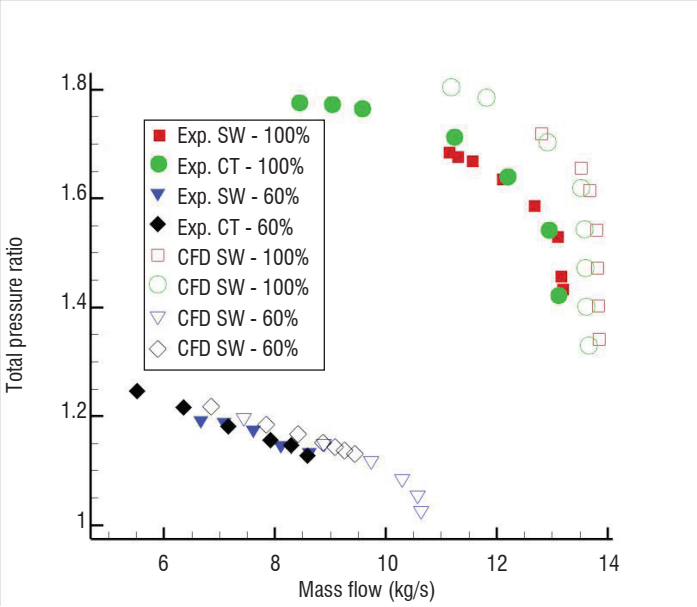

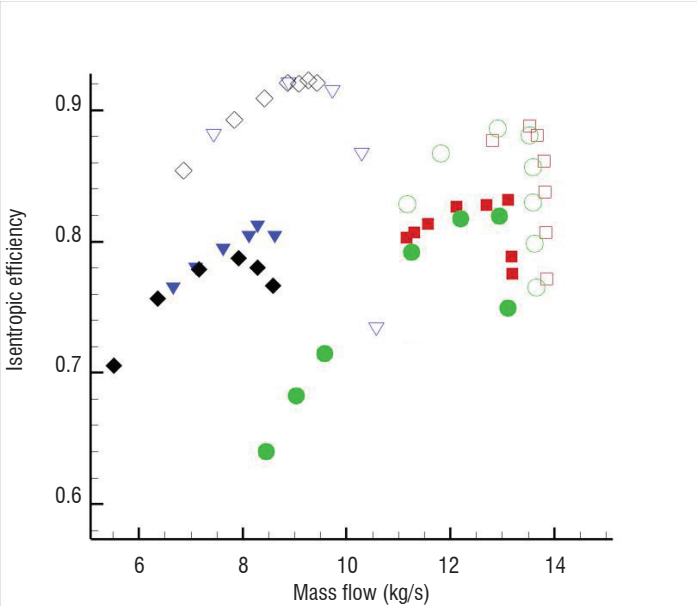

Figure 5 - Experimental and computed compressor maps

The experimental and computed compressor maps are presented in figure 5; the pressure ratio and the isentropic efficiency are plotted as a function of the massflow. Smooth wall calculations (SW), performed by removing the computational grid of the slots are compared to

Configuration	CB (Casing Blowing)	RF1(Recirculating flow configuration 1)	RF2(Recirculating flow configuration 2)
LE of the blowing groove	LE – 9.5%C_{ax}	LE + 30 %C_{ax}	LE – 9.5%C_{ax}
Width of the blowing groove	3.8%C_{ax}	10 %C_{ax}	3.8%C_{ax}
Blowing massflow	1% nominal massflow	1.9% choke massflow	1% nominal massflow
Angle between the blowing groove axis and the rotation axis 'x', in (x,R) plane	14°	30°	15°
LE of the suction groove	–	TE + 5 %C_{ax}	TE + 5 %C_{ax}
Width of the suction groove	–	10 %C_{ax}	10 %C_{ax}
Suction massflow	–	1.9% choke massflow	1% nominal massflow
Angle between the suction groove axis and the rotation axis 'x', in (x,R) plane	–	-30°	-30°

Table 2 - Characteristics of active flow control devices. LE and C_{ax} mean respectively rotor leading edge and rotor axial chord length

casing treatment (CT) configurations, for two rotation speeds (60% and 100% of the rotor design wheel speed). Both experiments and CFD analysis show that the slots enable to increase the stall margin of the rotor, even if the extension improvement is underestimated in CFD. At nominal rotation speed, the casing treatment also induces a slight penalty on the peak efficiency and on the chocking massflow rate. The underestimation of the stall margin increase can be explained by the fact that the method is based on a phase-lag assumption, which assumes that the flow is periodic, this hypothesis being far from true near stall. Nevertheless, the key point is that a significant impact of the casing treatment is observed in the calculation. Results obtained with the experimental BUAA configuration show that the method correctly reproduces the effect of the stall margin increase induced by the casing treatments, even if the stall margin increase is underestimated in the CFD analysis.

Tip Blade Suction and Blowing, Recirculating flow

Casing treatments are passive control devices, since no external energy source is required. Active control devices have been also investigated, as supplying momentum in the main flow path using an axisymmetric groove. The injected massflow can be provided by an aspiration slot located downstream. In this case, a recirculating flow occurs (figure 6). The current study focuses on three configurations. The main characteristics of these configurations are reported in table 2. The configuration RF1 is based on the work of Hathaway [23].

The experimental facility is again the first rotor of the research compressor CREATE, which has been described in the previous section. The blowing and suction grooves are included in the simulation using the Chimera method. The computational domain consists of one rotor blade channel and the active control grooves. The mesh density is 4.5.106 points for the CB configuration and 4.7.106 points for both recirculating flow configurations. The values of y+ at the blade wall are lower than 1 in the entire domain.

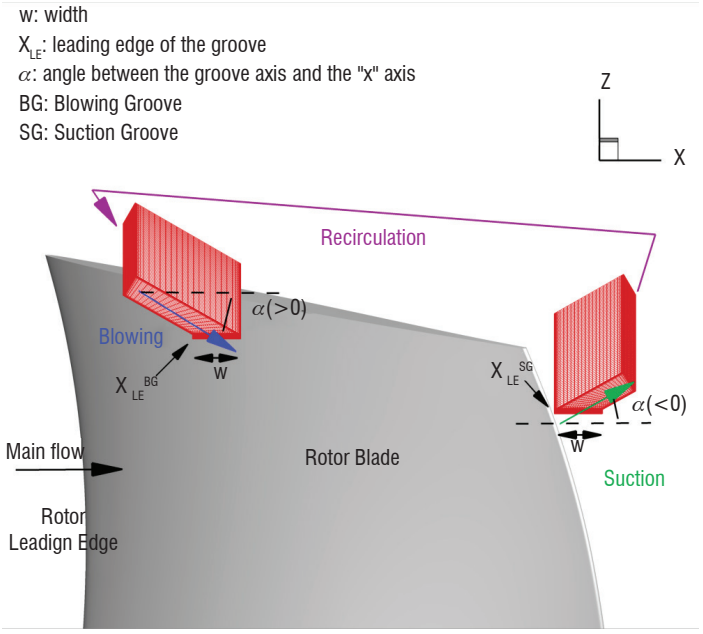

Figure 6 - Schematic set up of the recirculation device (RF1 configuration)

Figure 7 shows the entropy distribution at several axial planes in the main flow path at the nominal operating point. The modification of the topology of the tip leakage vortex is observed. As for the casing treatments, these devices limit the expansion of the tip leakage vortex in the direction perpendicular to the blade chord. Moreover, the entropy is a rational measure of loss in an adiabatic machine [15]. The entropy field shows the significant reduction of the high loss levels with the active control device CB. The losses induced by the tip leakage vortex are lower and the radial and azimuthal extension of the high loss area is smaller. This reduction is increased with the RF2 case. The casing boundary layer thickness and the losses are smaller than the CB ones. The RF2 seems to be the best active control device of this study. The configuration RF1 decreases the casing boundary-layer thickness significantly, but the loss extension is still large, especially in the radial direction.

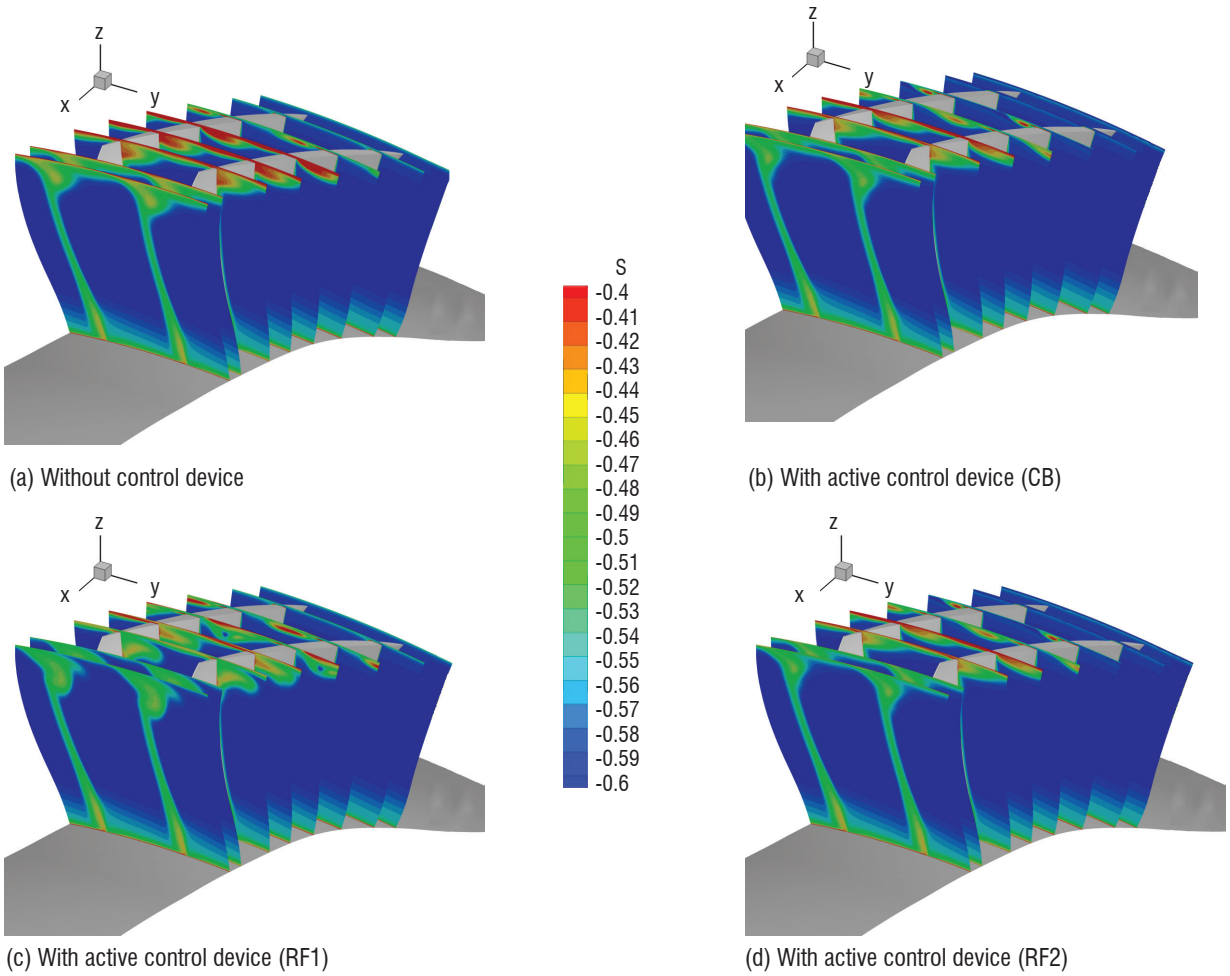

Figure 7 - Entropy field in the main flow path. The blowing and suction grooves are hidden

Corner and Boundary Layer Flow Control

Aspirated compressor

Experimental investigation

Among flow control techniques investigated to overcome boundary layer separation in highly loaded compressors, Merchant et al. ([32] [33]) and Dang et al. [14] showed that aspiration by boundary layer suction is very promising. In particular, their work has shown that to fully take advantage of aspiration, this flow control technique must be incorporated into the compressor blade design process as early as possible.

Consequently, a 2D direct design method for subsonic aspirated compressor blades was developed at Onera [18]. It provides a simple, fast and reliable means to include aspiration in compressor blade design. It combines a passive separation control with curvature and diffusion, with an active flow control by aspiration ([18][19][20]). One advantage of this approach is to set the aspiration massflow rate necessary to re-attach the flow, quasi-insensitive to inlet Mach number. Continuing the previous developments of this method carried out on a 2D curved diffuser [19] and a 2D subsonic aspirated compressor profile [20], its validation on a test cascade is presented in the following sections [21]. It is intended to show the viability of the aspiration strategy and design criteria as well as the numerical tools and methods employed during the development of this method.

The aspirated cascade blade shown in figure 8-b is built by extrusion of the aspirated blade profile in figure 8-a. The cascade is composed of twelve aspirated blades (marked 1 in figure 8) airtight cantilevered in glass endwalls. With the aid of an auxiliary fan (marked 5 in figure 8), the boundary layer is aspirated by the slot and driven through the blade cavity, then extracted outside of the cascade at each end of the blade (small blue arrows in figure 8-b). All of the blades are connected to aspiration plenums (marked 2 in figure 8) on each side of the cascade. These plenums collect the aspirated air and ensure the same level of aspiration for each blade. Finally, the aspirated air is evacuated from the plenums with pipes towards the aspiration fan. A CAD model of the experiment is presented in figure 8, as well as an enlarged picture of the cascade test section in the *Laboratoire de Mécanique des Fluides et d'Acoustique* at *Ecole Centrale de Lyon* (LMFA).

During the experimental phase of the validation process, the main objective is to determine the performance of the aspirated cascade at mid-span, where the flow surrounding this location approaches 2D conditions. The other objective is to assess the potential of the design method in severe off-design conditions. Thus, the measurements are performed for an inlet flow angle equal to 65°, i.e., at the off-design condition corresponding to +5° of incidence compared to design inlet flow angle of 60°. Particle Image Velocimetry (PIV) is used to measure the velocity in the central blade passage. The PIV set-up is shown in figure 8-d.

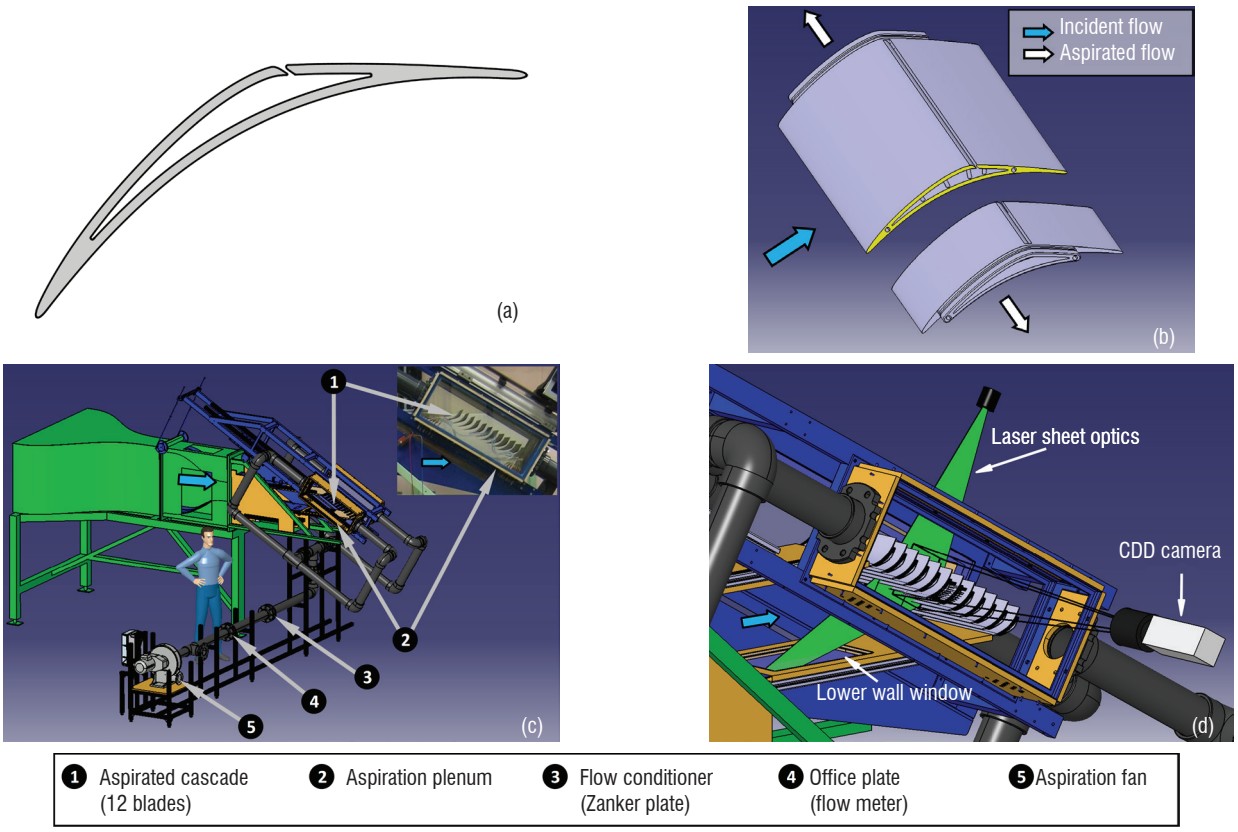

Figure 8 - Aspirated cascade (a) Blade profile (b) Cascade blade (c) Experimental setup (d) PIV setup

The velocity fields, without and with aspiration, measured by PIV in the central blade passage at mid-span are presented in figure 9. They validate capabilities of flow control by aspiration and the relevance of the design method. These results are also remarkable in the sense that they constitute, to the knowledge of the authors, the first PIV measurements of the complete velocity field inside an aspirated cascade. The separated flow without aspiration in figure 9-a, which is induced by a strong variation in blade curvature and diffusion, is reattached with aspiration in figure 9-b. An acceleration of the flow due to aspiration is clearly visible just upstream of the slot in figure 9-b. With the help of the velocity fields in figure 9 in addition to upstream and downstream measurements, the characteristics of the aspirated cascade are calculated. They are summarized in table 3.

M_0	M_1	α_0	α_1	C_q	ω_1	DF
0.123	0.0833	64.7°	2.7°	3.3%	8.62%	0.50

Table 3 - Experimental characteristics of the aspirated cascade

Table 3 shows that the flow deflection is approximately achieved by the cascade ($\Delta\alpha=62°$), but the aerodynamic loading represented by the Lieblin diffusion factor DF is approximately 60% lower than expected for this flow deflection. This originates from a reduction of the flow diffusion, mainly caused by the presence of massive corner separation invading approximately two thirds of the blade span in total, at the trailing edge. With aspiration, the total pressure loss coefficient ω_1 related to the blade passage reaches 8.62%. This high value comes from the velocity gradient in the pitchwise direction of cascade (visible in figure 9), passed on the total pressure profile downstream of the cascade. Without aspiration, the total pressure loss coefficient reaches 12.58%, which underlines the capacity of aspiration to reduce total pressure losses occurring in the cascade. The velocity field in figure 9-b is obtained with an aspirated mass-flow rate of 3.3%. This value may not be suitable for practical turbomachinery applications since the necessary pressure difference to naturally aspirate this mass flow rate may not be available. However, the aspirated blade profile presented in this paper has not been optimized regarding the aspirated mass flow rate at high incidence angles. Therefore, this value could be improved with blade profile geometry modifications.

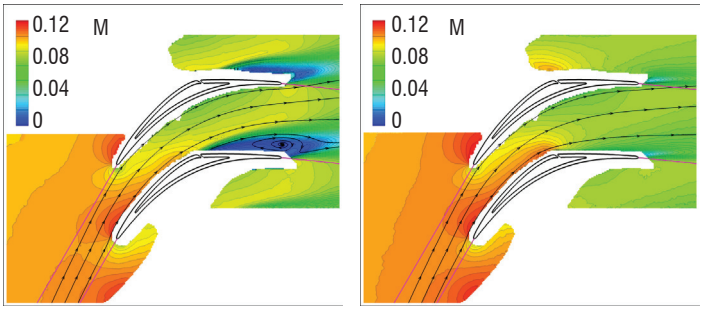

(a) Aspiration off (b) Aspiration On

Figure 9 - Experimental Mach number contours at mid-span

Numerical investigation

The numerical phase of the validation process aims at reproducing the off-design operation of the experimental aspirated cascade. Due to the significant 3D phenomena observed in the experiment, 3D numerical computations are performed. The numerical simulations of the experimental aspirated cascade used structured grids as shown in figure 10. For an improved aspiration management, the Chimera technique is used to model the technological effect of the shape of the slot and its influence on the main flow.

The structured meshes contain approximately $3.25.10^6$ nodes in total with an average y^+ value at the walls equal to 1. Fully-turbulent computations are performed with a Differential Reynolds-Stress Model of turbulence (DRSM). This kind of model is adapted to this case since it takes explicitly into account, without additional modeling, the strong curvature that the streamlines will undergo due to the geometry of the wall, the aspiration and the massive corner separations which are likely to appear. The model used here is the low-Reynolds formulation developed by Speziale et al. [47].

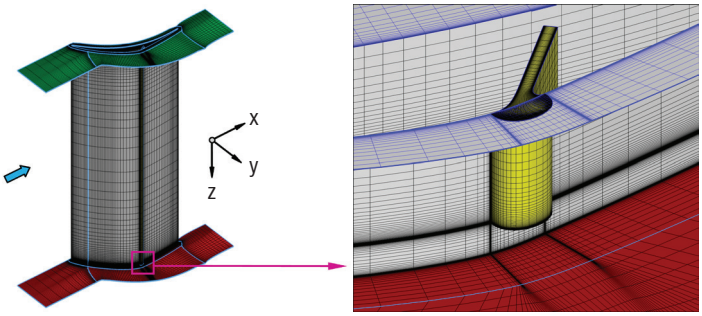

(a) General view (b) Close-up view near an endwall (truncated)

Figure 10 - Computational grids for the simulation of the aspirated cascade experiment.

The comparison between the experimental and numerical results allows assessing the capabilities of CFD in the presence of aspiration and will give further insight on factors influencing the flow behavior with aspiration like the aspiration distribution along the blade span. Due to technical reasons, this feature was not measured during the experiment. Thus, two different aspiration distributions, one uniform (named "3DU") and one non-uniform (named "3DNU") along the spanwise direction are applied and tested in the numerical simulations. They both correspond to an aspiration massflow rate of 3.3%. The non-uniform aspiration distribution profile stems from experimental results obtained on a simplified version of the aspirated blade [18].

The velocity field in the mid-span plane, obtained without aspiration, is presented in figure 11-a. Given the limitations of the RANS approach in simulating separated flow, the general shape and axial extent of the separation is well rendered. However, differences in shape and location of the separation indicate 3D RANS simulations remain qualitative in presence of massive separation.

The 3D RANS simulations perform well with aspiration, as shown in figure 11-b and figure 11-c. Both aspiration configurations "3DNU" and "3DU" are able to reproduce the characteristic features of aspiration described above, namely the flow acceleration upstream of the aspiration slot and the sudden diffusion in the region of the slot. The best agreement with the experimental velocity field is clearly obtained with a uniform aspiration distribution along the blade span. The difference with the non-uniform aspiration distribution is particularly visible in the velocity level upstream of the slot.

The performance of the cascade is summarized in table 4 for both aspirated configurations. In this case, the diffusion factor values at mid-span disclose the difference of the diffusion processes due to the aspiration distribution along the blade span, between the "3DNU" and "3DU" configurations. The higher level of diffusion in the "3DNU" configuration, results in a higher level of the loss coefficient ω_1. However, the computed values are smaller than the experimental ones. The different intensity of the velocity gradient along the pitchwise direction, in the trailing edge region explains such a disparity. Without aspiration, the total pressure loss coefficient calculated from numerical total pressure outlet profiles is equal to 11.19%. The analysis of the previous results shows that the aspiration distribution is also a key aerodynamic feature to take into account for successful design of highly-loaded 3D subsonic aspirated blades.

	M_0	M_1	α_0	α_1	C_q	ω_1	DF
3DNU	0.123	0.0670	64.7°	4.0°	3.3%	7.69%	0.63
3DU	0.123	0.0785	64.7°	3.5°	3.3%	7.43%	0.54

Table 4 - Numerical characteristics of the aspirated cascade, with 3DNU and 3DU aspiration distribution

Vortex Generators

Secondary flow effects like endwall cross-flow or corner separation are responsible for a large part of total pressure losses in a compressor stage. An extensive numerical study of flow control by means of vortex generators applied to the second stage of the CREATE compressor was performed in order to decrease the separation and reduce the losses [38]. The objective of these flow control devices is to produce strong vortices, which enhance mixing between main flow and the decelerated boundary layer at side wall. Different vortex generator geometries and arrangements have been considered on several positions in the compressor flowpath, both at the surface of side walls and on the blades.

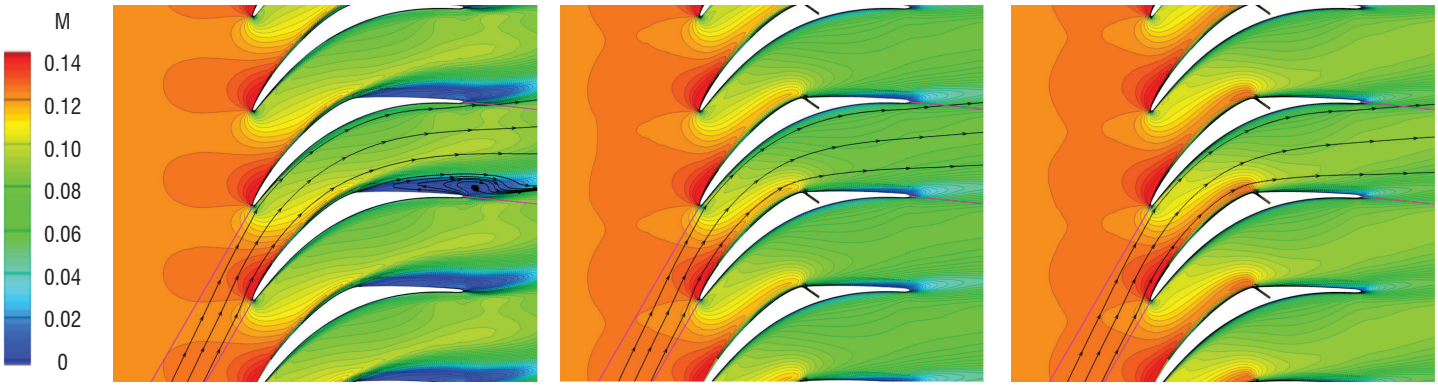

(a) Aspiration off (b) Aspiration on with 3DNU aspiration distribution (c) Aspiration on with 3DU aspiration distribution

Figure 11 - Numerical Mach number contours at mid-span

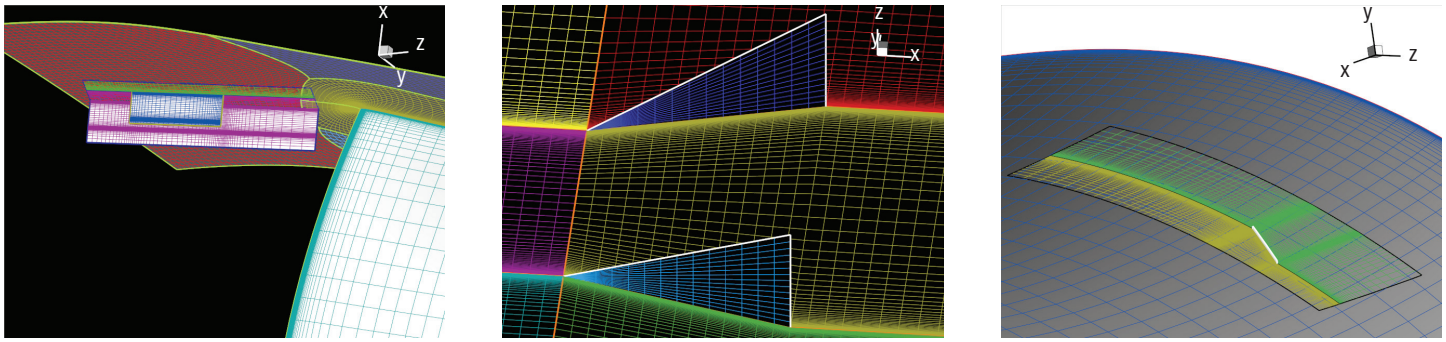

Figure 12 - Details of the overset vortex-generators mesh ahead of the rotor passage (left), mesh for a pair of counter-rotating triangular vortex-generators (center) and for a single rectangular vortex-generator on the blade surface (right)

One critical issue is the way of representing the vortex generators in the Navier-Stokes calculations. Such thought was also made by Chima [11] who developed a body force model to simulate the effects of vortex generators without requiring complicated grids. In the present work, CFD investigations were carried out without using an external body force model but rather by discretizing explicitly the walls of the vortex generator in the CFD grid within the Chimera method.

All computations have been performed under fully turbulent flow assumption, using the k-ε turbulence model. The generation of the VG grids is achieved independently of the surrounding grid for the smooth configuration. A dedicated grid generator has been developed for straight zero-thickness vortex generators with rectangular or triangular planforms. The grid generator enables the automatic discretization of single or several arrangements of vortex, at any position required on the side walls (hub/casing) or on the blade surface (rotor/stator). For each vortex generator, the effects of shape, size, incidence and position as well as mesh extension/refinement parameters are given as input data for the grid generator. The accuracy of the Chimera method then only depends on the mesh definition for the flowpath in which the VG grids are immersed, and its ability to ensure a proper and accurate overlap. A typical representation of the composite mesh for a configuration with one vortex generator per stator passage ahead of a stator vane is shown in figure 12 left.

The vortex generators were sized according to the local boundary layer thickness and blade dimensions. Beside geometrical considerations, the relative position between the vortex generators and the blade and above all the angle of attack relative to the local velocity field are of major importance for the flow control. figure 12 center and right illustrates grids generated for other possible vortex-generators configurations in the framework of the Chimera method. Other possible vortex-generators geometries have been considered within both numerical and experimental investigations ([25][36]).

Both steady and unsteady configurations have been investigated, basically considering fixed rows of vortex generators at the casing ahead of the stator (steady) or ahead the compressor stage (unsteady). Rays of vortex generators distributed radially on the suction side of the stator according to Chima [11] have also been applied for the reduction of the corner stall. Different operating points have been considered. In the two following figures, we show a typical result for an arrangement with 3 VG per blade passage located at the casing ahead of a stator operating at design point. The streamline flow patterns are represented on the stator suction side in the boundary-layer, for the uncontrolled baseline configuration (figure 13 left) and the controlled configuration (figure 13 right). For the baseline configuration, secondary flows in the stator vane passage produce the classical S-shaped flow patterns due to the corner separation: the flowfield entering the blade passage on the suction side is responsible for a cross-passage secondary-flow. For the controlled configuration, the three vortex generators were designed to produce strong counter-rotating vortices relative to the flow direction of the cross passage flow. The dramatic improvement in the flow pattern indicates a large effect on the stator vane flowfield, rising up to nearly half of the blade span at the end of the passage. Actually the secondary flow migration is blocked by the cumulated effects of counter-rotating vortices and the losses are reduced from the mid-height of the blade up to near-wall region. However, in the near-wall region, losses are increased for the controlled case similarly to what has been found and described in [36]. At off-design conditions near stall, a strong flow overturning especially coming from the tip leakage vortex of the previous rotor is responsible for a strong shear-flow in the casing boundary layer. The local velocity flowfield then becomes aligned with the straight vortex generators and vortices are no longer produced. It is anticipated that VG with thickness and camber may be more efficient near stall.

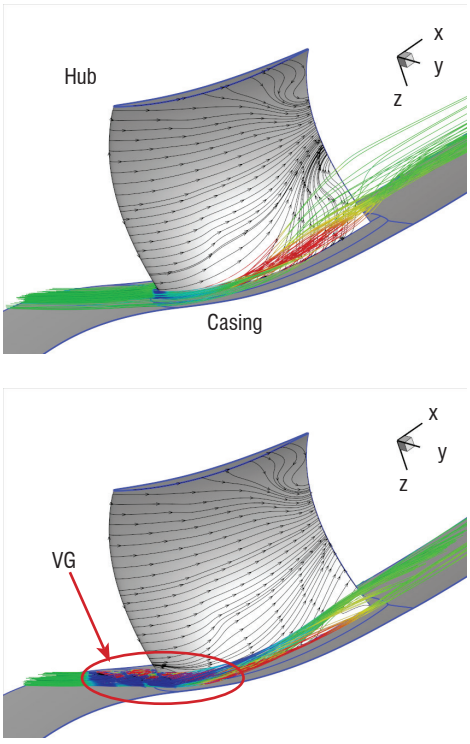

Figure 13 - Corner stall on a stator casing for the baseline stator configuration (left) and reduction of the corner stall for the controlled stator configuration (right)

These preliminary numerical results have shown the ability of vortex generators to reduce secondary flows produced by corner stall in a stator passage at design point. In the vortex-generator design process, it has also been shown that a compromise must be reached between the vortex strength considered to reduce secondary flow phenomena and additional losses associated with the vortex generators and their induced vortex flows.

Conclusion

This overview of a CFD framework for flow control analysis in turbomachinery applications shows that a wide range of control devices can be modeled and used to improve the efficiency and the operating range of a gas-turbine. The axisymmetrical and non-axisymmetrical slots, injection or recirculating grooves are efficient approaches to extend the stable operating range, especially by increasing the stall margin of a compressor system. The aspirated compressor and vortex generators are also efficient approaches to control the hub corner stall.

The different passive and active control devices are applied to many compressors (CREATE, BUAA, etc.). The integration of several control devices into a single application will be investigated in a future study.

The effectiveness of the control device depends strongly on the smooth configuration. A control device developed on a specific configuration is not directly applicable to another case. A way to overcome this problem is to include the control device design in the global process or within an optimization loop, which will be a further step for improving the design and the effectiveness of control devices for internal flows ■

Acknowledgements

The authors wish to thank Snecma (SAFRAN) for its permission to publish this paper.

References

[1] D. ARNAUD, X. OTTAVY, A. VOUILLARMET - *Experimental Investigation of the Rotor-Stator Interactions, within a High Speed, Multistage, Axial Compressor. Part 1 - Experimental Facilities and Results*. ASME Turbo Expo 2004, June 14-17, Vienne, Austria, ASME Paper GT2004-53764, 2004.
[2] D. ARNAUD, X. OTTAVY, A. VOUILLARMET - *Experimental Investigation of the Rotor-Stator Interactions, within a High Speed, Multistage, Axial Compressor. Part 2 - Modal Analysis of the Interactions*. ASME Turbo Expo 2004, June 14-17, Vienne, Austria, ASME Paper GT2004-53778, 2004.
[3] J.A. BENEK, J.L. STEGER, F.C. DOUGHERTY - *A Flexible Grid Embedding Technique with Application to the Euler Equations.* AIAA Paper 83-1944, January 1983.
[4] J.A. BENEK, J.L. STEGER, F.C. DOUGHERTY - *A Chimera Grid Scheme.* ASME mini-symposium on advances in grid generation, Houston, 1993.
[5] C. BENOIT, G. JEANFAIVRE, E. CANONNE - *Synthesis of Onera Chimera Method Developed in the Frame of CHANCE Program.* 31st European Rotorcraft Forum, Florence, 2005.
[6] J. BONET, J. PERAIRE - *An Alternating Digital Tree (ADT) Algorithm for 3D Geometric searching and intersection Problems*. International Journal for Numerical Methods in Engineering, Vol. 31, pp-1-17, 1991.
[7] L. CAMBIER, M. GAZAIX - *elsA: an Efficient Object-Oriented Solution to CFD Complexity.* 40th AIAA Aerospace Science Meeting & Exhibit, Reno, USA, 2002.
[8] L. CAMBIER, J.P. VEUILLOT - *Status of the elsA CFD Software for Flow Simulation and Multidisciplinary Applications*. 48th AIAA Aerospace Science Meeting and Exhibit, 2008.
[9] L. CASTILLON, S. PÉRON, C. BENOIT, G. BILLONNET - *Numerical Simulations of Technological Effects Encountered on Turbomachinery Configurations with the Chimera Technique.* 27th International Congress of the Aeronautical Sciences, Nice, France, September 2010
[10] L. CASTILLON, G. LEGRAS - *An Unsteady Overset Grid Method for the Simulation of Compressors with non Circumferential Casing Treatments.* ISABE-2011-1229, Goteborg, Sweden, Sept. 2011.
[11] R.V. CHIMA - *Computational Modeling of Vortex Generators for Turbomachinery*. NASA TM 2002 211551, 2002
[12] E. COLOMBO - *Investigation on the Three-Dimensional Flow Mechanisms in Annular Axial Compressor Cascades for Aero Engines with Flow Control by Aspiration on the Hub and on the Blades*. EPFL PhD Thesis, http://library.epfl.ch/theses/?nr=5241, 2011
[13] A.J. CROOK, E. M. GREITZER, C.S. TAN, J.J. ADAMCZYK - *Numerical Simulation of Compressor Endwall and Casing Treatment Flow Phenomena*. ASME J. Turbomach., 115, pp. 501–512, 1993
[14] T. DANG, M. VAN ROOIJ, L. LAROSILIERE - *Design of Aspirated Compressor Blades Using Three-dimensional Inverse Method*. Proceedings of the ASME Turbo Expo, GT-2003-38492, Atlanta, Georgia, USA, June 16-19, 2003.
[15] J.D. DENTON - *Loss Mechanisms in Turbomachines*. Journal of Turbomachinery, 115:621–656, October 1993.
[16] H. FUJITA, H. TAKATA - *A Study of Configurations of Casing Treatment for Axial Flow Compressors.* Bull. of JSME, Vol. 27, No. 230, pp. 1675-1681, 1985.
[17] S.A. GBADEBO, N.A CUMPSTY, T.P. HYNES - *Control of Three-Dimensional Separations in Axial Compressor by Tailored Boundary Layer Suction*. Journal of Turbomachinery, 130:011004–1–8, January 2008.
[18] A. GODARD - *Etude Numérique et Expérimentale d'un Compresseur Aspiré.* PhD Thesis, Ecole Centrale de Lyon, Lyon, France, 2010.
[19] A. GODARD, S. BURGUBURU and F. LEBOEUF - *Parametric Study of an Aspirated Diffuser.* Proceedings of 7th European Turbomachinery Conference, Athens, Greece, March 5-9, 2007.
[20] A. GODARD, A. FOURMAUX, S. BURGUBURU, F. LEBOEUF - *Design Method of a Subsonic Aspirated Cascade*. Proceedings of the ASME Turbo Expo, GT-2008-50835, Berlin, Germany, June 9-13, 2008.
[21] A. GODARD, F. BARIO, S. BURGUBURU, F. LEBOEUF - *Experimental and Numerical Study of a Subsonic Aspirated Cascade*, Proceedings of the ASME Turbo Expo, GT-2012-69011, Copenhagen, Denmark, June 11-15, 2012.

[22] E.M. GREITZER, J.P. NIKKANEN, D.E. HADDAD, R.S. MAZZAWY, H.D. JOSLYN - *A Fundamental Criterion for the Application of Rotor Casing Treatment.* J. of Fluids Engineering, 101(3), pp. 237–243, 1979.
[23] M.D. HATHAWAY - *Self-Recirculating Casing Treatment Concept for Enhanced Compressor Performance.* ASME TurboExpo, June 3–6, 2002 , Amsterdam, The Netherlands, ASME Paper GT2002-30368, 2002
[24] M.D. HATHAWAY - *Passive Endwall Treatments for Enhancing Stability.* VKI LS 2006-06 on Advances in Axial Compressor Aerodynamics, 2007.
[25] A. HERGT, R. MEYER - *Effects of Vortex Generators Application on The Performance of a Compressor Cascade.* ASME Turbo Expo 2010, GT2010-22464, Glasgow, UK, 2010
[26] G. JEANFAIVRE, C. BENOIT, M.C. LEPAPE - *Improvement of the Robustness of the Chimera Method*, 32nd AIAA Fluid Dynamics Conference, 2002.
[27] G. LEGRAS, N. GOURDAIN, I. TREBINJAC - *Numerical Analysis of the Tip Leakage Flow Field in a Transonic Axial Compressor with Circumferential Casing Treatment.* Journal of Thermal Science, Vol. 19, Issue 3, pp 198-205, June 2010.
[28] G. LEGRAS, L. CASTILLON, N. GOURDAIN, I. TRÉBINJAC - *Flow Mechanisms induced by Non-Axisymetric Casing treatment in a transonic Axial Compressor.* ISAIF10-158, Brussels, Belgium, 4-7 July 2011.
[29] G. LEGRAS, I. TRÉBINJAC, N. GOURDAIN, X. OTTAVY, L. CASTILLON - *A Novel Approach to Evaluate the Benefits of Casing Treatment in Axial Compressors.* International Journal of Rotating Machinery, vol. 2012, Article ID 975407, 19 pages, 2012
[30] F. LIN, F. NING, H. LIU - *Aerodynamics of Compressor Casing Treatment Part I: Experiment and Time-Accurate Numerical Simulation.* ASME Turbo Expo 2008, GT2008-51541, Berlin, Germany, 2008.
[31] R.L. MEAKIN - *Object X-Rays for Cutting Holes in Composite Overset Structured Grids*. AIAA 2001-2537, 2001.
[32] A. MERCHANT - *Design and Analysis of Axial Aspirated Compressor Stages*. PhD Thesis, Massachusetts Institute of Technology, Cambridge, Massachusetts, USA, 1999.
[33] A. MERCHANT, J. KERREBROCK, J. ADAMCZYK, E. BRAUNSCHEIDEL - *Experimental Investigation of a High Pressure Ratio Aspirated Fan Stage.* Journal of Turbomachinery, Vol. 127 (1), pp. 43-51, 2005.
[34] M.W. MÜLLER, H.-P. SCHIFFER, M. VOGES, C. HAH - *Investigation of Passage Flow Features in a Transonic Compressor Rotor with Casing Treatments*. ASME Turbo Expo, Vancouver, British Columbia, Canada, ASME Paper GT2011-45364, June 6-10, 2011.
[35] F. NING, L. XU - *Aerodynamics of Compressor Casing Treatment Part II: A Quasi-Steady Model for Casing Treatment Flows*. ASME Turbo Expo 2008, GT2008-51542, Berlin, Germany, 2008.
[36] J. ORTMANNS, C. PIXBERG, V. GÜMMER - *Numerical Investigation of Vortex Generators to Reduce Cross Passage Flow Phenomena in Compressor Stator Endwalls.* European Turbomachinery Conference 2011, Istanbul, Turkey, Paper ETC9 C075, 2011
[37] R.E. PEACOCK - *Boundary-Layer Suction to Eliminate Corner Separation in Cascades of Aerofoils*. A.R.C. R&M 3663, 1971
[38] A. PESTEIL, D. CELLIER, O. DOMERCQ, V. PERROT, J.C. BONIFACE - *CREATE: Advanced CFD for HPC Performance Improvement.* ASME Turbo Expo 2012. ASME Paper GT2012-68844, Copenhagen, Denmark, 11-15 June 2012
[39] V. PERROT, A. TOUYERAS, G. LUCIEN - *Detailed CFD Analysis of a Grooved Casing Treatment on an Axial Subsonic Compressor*. Proceedings of the 7. European Turbomachinery Conference 2007, March 5-9, Athens, Greece, paper ETC7 016, 2007
[40] D.C. RABE, C. HAH - *Application of casing circumferential grooves for improved stall margin in a transonic axial compressor.* Proceedings of ASME Turbo Expo 2002, Amsterdam, The Netherlands, June 3-6. Paper GT-2002-641, 2002.
[41] A. SACHDEVA - *Analyse, intégration et valorisation des technologies d'aspiration d'aubages dans les compresseurs de turboréacteurs.* PhD Thesis, http://bibli.ec-lyon.fr/exl-doc/TH_T2194_asachdeva.pdf, 2010
[42] TH. SCHWARZ - *Development of a Wall Treatment for Navier-Stokes Computations using overset Grid technique*. Proceedings of the 26th European Rotorcraft Forum, The Hague, September 2000.
[43] G.D.J. SMITH, N. A CUMPSTY - *Flow Phenomena in Compressor Casing Treatment*. ASME Journal of Engineering for Gas Turbines and Power, Vol. 117, pp. 532-541, 1985
[44] Z.S. SPAKOVSZKY, H.J. WEIGL, J.D. PADUANO, C.M. VAN SCHALKWYK, K.L. SUDER, M.M. BRIGHT - *Rotating Stall Control in a High-Speed Stage With Inlet Distortion: Part I - Radial Distortion*. ASME J. Turbomach., 121, pp. 510–516, 1999.
[45] Z.S. SPAKOVSZKY, H.J. WEIGL, J.D. PADUANO, C.M. VAN SCHALKWYK, K.L. SUDER, M.M. BRIGHT - *Rotating Stall Control in a High-Speed Stage with Inlet Distortion: Part II - Circumferential Distortion*. ASME J. Turbomach., 121, pp 517–524, 1999.
[46] P.R. SPALART, S.R. ALLMARAS - *A One-Equation Turbulence Model for Aerodynamic Flows.* La Recherche Aérospatiale, 1:5–21, 1994.
[47] C. SPEZIALE, S. SARKAR, T. GATSKI - *Modelling the Pressure–Strain Correlation of Turbulence: an Invariant Dynamical Systems Approach*. Journal of Fluid Mechanics, 227, pp. 245-272, 2006.
[48] K.L. SUDER, M.D. HATHAWAY, S.A. THORP, A.J. STRAZISAR, M.B. BRIGHT - *Compressor Stability Enhancement Using Discrete Tip Injection.* ASME Journal of Turbomachinery, vol. 123(1), pp. 14-23, 2001
[49] A. TOUYERAS, M. VILLAIN - *Aerodynamic Design and Test Result Analysis of a Three Stage Research Compressor*. ASME Turbo Expo 2004, June 14-17, Vienne, Austria, ASME Paper GT2004-53940, 2004.
[50] H.J. WEIGL, J.D. PADUANO, L.G. FRECHETTE, A.H. EPSTEIN, E.M. GREITZER, M.M. BRIGHT, A.J. STRAZISAR - *Active Stabilization of Rotating Stall and Surge in a Transonic Single Stage Axial Compressor.* ASME J. Turbomach., 120, pp. 625–636, 1998.

Nomenclature

Latin

$AVDR$	Axial velocity density ratio, $AVDR=(1-C_q)\cdot[\rho_1 V_{x1} / \rho_0 V_{x0}]$
Cp	Static pressure coefficient $C_p = (P_{s0} - P_s) / (P_{t0} - P_{s0})$
Cq	Aspirated mass flow rate $C_q = q_f / q_0$
c	Blade chord
DF	Lieblein diffusion factor, $DF = 1-(V_1 / V_0) + (\lvert V_{y1} - V_{y0} \rvert / 2\cdot\sigma\cdot V_0)$
H	Blade span
M	Mach number
P_t	Total pressure
P_s	Static pressure
p	Blade spacing
q	Mass flow
Tu	2D freestream turbulent intensity
V	Absolute velocity magnitude
(x,y,z)	Cartesian coordinates

Greek

α	Absolute flow angle
β	Yaw angle (pneumatic probe)
ρ	Density
σ	Solidity
$\sigma(G)$	Measurement uncertainty of quantity G
ω_1	Total pressure loss coefficient, regarding the blade passage : $\omega_1 = (1-C_q)\cdot[(P_{t1} - P_{t0}) / (P_{t0} - P_{s0})]$

Subscripts

0	Cascade inlet station
1	Cascade outlet station
atm	Atmospheric conditions
f	Slot outlet station
m	Average value
x,y,z	Components relative to the x-, y-, z-directions

Acronyms

3DNU	(Three-Dimensional Non-Uniform distribution)
3DU	(Three-Dimensional Uniform distribution)
BUAA	(Beijing University of Aeronautics and Astronautics)
CB	(Casing Blowing)
CREATE	(Compresseur de Recherche pour l'Etude des effets Aérodynamiques et TEchnologiques)
CT	(Casing Treatment)
DRSM	(Differential Reynolds-Stress Model)
ECL	(Ecole Centrale de Lyon)
HCT	(High Casing Treatment ([34]))
LE	(Leading Edge)
LMFA	(Laboratoire de Mécanique des Fluides et d'Acoustique)
PIV	(Particle Image Velocimetry)
RANS	(Reynolds-Averaged Navier-Stokes)
RF	(Recirculating Flow configuration)
SCT	(Small Casing Treatment ([27]))
SW	(Smooth Wall)
TE	(Trailing Edge)
VG	(Vortex Generator)

AUTHORS

Julien Marty graduated from Ecole Nationale Supérieure de Mécanique et Aérotechnique (ENSMA) in Poitiers, France. He did a Ph. D thesis in 2010 at Onera Toulouse. He received a Ph. D award from the ISAE-SUPAERO Foundation in December 2011 for his work on the near stall prediction of high pressure compressors. He joined the Applied Aerodynamics Department of ONERA Meudon in 2009 as a research engineer and worked on helicopter rotor optimization using the adjoint method. Since 2011, his main research interests have been the turbulence modeling of separated or vortical flows in compressors and turbines, especially Large-Eddy Simulation and Zonal Detached-Eddy Simulation, transition modeling and the conjugate heat transfer for turbine applications.

Lionel Castillon graduated from the Ecole Polytechnique engineering school (Paris) in 1998 and joined Onera in 2000 after a 2 year scholarship at the ENSTA engineering school. He has been working at the Applied Aerodynamic Department on the development and validation of in-house CFD codes for turbomachinery applications.

Jean-Christophe Boniface obtained a Master's degree in numerical analysis from the J.-L. Lions laboratory of the University of Paris in 1990, which he completed with a PhD thesis in Computational Fluid Dynamics from the Ecole Nationale Supérieure d'Arts et Métiers (ENSAM, 1995). For 10 years he was involved in CFD code developments at the CFD and Aeroacoustic Department of Onera, especially in the field of rotorcraft flowfield predictions. He then spent 4 years at the University of Milan (Politecnico Di Milano, 2004-2008) as research assistant, working on highly implicit methods and low-speed preconditioning applied to the RANS equations. Since 2008, he joined the Applied Aerodynamics Department of ONERA and is basically working on flow control and optimization for both internal and external aerodynamics.

Stéphane Burguburu graduated from the National Institute of Applied Sciences (INSA) in 1995. After a short stay at Onera during his military service, he joined General Electric/Nuevo Pignone as design engineer for centrifugal compressors. After four years, he returned to aerospace as an aerodynamic engineer in the Applied Aerodynamics Department of Onera. He first focused on turbomachinery blade optimization and aeroacoustics, then on the study of the aerodynamics of propellers and open-rotors. Finally, he was the focal point for fans at Onera. He is currently working at Snecma as R&T project leader for low pressure spool aerodynamics and acoustics.

Antoine Godard currently holds the position of Research Engineer at the Laboratoire de Mécanique de Fluides et d'Acoustique (LMFA) of the Ecole Centrale de Lyon, France. Prior to this, he was a Research Associate in Compressor Aerodynamics at the Whittle Laboratory of the University of Cambridge, in the United Kingdom. He obtained his doctorate in 2010, in Applied Aerodynamics working at the Office National d'Etudes et de Recherches Aérospatiales (Onera) in cooperation with the Ecole Centrale de Lyon, France. He completed a Master's degree in Mechanical Engineering at the Georgia Institute of Technology in 2004. That same year, he also received his engineering diploma (Diplôme d'ingénieur) from the Ecole Nationale Supérieure d'Arts et Métiers (ENSAM). His current research interests are flow-controlled compressor design, separated flow patterns, compressor aerodynamic stability, experimentation and design of experimental facilities.

D. Caruana, F. Rogier,
G. Dufour, C. Gleyzes
(Onera)

E-mail: daniel.caruana@onera.fr

The Plasma Synthetic Jet Actuator, Physics, Modeling and Flow Control Application on Separation

Practical application of active flow control is dependent upon the development of robust actuators that are reliable, small, easy to integrate and have no or very small delay. Onera is developing Plasma Synthetic Jet actuators, PSJ, in order to show the potential of such electrical devices to act on aerodynamic phenomena like separated flows. The characterization of the pulsed jet produced by a PSJ actuator is investigated with experimental techniques, helping the validation of theoretical and numerical studies carried out in parallel. This article mainly describes the physics of PSJ actuators with numerical and experimental studies on the characterization of the PSJ device with and without flow and on the ability of PSJ actuators to reduce the separated flow region on a decelerating ramp and on an NACA-0015 airfoil. PSJ actuator efficiency has been quantified using the PIV technique, in order to estimate the decrease of the separated flow region induced by the actuation and consequently the drag reduction. The results show very promising effect with a separation almost completely cancelled.

Introduction

Flow control with active actuators requires efficient, robust, easy to integrate and low energy consumption devices. Inspired by the "sparkjet" device, proposed by Grossman [1] from the Hopkins University Applied Physics Laboratory, Onera, in cooperation with the CNRS/LAPLACE laboratory, is studying and developing a very promising synthetic jet plasma generator, which can produce a high-velocity synthetic jet without any moving part and without any external fluid injection. In order to determine the operational characteristics of this actuator needed for flow control and to improve its conception, several studies have been conducted within the framework of the PLASMAERO project funded by the European Community in a specific task that deals with showing that these devices are able to postpone the trailing edge separation phenomenon occurring in a high lift configuration (low velocity, high incidence angle).

Description and principle of the PSJ actuator

PSJ is a zero-net-mass-flux device mainly composed of 2 electrodes embedded in a cavity manufactured from a ceramic material, in connection with the external medium, with the help of a small dedicated orifice (figure 1). By applying a voltage difference greater than the disruptive voltage of the gas located inside the cavity (5 kV for Onera's actuators), an electrical arc is created between the 2 electrodes, leading to an increase in the internal energy. Since the air is confined, the temperature and pressure increase very quickly inside the cavity. Fluid relaxation can be performed through a dedicated orifice, producing a pulsed air jet. At the end of this blowing phase, the cavity pressure drops below the external pressure value, activating a suction stage within the cavity. The actuator is ready for another cycle (figure 2).

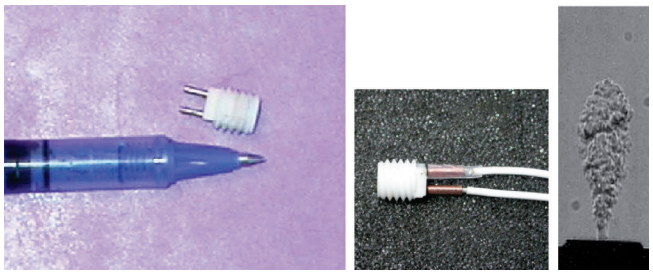

Figure 1 - PSJ device (ϕ 8mm), generated micro-jet

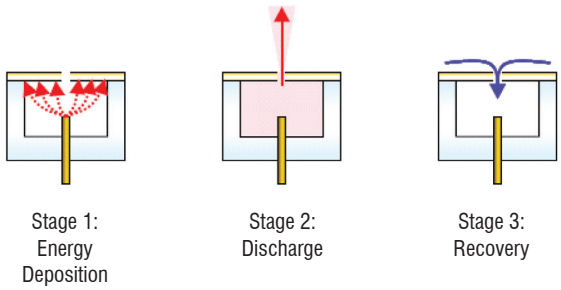

Figure 2 - Principle of PSJ functioning - (from [1])

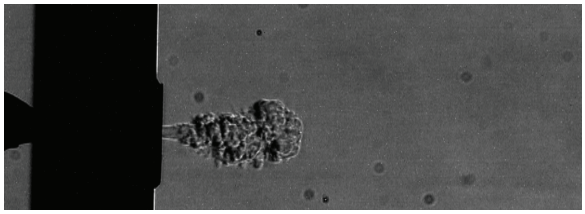

Video 1 - PSJ micro-jet characterisation. Schlieren visualisation
http://www.aerospacelab-journal.org/al6/plasma-synthetic-jet-actuator-physics-modeling-and-flow-control-application-on-separation

The characteristics of this device depend on the cavity geometry, the energy deposition and on the electrical parameters. In order to create the discharge, a high power supply is essential. Developed by the Laplace laboratory, the solution using a low voltage power supply associated with a high voltage transformer (m) and a transistor (IGBT) has been chosen, (figure 3) [2]. The IGBT can be easily controlled to adjust the frequency and the energy accumulated within the transformer.

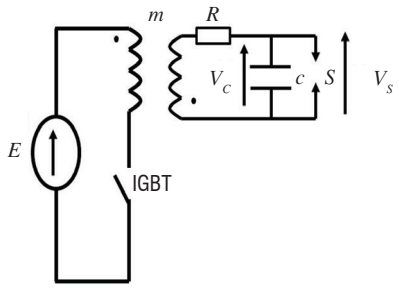

Figure 3 - Capacitive power supply

This power supply can control the frequency, the phase and the energy dissipated in the discharge for each device itself. The maximum frequency actuation is 2000 Hertz for a capacitor value of 20 nF and can be increased for lower capacitor values. The delay can be undependably fixed for each PSJ (the precision is less than one micro-second).

Electrical characterization of the PSJ

The PSJ actuator is connected to the capacitor by means of a wire, which is modeled as an inductance of 2 μH and a resistance of 0.5 Ω. These considerations allow the calculation of the discharge voltage from the current and the measurement of the capacity voltage [2].

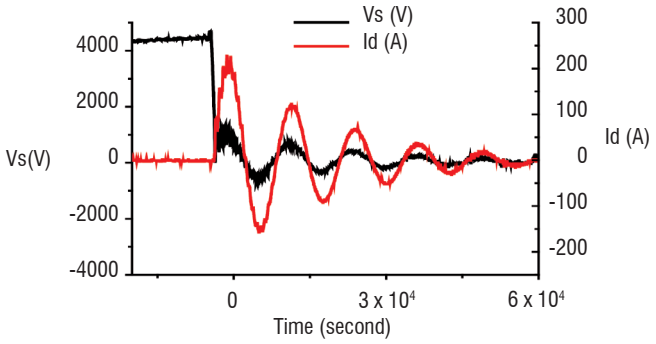

Figure 4 - Discharge and current voltage - C=15 nF

During the ignition time, the discharge voltage drops down to zero within a few nanoseconds (figure 4). Following ignition, the current and the voltage discharge are sinusoidal and in phase. This suggests that plasma in the PSJ actuator behaves as a resistance. Calculations, not provided in this paper, show than the value of the resistance can amount to several Ohms [2]. Therefore, the plasma is very conductive. This explains why the temperature of the plasma is higher than 10,000 K. Furthermore, the maximum current is proportional to the breakdown voltage and in all cases higher than 100 A for a few nano-seconds.

The change in the discharge luminosity has been obtained using short exposure time photography, taken with an intensified CCD camera (figure 5).

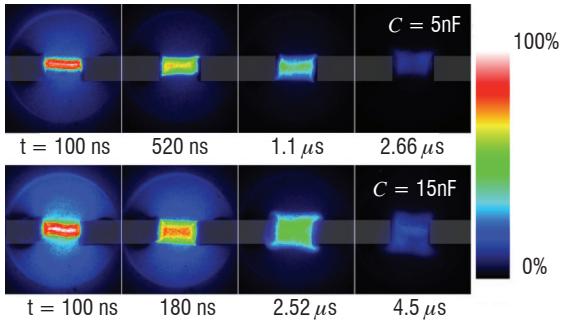

Figure 5 - ICCD images of light emission for two different capacitances (5 nF and 15 nF)

The maximum luminosity is however three times more intense for 15 nF than for 5 nF. It is relevant that the luminosity of the discharge decreases with time; indeed, the current also diminishes with time. For both cases, the behavior is similar ; the discharge looks cylindrical, since the luminosity is shared out symmetrically between the two electrodes. After ignition (t> 600 ns), the discharge is homogenous and the diameter of the discharge does not change. Furthermore, the height of the discharge is wider for 15nF (and covers the electrodes) than for 5 nF. Consequently, the 15 nF discharge heats a larger volume of gas and for longer times than the 5 nF discharge does.

Aerodynamic characterization of the PSJ

The characteristics of the micro-jet produced by the PSJ actuator are closely connected to the electrical energy 'E_c' loaded in a capacitor before being transferred to the device after the breakdown outbreak. This energy level depends on the breakdown voltage 'V_b' and the capacitor value 'C', according to the following formula: $E_c = 0.5 \times C \times V_b^2$. For the geometrical and electrical configuration studied, the maximal jet velocity can reach 280 m.s^{-1}, with a temperature level of about 400 K (figure 6-top), depending on the capacitor value and on the running frequency, which can be of up to 2000 Hz. For a given frequency, a saturation effect appears on the velocity levels when the capacitor value is increased, because the heating of the device induces the dropping of the breakdown voltage and, consequently, a decrease in the electrical energy transferred during the spark discharge. The heating is also responsible for the velocity decrease induced when the running frequency is increased. Since the PSJ actuator produces a pulsed jet with a quasi-constant duration of 150 μs, the duty cycle increases linearly with the frequency, as can be observed in figure 6 – right [3] and [4].

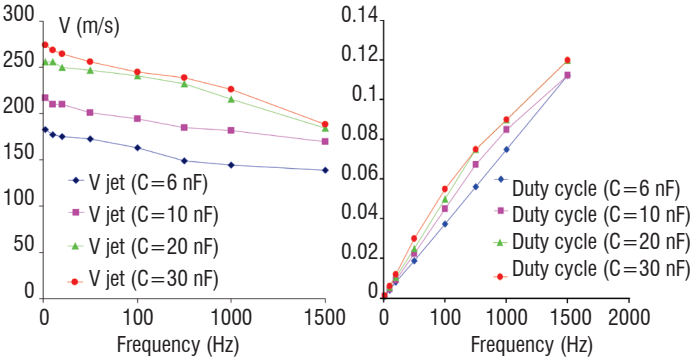

Figure 6 - Micro-jet velocities and duty cycle versus PSJ running frequency

PSJ modeling and numerical parametric study

A full model of the PSJ actuator has been developed. It includes physics insights (real gas effect, discharge modeling, etc...) and provides information on the gas within the cavity, as well as in the plume. The objective was to obtain a better understanding of the thermal energy transfer supplied by the arc discharge to the gas.

The model has been split into two coupled sub-models (figure 7). The first one deals with the energy deposition through electric arcing in the vicinity of the electrodes, in the absence of the cavity. It describes the plasma formation between both electrodes in an axisymmetrical configuration. This model is coupled with the RLC circuit equations describing the electrical supply by the external generator. The second sub-model focuses on the flow heating the cavity and the actuator operation It uses the energy distribution computed by the first sub-model as a source term and calculates the resulting effects on the actuator. It provides the flow mass rate, momentum and energy at the PSJ's exhaust versus time. To perform a full PSJ's simulation, both codes are running. A simulation of the arc is first performed and then the PSJ's simulation is performed.

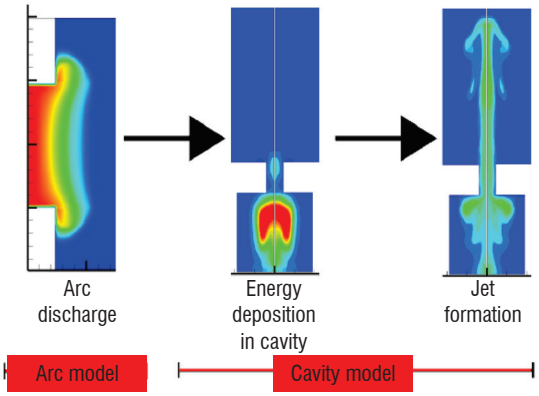

Figure 7 - Scheme of the PSJ modeling

Real Gas thermodynamic and modeling assumptions

The modeling relies on a certain number of assumptions. First of all, the arc created in the PSJ cavity, which corresponds to the location of the energy deposit, is supposed to be elongated and characterized by an azimuthal symmetry. Because of the strong current and of the short gap between the electrodes, we assume that the arc is cylindrical as well.

In this case, the complexity of the problem can be reduced to solving a 2D axisymmetric problem where all of the variables only depend on the radius r and on the height z (figure 8). Real configuration is genuinely 3D because of the way in which the electrodes are placed inside the cavity. The amount of heating provided by the arc discharge is so large that real gas properties must be taken into account in the description of the flow. The ionization and dissociation reactions at higher temperatures cause very strong non-linearities in the evolution of the thermodynamic coefficients. As a consequence, a "real gas" model is generally considered to compute transport and thermodynamic coefficients, which must be injected into the system. In this case, the "real gas" representation has been made using the coefficients that depend on pressure and temperature calculated by Capitelli et al. [7], over a range that extends from 300 to 60,000 K and from 0.01 to 100 atmospheres.

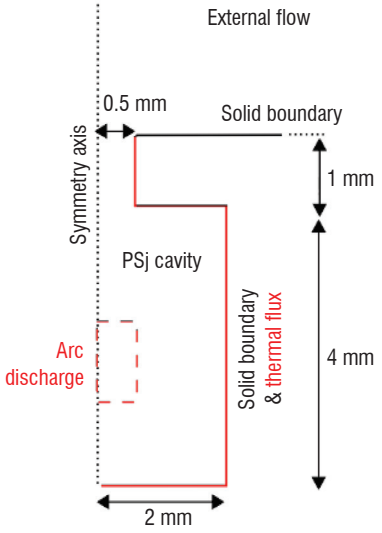

Figure 8 - Description of the geometry

Non-confined arc modeling

The arc geometry is still considered as a 2D axisymmetric problem. Moreover, the arc is considered to be in local thermal equilibrium (LTE) by looking at the high temperatures and pressures that generally characterize this type of device. Therefore, there is no distinction between heavy particle and electron behavior. This assumption thus offers the possibility of taking into account a unique temperature, to represent the thermal behavior of all of the species as a global single fluid. Viscosity effects are neglected. Thus, the flow evolution is governed by the 2D inviscid Euler equations, with thermal diffusion and Joule heating. Radiative energy losses are also taken into account proportionally to the net emission coefficient (NEC), whose value is given by tables depending on Temperature and Pressure provided by the LAPLACE CNRS laboratory. The plasma resistance results from the conductivity, which depends analytically on the temperature between the electrodes. The current I is then obtained by the RLC circuit equations and the electric field is obtained from the discharge current using Ohm's law.

The modeling does not describe the arc formation step during the first nanoseconds. It is assumed that the initial state is known after the first current pulse. Figure 9 shows the pressure wave resulting from the energy deposition by the electrical circuit at t=5 ns.

Figure 10 shows a comparison between the experimental and computed current discharge. It must be noted that, to obtain these results, it has been necessary to add a virtual resistance to represent the voltage drops occurring in the areas close to the electrodes and which cannot be solved by the modeling (presence of sheaths).

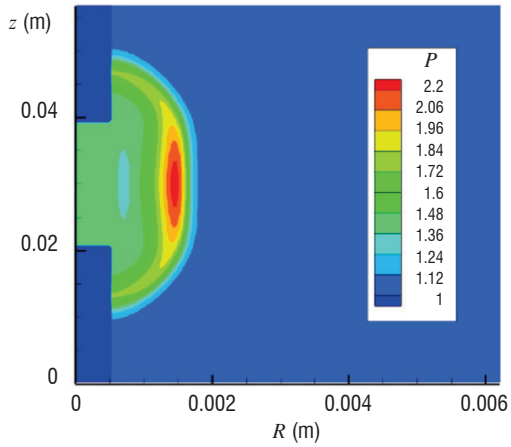

Figure 9 - Pressure wave at t =5 ns (P x 10^{5}Pa)

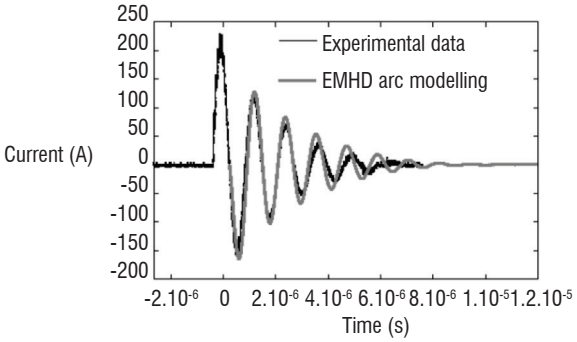

Figure 10 - Discharge current versus time

Simulation of the Plasma Synthetic Jet

The simulation of the working PSJ is first performed using non-confined arc modeling. An energy source distribution term is computed and introduced as input into the PSJ solver. Due to the geometry of the cavity, its cooling is only possible through convective heat transfers at the walls (the heat transfer at the electrodes is neglected). A thermal flux has been prescribed on the wall PSJ.

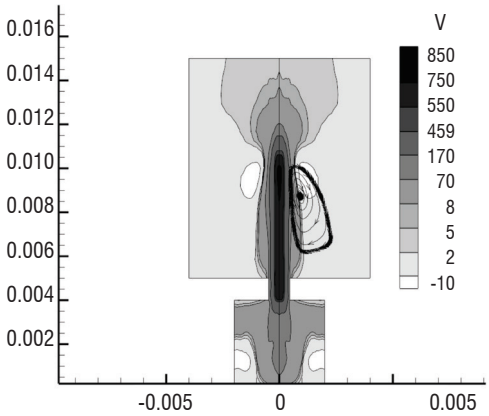

Figure 11 - Simulation of the PSJ – Micro-jet velocity (m/s) inside and outside the cavity

At this point, the arc discharge no longer delivers power and the fluid behavior is only governed by pressure and thermal gradients. This energy deposition generates an overpressure inside the cavity (of the order of 0.4 bar), which forces the high velocity flow outside the cavity. This creates velocities as high as 700 m/s within the core of the jet (figure 11), although the tip of the jet moves much slower (at around 160 m/s) between 0.5 and 1 cm outside the neck of the cavity ; this value corresponds to the measurements for a low frequency actuator). The high velocity jet assumes an arrow-shape which is visible.

Simulations of more than one discharge pulse led to the quasi-static periodic behavior of the actuator after approximately 25 pulses. The breakdown voltage depends on the initial gas state as an analytical function. Thus, after one pulse, the gas in the cavity is heated and the initial condition of the breakdown voltage will change. A simple breakdown voltage law is introduced in the model, to take into account the modification of the gas properties after the pulse. The quasi-static behavior of the actuator is readily visible in 2D views of the flow. However, some graphs, such as the total mass contained and the mean fluid temperature within the cavity, show this periodicity even more clearly (figure 12). This simulation has been carried out for an actuator operating at a frequency of 1 kHz, using a 15 nF capacitor and a constant breakdown voltage of 2.7 kV. Once the quasi-static behavior is obtained, 7 mJ of electric energy are deposited in the fluid during each pulse. For these graphs, fluid in the nozzle has been taken into account as well. Quasi-static behavior is obtained after roughly 10 ms (or 10 pulses) for all represented graphs. As from this time, the jet is truly synthetic, as seen in figure 12 (i.e., its net mass flow is null over one period). Afterwards, the jet expels about 5.2 mg (8.5% of the PSJ's initial mass) during each pulse, at a mass flow rate of approximately 49 mg/s. The fluid inside the cavity becomes relatively hot with a stabilized temperature never falling below 900 K.

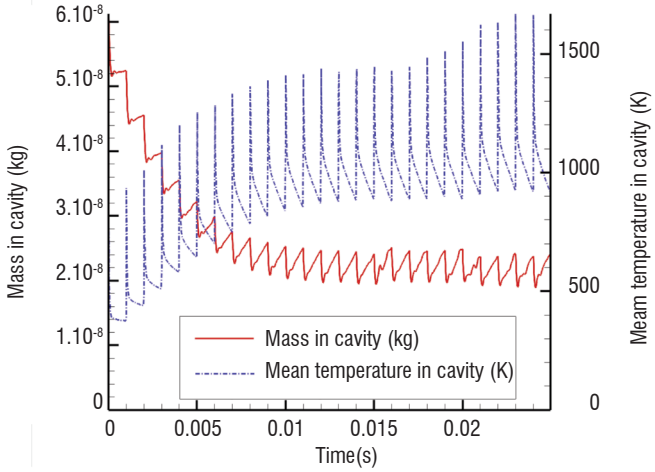

Figure 12 - Mass and mean temperature inside PSJ cavity for the 25 first pulses – f=1 KHz

Parametric study

A qualitatively study of the influence of several parameters on both energy deposition and cavity geometry is presented. These parameters were chosen around a reference actuator, composed of a 15 nF capacitor operating at 1 kHz, with a cavity ending in a 1 mm wide cylindrical neck. It should be kept in mind that, because of the inaccuracy of the energy deposition phases (energy loss in sheaths and constant breakdown voltage), only qualitative differences between the different configurations are presented.

Operating frequency

The behavior of the actuator for several operating frequencies seems physically correct (figure 13): qualitatively, we observe that the higher the frequency is, the hotter the cavity is and the less mass is expel-

led (because of the less efficient refill). Experimentally, the actuator should deposit less and less energy.

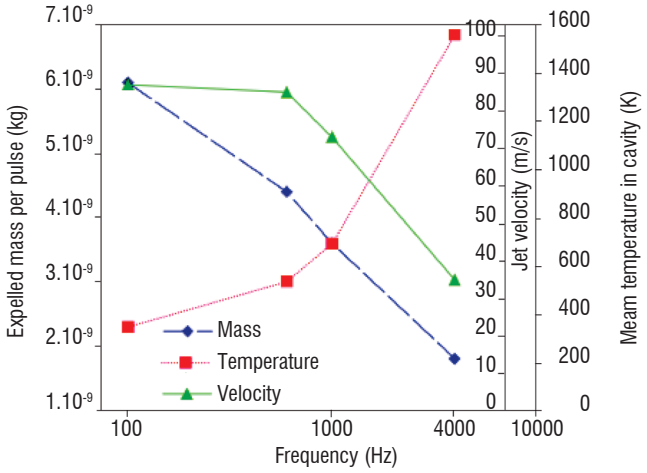

Figure 13 - Parametric study operating frequency

Actuator geometry

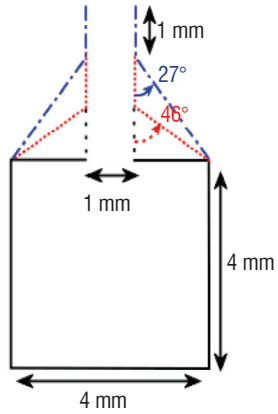

Figure 14 - Modeled geometries

Simulations in this section are performed for several geometries of the cavity neck (figure 14). Three different half-cone angles were used for this converging section: 90° (no cone), 45° and 27°. Arguably, this introduces a variation in the volume of the cavity. Even though the cavity volume changes slightly, figure 15 shows that, with the same entry section, the refill is much more efficient in the case of a converging cavity shape.

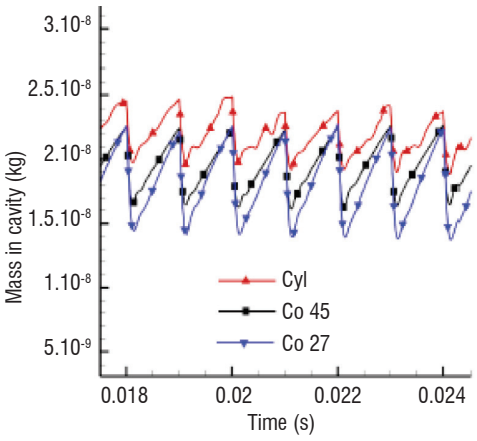

Figure 15 - Parametric comparison between geometries

Flow control strategy - PSJ / flow interaction

The strategy retained to delay the flow separation in subsonic configuration is to use PSJ actuators as vortex generator devices.

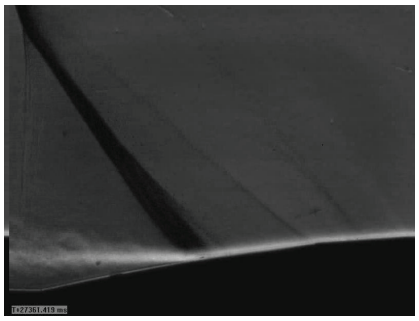

Video 2 - Separation & buffet Control - PSJ micro-jet/Boundary Layer interaction. Schlieren vortex visualisation - 0,2<M0<0,9
http://www.aerospacelab-journal.org/al6/plasma-synthetic-jet-actuator-physics-modeling-and-flow-control-application-on-separation

The produced longitudinal vortices should increase the momentum in the lower part of the turbulent boundary layer, in order to reduce its sensitivity to adverse pressure gradients, as shown by Lin [5]. Even though experimental and numerical results on synthetic jets are less widespread, these devices have received a great amount of attention from the fluid dynamics community, as mentioned by Gilarranz [6].

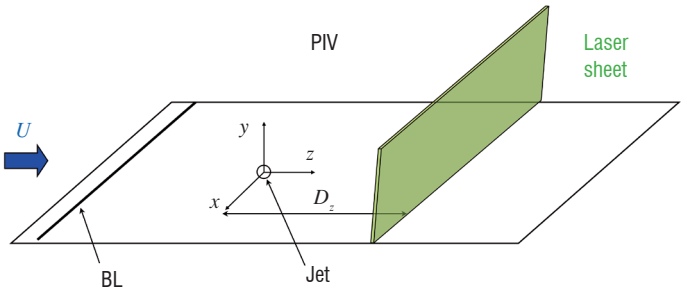

Figure 16 - Geometric configuration implemented for the PIV measurements

The vortex generated by the interaction between the main flow and the jet produced by a PSJ actuator embedded in a model has been characterized in subsonic flow, for a zero pressure gradient configuration, using the PIV technique. This experimental work was conducted in an Onera subsonic wind tunnel. For these tests, a flat plate was mounted into the test section, equipped with glass windows dedicated to optical diagnosis techniques. The PSJ actuator was located 250 mm downstream from the leading edge of the flat plate. The values of the pitch "α" and skew "β" angles for the jet exhaust were fixed at 30° and 60° respectively, in order to produce a vortex resulting from the interaction between the jet and the main flow. Since these angular values have been chosen from computation results performed on a continuous jet blowing configuration; complementary tests have been carried out, in order to check the suitability of this exhaust jet direction and particularly of this brief impact generated pulsed jet. The incoming boundary layer was tripped with a 0.8 mm diameter cylindrical rod, located 200 mm upstream from the PSJ actuator, in order to obtain a fully developed turbulent boundary layer in the vicinity of the jet. In this case, the boundary layer thickness was 8 mm for an upstream velocity equal to 40 m/s. The 3-component PIV technique was implemented to

characterize the formation of the vortex and also its convection by the main flow, using phase-shifting time-averaged measurements. The spark discharge into the PSJ actuator was chosen as the origin of the time scale ("T_o"). Figure 16 shows the geometric configuration implemented for the PIV technique.

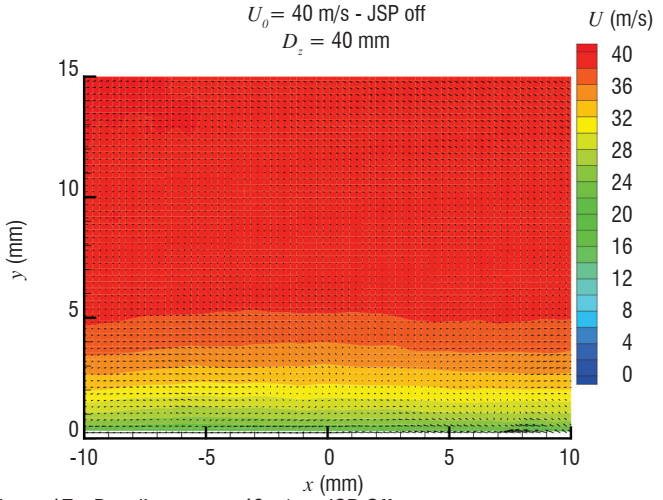

Figure 17 - Baseline V_{flow} =40m/s – JSP Off

The acquisition of phase-averaged velocity fields has been performed in a cross-plane configuration, for 5 equidistant "D_z" stations, from 20 mm to 100 mm downstream from the jet exhaust. The frequency of the spark discharge and then for the jet production was fixed at 10 Hz. The delay "T" defined to seize phase averaged PIV measurements was varied from 0 to 1.6 ms with a 50 μs step. Figures 17, 18, 19 and 20 present the results obtained at the D_z=40 mm station, for a capacitor value of 20 nF mounted in the power supply circuit. This capacitor value leads to an energetic level of 90mJ transferred to the actuator. Figure 17 shows the velocity field obtained with a PSJ actuator switched-off (baseline case). Figures 18 and 19 describe the changes in the vortex (velocity and vorticity). The detection of the vortex can be performed using vorticity computation on PIV data. A vertical velocity profile obtained at X=-2 mm for a delay value of T=T_0+1 ms is presented in figure 20, showing the momentum increase in the boundary layer, generated by the vortex resulting from the interaction between the JSP actuator and the flow.

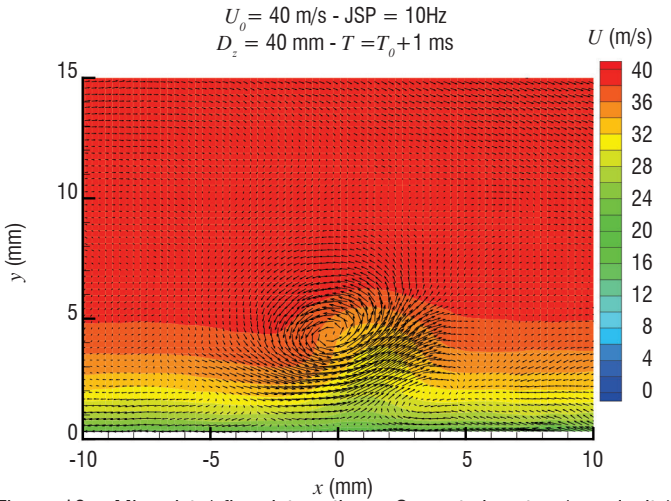

Figure 18 - Micro-jet / flow interaction - Generated vortex (U velocity) - V_{flow} =40m/s – JSP On

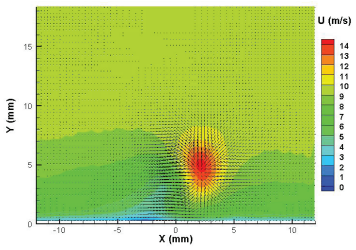

Video 3 - Separation Control - PSJ micro-jet/Boundary Layer interaction Vortex PIV measurement -U_{moy} - V_0= 40m/s
http://www.aerospacelab-journal.org/al6/plasma-synthetic-jet-actuator-physics-modeling-and-flow-control-application-on-separation

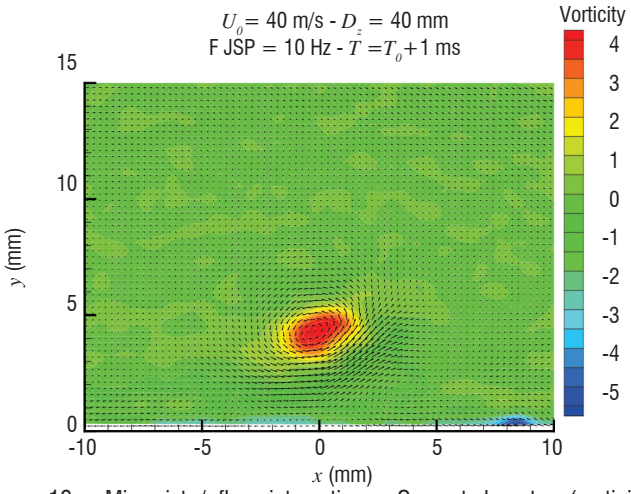

Figure 19 - Micro-jet / flow interaction - Generated vortex (vorticity) - V_{flow} =40 m/s – JSP On

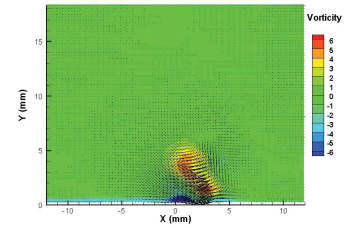

Video 4 - Separation Control - PSJ micro-jet/Boundary Layer interaction Vortex PIV measurement - Vorticity - V_0=40m/s
http://www.aerospacelab-journal.org/al6/plasma-synthetic-jet-actuator-physics-modeling-and-flow-control-application-on-separation

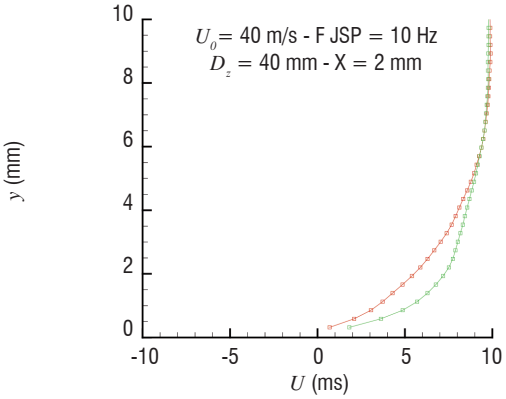

Figure 20 - Micro-jet / flow interaction - Generated vortex (Velocity profile) - V_{flow} =40 m/s

These PIV results have been exploited to extract the duration of the vortex in the various cross-planes (500 μs). Also, the elevation of the vortex along the longitudinal axis has been brought to light. If we make the assumption that this coherent structure is convected with a velocity close to the upstream velocity (40 m/s), we can determine its trajectory along the flat plate. Figure 21-top shows the vortex location estimated at the various cross-plane stations implemented for the PIV technique. The colors are related to the vorticity levels. We must note that the vortex comes up to 6 mm away from the wall at D_z=100 mm station. This elevation remains too significant to obtain sufficient momentum from the external part of the boundary layer, in order to make it more stable and then to delay the separation. The vortex generated by a less energetic PSJ actuator has been investigated, using a smaller value for the capacitor (C=5 nF / E_c=20 mJ) mounted into the electric circuit dedicated to the PSJ actuator power supply.

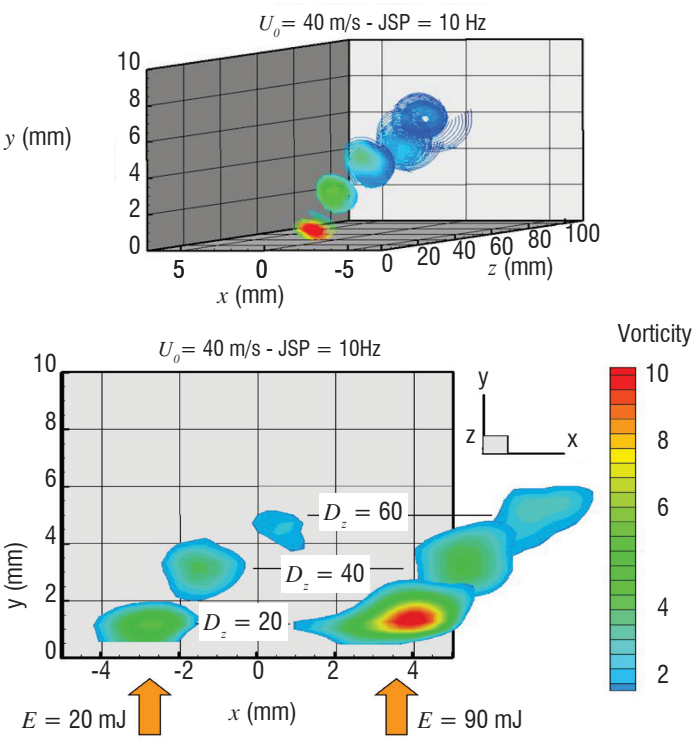

Figure 21 - Micro-jet / flow interaction - Generated vortex (vorticity) - V_{flow}=40m/s – JSP On

Figure 21-bottom shows the location of the vortex generated by the PSJ actuator for 2 energy levels (20 mJ and 90 mJ), obtained at 3 different "D_z" stations (D_z=20 mm, D_z=40 mm and D_z=60 mm). Note that reducing the energy level does not really affect the elevation of the vortex, but leads to a decrease in the vorticity levels. For the lower energy case, the vortex vanishes earlier. Since the jet remains very impacting, even with a lower energy level, the trajectory seems to be fixed by the orientation angles of the jet exhaust.

Separation delay on a ramp with PSJ

In order to investigate the efficiency on separation of the vortices generated by the interaction between the jet produced by PSJ actuators and the main flow, a ramp model has been manufactured and wind tunnel tests have been performed. This model is composed of 2 parts. The first concerns an accelerating ramp followed by a plateau. In the downstream region of this plateau, an insert has been manufactured in order to receive 5 PSJ actuators (figures 22 & 23). The second part concerns a decelerating ramp with an angle of 20 °. RANS computations have been performed to optimize the geometry of the model.

Figure 22 - Ramp model into the WT test section

Five PSJ exhausts have been distributed along 2 lines (figure 23). The pitch and skew angles for the PSJ exhausts remain the same, compared to the previous experiments carried out for the zero pressure gradient configuration (α=30°; β=60°). The boundary layer has been tripped, in order to have a fully turbulent boundary layer in the vicinity of the actuators.

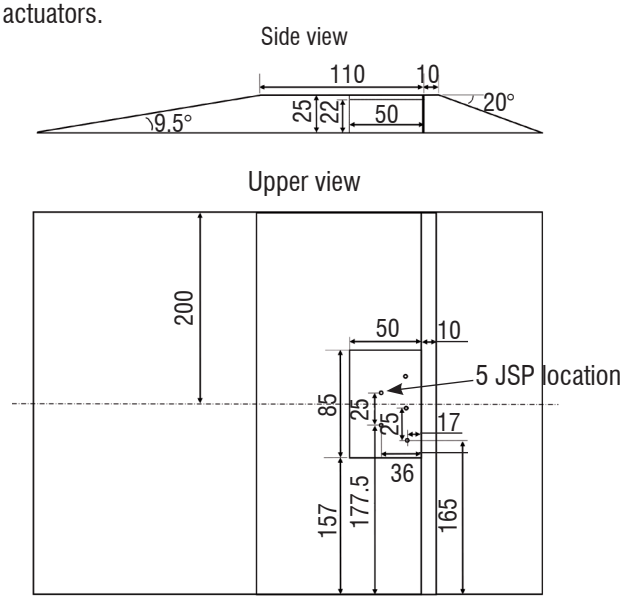

Figure 23 - Geometry of the ramp model and location of the PSJ exhausts

Experimental results have been obtained for three different upstream velocities (20 m/s, 30m/s and 37 m/s), using the 2-component PIV technique, in order to characterize the separation generated in the decelerating ramp area (figures 24 & 25).

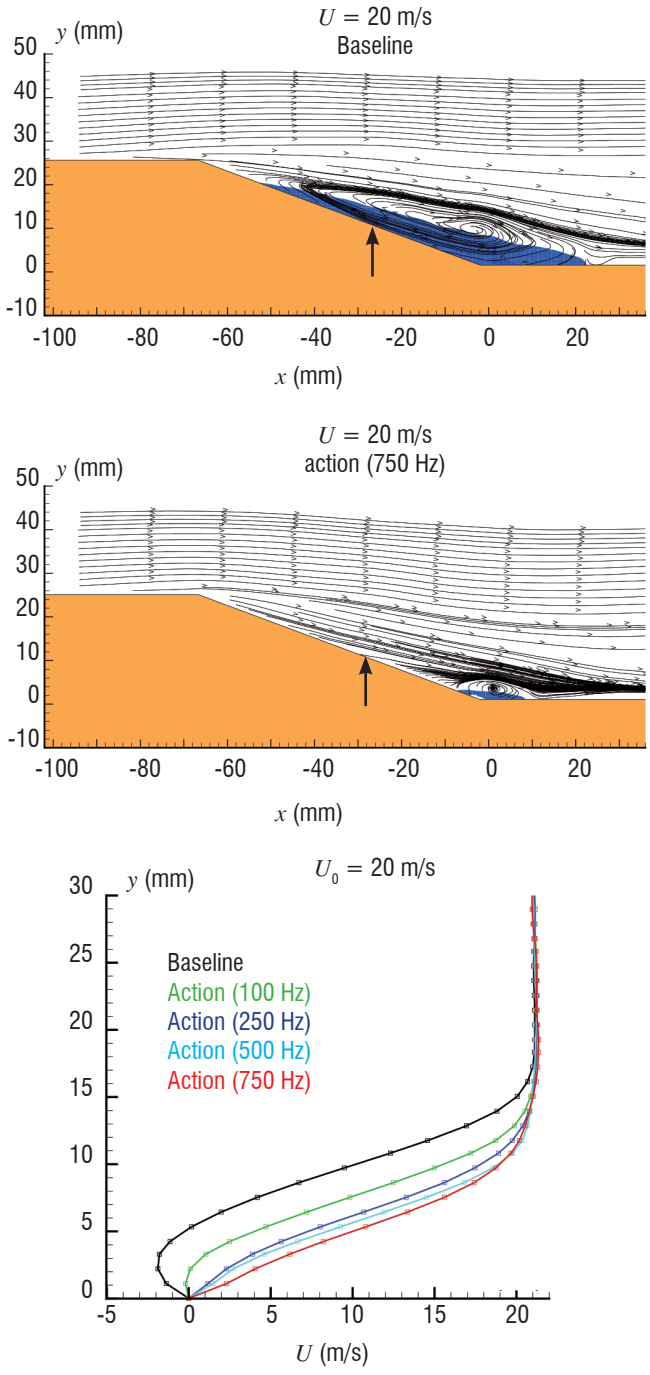

Figure 24 - PIV measurements of the streamlines and the separation area, PSJ off and on - V_{flow}=20 m/s

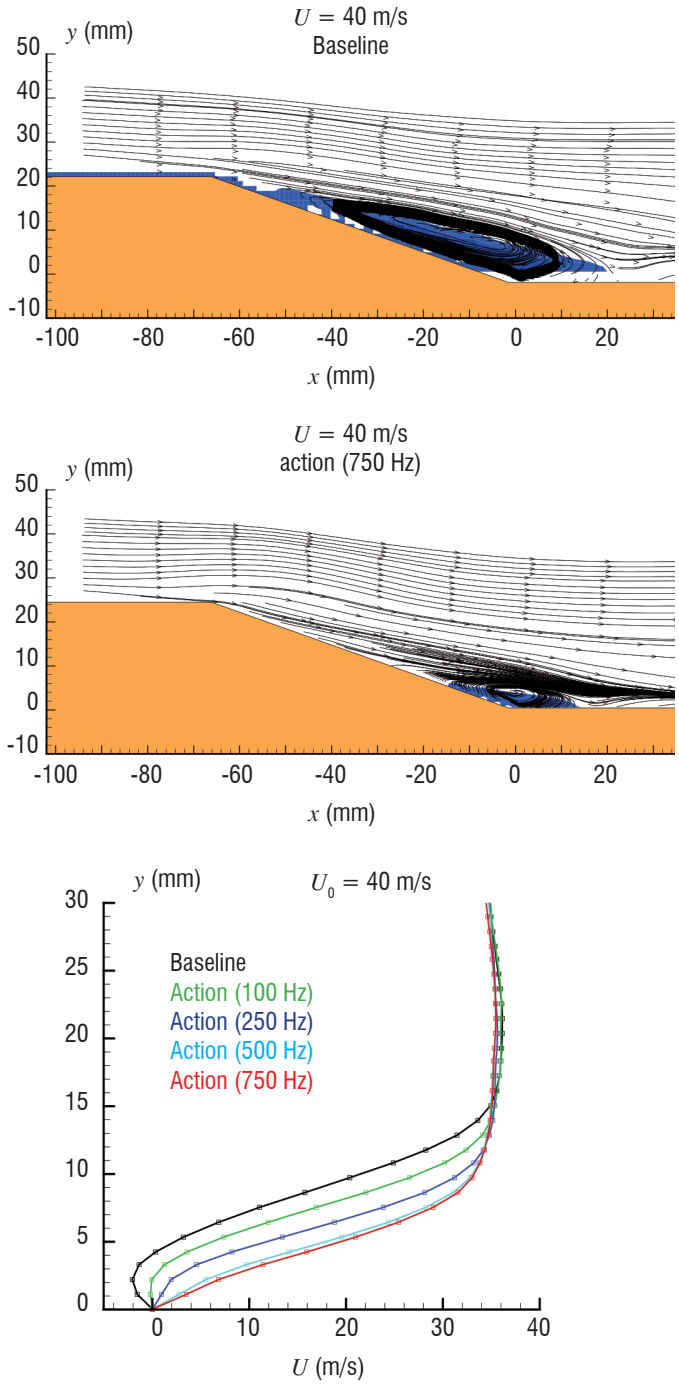

Figure 25 - PIV measurements of the streamlines and the separation area, PSJ off and on - V_{flow}=40 m/s

For each aerodynamic configuration, the baseline case (PSJ OFF) shows the expansion of the separated flow in the decelerating ramp region, represented in dark blue in the figures. In the lower velocity case (20 m/s), the separated region starts very close to the edge of the decelerating ramp. The decrease in the size of the separated flow area induced by the PSJ action is very significant, since it can be noticed in the mean velocity field obtained with the PIV technique. Vertical profiles of the longitudinal velocity obtained in the middle of the decelerating ramp are given. The effect of the PSJ actuator running frequency is clearly shown for these profiles. Even at low frequency levels (100 Hz), the separated region is reduced. The best reduction is obtained for the maximal frequency tested (750 Hz) even though a saturated level seems to be achieved from the frequency of 500 Hz. In this case, the separated region is confined to the lower part of the decelerating ramp. The implementation of PSJ actuators in the middle of the decelerating ramp could cancel this small separated flow region. The PSJ efficiency is also shown for higher velocity configurations (up to 37 m/s), even though the remaining separated area, located in the lower end of the ramp, is larger than in the case of the low velocity configuration. In these cases, we can also notice the saturation effect on the decrease of the separated area, obtained for a running frequency greater than 500 Hz.

This experimental facility should be helpful to study the interaction between the vortices generated by a group of PSJ actuators and the mean flow, one of the keys of control strategy description.

Trailing edge separation delay with PSJ on an NACA0015 airfoil

Validation tests concerning trailing edge separation control have been conducted at the "Beton" wind tunnel of the Pprime institute (CNRS-LEA). The NACA-0015 model (chord=500 mm) dedicated to these PSJ tests has been previously equipped with a metallic removable part able to receive 20 actuators evenly distributed along a line located 32% downstream from the leading edge. The geometry of the actuators implemented is given in figure 26.

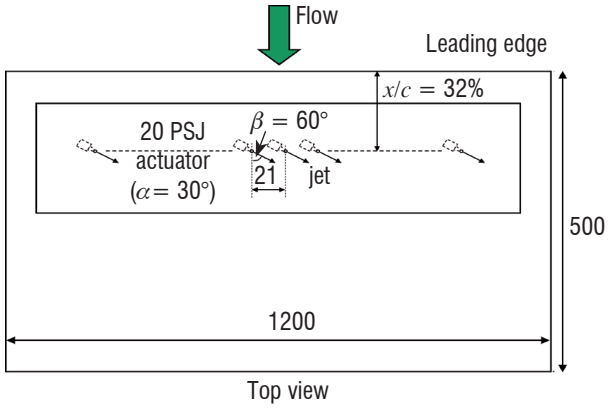

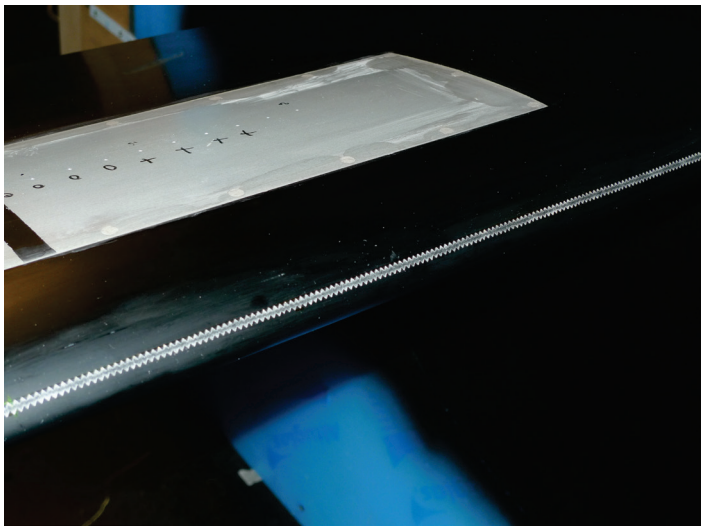

Figure 26 - Location of the 20 PSJ actuators in the NACA-0015 model

The pitch and skew angles for each actuator have been fixed at 30° and 60°, respectively. The boundary layer is turbulent. It has been tripped with Carborundum dots. According to the results obtained from the calibration bench (figure 6), the micro-jet velocity is 200 m/s and its duration is about 150 μs. The upstream flow velocity was between 20 m/s and 40 m/s (0.6 million $< Re_c <$ 1.2 million) and the airfoil angles of attack are between 10 and 13.5°. The separation area depends on the angle of attack of the model, limited trailing edge, mid-chord and full leading edge. The limited configuration has been chosen, in order to check the length for which the generated vortex can be convected by the flow and can act on separation. According to the chosen flow control strategy, the geometry and the location of the PSJ actuators is not suitable to act on full leading edge separation.

Limited trailing edge separation

In order to estimate the efficiency of the 20 PSJ actuators on the trailing edge separation phenomenon, the 2-component PIV technique has been implemented to obtain velocity fields in the interesting region of the studied flow, i.e., in the vicinity of the trailing edge. A laser source has been mounted above the test section, in order to generate a longitudinal laser sheet impacting the middle of the model span.

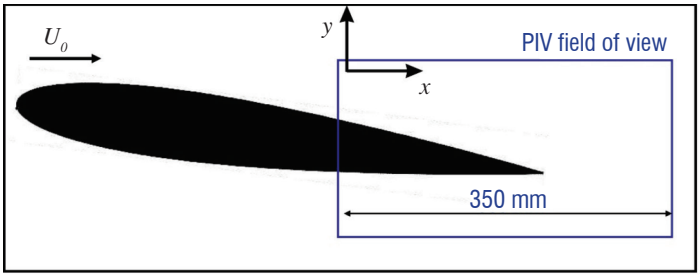

Figure 27 - Illustration of the PIV field of view

The high-resolution CCD camera (2048x2048 pixels) was aimed at the laser sheet in a perpendicular direction, focusing on the trailing edge region of the model (from 55 to 100% of the chord length), as well as on the immediate near-wake region (figure 27). The resulting resolution of the velocity field is one vector every 1.4 mm. The time-averaged velocity fields have been computed from the acquisition of 500 instantaneous fields, obtained at a rate of 7 Hz, in order to assume the convergence of the first-order moments. This assumption has been validated during preliminary tests.

Furthermore, useful information was provided by 10 static pressure taps located in the interesting region of the model suction side (from x/c = 0.50 to x/c = 0.95). Each time-averaged pressure measurement has been obtained from the acquisition of 1024 points at a rate of 200 Hz. The pressure tap measurements reveal the increase of the external velocity induced by the actuation in the downstream region of the PSJ exhaust (x/c=50 %). This effect increases with the value of the PSJ actuator running frequency (figure 28).

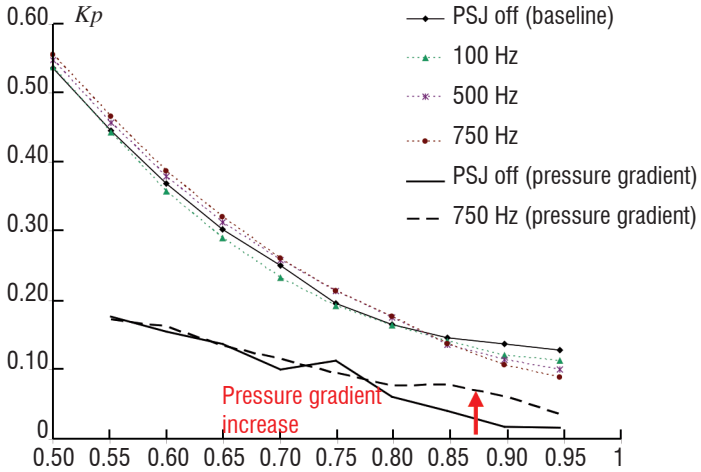

Figure 28 - Pressure distribution curves obtained for a Limited Trailing Edge Separation configuration (U_∞=20 m/s - α =13°)

The actuation efficiency on this separated flow is shown by the increase in the pressure gradient in the trailing edge region, computed from the pressure distribution curve (figure 28). Also, it can be noted that a small value for the PSJ running frequency affects the pressure distribution.

A first example of PIV results obtained for this configuration is presented in figures 29 and 30. The baseline case (PSJ off) is provided, along with the most efficient actuation obtained during these tests, i.e., with the maximum PSJ running frequency (750 Hz). In these

figures, the dark blue area corresponds to the separated flow area, which is no longer present for the “ON” case. Also, vertical velocity profiles obtained 50 mm downstream from the trailing edge, show a 19% drag reduction induced by the actuation (figure 31). Another example of PIV results, obtained with a higher Reynolds number and mean flow velocity is presented in figures 32 & 33.

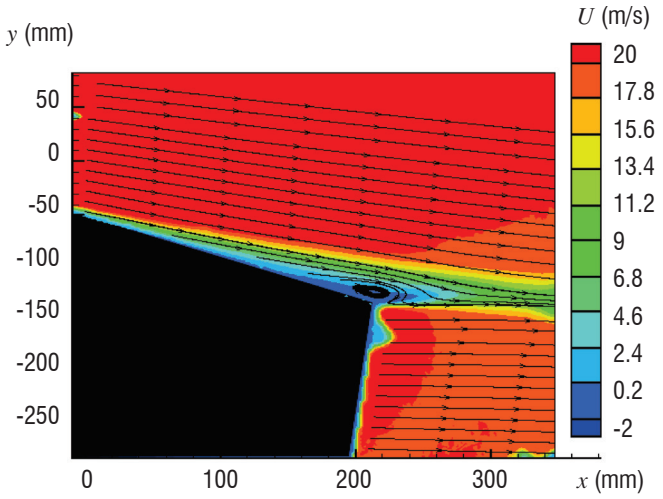

Figure 29 - Baseline flow for a Limited Trailing Edge Separation - U_0=20 m/s – α=13°

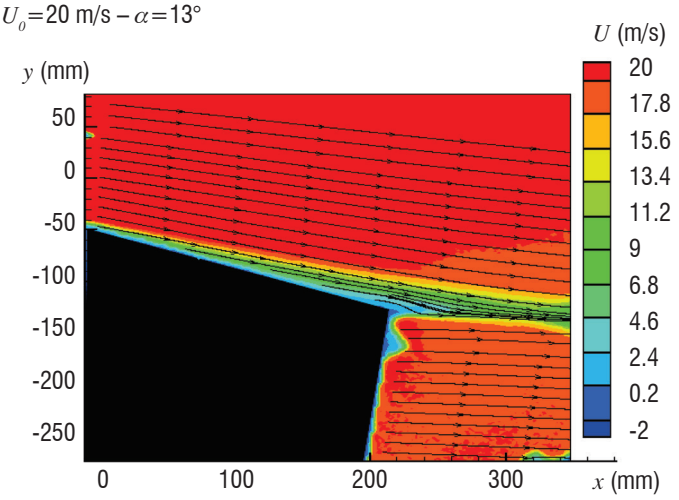

Figure 30 - PSJ actuator efficiency on a Limited Trailing Edge Separation - U_0=20 m/s – α=13°

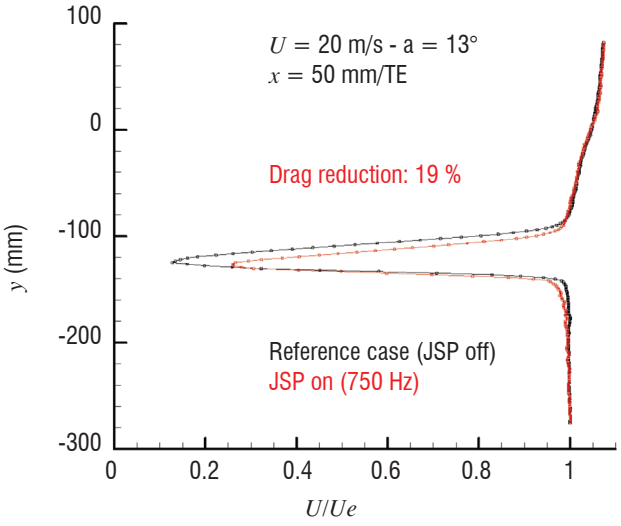

Figure 31 - Efficiency of the PSJ actuators on a Limited Trailing Edge Separation

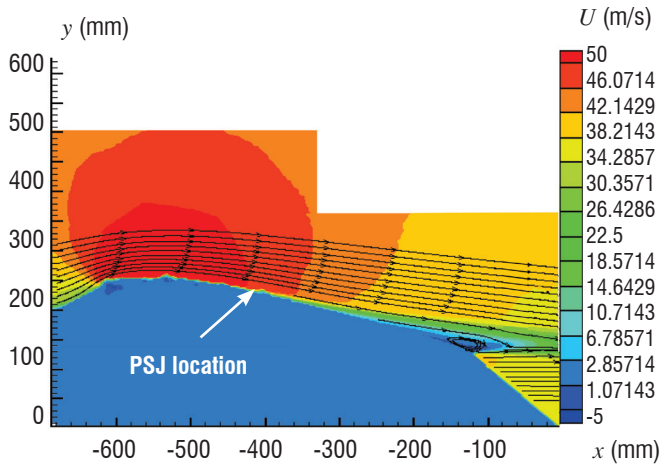

Figure 32 - Baseline flow for a Limited Trailing Edge Separation - U_0=40 m/s – Re=1.2 million

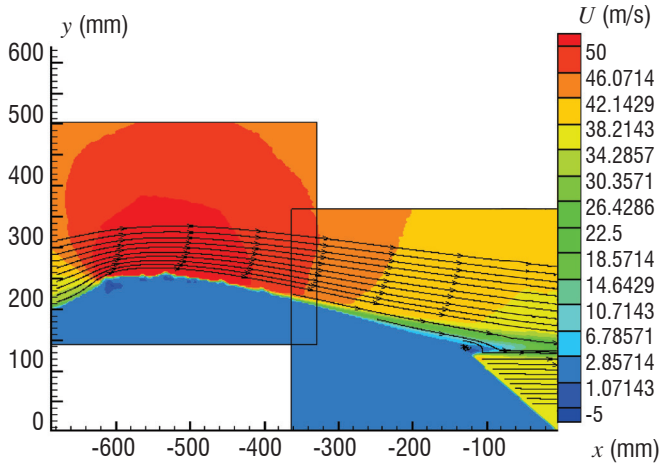

Figure 33 - PSJ actuator efficiency on a Limited Trailing Edge Separation - U_0=40 m/s – α=11° - Re=1.2 million

However, this configuration of limited separation shows that vortexes are convected by the flow on a long distance and that these PSJ generated vortexes keep sufficient energy to act on separation even if actuation is located far upstream. But, the interest could be also to delay massive separations.

Mid chord trailing edge separation

The separation area increases with the angle of attack. A mid-chord separation is obtain for α=11,5° for a Reynolds number of 1.3 10^6 corresponding to a reference velocity of 40 m/s and the 500 mm chord airfoil (figure 34, baseline flow). Three Different frequency actuations have been tested. It can be observed an important delay of separation from the 100 Hertz frequency (figure 35). The separation is almost totally cancelled with the PSJ's actuation at f=250 Hz and f=750 Hz (figures 36 & 37).

Longitudinal velocity profiles along vertical lines in the vicinity of the trailing edge in the separation area can yield more details (figure 38). The red symbols correspond to the baseline flow (with a large reverse flow region). The blue, green and orange symbols correspond to increasing pulse frequencies. As seen in the flow patterns, 100 Hz actuation reduces the size of the bubble, but there is still a reverse flow at the upstream station. 250 and 750 Hz completely reattach the flow at this station and have the same action at the downstream station.

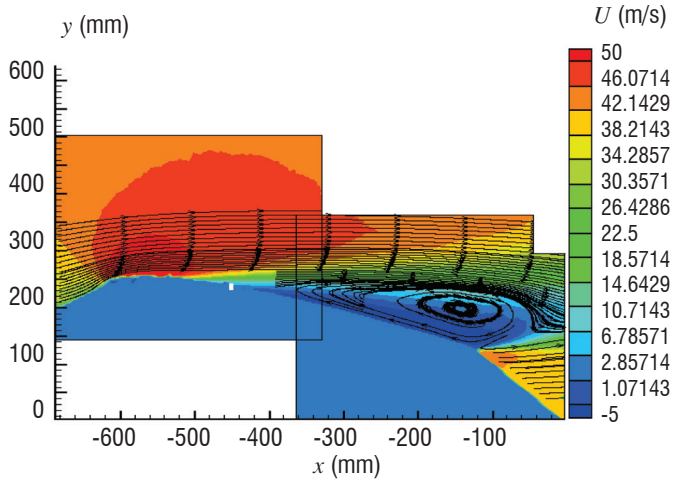

Figure 34 - Baseline flow - U_0=40 m/s - Re=1,2 million - α=11,5°

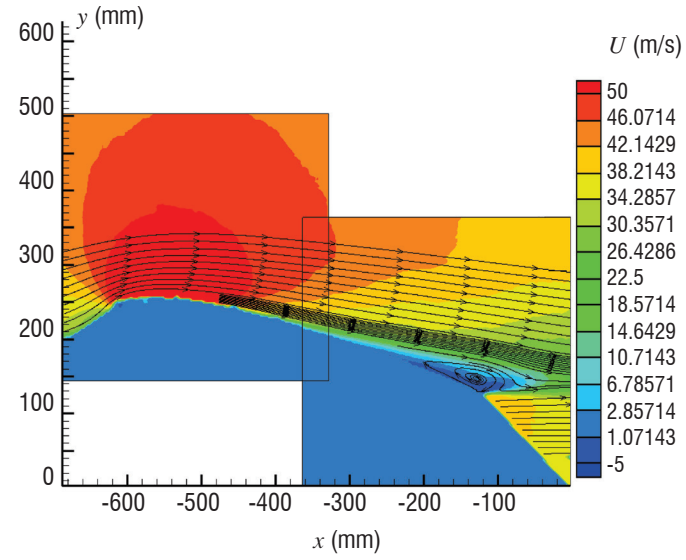

Figure 35 - PSJ on - f=100 Hertz - U_0=40 m/s - Re=1,2million - α=11,5°

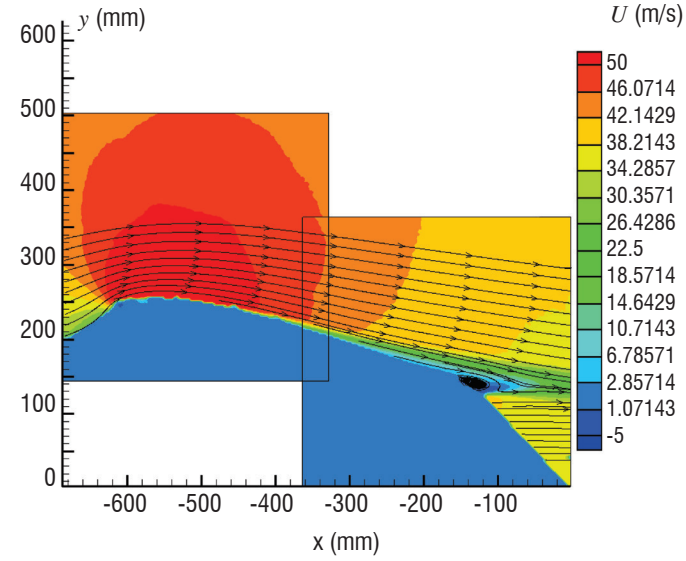

Figure 36 - PSJ on - f=250 Hertz - U_0=40 m/s - Re=1.2 million - α=11. 5°

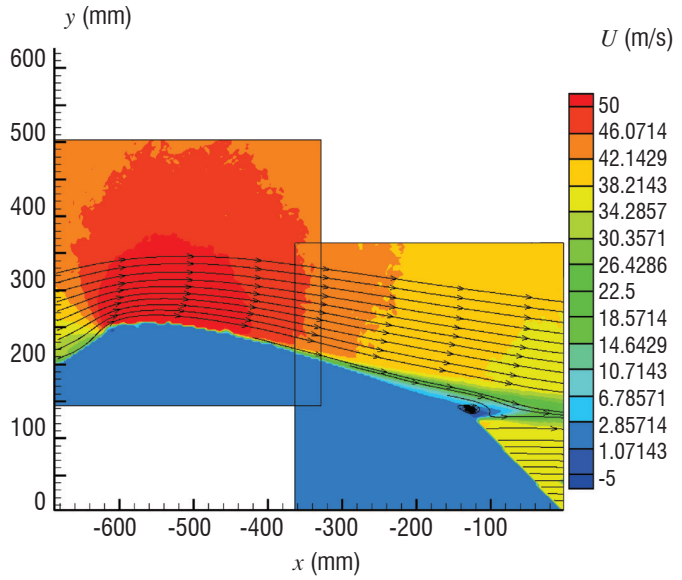

Figure 37 - PSJ on - f=750 Hertz - U_0=40 m/s - Re=1.2 million - α=11.5°

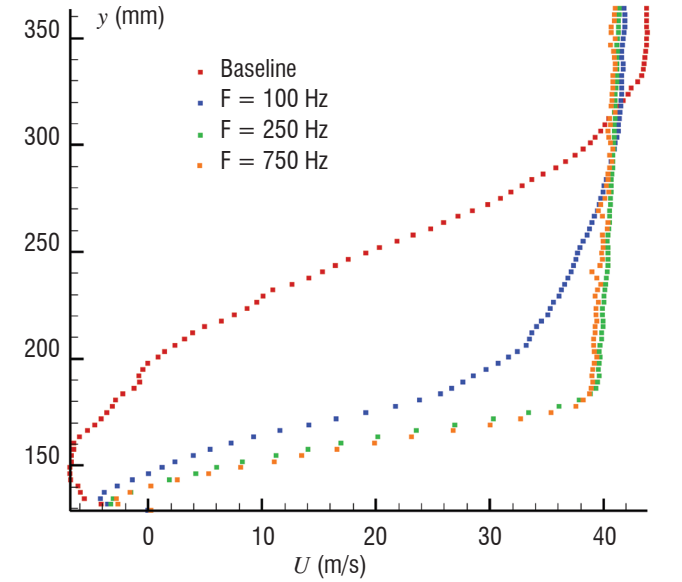

Figure 38: PSJ on - f=100 - 250 & 750 Hertz - U_0=40 m/s - Re=1.2 million - α=11.5°

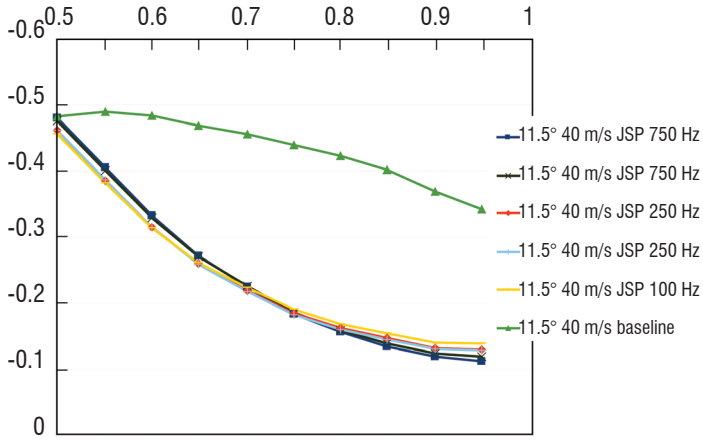

Figure 39 - PSJ on - f=100 - 250 & 750 Hertz - U_θ=40 m/s - Re=1.2 million - α=11.5° - Static Pressure distribution along the airfoil

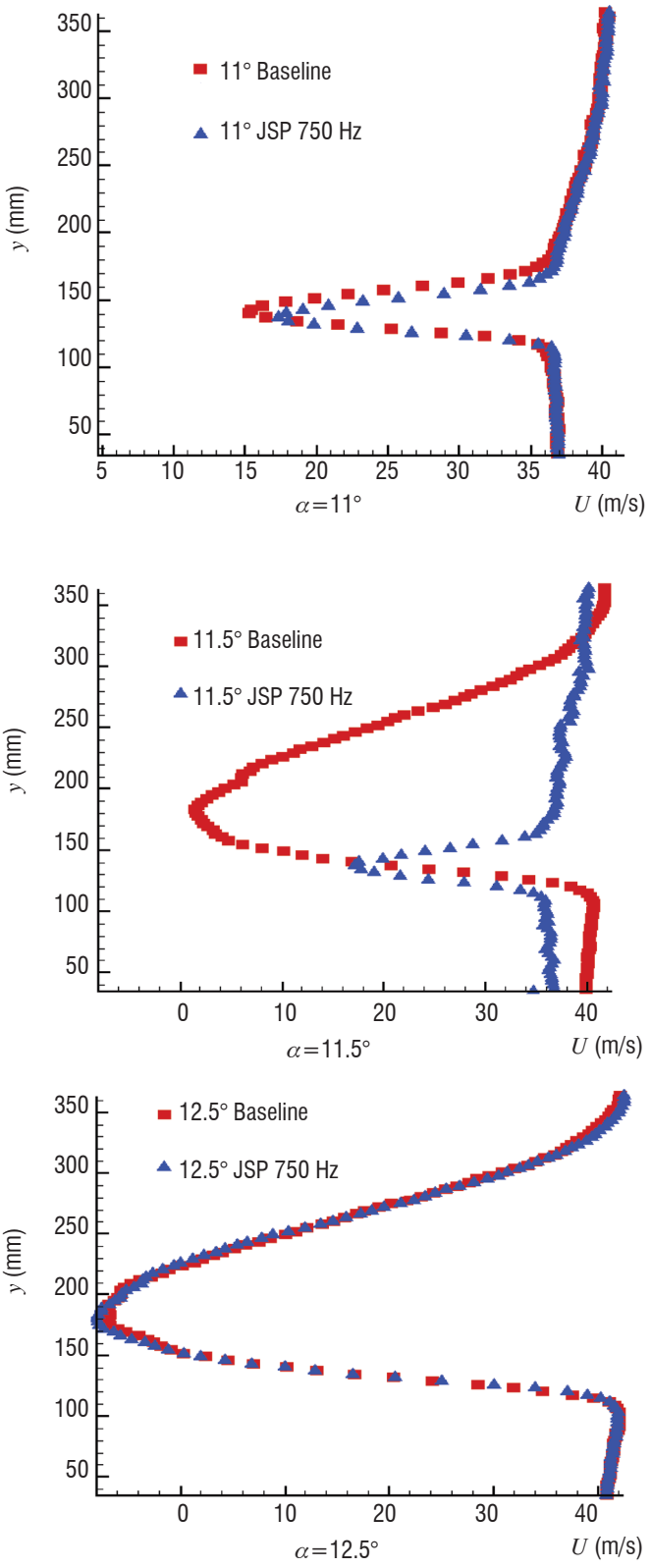

Figure 40 - Wake surveys for α=11 ° to 12.5° . Baseline (red) and PSJ on at 750 Hz (blue)

It appears that there is no visible interest in increasing the pulse frequency above a given threshold, but that below this threshold efficiency decreases with the frequency. These conclusions should be assessed more accurately and the ramp experiment is of additional interest with respect to this parameter.

Finally, the steady static pressure distributions on the rear part of the airfoil (figure 39) simply confirm the PIV results. The baseline flow exhibits a rather constant pressure (characteristic of a separated area), while the configuration PSJ on, shows a nice recompression, also with a slight qualitative effect of the frequency here.

Velocity profiles in the near wake of the airfoil confirm the weak effect at α=11° because of a reduced trailing edge separation, a maximum effect at α=11.5° on a massive separation and no effect at α=12.5° because the separation point is located upstream of the actuation line (figure 40).

The important effect found for 11.5° of incidence shows that the location of the PSJ in relation to the separation area must be precise. The various parameters of the micro-jet generated vortexes, including spacing between these vortexes and the vortex/flow interaction are a key point for understanding the action of these synthetic jets and the influence of the various parameters.

Conclusions

During the PLASMAERO project, the PSJ was developed and characterized, in order to delay airfoil leading edge separation. Mass flow creation by plasma is used to add energy to the flow to improve it. The general physics of the PSJ in the flow concerns the generation of a series of vortices produced at the pulse frequency, which induces a transfer of momentum towards the wall, with a stabilizing effect on the turbulent boundary layer, quite similar to the case of continuous jets, of course with the advantage of zero mass flow. The reaction of the flow to the generated micro-jet is expected to be the key point for understanding the influence of the various parameters. The basic ramp configuration has been a very useful tool to better understand the physics of this action and to determine the parameters driving the efficiency of these devices ■

Acknowledgements

We would like to thank Jean-Pascal Cambronne and Antoine Belinger (Laplace laboratory, Toulouse University) for the definition and realization of the PSJ power supply and for their important support on plasma physics and characterization. We would like to thank Eric Moreau & Antoine Debien (Pprime laboratory, Poitiers University) for providing us with a very good environment for the NACA0015 tests. This work has been performed within the framework of the PlasmAero project (www.plasmaero.eu) funded by the European Community's Seventh Framework Program FP7/2007-2013 under grant agreement N°.234201.

References

[1] K.R. OSSMAN, B.Z. CYBYK, D.M.V.WIE - *SparkJet Actuators for Flow Control*. AIAA 2003-0057.
[2] A. BELINGER & al.- *Influence of the Energy Dissipation Rate in the Discharge of a Plasma Synthetic Jet Actuator.* J.Phys.D : Appl. Phys. 44
[3] D. CARUANA & al. - *The "Plasma Synthetic Jet" Actuator – Aero-Thermodynamic Characterization and First Flow Control Application.* AIAA-2009-1307
[4] P. HARDY & al. - *Plasma Synthetic Jet for Flow Control*. AIAA-2010-5103
[5] J.C. LIN - *Control of Turbulent Boundary-Layer Separation using Micro-Vortex Generator.* AIAA 99-3404
[6] J.L. GILARRANZ & al, - *A New Class of Synthetic Jet Actuators.* Journal of Fluids Engineering, March 2005, Vol. 127 /377-387.
[7] M. CAPITELLI & al, -*Transport Properties of High Temperature Air in Local Thermodynamic Equilibrium*. The European Physical Journal D - Atomic, Molecular, Optical and Plasma Physics, 11:279#28

Nomenclature

C	Capacity of the power supply capacitor
E, E_c	Energy transferred to the Plasma Synthetic Jet
IGBT	Insulated-gate bipolar transistor
F	Frequency of the discharge (Hertz)
M_0, U_0	Free stream Mach number, velocity (m/s)
T	Temperature (K)
V	Plasma jet velocity (m/s)
V_b	Voltage breakdown of the air gap (Volt)

Acronyms

PLASMAERO	(PLASMas for AEROdynamic control , (www.plasmaero.eu))
PSJ	(Plasma Synthetic Jet)
IGBT	(Insulated Gate Bipolar Transistor)
CCD	(Charge Coupled Device (camera))
PIV	(Particle Image Velocimetry)

AUTHORS

Daniel CARUANA is a graduate of the C.N.A.M. (Conservatoire National des Arts et Métiers) and currently a Senior Research Engineer at Onera. He is in charge of plasmas for flow control and also involved in many aeronautics studies for aerodynamic and aero-acoustic control, flow physics, actuators definition and design, control technique. His current research activities focus on flow physics and control (separation, buffeting, jet noise, etc.), plasma physics, actuators (fluidic vortex generator, synthetic jet, plasmas, Trailing Edge Devices), and flow control methods. He has been the coordinator of the PLASMAERO European project (2009 – 2012).

François ROGIER, Engineer of Ecole Centrale de Paris and PhD in Applied Mathematics from Pierre et Marie Curie University, is a Senior Research Engineer at Onera. He is responsible of the UNIT research M2SN (Modelling Mathematics and Numerical Simulation). His current research activities is focused on modelling of plasma flow interactions for subsonic and supersonic applications.

Guillaume DUFOUR received his PhD in Applied Mathematics in 2005 from the University of Toulouse, France. Currently, he is a Research Engineer in the Department of Models and Information Processing at Onera. His research interests include Multi-scale and Numerical Modelling applied to Plasma Discharges.

Christian GLEYZES is a graduate of "Ecole Nationale Supérieure des Techniques Avancées" and is a Senior Research Engineer at Onera. His principal researches were on flow turbulence modelling. Since 2009, his activities focused on flow control by plasma. He is now retired.

T. Yehoshua, A Seifert
(School of Mechanical Engineering,
Faculty of Engineering
TelAvivUniversity)

E-mail: seifert@eng.tau.ac.il

Empirical Model for the Evolution of a Vortex-Pair Introduced into a Boundary Layer

A linear, empirical, low-order-model was developed with the aim of describing the evolution of a 2D vortex-pair ejected into a boundary layer from a slot-in-the-wall. The model describes the evolution of a counter-rotating pair of Lamb-Oseen vortices in the proximity of a wall on which a cross-flow Blasius boundary layer exits. Two inputs from experimental measurements are used. First, the initial locations where the vortices form and pinch-off from the excitation slot boundary layers. Second, the time evolution of the vortex circulation in still-air. With this input, the model predicts the trajectories and vorticity distribution during the interaction. Such a model could be a viable tool for the development of a low-order-model to be implemented as a simplified boundary condition in CFD simulations, with the aim of reducing the requirement to fully resolve the vicinity of the excitation slot in active flow control simulations.

Introduction

In the words of Saffman [1] relating to vortex rings: "…one particular motion exemplifies the whole range of problems of vortex motion… vortex rings…Their formation is a problem of vortex sheet dynamics, the steady-state is a problem of existence, their duration is a problem of stability and if there are several, we have a problem of vortex interactions". It could be added, if we generate desired vortices in a shear layer – we have flow control. Boundary layer sensitivity and adaptivity to high-amplitude periodic-excitation emanating from a slot-in-the-wall is a determining stage in the efficacy of Active Flow Control (AFC) systems. Understanding the governing mechanisms of this interaction and identifying its leading parameters and their optimal values, will allow the boundary layer evolution (e.g., separation delay) to be managed efficiently. Arriving at a CFD design tool is of immense practical importance while the necessity of properly resolving the actuator-slot region is a limiting factor. Therefore, modeling the interaction and providing a low-order, simplified boundary condition for CFD simulation is highly desired.

The inherent complication of even the most conventional AFC application, such as boundary layer reattachment, is expressed by the large parameter space that the designer must optimize. This parameter space is a collection of the baseline flow parameters (boundary layer Reynolds number, turbulent vs. laminar flow, pressure gradient, curvature and more) as well as the excitation parameters (steady vs. oscillatory, slot/hole location and orientation, magnitude (peak slot exit velocity is currently used), frequency and more, as presented by the relevant Strouhal, Reynolds and Stokes numbers.

The aim of the experimental part of the study [2-4] was to methodically isolate and document the effects of the governing parameters of this complicated problem, with an emphasis on the excitation parameters. The huge parameter space was limited to the case of a laminar boundary-layer with zero pressure-gradient and to Zero-Mass-Flux (ZMF) oscillatory excitation from a slot-in-the-wall. The key parameters under study were the excitation magnitude, frequency, orientation (wall normal, upstream or downstream directed shallow-angle excitation) and frequency (only pure sine excitation would be considered here), maintaining nominally 2D conditions. Two-dimensional Particle Image Velocimetry (PIV) measurements, as well as hot-wire, temperature and pressure measurements were performed, in order to achieve high spatial and temporal resolution of the physical processes taking place during the complex interaction.

The nature of the excitation in quiescent fluid was initially studied [2], [4], in order to document the effect of each of the leading parameters without the presence of the cross-flow boundary layer. The measurements show that different boundary conditions at the actuator's exit-slot dictate an entirely different vorticity dynamics, which results in different initial vortex circulation, different formation locations, different decay rates and circulation signs that "survive" to later interact with the boundary layer and significantly different vortex convection velocities.

A threshold excitation magnitude was identified, in agreement with published vortex escape criteria [5]. When the excitation magnitude was lower than the threshold, the vortices were sucked back into the actuator cavity and the average external flow field remained practical-

ly stagnant. For supercritical cases, in which the excitation magnitude was sufficient to release vortices, the vortex circulation and convection velocity were found to approximately scale with the excitation magnitude [4].

The interaction of the excitation with the cross-flow laminar-boundary-layer was measured and is currently being analyzed and modeled. The excitation direction was found to be a leading parameter when considering the resulting vorticity dynamics. Details of the vortex circulation and trajectories will be presented and compared to the model. In practical terms, upstream directed excitation was the most effective in tripping a sub-critical boundary layer [3]. Downstream directed excitation was proven to be the most efficient for applications such as boundary layer reattachment due to the increased skin-friction, whereas wall-normal excitation was the least effective configuration tested in the context of practical active flow control applications. However, for simplicity and convenience, we initially model the wall-normal excitation boundary-layer interaction.

The process of vortex generation due to high-amplitude slot or hole excitation is tightly linked to the physical process enabling the generation of vortex rings in still fluid [6]. The vorticity ejected from the inner slot-channel during the blowing part of the cycle is generally accepted [7] to determine the resulting vortex circulation.

While the analogy to vortex ring generation by a piston-and-cylinder arrangement is quite appealing, especially for ramp-up-ramp-down piston motion, it breaks down because the piston only moves out and comes to a halt. This contrasts with the nature of the ZMF actuator generating high-amplitude excitation, for which half of its operation cycle is characterized by suction.

Models for the development of ZMF excitation in still air are rare. One example can be found in [8], which presents a low-order-model of computationally generated ZMF excitation in still-air. The authors use Proper Orthogonal Decomposition (POD [9]) to model the flow field in the actuator vicinity and show that only four modes are needed to represent this simple flow quite successfully. However, it is clear that this simplicity and low order cannot be maintained in more complex situations and certainly will not be capable of predicting situations dominated by cross-flow, three-dimensionality and transition to turbulence. An idea on the complexity of real-life 3D interaction of jets in cross-flow can be gained from [17].

Models describing vortices moving towards a wall are relevant to the current application, with the motion direction reversed. Such models take into account the image vortex system due to the vicinity of the wall. Lamb [10] proposed a simple model to describe a vortex-pair interaction with a wall. Clearly, away from the wall, the 2D vortices induce a constant velocity on each other, leading to their constant convection rate and straight, wall-normal trajectory. As the vortex pair approaches the wall, the image vortices have a growing effect, pushing the vortices away from each other. The trajectories were also computed as (for constant circulation): $x_1^2\left(x^2+y^2\right)=x^2y^2$, where y is the wall normal direction and x the wall tangential direction, with the origin at the slot exit (see figure 3) and $2x_1$ is the separation between the vortices in the pair far from the wall. Certainly, a family of such trajectories can be found to pass through every set of initial vortex-pair locations, $x=\pm x_1$ and $y=y_1$. The challenge, as in the model to be detailed in this paper, is to select a relevant initial vortex-pair location, and define its circulation based on a given actuator design. More importantly, derive actuator design laws that will maximize the desired alternation in the boundary layer vorticity distribution.

A family of point-vortex models has been developed by Karwiet [11] and Sheffield [12], describing the motion of a vortex pair close to an opening in a wall or a pipe inlet. Case I in the work by Sheffield is actually the closest in geometry to the present wall-normal excitation. As Karweit explains: "if the hole (opening) is large enough, the vortices will pass through; if it is too narrow (relative to the distance between the vortices), they will separate and follow diverging paths without going through". In the words of Sheffield: "If the vortex pair starts too close to the wall, then it will not travel away from the wall, but into the channel". It has been noted experimentally that as the peak velocity of the piston or slot exit velocity increases, not only the vortex circulation increases, but the location from the slot exit in which the vortex reaches its peak circulation and pinches-off also increases. Therefore, knowing the initial vortex location and accepting that its initial location depends on the excitation magnitude will allow the "vortex formation criteria" of Holman et al. [5], which have also been identified in several earlier studies, to be modeled. The Karweit [11] and Sheffield [12] potential flow vortex models use a single vortex placed close to half the width of the opening geometry (assuming a symmetry line) and using the Schwartz-Christoffel transformation to map the flow. In the transformed flow, the Routh [13] quasi-stream-function allows the vortex trajectory to be calculated. Despite its capability to describe the complex behavior of the vortex-pair in the vicinity of the slot, this approach cannot be extended to consider the interaction of the vortex-pair with a cross-flow boundary layer, or even consider the case where the magnitudes or initial locations, or the vortices in the pair, are not identical, as is the case for an inclined slot. Therefore, the development of a numerical model composed of similar elements is warranted. The basic ingredient in every such model is the isolated vortex.

The selection of an isolated vortex model is not straightforward. Many inviscid vortex models exist [14]. It is obvious that for the current application, a point vortex is not suitable. Also, the decay of the vortex circulation during the second half of every excitation cycle cannot be neglected. This effect would be modeled based on experimental findings of a vortex pair evolution in still-air [2-4].

The interaction of the vortex-pair with the external cross-flow boundary-layer will be performed by a simple superimposition of the vortex system with a Blasius boundary layer. Since we are dealing also with the imaged vortex-pair system, the image boundary layer will also be modeled, otherwise the wall could not remain a symmetry line.

The paper includes an empirical mathematical modeling of the excitation developed in still-air and in the presence of a laminar cross-flow boundary-layer. It also provides a detailed comparison with experiments. The experimental set-up will not be presented here. The reader is referred to earlier papers by the current authors for that matter.

Model and Results

Isolated vortex model

The first choice to be made before attempting to model the interaction between high-amplitude excitation with still or co-flowing fluid is the type of vortex model to use. Many models with increasing levels of

complexity exist (e.g., [14],[15]) and it is beyond the scope of this paper to review these options. Rather, an appropriate vortex model can be selected by considering the current experimental results [4].

The choice of a vortex model and its validation should be performed as close as possible to the excitation slot, but after the vortex-pair had been formed. This is because once a vortex model had been selected, only its initial position and circulation will determine the entire evolution sequence and enable its dynamic evolution through the first oscillation cycle to be modeled.

The data presented below clearly shows that the vortices generated by the apparatus described in [4] can be represented fairly well by the two-dimensional Lamb-Oseen vortex model (Lamb [10]; Batchelor [16]) as detailed below and compared to experimental data. The Lamb-Oseen vortex is a solution of the Navier-Stokes-equations only under the assumption of axial symmetry. Axial symmetry can be assumed locally valid only if the distance between the vortices is large compared to their radius. Since the axial symmetry should be allowed to break, to empirically model the experiments, each vortex forming the 2D pair is modeled individually. In the current model we allow the distances between the vortex cores to become of the same order as the vortex radii, and our only justification is success in modeling the interaction.

The circumferential velocity, v_θ, out-of-plane component of vorticity, ω, circulation, Γ and radius scaling factor, δ, of the Lamb-Oseen vortex model are given by the following expressions:

$$v_\theta = \frac{\Gamma_0}{2\pi r}\left[1-\exp\left(-\frac{r^2}{\delta^2}\right)\right] \quad (1)$$

$$\omega = \frac{\Gamma_0}{\pi\delta^2}\exp\left(-\frac{r^2}{\delta^2}\right) \quad (2)$$

$$\Gamma = \Gamma_0\left[1-\exp\left(-\frac{r^2}{\delta^2}\right)\right] \quad (3)$$

$$\delta^2 = r_0^2 + 4\nu t \quad (4)$$

Where r_0 is the initial vortex radius (at $t=0$) and ν is the kinematic viscosity.

Figure 1 presents experimental data and a curve fit of the vertical velocity profile taken between the centers of the vortex pair as measured experimentally (and along the horizontal line, as shown in figure 3). The fitted curves for the wall-normal velocity, v, are in the form:

$$v = v_\theta = \frac{\Gamma_1}{2\pi(x-x_1)}\left[1-\exp\left(-\frac{(x-x_1)^2}{\delta_1^2}\right)\right] + \frac{-\Gamma_2}{2\pi(x+x_2)}\left[1-\exp\left(-\frac{(x+x_2)^2}{\delta_2^2}\right)\right] \quad (5)$$

Which resulted in $R^2=0.99$, where x_1 and x_2 are the vortex centers and δ_1 and δ_2 are the vortex radii. Note also that we do not limit our discussion to identical circulation vortices or even radii, since inclined and non-straight excitation slots will generate uneven vortices.

Figure 1 shows vorticity contours calculated from experimental PIV data (snapshot, phase locked, [2]) showing velocity vectors also. The jet emanating from the actuator slot and the vortex pair can be clearly identified. The dashed horizontal and vertical lines represent the lines on which velocity and vorticity data was extracted and fitted, in figures 2 and 3 respectively.

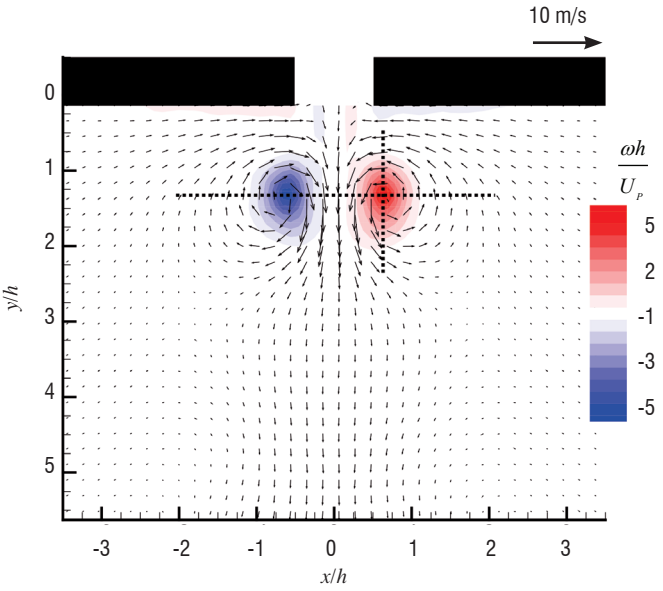

Figure 1 - Velocity vectors and vorticity contours of wall-normal excitation in still-air [2], The dashed lines represent the locations of the velocity profiles that were fitted and presented in figures 2 and 3. The slot width h=1mm.

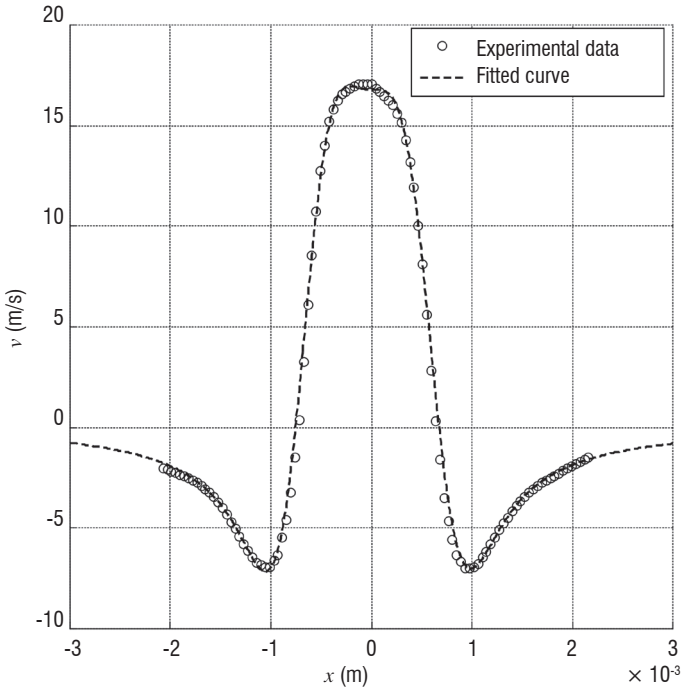

Figure 2 - Vertical velocity at t/T=0.625 (with respect to the velocity cycle at the slot) and its Lamb-Oseen curve fit (Eq. 5). Wall-normal excitation, $St=fh/U_p$=0.059 (f=1060Hz), with $ReU_p=hU_p/\nu$ =1200 (U_p=18m/s) in still-air. Where h is the slot width h=1mm), f is the excitation frequency, Up is the slot peak velocity and ν is the kinematic velocity

In order to validate the model, a Gaussian distribution was fitted to the vorticity profile calculated from the PIV measured velocities, along the horizontal line that is shown in figure 1. The vorticity profile and the

fitted curves are in very good agreement, as can be seen in figure 3. It is stressed that while the Lamb-Oseen vortex model is strictly valid in axis-symmetric flow and therefore at large distances between the vortex centers, we will use it empirically to model the current vortices, even when the distance between the vortices forming the pair is of the same order as their diameter. The results shown in figures. 1-3 clearly show the suitability of the Lamb-Oseen vortex model to describe the evolution of a single vortex forming a vortex-pair in still air. In the following sections, each vortex is modeled independently and symmetry is not imposed. It should be mentioned that the fit between the experimental data and the empirical Lamb-Oseen model are not always as good as seen in figures 2-3 and a comprehensive uncertainty analysis has not been performed. Furthermore, in the subsequent model the circulation, Γ_0, is not constant as in the original Lamb-Oseen model, but rather it is allowed to be *empirically* time dependent, according to the experimental findings in still-air.

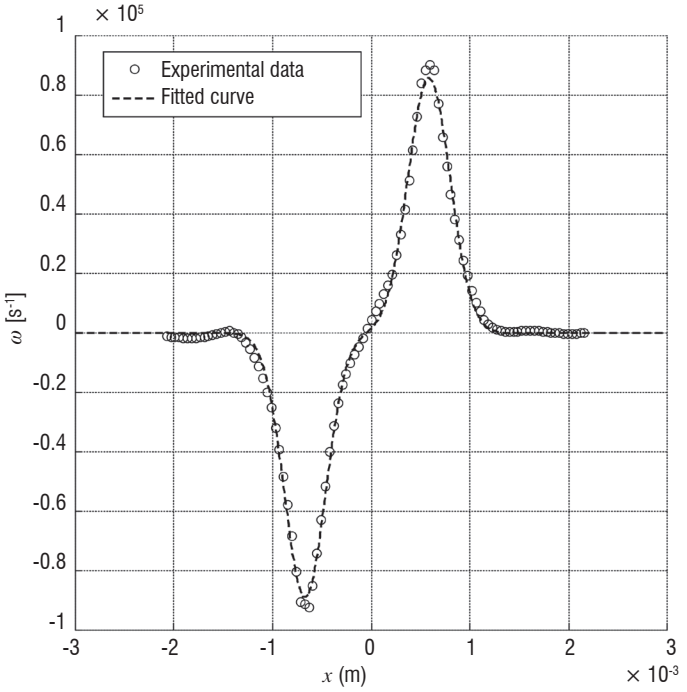

Figure 3 - Vorticity distribution at t/T=0.625 (with respect to the velocity cycle at the slot) and its Lamb-Oseen curve fit (eq. 2). Wall-normal excitation, St=0.059 (f=1060Hz), with Re_{U_p}=1200 (U_p=18 m/s) in still-air.

Four vortex interaction model

We initiate the analysis once the vortices have formed near the slot exit and define a system of four Lamb-Oseen vortices, as shown in figure 4. Each vortex in the system is defined according to eqs. 1-5. The wall is modeled as a symmetry line along the x axis, at y=0. The existence of the excitation slot is not included in the current state of the model.

The empirical justification to use the above approach stems from the success of the two vortex model to simulate still-air experiments. Hence, we attempt to expand it, although we do not use point vortices. Obviously, in viscous fluid, four vortices with no wall are not equivalent to two vortices and a wall. The assumption should be that the distance of the vortices from the wall is large compared to their diameters. Since this is not the case presently, we still have to convince the reader that the model works out of its designed range of formal applicability.

Let us consider the kinematic equations of motion for the 1st vortex, with a circulation $\Gamma_{0,1}\equiv\Gamma_0$, as described by its position vector $\vec{x}_1=(x_1,y_1)$. Once the position vector for the 1st vortex is defined, as well as its circulation, the following statements can be made regarding the four-vortex model, as shown in figure 5:

1. The coordinates of the other vortex forming the pair are given by $\vec{x}_2\equiv(x_2,y_2)=(-x_1,y_1)$, and its circulation is given by $\Gamma_{0,2}=-\Gamma_{0,1}$;
2. The images of vortices 1 and 2 are represented by vortices 4 and 3, respectively. Their coordinates are given by $\vec{x}_3\equiv(x_3,y_3)=(x_2,-y_2)$ and $\vec{x}_4\equiv(x_4,y_4)=(x_1,-y_1)$, and their circulations are given by $\Gamma_{0,3}=-\Gamma_{0,2}$ and $\Gamma_{0,4}=-\Gamma_{0,1}$.

Once all the vortex positions and circulations are defined, the kinematic equations of motion for Vortex 1, due to the induced velocities from the other three vortices in the system, can be written in the following manner, in terms of x_1, y_1 and Γ_0 only:

$$\dot{y}_1=\frac{\Gamma_0}{2\pi}\left\{\frac{1}{2x_1}\left[1-\exp\left(-\frac{4x_1^2}{r_0^2+4\nu t}\right)\right]-\frac{x_1}{2\left(x_1^2+y_1^2\right)}\left[1-\exp\left(-\frac{4\left(x_1^2+y_1^2\right)}{r_0^2+4\nu t}\right)\right]\right\} \tag{6a}$$

$$\dot{x}_1=\frac{\Gamma_0}{2\pi}\left\{-\frac{1}{2y_1}\left[1-\exp\left(-\frac{4y_1^2}{r_0^2+4\nu t}\right)\right]+\frac{y_1}{2\left(x_1^2+y_1^2\right)}\left[1-\exp\left(-\frac{4\left(x_1^2+y_1^2\right)}{r_0^2+4\nu t}\right)\right]\right\} \tag{6b}$$

In a similar manner, the motion of all other vortices can be calculated using the above definitions, as presented hereafter.

The peak vorticity magnitude of a single vortex model is found by substituting r=0 into eq. 2:

$$\omega_{\max}=\frac{\Gamma_0}{\pi\left(r_0^2+4\upsilon t\right)} \tag{7}$$

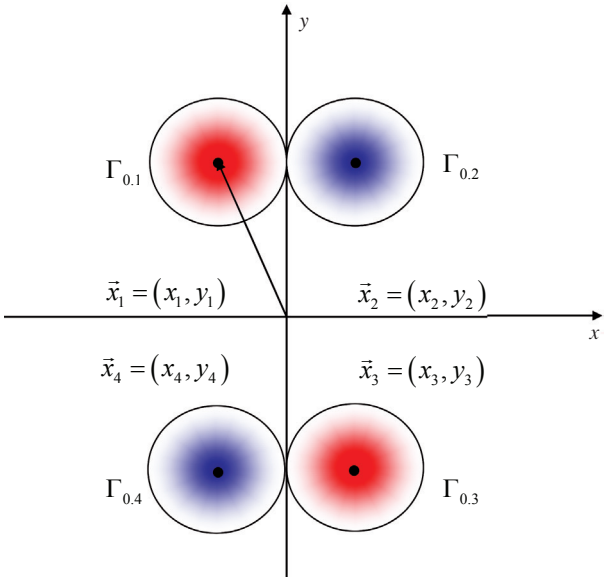

Figure 4 - A system of four Lamb-Oseen vortices

One of the prime targets of the current effort is to empirically model the time development of the experimental interaction of a vortex-pair with a cross-flow laminar boundary layer, including the time evolution of the vorticity. The initial vortex position vector is $\vec{x}_i(t=0)$.

The equations of motion for the vortices, as described above, can be written as a combination of the induced velocities at the vortex position. It is possible to calculate the motion of the *i-th* vortex in the above system using the following general equations:

$$\dot{\vec{x}}_i = \sum_{i \neq j} \vec{u}_j^{ind}\left(\left\|\vec{x}_i - \vec{x}_j\right\|, \Gamma_{0,j}(t)\right) \quad (8a)$$

$$\dot{\Gamma}_{0,i} = \dot{\Gamma}_{0,i}^{Baseline} \quad (8b)$$

The induced velocities are calculated from a vector summation of eq. 1 (or according to eqs. 6a and 6b). Equation 8 simply states that the motion of the *i-th* vortex is due to the superimposition of the induced velocities by the other three vortices (meaning the counter rotating vortex-pair and their corresponding images) and the velocity of the boundary layer at the vortex core locations (when the boundary layer free-stream velocity $U_e \neq 0$). Within the framework of the current model, a time dependent circulation of the *i-th* vortex, $\Gamma_{0,i}(t)$ is used. The evolution of the vortex circulation is obtained from the still-air experiments and used as input to the empirical four-vortex boundary layer interaction model. This is due to the Lamb-Oseen vortex model, which does not allow the circulation to decay during its entire "lifespan", whereas the measurements [2-4] clearly show that the vortex circulation decays with time. Modeling the physical mechanism that is responsible for the circulation decay is beyond the scope of this paper.

The time dependent vortex radius, $\delta(t)$, which is affected only by diffusion in the original Lamb-Oseen model, should grow with time to account for vorticity diffusion, but not dissipation.

From the experimental observations, one can hypothesize that the vortex evolution and resulting circulation is affected by several factors. The vortices do not remain circular, but rather they become elliptic, especially when they are very close together. To better represent experiments, the model vortices remain circular, but when compared to the experimental data, their circulation is reduced artificially using the "proximity factor", which will be discussed in the following section.
In the following section, we define and examine the meaning of each parameter affecting the vortex boundary layer interaction.

Vortex Circulation

The calculation of the vortex circulation was performed numerically on experimental findings. The termination of the surface integral of the vorticity distribution should be performed at a comparable level of vorticity, as compared to the peak vorticity of the vortex at that specific time and location, $\omega_l/\omega_{max}(t)$. A relative level $\sim O(10^{-2})$, was used throughout. Sometimes, a line rather than surface integral was used, according to the Stokes theorem:

$$\Gamma = \int_{A_{vortex}} \omega(x,y)\,dA = \oint_c \vec{u}.\vec{dl} \quad (9)$$

One can define the parameter A_{vortex} as the area enclosed by a contour C that corresponds to 1% $\omega_{max}(t)$ vorticity. In the model, this curve is always circular, as required by the undisturbed Lamb-Oseen vortex model.

In order to allow comparison of the model results to experiments, several ad-hoc assumptions need to be made. While in the model, the vortices are assumed circular;, they are not measured as such in the experiments. When the vortices are close together, they appear elliptic. In order to allow a comparison between the linear model (in which the circulation cannot alter due to the Helmholtz condition), a "proximity factor" was introduced. The mechanism, to be detailed below, is not used to alter the vortex circulation in the model, but rather only to compare the model results to the experiments once the model results have been obtained. Furthermore, the trajectories of the model are compared to the experiments without any assumption or correction.

Figure 5 presents two cases: (a) a single Lamb vortex and (b) two similar "near-by" counter-rotating Lamb vortices (with the same peak vorticity magnitude as in case (a), but of opposite sign). The same minimum vorticity level, ω_l, is presented in figures. 5a and 5b for each case (as the red line).

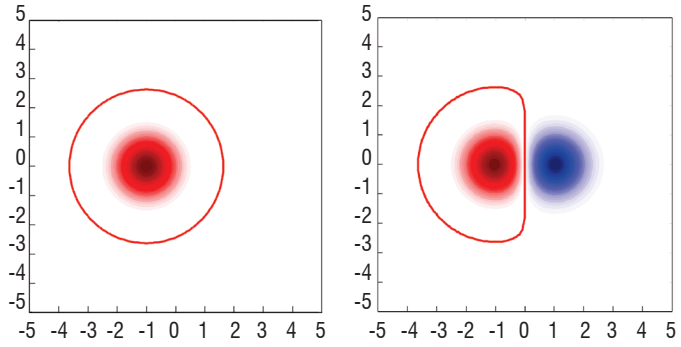

(a) A single Lamb vortex (b) Two near-by counter-rotating Lamb vortices

Figure 5 - A sketch showing the partial mutual cancellation of two nearby counter-rotating "Lamb" vortices with similar initial circulation (Γ_0, according to eq. 5) was used in both cases. The solid line represents the vorticity level ω_l

Clearly, the calculated circulation of the positive ("red") vortex will not be the same in both cases, due to the overlap of the vorticity from the opposite signed vortex, even though Γ_0 is identical in both cases. A sequence of such cases was analyzed, in order to calculate the effect of the proximity factor, s/δ (where s is the distance between the vortex centers, and δ is the undisturbed vortex radius), on the resulting calculated circulation, as measured in the experiments and calculated from experimental data. Figure 6 presents the ratio between the calculated circulation and the proximity factor.

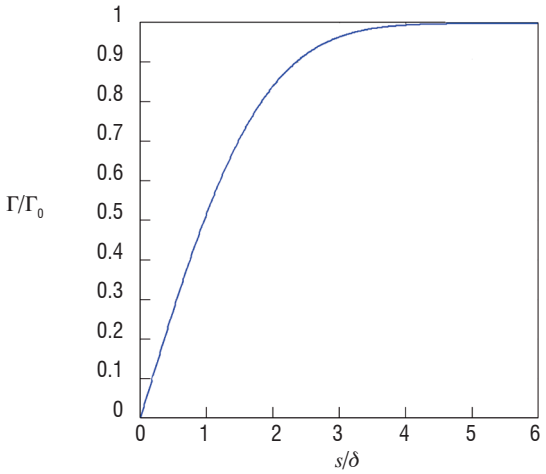

Figure 6 - Circulation reduction "measurement" due to the proximity (s/δ) between two counter rotating "Lamb-Oseen" vortices. δ is the calculated circulation; Γ_0 is the model circulation, as substituted into eqs. (1)-(3)

Naturally, when the distance between the two vortices is zero, the vortices completely overlap in such a way that the circulation calculated on a surface containing both becomes null. Generally, this is the case in any other closed line containing two identical magnitudes and opposite signed 2D vortices. Also, when the distance is large enough, say $s/\delta>5$, the vortices do not overlap. When the distance between the vortex centers is O(1), as seen experimentally, some 50% of the circulation, measured around one of the vortices only, should be reduced in order to match the experiments.

A vortex-pair in still-air

In order to fit the parameters of the Lamb-Oseen vortex model to the experimental data, the time evolution of the vortex circulation, $\Gamma_0(t)$, and the initial vortex radius, r_0, should be extracted from the phase-locked PIV data. These parameters, with the effect of the "proximity factor" (increasing the circulation to be used in the model with respect to the experiment) should enable the prediction of the flow field evolution reasonably well, initially in still-air.

The time evolution of the vortex-pair circulation in still-air for the wall-normal excitation, is presented in figure 7a. Previous publications have shown that the circulation time evolution is fairly self-similar (for the cases where the excitation magnitude is supercritical, i.e., the vortices "escape" the suction effect) for several boundary conditions. In a modeling effort, the critical vortex formation condition can be predicted for both line and ring vortices, using the St-Re condition of Holman et al. [5]. In contradiction to known vortex models, the circulation of the vortices forming the vortex-pair, even in still-air, decays with time in experiments. This decay could be explained by several possible mechanisms. First, partial overlap of the vorticity with opposite signs forming the pair, once the distance between the vortices forming the pair is smaller than two diameters. It was established however, that this effect cannot explain the magnitude of the circulation decay. Interaction with residual circulation of opposite sign at the vicinity of the slot and the effect of viscosity induced decay can also affect it. Three-dimensional effects, transition to turbulence and interaction with turbulent structures can also reduce the measured circulation. Certainly, under turbulent flow conditions, the 2D assumption no longer holds.

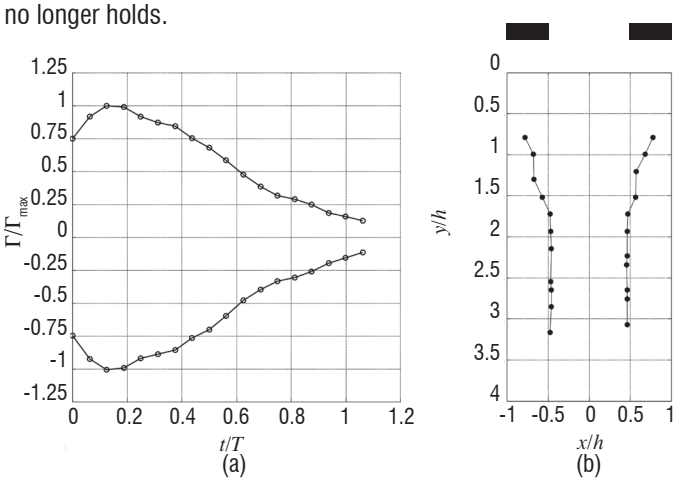

Figure 7 - (a) Normalized computed circulation time evolution for the PIV measured wall-normal excitation and (b) vortex trajectories (the left curve is that of the negative circulation vortex and the right one is for the positive one). U_p=18[m/s] f=1060[Hz]. The slot is 1h wide (h=1mm) and centered on (0,0)

In this paper. t=0 is defined as the first instant when a coherent vortex can be detected in the flow field (and not when V=0 at the center of the slot exit and at the beginning of the blowing cycle). The time lag between the initiation of the blowing velocity cycle at the slot and the formation of a vortex at the vicinity of the slot must be modeled using detailed experiments, CFD and available theoretical considerations. Experimental vortex trajectories are presented in figure 7b, where the vortex location was identified by the peak vorticity (and not by the peak angular momentum, as presented in previous publications by the current authors, due to modeling convenience).

The time evolution of the circulation computed from the experimental data in still-air, using a surface integral on the vorticity, as presented in figure 7a, might be biased due to the effect of partial overlap of the vortex vorticity, as discussed above. Therefore, a "proximity factor" s/δ (where s is the distance between the two vortex centers and δ is the vortex radius) is introduced and it could be computed from the trajectories presented in figure 7b. An initial estimation of this distance, based solely on the initial vortex locations, can be computed from the Lamb-four-vortex model [10] or by the Karweit [11] and Sheffield [12] models.

An additional variable that must be defined for the subsequent computation of the proximity factor is the vortex radius, $\delta(t)$. The Lamb-Oseen model states that the vortex radius increases due to diffusion, according to $\delta^2(t)=r_0^2+4\nu t$. Lamb-Oseen vortex models had been fitted to the measured vorticity field in two directions. Clearly, it is desired to calculate a representative radius based on some integral feature, but the procedure below is used merely in order to establish the limits. The first fit was on a horizontal dashed line passing through the centers of the two vortices, as shown in figure 1, and according to eq. 5a, as shown in figure 3.

The second type of fit was performed along the vertical line passing through the center of the positive vortex, as shown by the vertical dashed line in figure 1, and was in the form:

$$\omega(y)=\frac{\Gamma_1}{\pi\delta_1^2}\exp\left(-\frac{(y-y_1)^2}{\delta_1^2}\right) \qquad (10)$$

The resulting estimations for the vortex radius obtained from the above-mentioned fits are presented in figure 8b. One can note that there is a significant difference in the results according to the two methods for estimating $\delta(t)$. One should recall that the Lamb-Oseen vortex model is axisymmetric. The experimentally measured vortices undergo a significant stretching in the wall-normal direction as they travel away from the slot and therefore the radius in the wall normal direction increases significantly, as shown in figure 8b, while the radius in the horizontal direction remains approximately constant (these two directions could also be considered to be related to the small and large axes of an ellipse), as is also shown in figure 8b. The resulting circulation, calculated for a Lamb vortex with diameter obtained from a vertical (y) profile, will be significantly larger than that calculated according to a vortex radius calculated using the radius obtained from a cut through the vortex in a horizontal plane. The same magnitude of the vorticity peak is used in the model, regardless of its stretching. An example of this effect is shown in figure 8a. Three sets of data are shown. The "numerical integration" is calculated directly from the experimental data. The two other sets are calculated assuming a circular Lamb vortex, with the same peak vorticity but with $\delta(t)$ from figure 8b. The differences are self-explanatory. Currently, the vertical cross-section through the vortex core (along the dashed vertical line in figure 1) is used to evaluate the vortex radius. The linear fit to the vortex radius, as computed by the horizontal cut through the experimental vorticity data, is:

$$\delta^2 = 5.1*t/1000+8.7*10^{-8} \quad (11)$$

Its slope is significantly larger than 4ν (the radius squared, according to eq. 4, is also shown in figure 8b), but the evolution is linear, as Lamb's model requires. The above equation represents a much faster expansion rate than the Lamb-Oseen vortex model predicts, because it accounts only for laminar vorticity diffusion. As a first order approximation, the model for the vortex radius, as expressed in eq.11, is used for the following computations to be subsequently presented. We will allow the slope of to vary, in order to better fit the data of the vortex-boundary layer interaction. Other vortex pair data sets are required to formulate a more general form of the vortex radius. The logic for allowing the same trend but with a different viscosity could be justified on similar arguments that lead to the widely accepted turbulent eddy viscosity model. Higher turbulence levels could also explain the rapid decay rate of the circulation. Figures 9a and 9b present the resulting proximity factor, s/δ, and the ratio between the model circulation and the expectation to the measured circulation, Γ_{exp}/Γ_0, as a function of time, respectively. One can note that the experimentally measured vortices are expected to show approximately 30% lower circulation in comparison to their potential counterpart, due to the partial overlap (figure 9b).

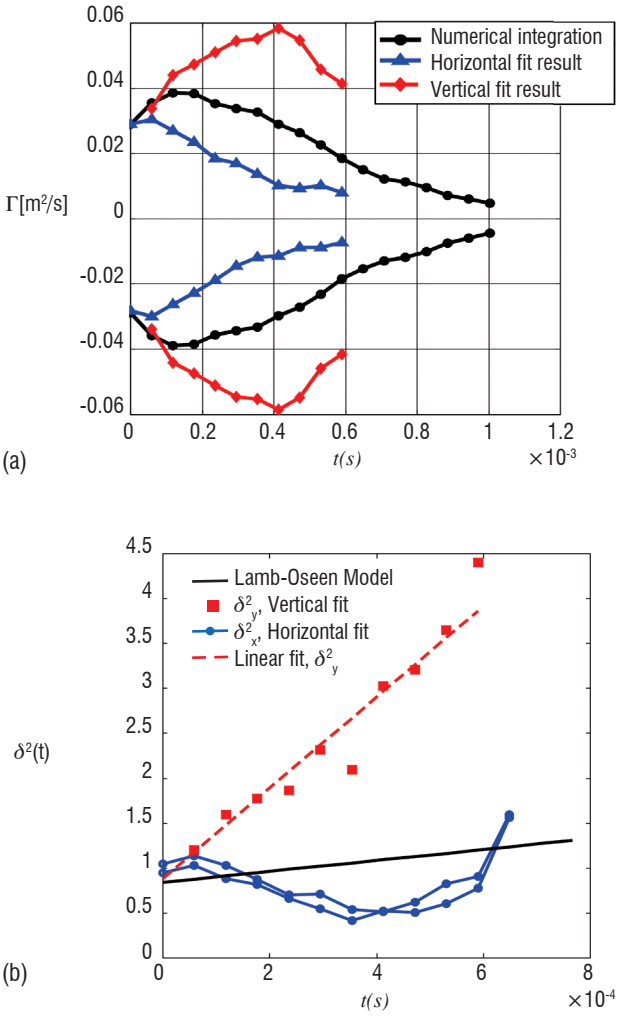

Figure 8 - (a) Circulation time evolution comparison for wall-normal excitation, as fitted by horizontal and vertical profiles and as computed using 2D integration scheme. (b) Radii of the vortices, as fitted by horizontal and vertical profiles. The black line in (b) is $\delta^2(t) = r_0^2 + 4\nu t$, with r_0^{-1}

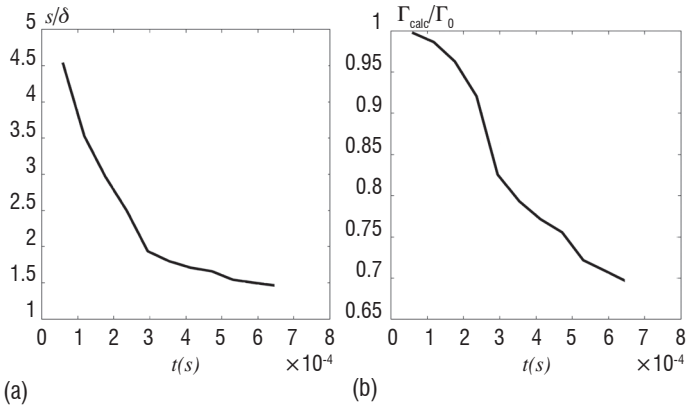

Figure 9 - (a) The experimental proximity factor for the vortex-pair in still-air using the factor shown in figure 6 on the data of figures 7b and 8b (for the distance between the cores and the vortex radii), respectively and (b) the "experiment" circulation calculated using the proximity factor in (a) applied to the experimental model

The time evolution of the "corrected" circulation, to be computed from the model assuming a circular rather than squeezed elliptic vortex, is presented in figure 9c. The model peak circulation must be increased by about 15% compared to the experimentally computed circulation and it also occurs at a later time. Furthermore, the circulation used in the model is essentially constant for about half of an excitation cycle (~0.5 msec) and is significantly attenuated at later times.

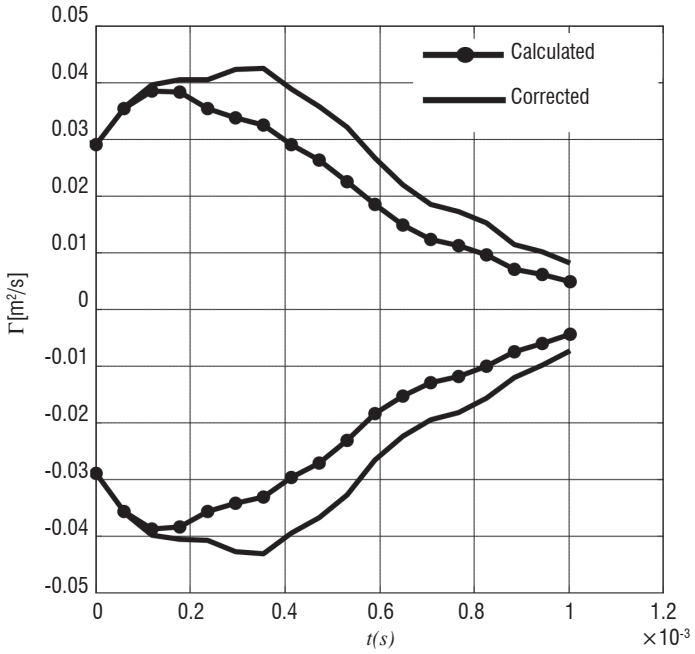

Figure 9c - Comparison between the experimentally calculated and corrected model circulation curve

The "corrected" circulation from the still-air experiments (figure 9c), as well as the expression for the vortex radius (eq.11), were introduced into the four-vortex model as described above, in order to validate and calibrate the model that will be used for the excitation interaction with the cross-flow, initially against the still-air data .

A Gaussian curve was fitted to the "corrected" circulation curve (as shown in figure 9c) for the convenience of subsequent numerical treatment.

Figures 10a and 10b present the trajectories and time evolution of the circulation, as predicted by the current four-vortex model and compared to the still-air findings.

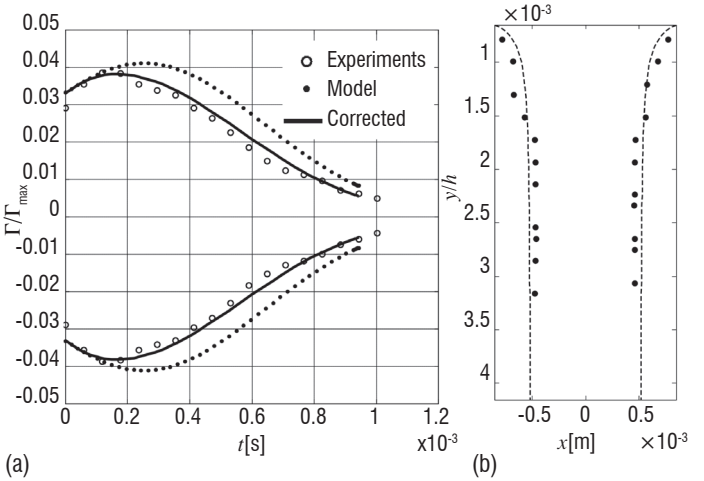

Figure 10 - (a) Model vs. Experimental circulation time evolution. "Model" here is the fitted Gaussian. "Corrected" is the circulation values with the partial overlap factor included. (b) Vortex trajectories from the model compared to experiment

It should be noted that the model circulation represented by the dots in figure 10a is larger than the experimentally computed circulation. This correction takes into account the reduction in the measured vortex circulation due to their proximity. However, for the model adherence to the theoretical considerations and its linear implementation, the circulation that is used for the simulation is increased according to the proximity factor, shown in figure 9b. Using this vorticity time evolution, the model computes the convection velocities, flow fields, circulation (due to the superimposition with the boundary-layer) and more. However, if we intend to compare its circulation to the still-air PIV measurements, we must take into account the proximity that causes the 2D integration method to "measure" a smaller circulation due to the overlap region of the finite radius vortices. Once we account for the proximity factor and its effect on the circulation, we obtain the "corrected" model circulation, which is in very good agreement with the measured PIV data, as shown in figure 10a. The vortex trajectories, shown in figure 10b, are in very good agreement with the experiments. Finally, the data shown in figures 10 merely serves as indication of the model fidelity and the reliability of its numerical implementation.

Interaction of a vortex-pair with cross-flow

The approach for modeling the vortex-pair in the proximity of the wall and interacting with a cross-flow boundary layer is outlined below. The expansion of the above four-vortex model is theoretically sound only if the cross-flow (boundary-layer) velocity is assumed to be constant. However, currently it represents a realistic shear flow, the Blasius boundary layer. Hence, even if one considers potential models, many point-vortex interactions must be considered. Furthermore, the Lamb-Oseen vortex model is not a point-vortex model. To simplify this complex situation, we note that the Blasius boundary layer *vorticity*, under the current experimental conditions, is negligibly small as compared to the peak vorticity within the vortex cores (on the order of 30:1) and, hence, in the leading order approximation it is reasonable to neglect it. However, this residual boundary layer vorticity will alter the relative circulation of the vortices forming the pair, making one stronger than the other, and the pair will eventually rotate.

The interaction of the vortices with the boundary layer is modeled by the following procedure;

1. Define the initial vortex positions, $\vec{x}_i(t=0)$ (where i=1,2 represent the counter rotating vortices and i=4,3 represent their images, meaning $\vec{x}_3=(x_2,-y_2)$ and $\vec{x}_4=(x_1,-y_1)$.
2. Define the initial vortex circulations, $\Gamma_{0,i}(t=0)$ (where i=1,2 represent the counter rotating vortices and i=3,4 represent their images, meaning $\Gamma_{0,3}=-\Gamma_{0,2}$ and $\Gamma_{0,4}=-\Gamma_{0,1}$) at any time.
3. Define the initial vortex radius, r_0 (currently identical for all vortices).
4. Calculate the time derivatives of the vortex locations and circulations in accordance with the following equations:

$$\dot{\vec{x}}_i=\sum_{i\neq j}\vec{u}_j^{ind}\left(\left\|\vec{x}_i-\vec{x}_j\right\|,\Gamma_{0,j}\right)+\vec{U}_{BL}\left(\vec{x}_i\right) \quad (12a)$$

$$\dot{\Gamma}_{0,i}=\dot{\Gamma}_{0,i}^{Baseline}+\oint_{C(t)}\omega_{BL}\left(\vec{U}_{BL}-\dot{\vec{x}}_i\right)\cdot d\vec{l} \quad (12b)$$

where the vortex radius can be calculated in each time step according to eq. 11.

5. Use a time marching numerical scheme to integrate equations 12a and 12b.

Note that the expression $\oint_{C(t)}\omega_{BL}\left(\vec{U}_{BL}-\dot{\vec{x}}_i\right)\cdot d\vec{l}$ in eq. 12b is the vorticity flux along the vortex boundaries $C(t)$. When there is no boundary layer, $\vec{U}_{BL}=0$, it is required that $\omega_{BL}(x,y)=0$ also, and eq. 12 reduces to the form of the still-air four-vortex model, as presented in eq. 8.

The above procedure allows the vortex circulation to effectively vary according to the level of the background boundary layer vorticity, according to the vorticity transport equation.

The following figures (11-12) show the vortex trajectories and circulation due to the interaction of the vortex-pair with a cross-flow Blasius boundary layer. The integral parameters of the boundary layer at the entrance to the computed domain were matched to the experimental baseline (undisturbed) boundary layer. The vortex pair evolution was computed according to steps 1-5, as defined above.

The initial conditions used for both simulations are provided in Table 1 below. Note that we have allowed an initial circulation difference between the vortices, in order to better account for the effect that the boundary layer vorticity has on the vortex circulation during the formation period, as seen experimentally.

As in the Lamb [10] model and the results of the still-air simulation, the vortices initially become closer due to the image vortices as they are carried away from the wall, due to the mutual induction. The effects of the cross-flow are twofold. The trivial effect is the downstream convection, which is height (y) dependent. The other effect is the alternation of the vortex circulation to account for the effect of the baseline boundary layer vorticity, as defined in step 5 above and seen in figure 11a. The overall agreement between the model and the experiment is fair, especially the evolution of the negative vortex, which is crucial to explain effects on a separating boundary layer.

Variable	Description	Case 1 (fig.11)	Case 2 (fig.12)
Ue	Free-stream velocity [m/s]	5.5	8.3
x_1	Initial x location, Positive vortex [mm]	0.9	0.9
y_1	Initial y location, Positive vortex [mm]	0.67	0.63
x_2	Initial x location, Negative vortex [mm]	0.95	0.86
y_2	Initial y location, Negative vortex [mm]	0.55	0.54
$\Gamma_{0.1}$	Initial circulation, Positive vortex [mm]	0.027	0.03
$\Gamma_{0.2}$	Initial circulation, Negative vortex [mm]	-0.032	-0.035

Table 1: Initial conditions for the two cases of excitation-vortex-pair interaction

It could be noted that initially, the agreement between the trajectory of the negative vortex and the experimental trajectory is not as good, possibly because the blockage effect that the positive vortex has on the boundary layer is not taken into account in the linear model. Additional effects that are not taken into account are the possible alternation of stationary vortex circulation, due to net vorticity transport across its boundaries and dissipation at the wall.

The circulation that is used for the model is marked by the dashed red and blue lines, in both figures 11 and 12, while for the sake of comparison to the experiment, it is multiplied by the proximity factor, calculated for the trajectories in the presence of cross-flow.

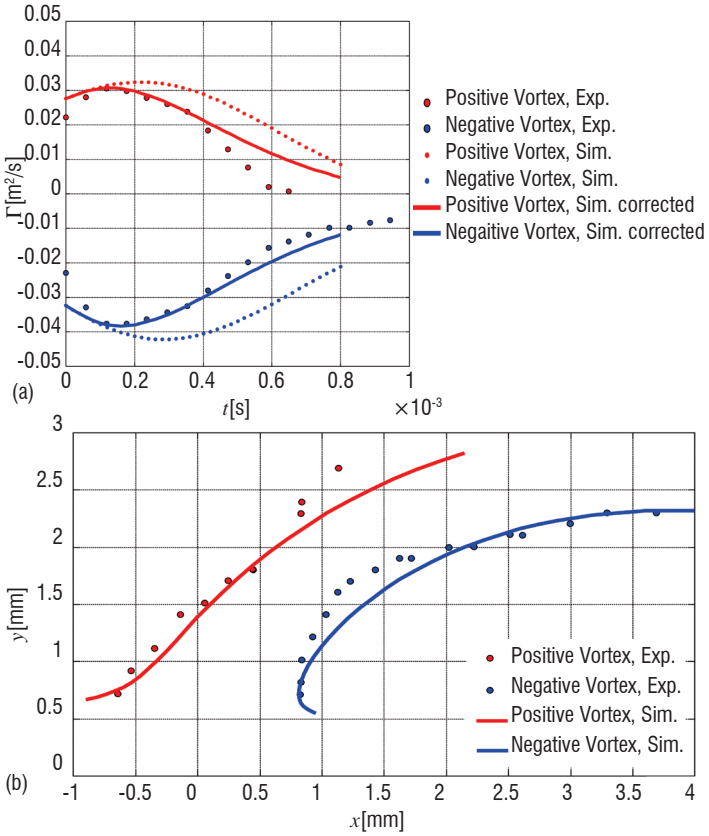

Figure 11 - The evolution of the vortex pair circulation (a) and trajectories (b) for vortex-boundary layer interaction, Case 1. U_p=18 m/s and U_e=5.5 m/s

Figures 12a and 12b present the vortex-pair boundary-layer interaction, with the same excitation parameters that were used in still-air and in the Case 1 cross-flow experiment, only for Ue=8.3m/s as the free-stream velocity. The remaining parameters are provided in Table 1. Due to the larger free-stream velocity, the trajectories are bent more towards the wall and into the downstream direction. The circulation of the two vortices diverges faster than in the lower free-stream velocity, due to the increased vorticity of the background boundary layer.

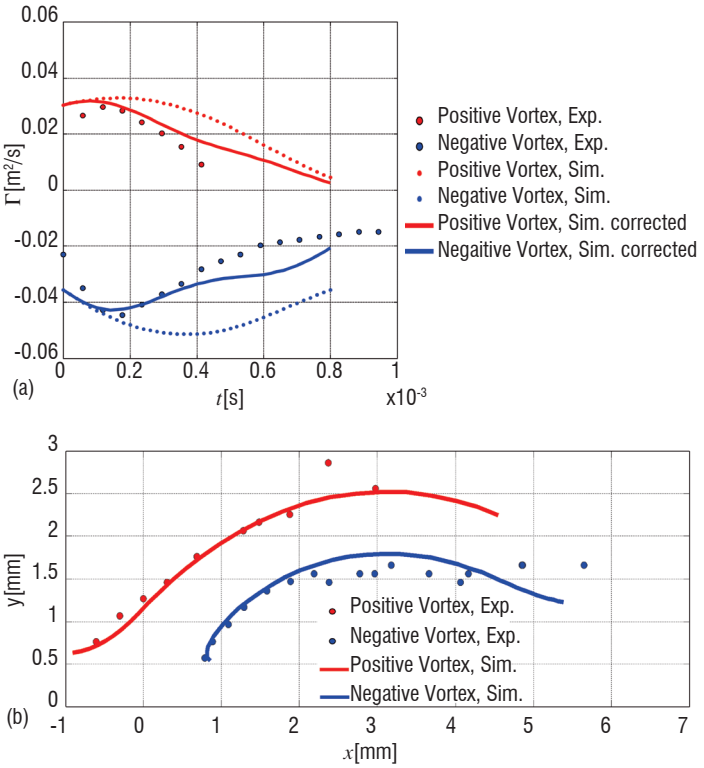

Figure 12 - The evolution of the vortex pair circulation (a) and trajectories (b),for vortex-boundary layer interaction. Case 2. U_p=18m/s and U_e=8.3m/s.

The interaction dynamics can be interpreted as follows. The vortex-pair starts to be convected in the wall-normal direction, due to the mutual induced velocities. The image vortices induce velocity mainly in the x direction, bringing the vortices closer. The boundary layer velocity in the initial position (and at the initial time) is small, compared to the induced velocities by the vortex-pair. As the Vortices move away from the wall, their circulation changes, due to the interaction with the boundary layer vorticity. The positive vortex decays because a negative vorticity flux "enters" its boundaries, whereas the negative vortex intensifies due to the same reason. This difference in the circulation causes the vortices to move along a curved trajectory (actually a circular trajectory whose radius increases with the difference of their circulation) as shown in figures 11b and 12b. The experiments show that the positive vortex circulation decays very fast (0.4-0.5[ms], figures 11a, 12a), within less than one excitation cycle. Therefore, the positive vortex ceases to induce velocity on the negative vortex and the negative vortex travels downstream with the boundary layer, almost parallel to the wall. However, the model does not seem to be capable of predicting the rapid decay seen experimentally. It is highly probable that after t>0.5 ms, 3D effects start to be important and other mechanisms cause the positive vortex to lose its circulation so rapidly.

The vortex dynamics highly depend on the initial conditions. If one starts the simulation closer to the wall, the wall images play a stronger role on the vortex convection velocities, making them reside longer in the presence of the stronger boundary layer vorticity and therefore exposing their circulation to the boundary layer vorticity for a longer

time. This will cause the positive vortex circulation to decay faster, until it vanishes in the boundary layer, and will cause the negative vortex circulation to rapidly grow.

Conclusions

A model for describing the evolution of a vortex-pair during the interaction with a laminar boundary layer was proposed, calibrated and validated against experimental data. The model is similar to the Lamb four-vortex model, adopted for finite radius vortices. One exception is that the vortex circulation is empirically allowed to vary with time, according to the experimental findings. This model explains the initial motion of the vortices towards each other in the proximity of the wall. The inclusion of the boundary layer effects is performed through two mechanisms. The first is vortex convection and the other is superimposition with the background boundary layer vorticity. The latter is altered as the vortex travels across the boundary layer. This approach can be implemented because the boundary layer vorticity is negligibly small compared to the vortex magnitude. The initial circulation and its time evolution from the still-air model are used for the cross-flow interaction. In order to make a comparison between the model results, assuming circular vortices, and the experimental findings, in which the vortices are not circular, especially when close together, a correction factor was introduced. The model was compared to experiments for wall-normal excitation with reasonable agreement.

It was noted that the evolution of the vortices is very sensitive to the initial formation locations. The link between the characteristics of the slot excitation and the initial circulation and locations of the vortices should be modeled, in order to allow the development of the current model with a simplified boundary condition for CFD simulations and further development as a low-order-model for flow control purposes■

Acknowledgements

The authors would like to thank G. Zilman and G. Iosilevskii for many helpful discussions and suggestions.

References

[1] P.G. SAFFMAN - *Dynamics of Vorticity.* 1981, JFM 106; pp. 49-58.
[2] T. YEHOSHUA, A. SEIFERT - *Boundary Condition Effects on Oscillatory Momentum Generator.* AIAA Paper 2003-3710, June 2003.
[3] T. YEHOSHUA, A. SEIFERT - *Active Boundary Layer Tripping Using Oscillatory Vorticity Generator.* Aerospace Science and Technology, 10 (3): 175-180 APR 2006a.
[4] T. YEHOSHUA, A. SEIFERT - *Boundary Condition Effects on the Evolution of a Train of Vortex Pairs in Still Air.* Aeronautical J., 110 (1109): 397-417 JUL 2006b.
[5] R. HOLMAN, Y.UTTURKAR, M.R. MITTAL, B.L. SMITH, L. CATTAFESTA - *Formation Criterion for Synthetic Jets.* AIAA Journal, 2005, vol.43 no.10 (2110-2116).
[6] A. GLEZER - *The formation of vortex rings, Physics of Fluids*. December 1988 -- Volume 31, Issue 12, pp. 3532-3542.
[7] N.DIDDEN - *1979, On the Formation of Vortex Rings: Rolling-up and Production of Circulation.* ZAMP (Zeitschrift für Angewandte Mathematik und Physik), Volume 30, Number 1 / January, 1979.
[8] O.K. REDINIOTIS, J. KO, X. YUE, A.J. KURDILA - *Synthetic jets, their reduced order modeling and applications to flow control.* AIAA paper 1999-1000 , Jan., 1999 (also AIAA J. 2002).
[9] P. HOLMES, J.L. LUMLEY, G. BERKOOZ - *(1996) Turbulence, Coherent Structures, Dynamical Systems and Symmetry.* Cambridge University Press, Cambridge, Great Britain,1996.
[10] H. LAMB - *1932 Hydrodynamics*. Dover.
[11] M. KARWIET - *Motion of a vortex pair approaching an opening of a boundary*. Phys. Fluids, 18: 1604-6, 1975.
[12] J.S. SHEFFIELD - *Trajectories of an Ideal Vortcx Pair Near an Orifice*. Phys. Fluids 20 : 543-545, 1977.
[13] E.J. ROUTH - Proc. Lond. Math. Soc. 12, 73, (1881).
[14] P.G. SAFFMAN - *Vortex Dynamics.* Cambridge University Press, 1992.
[15] K. SHARIFF, A. LEONARD - *Vortex Rings*. Ann. Rev. Fluid. Mech., Vol. 24: 235-279, 1992.
[16] G.K. BATCHELOR - *An Introduction to Fluid Dynamics*. Cambridge University Press (§4.5) 1967.
[17] R. KARAGOZIAN, ANN - *Progress in Energy and Combustion Science*. 36 ,531-553 (2010).

Nomenclature

x,y	Coordinates along a 2D axis
x_i, y_i	Vortices locations
v_θ	Circumferential velocity component
ω	Out-of-plane vorticity component
Γ	Circulation
Γ_0	Initial Circulation
δ	Vortex radius
r	Radial coordinate
r_0	Vortex radius at t=0
t	time
h	Actuator's slot width
U_p	Peak Velocity at the actuator's slot
f	excitation frequency
ν	kinematic velocity
St	Strouhal number, fh/U_p
Re_{U_p}	Reynolds number based on U_p, hU_p/ν
T	Time of excitation cycle, $1/f$
$\dot{(\cdot)}$	Time derivative
$\vec{u}^{IND}$	Induced velocity
$\Gamma_0^{Baseline}$	Vortex circulation as a function of time for a baseline flow, Ue=0.
U_e	Boundary layer free-stream velocity
A_{vortex}	Area enclosed by a contour C that corresponds to 1% $\omega_{max}(t)$ vorticity
ω_l	Vorticity level
s	Distance between the vortices' centers
R^2	Correlation factor
ω_{BL}	Boundary layer vorticity
U_{BL}	Boundary layer velocity

AUTHORS

Avrahame Seifert is a Professor of Mechanical Engineering at Tel Aviv University and also the head of the Meadow Aerodynamics Laboratory. Prof. Seifert is an expert in low speed Aerodynamics and Active Flow Control. Dr. Seifert is developing methods and devices to alter the natural development of flows using localized, minute, unsteady energy expenditure, utilizing flow instability instead of brute force. Prof. Seifert received his entire education at Tel Aviv University, before leaving for a post-doc at NASA Langley. He has been a member of the Faculty at Tel Aviv University since 1999. Dr. Seifert has published close to 50 peer-reviewed Journal papers, has 5 patents (several more pending) and has educated more than two dozen graduate students. Prof. Seifert served as the Vice Dean for Research & Engineering and now serves as the Head at the School of Mechanical Engineering. His recent research interests focus on energy aspects of flow related systems and on the environment. Specifically, Aerodynamic drag reduction of heavy transportation systems (such as trucks, trains and buses) and enhanced effectiveness of wind turbines in urban settings and near transportation systems. Prof. Seifert is a world leader in developing actuators for flow control and four of his patents are in this area of R&D.
Personal homepage:
http://www.eng.tau.ac.il/~seifert/
Meadow Aerodynamics homepage:
http://www.eng.tau.ac.il/research/laboratories/Aerodynamics/

Tal Yehoshua is a Mechanical Engineering graduate student at Tel Aviv University. His main research interests are unsteady aerodynamics, flow control, boundary layers, vortical flows and flow instabilities, as well as optimization methods. Tal received his Bsc and Msc at Tel Aviv University and is currently leading several projects in the Aeronautical community in Israel.

V. Ciobaca , J. Wild
(DLR)

E-mail: vlad.ciobaca@dlr.de

An Overview of Recent DLR Contributions on Active Flow-Separation Control Studies for High-Lift Configurations

This is an overview of flow control experiments and simulations for flow separation control on high-lift configurations performed over the last seven years at the German Aerospace Center within national and European projects. Emphasis is placed on the low speed atmospheric and cryogenic experimental setups using the DLR F15 high-lift airfoil and on the numerical verification and validation of the Reynolds Averaged Navier Stokes (RANS) solver TAU for active flow control (AFC) simulations. The wind tunnel studies concern leading edge boundary layer control and flap separation control, both by means of pulsed blowing. The computational effort is mostly dedicated to the most promising technology out of the two concepts, namely the pulsed blowing through slots on the trailing edge flap. Experimental examples of successful flow control for enhancement of lift are given for moderate and high Reynolds numbers to prove the feasibility of the technology for implementation on real aircraft. The computational process chain is validated with wind tunnel measurements, but also applied for an optimization of the trailing edge flap shape for separation control.

Introduction

Future transport aircraft can benefit from matured active flow separation control techniques that can support the achievement of a reduced environmental impact of air traffic [1]-[4]. The research results published over the last two decades show the potential of modern flow control for lift increase, drag reduction and dynamic control through problem specific implementation. In addition, the upcoming active technologies, especially the enabling of laminar wing technology, is foreseen to be substantially able to decrease fuel burn by means of aerodynamic enhancements. Therefore, slatless wing configurations with active flow control have become of interest as an alternative to current leading edge devices, like slats or Krueger flaps. By omitting these classical devices, the tracking systems can be suppressed and a benefit in costs and weight is expected. Beyond the complexity improvements, an active control system can support the laminar flow for the upper and lower side of an airfoil, whereas a Krueger for example can typically only assure a laminar flow on the wing suction side, because a backward facing step of small height can be responsible for the transition to turbulent flow on the pressure side and one third of the potential drag reduction is therefore compromised according to recent studies.

On the other hand, slats and Krueger flaps are powerful passive devices for achieving high values of maximum lift [5]. To be applicable, the lift loss resulting from their removal must be recovered. If an increase of approach and landing speed is not meaningful, the lift can only be recovered by increasing the wing area or enhancing the lift coefficient by means other than a leading edge device. The solutions discussed nowadays are more complex trailing edge devices and active flow separation control.

Today, there are no civil aircraft flying an active flow control system, and this is more than a decade since McLean [3] concluded that modern flow control is the most promising for high-lift applications. The use of active flow control, such as constant or pulsed blowing, suction or zero-mass flux synthetic jet actuation (SJA), or dielectric barrier discharger actuators (DBD), has been since intensively investigated worldwide. The primarily reported drawbacks for implementation on aircraft have been related to the lack of efficient actuation systems, to the structural integrity or, for example, due to too high power demands. Some technologies have reached a specific maturity concerning the aerodynamic discipline. Therefore, an overview of the existing results for specific active technologies is worth discussing.

Over the last seven years, DLR has supported studies of active flow control for high-lift by means of pulsed blowing through inclined holes and slots, with a strong collaboration with universities, namely the Technical University of Berlin (TUB), and the Technical University of Braunschweig (TUBS). Two flow control technologies have shown previously under laboratory conditions to have a high potential for separation control and lift improvement. Tinnap et al. [6] proved the feasibility of flow control through slots with a low Reynolds number

and low-speed flows. Petz et al. [7] investigated the influence of excitation parameters on the efficiency of this flow control method, on a 2D configuration consisting of two NACA airfoils and Becker et al. [8] contributed control strategies to these AFC attempts. Ortmanns and Kähler [9] investigated jet vortex generators placed on a simple flat plate within a detailed parametric study at low speed and low Reynolds numbers. Scholz et al. [10] implemented the most promising of these pneumatic round-jet actuators in the nose region of an airfoil to successfully prevent leading edge separation.

Therefore, DLR has supported experiments for a state-of-the-art supercritical high-lift airfoil, namely DLR-F15, as a platform for combined flow control on the wing leading edge and trailing edge flap. DLR provided access to a large scale experimental test bed that allowed studies at flight relevant inflow speeds and Reynolds numbers, while flow control techniques were implemented by the universities. Summaries of the experimental results will be presented in this article.

Besides the wind tunnel experiment, numerical simulation has become a pillar for the aerodynamics discipline. Numerical simulation is an important method for rapid design and for optimization processes, as well as for the study of scaling effects. Therefore, DLR is keen to make the corresponding numerical simulation methods accessible for the use of modern AFC methods on future transport aircraft. Important progress has been made over the last decade, but numerical tools still require active development for practical solutions of various AFC methods, including validation with high-fidelity experiments. Therefore, the active flow control applications on the DLR F15 airfoil were used for numerical simulations dedicated to the evaluation of flow control capabilities, as well as for direct comparison with the wind tunnel experiment. Basic test cases, such as single-actuator simulations on a zero-pressure gradient flat plate, served as a starting point for the validation of the numerical method [11]. The numerical analysis addressed the constant and the pulsed blowing. Later, the focus was on separation control for the trailing edge flap by the unsteady actuation through slots [12]; [13]. In general, the Computational Fluid Dynamics (CFD) studies discuss the trends for flow control application by parameter variation, such as the blowing frequency, the actuation intensity, or the geometrical actuation direction. Here, the overview includes the specific major findings by CFD and the level of agreement with the experiment. Additionally, it is presented an example of shape optimization for separation control application.

In the following, the flow control experiments carried out at the German Dutch Wind Tunnel (DNW) low speed facilities NWB and KKK are summarized. The DLR F15 tests cover the application of state-of-the-art pulsed blowing actuators for tunnel testing and allow the discussion of the potential to increase lift and control the flow separations at moderate and high Reynolds numbers. Afterwards, numerical steady and unsteady RANS simulations in conjunction with the DLR F15 high-lift airfoil are reported. The computational findings allow the validation with the experiment to be presented and allow the major trends of the various control parameters that can support the later optimization of the energy requirements and/or geometrical parameters to be revealed.

Flow Control High-Lift Experiments

Wind tunnel model DLR-F15

The DLR-F15 wind tunnel model shown in figure 1 is a 2D wall-to-wall high-lift model. The modular main wing allows leading and trailing edges to be exchanged. Therefore, different types of high-lift elements can be investigated and compared at the same baseline geometry. The clean wing section is derived from a generic high-lift wing investigated in the nationally funded project ProHMS [14] and represents a state-of-the-art transonic turbulent airfoil for a modern civil transport aircraft. The setup of interest for flow control is a 2-element configuration that features a clean leading edge and a single-slotted flap. The device is mounted on continuously adjustable brackets, allowing the free positioning of this element in all three degrees of freedom. The model is equipped with about 220 static pressure taps. One dense pressure distribution is located in the center section and is used for the integration of the aerodynamic coefficients. In addition, two less dense pressure distributions are located close to the tunnel walls, in order to assess the two-dimensionality of the flow. As described in [16], the pressure distribution has been discovered to not be dense enough for an accurate integration of drag coefficients, leading to errors of up to 20%. The pure integration error for lift coefficients is of about 1% and an accuracy of about 3% is achieved for the pitching moment coefficient.

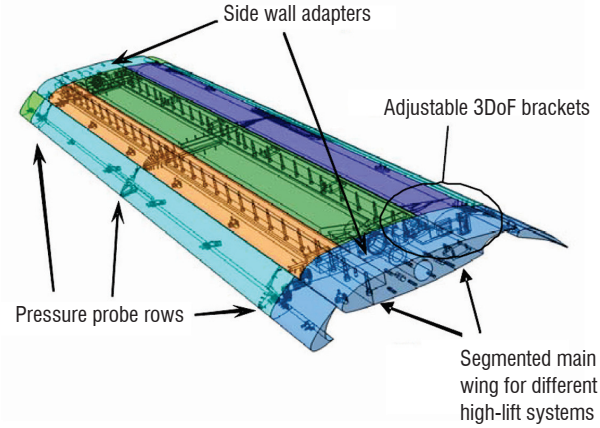

Figure 1 - General arrangement of the DLR F15 two-dimensional high-lift model in 3-element configuration

Wind tunnel test sections

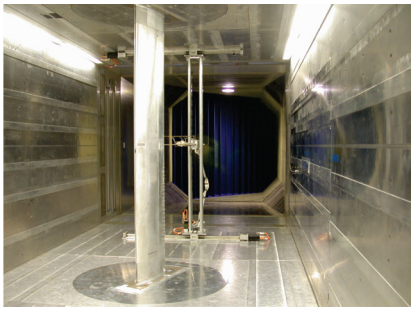

(a)in DNW-NWB, atmospheric tunnel

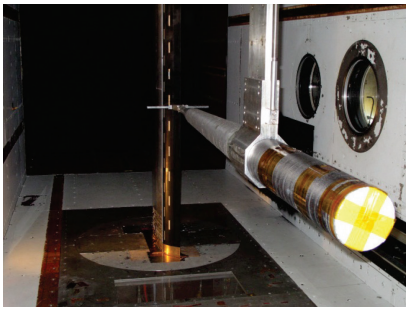

(b) in DNW-KKK, cryogenic tunnel

Figure 2 - DLR F15 two-dimensional high-lift model mounted in closed test sections of DNW low speed wind tunnels

The reported tests were carried out in the atmospheric wind tunnel DNW-NWB in Braunschweig [15] and in the cryogenic facility DNW-KKK in Cologne (figure 2). These are closed loop low-speed tunnels that operate at approximately ambient pressure. The DNW-NWB facility has a maximum Mach number of $M = 0.27$ and the test section has a cross-section of 3.25 x 2.8 m^2. In DNW-KKK the temperature can be regulated between ambient and $T = 100$K; Mach numbers can range between $M = 0.1$ and $M = 0.3$ and the test section has a cross-section of 2.4 x 2.4 m^2. Based on the aerodynamic clean chord $c = 0.6$ m, the maximum Reynolds number achieved was $Re = 3\text{x}10^6$ for atmospheric conditions and $Re = 12\text{x}10^6$ for the cryogenic testing.

The experimental Mach and Reynolds number dependencies, including the stall behavior of the baseline airfoil without flow control, can be found in [16]. In order to reduce the wall interference effects for this wall-to-wall mounted high-lift configuration, vortex generators have been applied on the upper side of the main wing, as described in [16].

Actuation systems for wind tunnel testing

The actuation systems that are the focus of this publication are presented in figure 3. These are implemented at the model wing leading edge and at the trailing edge flap. Each actuation system consists of a pressure supply, a fast switching valve and an actuation chamber. The shape of these actuation chambers is designed for the specific applications. At the wing leading edge, there is a flow through round inclined holes and the flow control methodology is known as vortex generator jets (VGJs). At the trailing edge flap, the actuator chambers have a rectangular-exit shape that is used for the pulsed blowing flow control method.

The applications with VGJs have a long tradition at TUBS. For two-dimensional models, the optimized actuation has counter-rotating pairs of vortices as used by Scholz et al. in [17], whereas Hühne et al. [18] reported, for a swept wing application, a co-rotating actuation that was found by numerical research to be more favorable. All studied cases with leading edge control have targeted the delay of the wing stall, with a leading edge-stall type characterizing the baseline configuration. The position of the actuators was of early concern and the best compromise was found to be a lower side actuation at 1%c, since the local velocity ratio is higher than for an application on the leading edge upper side. With actuator diameters of the order of $d =$ 1mm, the actuation exit maximum velocities are close to the speed of sound. The application of VGJs allows the formation of strong streamwise vortices that transfer high-momentum close to the airfoil surface and can delay the occurrence of flow separation. The use of the VGJs in a pulsed mode was found to be more energy efficient than continuous blowing.

The trailing edge actuation concerned single and multiple actuation slots for the NWB and KKK tests respectively. The slots are inclined downstream with $\alpha_{jet} = 30°\text{-}45°$, but not tangential, and have a thin opening of only $w = 0.3$mm, which was reported by Haucke et al. [19] to be suitable for separation control. This control technique has a long tradition at TUB. The flap flow control systems are designed for actuation intensities with Mach numbers $M < 1$, but higher than the corresponding incoming flow. The actuators are positioned on the flap upper side and ideally close to the separation onset location. Here, the single actuation is at 20%c and an additional 50%c location was taken into account for the multiple-actuation. The length of the actuator-slot is typically infringed by the installation space in the flap. The slotted pulsed blowing actuation allows the formation of spanwise vortices. When the actuation frequency exceeds a specific value, mostly related to the shedding vortices of the baseline flow separation, then the vortices that roll downstream can effectively suppress the separation in a time-average sense. However, vortical structures exist above the actuated surface for every time-instant. Contrary to a tangential continuous blowing, like a Coanda flap, the actuation direction is not efficient for a non-separated baseline flow. The inclined downstream

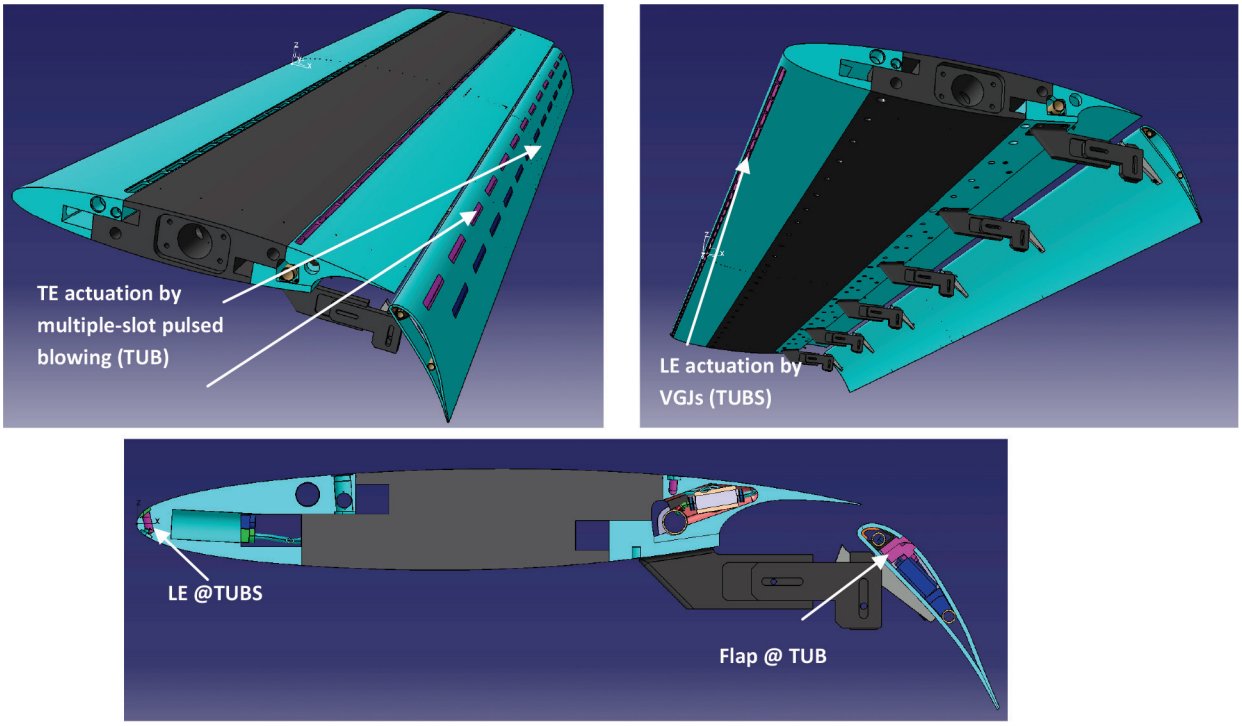

Figure 3 - Actuation systems implemented on the DLR F15 model

actuation velocity vector with α_{jet} = 30°-45° can be divided into two components: a normal and a tangent vector. The first allows for the formation of spanwise vortices that transfer high momentum to the surface during the time-dependent actuation. The latter introduces a thin jet of high-pressure air into the boundary layer to re-energize it, with local velocities higher than those of the outer flow. The resulting velocity vector is favorable for the time-dependent pulsed blowing actuation for separation control.

The parameters used in relation with the active flow control application are the blowing momentum coefficient $C\mu$, the non-dimensional actuation frequency F^+ and the actuation duty cycle DC. The blowing momentum coefficient was first introduced by Poisson-Quinton [20] and, for this application, is defined as:

$$C_\mu = \frac{\dot{m}_{jet} \times u_{jet}}{\frac{1}{2} \times \rho_\infty \times U_\infty^2 \times A_{ref}} \quad (1)$$

where, in the fraction numerator, $\dot{m}_{jet}$ is the time-averaged actuation mass-flow and u_{jet} is the time-averaged jet velocity. The fraction denominator is the product of the dynamic pressure ($0.5\rho U^2$) and the airfoil reference area, A_{ref}. This variable is a measure of energy consumption. For the active flow control application, a drag coefficient can be associated with the local actuation jet and this is defined, for example, according to Engler [21], as

$$C_D = C_\mu \frac{U_\infty}{u_{jet}} \quad (2)$$

The non-dimensional actuation frequency F^+ is defined as:

$$F^+ = \frac{f \times c_F}{U_\infty} \quad (3)$$

where f is the physical actuation frequency. The characteristic length for determining this variable is the flap chord length c_F and the characteristic velocity is the reference inflow speed.

The actuation duty cycle DC shows the percentage of time in which the actuation valve remains open relative to the actuation period T:

$$DC = \frac{t_{open}}{T} \quad (4)$$

Other characteristics of the actuation components and design specifications can be found in the above mentioned references, e.g. [10]; [18]; [19].

Results

Figure 4 shows the maximum lift increments by separated and combined wing leading edge and trailing edge flap active flow control from the atmospheric wind tunnel testing. The actuation on the wing leading edge mostly shows an increase in the maximum angle of attack, where the flap actuation promotes a shift of the C_L-α-curve. The combined flow control applications show a significant increase in maximum lift, in comparison with the baseline configuration. Each flow control system seems to allow for lift increments of the order of $\Delta C_L \approx 0.15$ and the combined actuation delivers an increase of $\Delta C_L \approx 0.3$ with a $\Delta\alpha_{CL,max} \approx 5°$.

Figure 5 illustrates the maximum lift increments by separated and combined wing leading edge and trailing edge flap active flow control from the cryogenic wind tunnel testing. Here, a more complex flap flow control setup is in use, namely by multiple-slot actuation. Like for the atmospheric tunnel testing, the wing leading edge mostly shows an increase in the maximum angle of attack where the flap actuation promotes a shift of the C_L-α-curve, now at high Reynolds number. The combined actuation is able to illustrate both enhancements for the maximum lift, as well as for the corresponding maximum angle of attack. The trailing edge actuation shows a lift enhancement of the order of $\Delta C_L \approx 0.6$ in the linear lift regime and $\Delta C_{L,max} \approx 0.4$, whereas the VGJs at wing LE show an increment of $\Delta C_{L,max} \approx 0.1$. The combined actuation indicates a noticeable maximum lift increase and proves the feasibility of the technologies, also at high Reynolds numbers.

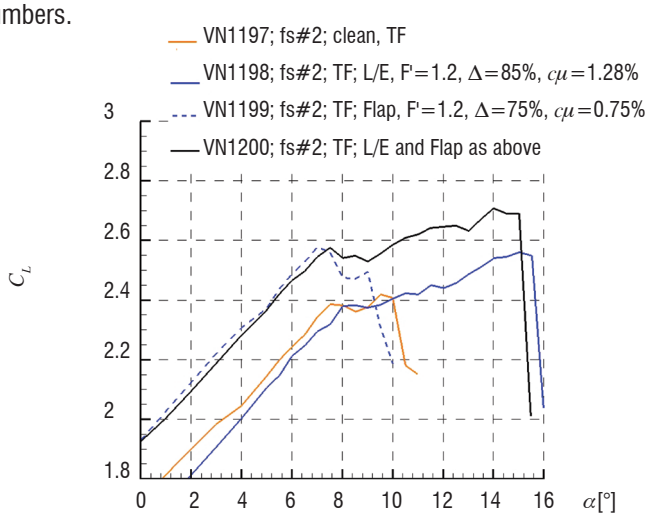

Figure 4 - The maximum lift improvements by vortex generator jets applied at the wing leading edge and single slot pulsed blowing at the trailing edge flap (M=0.15, Re=2x10^6, T=290K, atmospheric wind tunnel testing)

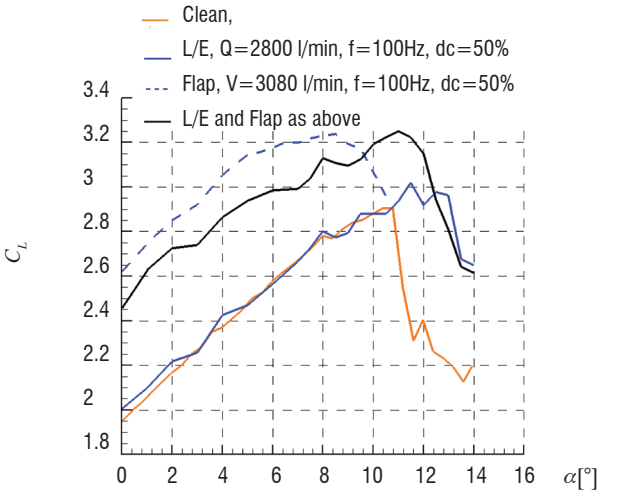

Figure 5 - The maximum lift improvements at high Reynolds number by vortex generator jets applied at the wing leading edge and multi-slot pulsed blowing at the trailing edge flap (M=0.15, Re=4.2 x10^6, T=170K, cryogenic wind tunnel testing).

Cryogenic flow control applications have used blowing momentum coefficients of the order of $c_\mu \approx 0.5\%$ for the leading application and $c_\mu \approx 0.15\%$ for the flap actuation, where the frequencies tested are of the order of hundreds of Hertz. Complex cryogenic wind tunnel testing has been very challenging in regard to system implementation, monitoring and results analysis. The reader is advised that individual detailed results concerning the Mach number and Reynolds number variations can be found in the work of Casper et al.[22] and Haucke

and Nitsche [23]. In general, the leading edge flow control shows maximum lift increments up to the flight Reynolds number for moderate mass-flow requirements. Unfortunately, the lift improvement decreases with the increase in Reynolds number and remains below a desired $\Delta C_L \approx 0.5$. Nevertheless, further lift improvements with this actuation system are not excluded. The flap flow control showed a high potential to suppress the local separation with moderate mass-flow requirements at high Reynolds numbers, where tests up to $Re = 7\text{x}10^6$ (not shown here) indicate no detrimental impact of the increase in Reynolds number. Moreover, the baseline flow showed an increase in flow separation above the flap, which allows larger overall lift increments by AFC than noticed at low Reynolds.

Flow Control numerical simulations

The numerical results reported in this article concern steady and unsteady Reynolds Averaged Navier-Stokes computations. Research communities worldwide use various RANS solvers for solving different flow control problems, on a large scale. Among these, the reader is advised to consult the published works with the numerical solvers: elsA at Onera, France (e.g. Menuier [25], Dandois [26]), FUN2D at NASA, USA (e.g. Anders [27]), OVERFLOW at Boeing, USA (e.g. Shmilovich [28]), and Edge at KTH, Sweden (e.g. [29]). In the following, the typical DLR TAU solver setups, the mesh generation approach and corresponding results are presented.

The numerical method

The flow solver used is the finite volume compressible solver TAU developed at the German Aerospace Center (DLR) [30]. A second order central scheme is used for the discretization of the convective fluxes. Artificial dissipation is applied, with a 2nd order dissipation term of 1/2 and a 4th order dissipation coefficient of 1/64. The chosen approach for the time integration is either a 3-stage Runge-Kutta time integration method using a CFL number of the order of

Box 1. Active Flow Control on the swept wing high-lift model DLR-F15 in the DNW-NWB wind tunnel

By the end of 2011, wind tunnel investigations have been successfully carried out for the first time with the swept DLR-F15 high-lift airfoil. A unique study to evaluate the capability for aerodynamic enhancement by active flow control (AFC) was addressed within the European program JTI-SFWA [24] at the DNW-NWB facility, in close cooperation with Airbus, TU Berlin and TU Braunschweig. The 2.5D mid-scale test (30° sweep) was performed for a slatless configuration with the most receptive flap setup for AFC; a setup that allowed for the largest lift gains in previous 2D experiments. The results show significant lift enhancements by AFC beyond the optimized clean configuration, especially for moderate angles of attack; the major contributor is the trailing edge AFC application, as indicated by the image. The results confirm previous findings on the 2D wall-to-wall setup of the DLR-F15 and are valuable towards achieving a higher technology readiness level of the AFC technology.

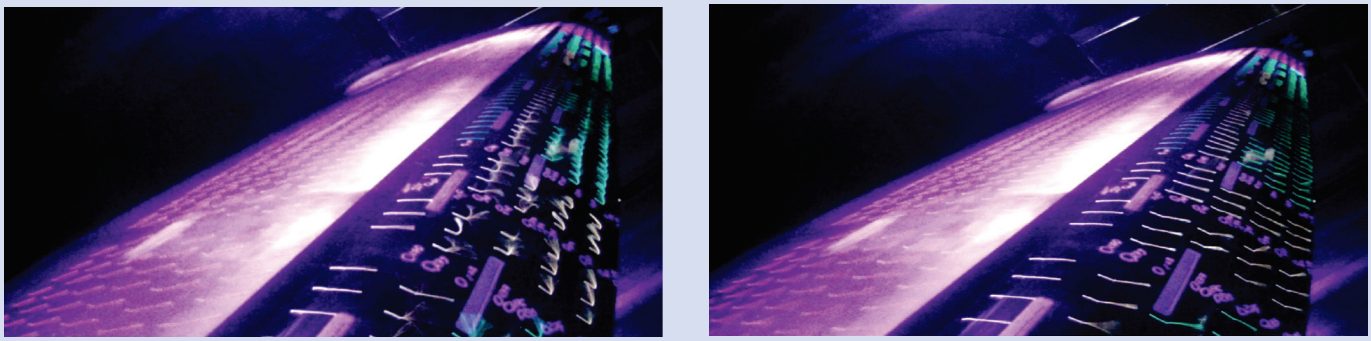

(a) without flow control (b) with flow control

Figure B1- 01 Tufts visualizations, focusing on the trailing edge flap for the lift enhancement by active flow control

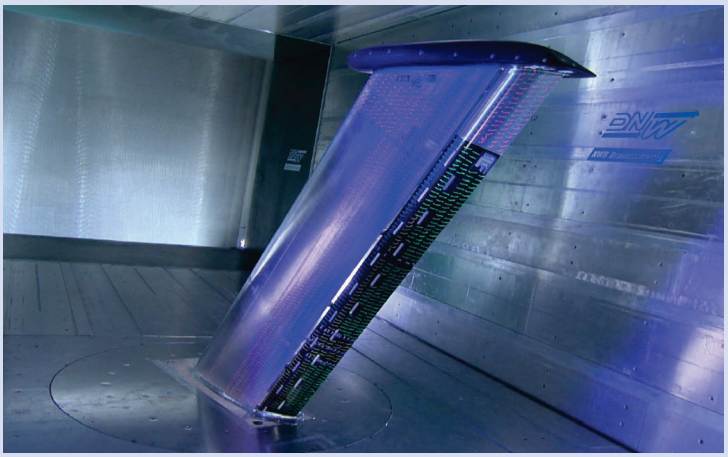

Figure B1- 02 Overview of the mounted swept DLR-F15 model in a DNW-NWB low speed atmospheric tunnel

1.2, or a semi-implicit Lower Upper Gauss-Seidel scheme with a CFL number of the order of 5. In addition to a point explicit residual smoother, convergence is typically accelerated with a 3W-multigrid cycle. For flow control simulations, a transpiration boundary condition that defines the inflow parameters at the actuation surface is implemented.

The grid generation

Perhaps one of the most time-consuming parts of the numerical simulation for high-lift flow control with RANS is the mesh generation. Today, there is no ideal tool for grid generation, but the available software supports the desired mesh topologies that include portions of the slot for a more accurate flow control simulation. The first examples concern applications with the DLR structured-dominant mesh generator MegaCADS [31], [32]. The other computations make use of the hybrid unstructured grid generator, Centaur [33].

For geometries of moderate complexity, a fully structured mesh generation is considered favorable for accurate numerical simulations. However, especially for complex high-lift configurations, or simply with the introduction of slot-actuator portions in the numerical domain, an unstructured approach is more time-efficient. Figure 6 shows the overview for the approach used for round-jet actuators, namely the discretization of the round actuator with quadrilaterals and triangles for the surface vicinity of the VGJ. This approach was successfully verified for single and multiple actuators, including the application of high-lift airfoils. The mesh for the single actuator on a long flat plate has 3 million points and the airfoil mesh contains about 10 million grid nodes. A grid refinement study concluded that the number of structured stacks required for boundary layer flow control is about twice that without control and this is about 60 grid points for the boundary layer discretization. These meshes allow the use of structured cells with large aspect ratio and typically tetrahedrons at the outer domain boundary. Figure 7 shows the second grid generation approach

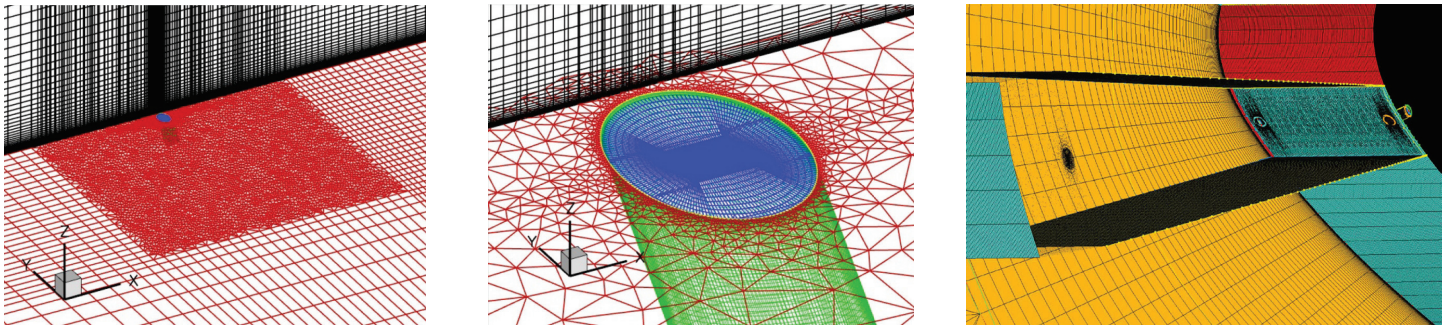

(a) flat plat with single VGJ (b)detail of graph (a) (c) airfoil LE with two VGJs

Figure 6 - Overview of the unstructured mesh topology for the round jet simulations, according to [11]

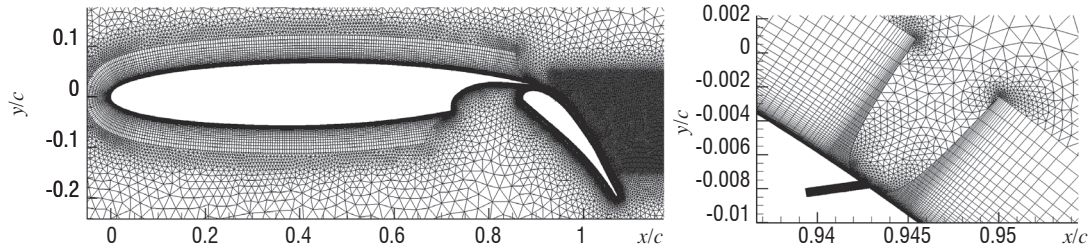

(a) two-dimensional grid for the DLR-F15 airfoil with single-slot-actuator

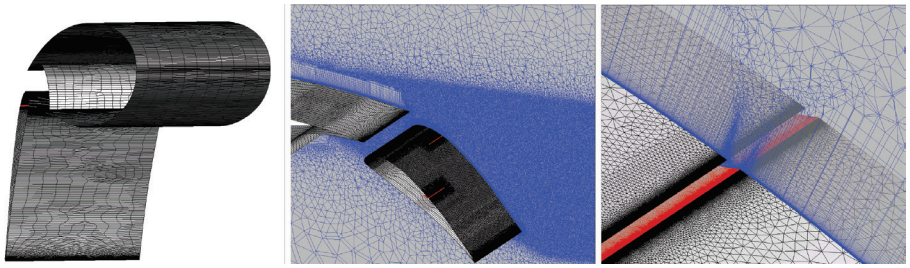

(b) three-dimensional grid for the DLR-F15 airfoil with two-slot-actuator

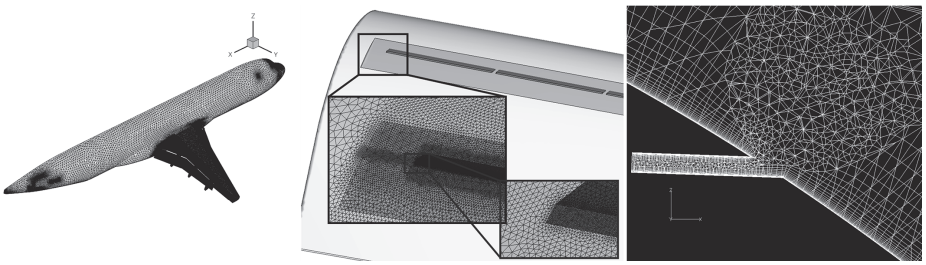

(c) three-dimensional grid for a wing-body configuration with 21 slot-actuators

Figure 7 - Overview of unstructured grid topologies for single and multiple slot actuation

frequently used for the flap flow control applications. With the use of the unstructured grid generator, the slits are modeled as a typical pipe with viscous walls. In between the structured stacks, triangular and tetrahedral cells are generated in 2D and 3D respectively. With this approach, grids for single and multiple-actuator have been generated up to a very high level of complexity, namely a wing-body configuration with a trailing edge flap that includes 21 actuators.

Constant blowing VGJs

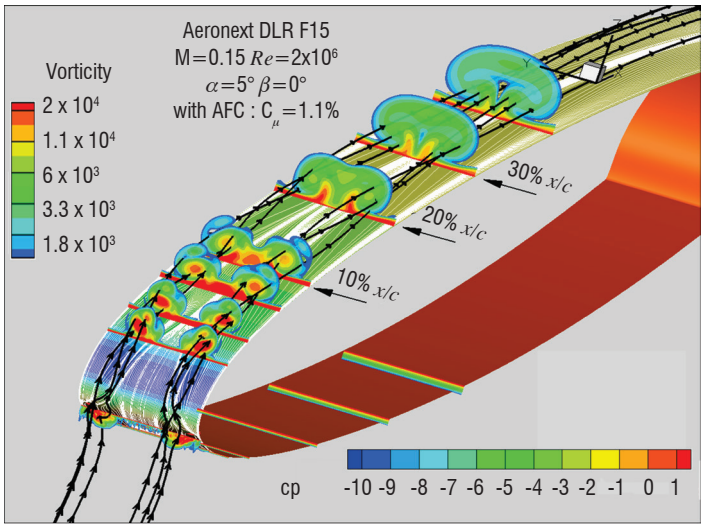

Figure 9 - Numerical simulations with the two-dimensional DLR-F15 airfoil actuated by skewed round jets on the wing leading edge pressure side

A single skewed round jet actuator mounted on a zero-pressure gradient flat plate is the most basic setup used for the verification and validation of the numerical steady RANS method. Constant blowing with an actuation velocity ratio relative to the inflow conditions larger than two promotes a strong streamwise vortex according to experiment and simulation. Figure 8 shows the computed and measured streamwise and normal velocity components in a plane downstream from the actuation. The graphs show the presence of so-called common flow-up and common flow-down, which are responsible for reduction and increase of the velocity magnitude close to the surface. Several state of the art turbulence models have been investigated and Togiti et al. [11] found that the vortex strength and its position are best simulated with a Reynolds Stress Model (SSG/LLR-ω) in comparison with the experiment. However, all models performed fairly well. Figure 9 illustrates the application of this numerical method with a two-dimensional high-lift airfoil actuated at the wing leading edge by a pair of divergent skewed round jet actuators. Streamwise vortices form on the wing pressure side and remain close to the airfoil surface on the wing suction side after passing the nose region, which is characterized by a very large negative pressure gradient. The vortices are visible over up to more than 30% of the wing chord, where these move closer to each other and become weaker the further the position downstream from the actuators is.

Pulsed blowing slot-actuation

A pulsed blowing application on the flap of a 2-element high-lift airfoil DLR-F15 is sketched in figure 10, for a moderate angle of attack. The single-slot actuation uses a square-shape signal and, over one actuation cycle, the flow above the actuated flap shows the evidence of time-dependent spanwise vortical structures. The time-averaged vorticity distribution shows that a separation persistent in the baseline flow field is reduced in size by active flow control. The aerodynamic lift coefficient is therefore increased as the airfoil circulation increases and the time dependent lift typically shows a periodic oscillation.

With the variation of the blowing momentum coefficient, which is a measure of energy requirements relative to the inflow conditions, the lift increment can be increased or reduced, for example, as required by the targeted flight conditions. Figure 11 illustrates the simulation results for this blowing momentum coefficient effect, where large increments can be obtained by moderate mass flows. However, there is a minimum blowing momentum that must be exceeded in order to obtain a benefit from the actuation. Also, saturation can be reached, which corresponds to an attached flow downstream the actuation.

The comparison of the computed aerodynamic lift coefficients and pressure distributions with the experiment is a matter of the validation process for the numerical method. Figure 12 illustrates the lift coefficients over the angle of attack for the baseline flow and for the best experimentally found actuated setup. The pulsed blowing is an unsteady phenomenon but, as before, the results are time-averaged. Despite particular differences, the aerodynamic behavior observed during the wind tunnel tests could be numerically restituted the lift increments by AFC for the linear lift regime are of the order of $\Delta C_L \approx 0.5$ and the effect on maximum lift is reproduced as well. The increased wing loading promotes a decrease in the measured maximum angle attack by a favorable AFC flap application that is correctly simulated. Figure 13 shows the sectional time-averaged pressure distribution, with and

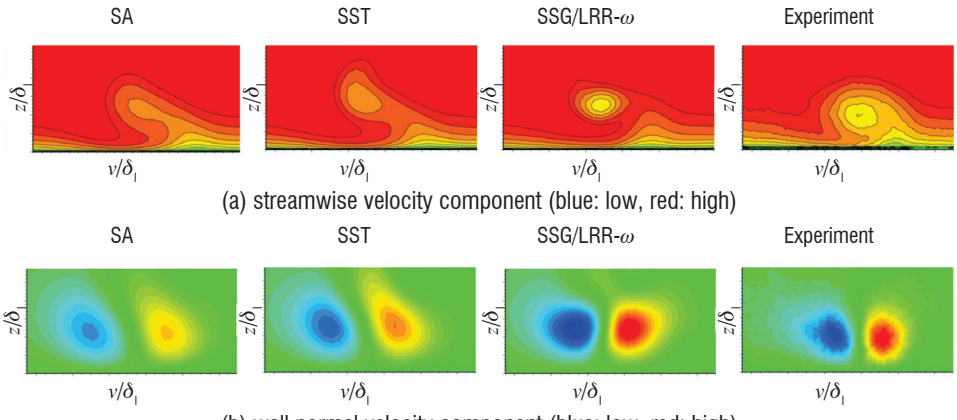

Figure 8 Numerical simulation with two eddy viscosity turbulence models and a Reynolds Stress model for the validation of constant blowing actuation through holes on a zero-pressure gradient flat plate at $2.4 \times \delta_l$ downstream the actuator, according to [11]

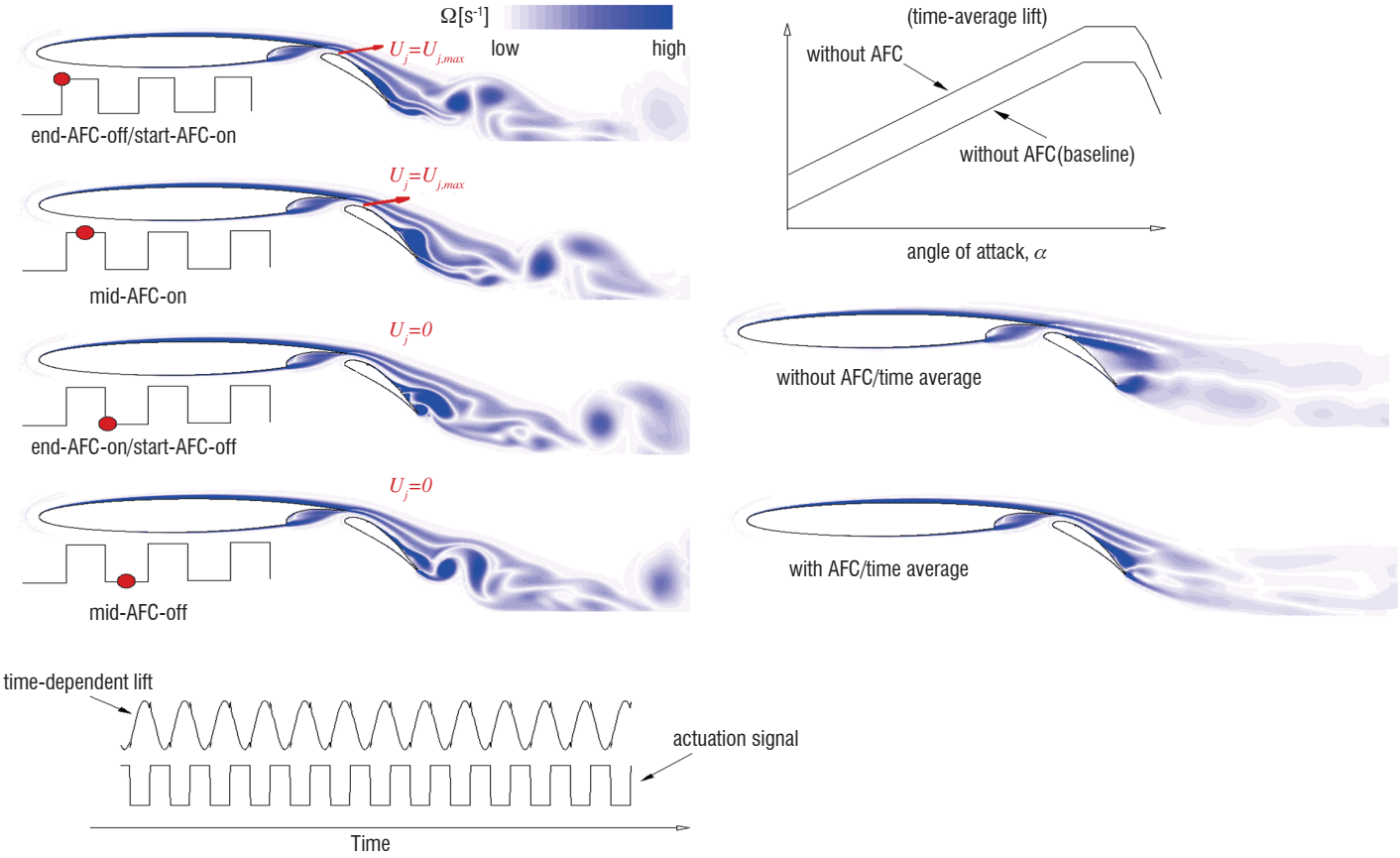

Figure 10 - Schematic view of aerodynamic changes for global and local quantities due to the time-depent pulsed blowing actuation, where the effects over one actuation cycle are shown with computed vorticity flowfields

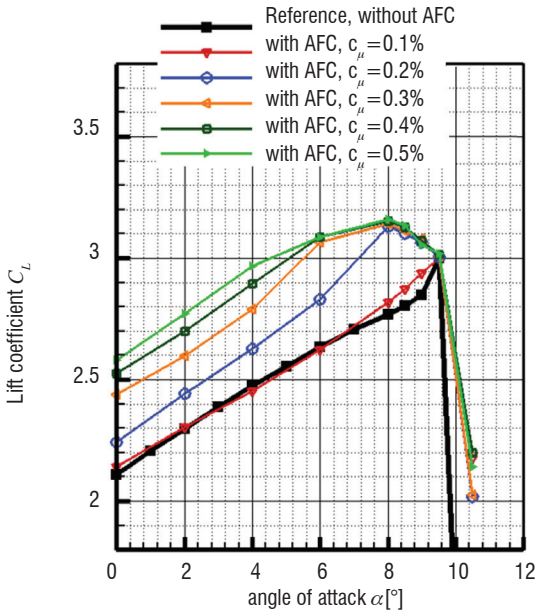

Figure 11 - Lift coefficient over the angle of attack for the DLR-F15 airfoil from URANS simulations, with and without AFC, according to [13]; configuration: 2eOpt49; inflow conditions: $M=0.15$, $Re=2 \times 10^6$

without AFC. The flow separation above the flap is evident in the baseline pressure plateau for the flap upper side, according to the black symbols and lines. This flow separation is considerably reduced as the actuation is switched on and the flap pressure indicates a higher suction peak. The increased flap circulation induces an increase in the wing trailing edge velocity, with a lower local static pressure and an overall wing circulation enhancement. With the unsteady RANS method, the time-averaged effects are accurately simulated in comparison with the wind tunnel test.

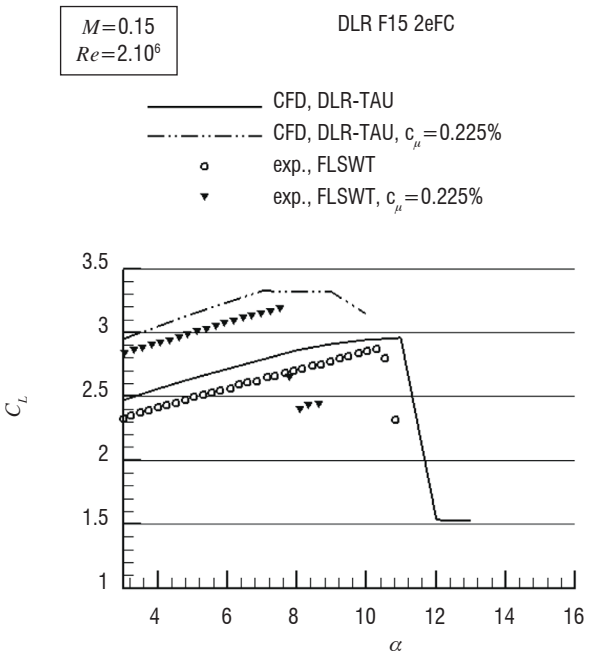

Figure 12 - Computed time-averaged lift over the angle of attack by URANS simulations in comparison with windtunnel measurements for the DLR-F15 airfoil, with and without flow control

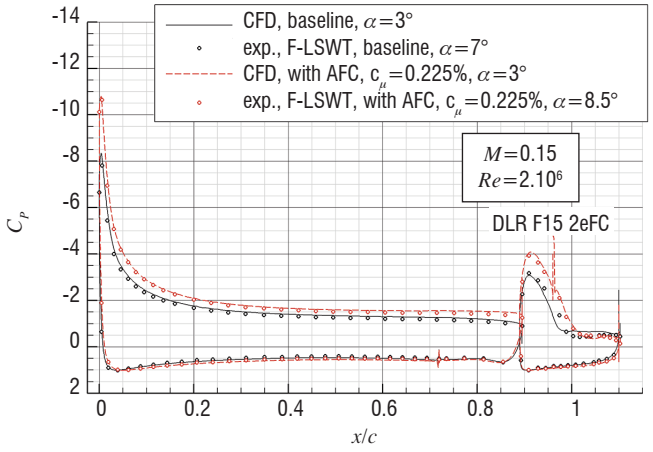

Figure 13 - Computed time-averaged pressure distributions by URANS simulations, in comparison with windtunnel measurements for the DLR-F15 airfoil, with and without flow control; configuration: 2eFC; inflow conditions: M=0.15, Re=2 x 10^6

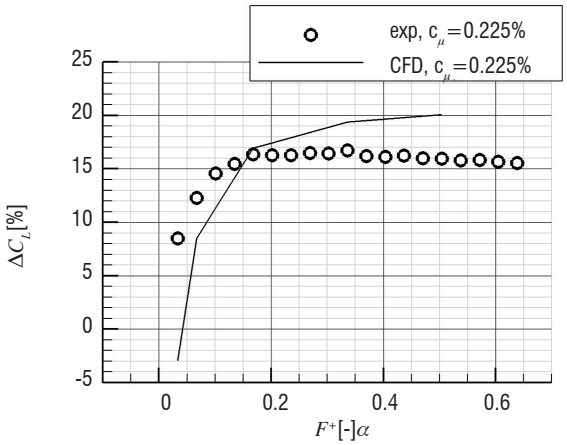

Figure 14 - Computed time-averaged lift over the actuation frequency by URANS simulations, in comparison with windtunnel measurements for the DLR-F15 airfoil with flow control at moderate blowing momentum coefficient; configuration: 2eFC; inflow conditions: M=0.15, Re=2 x 10^6

Early wind tunnel tests have shown that an actuation frequency of the order of hundreds of Hertz is sufficient for significant lift improvements. The variation in time of the actuation frequency, between 0…300 Hz, which corresponds to the non-dimensional actuation frequency F^+, of the order of 0…1, usually points out two major effects that are illustrated in figure 14. At low actuation frequency, the lift increments are low, but increase rapidly with the increase in frequency until $F^+ \approx 0.2$. At higher actuation frequencies, the lift remains mostly independent of this flow control parameter. This particular flow control effect is mostly accurately simulated with the numerical method. In addition, according to the simulations, the shedding frequency of the baseline flow separation above the flap is of about 0.4 (not shown here). These results agree with early experimental findings, for example Seifert et al. [34] and Greenblatt and Wygnanski [2], which reported a successful application for modern flow control at a frequency of the same order as the natural shedding frequency.

The pulsed blowing through slots using a square shape actuation signal was implemented and simulated for a wing body configuration representative to a narrow-body short range aircraft (see figure 15). The scope was to verify the capability of this flow control technology for application on a real aircraft configuration and to validate the numerical method with the experiment [35]. The aim of using AFC was to suppress the local flap separation for deflection angles at which the flow without control cannot follow the flap contour. Figure 15 shows an overview from the simulations with and without control. The lower side of the image illustrates the complexity of such a simulation, by integrating the slot-actuator and performing the unsteady simulations. The flow topology for the baseline flow is shown in the upper left picture, where on the right side the results are presented for the same inflow conditions but with active flow control. The shaded time-averaged streamwise velocity iso-surfaces located above the flap indicate the size and location of local flow recirculation regions. It is obvious that, from left to right, the flow situation was improved and only spare local flow separations remain visible, which are actually downstream the non-actuated flap portions. The static surface pressure decreases for wing and flap upper sides with the actuation switched on and this corresponds to an increased lift with about $\Delta C_L \approx 0.4$. Because the used blowing momentum coefficient remains moderate, $c_\mu \approx 0.4\%$, one can notice the success of the application for separation control on a real aircraft configuration. Nevertheless, the fact that there is to date no flight test in preparation for this technology shows that many questions concerning the actuation systems and structural integrity still need to be clarified.

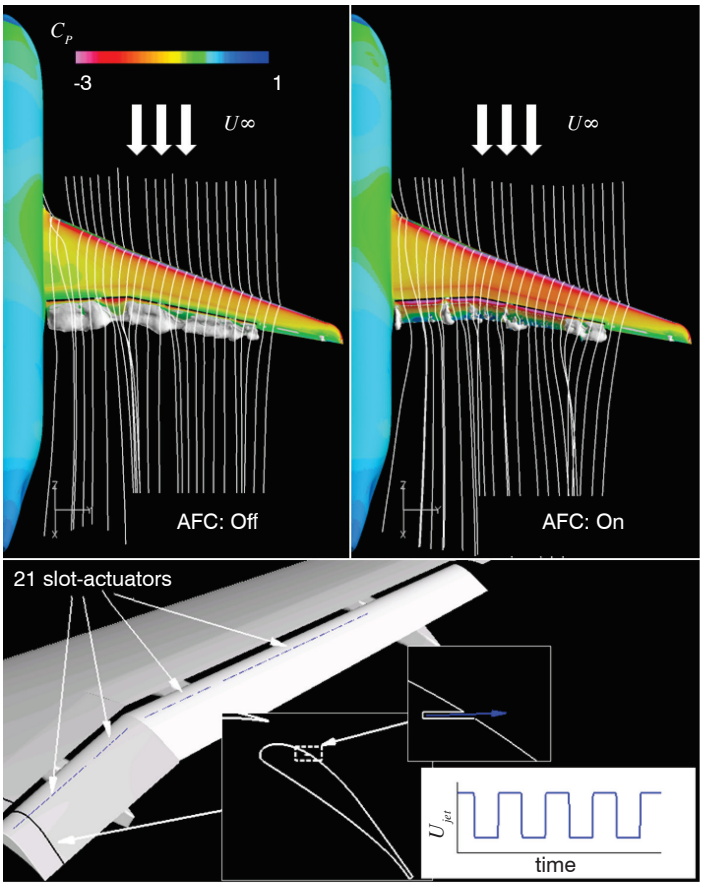

Figure 15 - Overview of numerical results for a high-lift wing body configuration with pulsed blowing separtion control

Pulsed blowing through slots proved over the last years to perform well experimentally and numerically. Therefore, there have been questions on how to obtain further improvements. E.g., Hoell et al. [36] were concerned with a distributed actuation in order to find the most appropriate spacing based on CFD for energy efficient actuation. One of the latest reported experimental results in the literature, by Haucke and Nitsche, also concerns multiple and distributed actuation [37]. Nevertheless, an open subject remains for the baseline flow, the configuration that is to be controlled and the past applications have

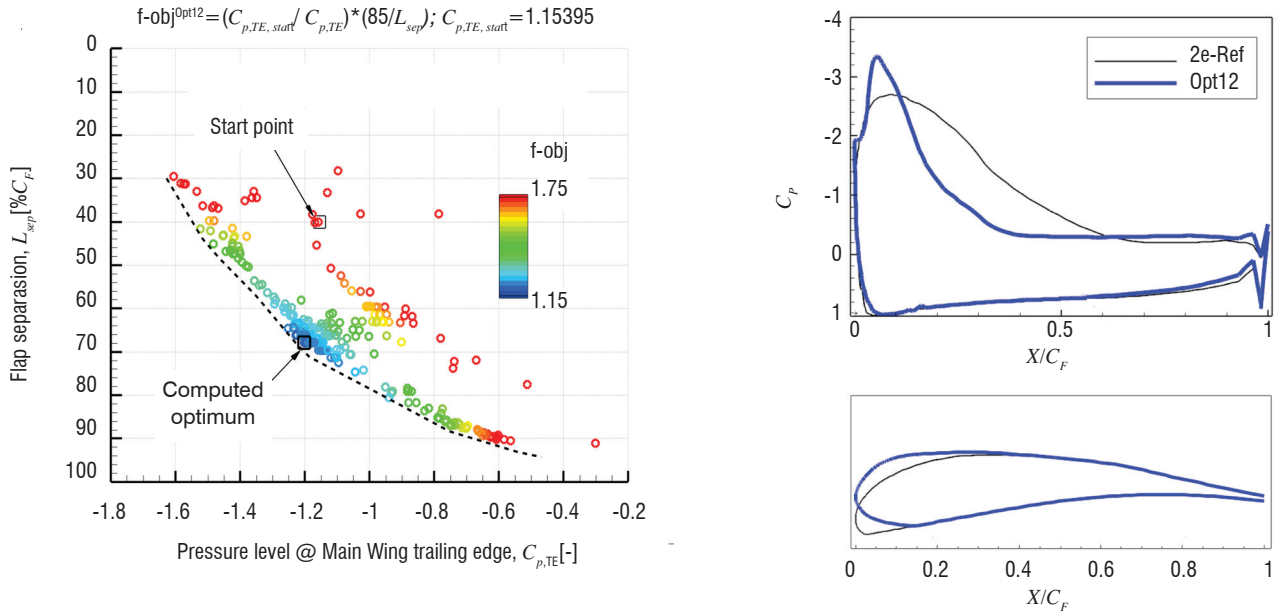

Figure 16 - Results of flap shape optimization for flow control application: pareto-front diagram (left) and corresponding shape and pressure distribution of the baseline flow from start point and optimized shape (right)

been a retrofit flap shape in most of the cases. A higher potential for flow control is expected for a dedicated flap designed for the modern flow control application. Figure 16 illustrates the results of a unique effort to optimize the flap contour through a numerical method, in the search for a better receptivity for the flow control application. The objective for the numerical algorithm was to minimize a function, which corresponds to the increase of flap separation, while decreasing the wing upper trailing edge static pressure. The Pareto front is illustrated in the left-image and it indicates the optimum for a 70%c_F separated flap flow and with a moderately increased flap suction peak. The nose-up movement for the flap with more flattened upper side for this optimized shape can be seen in the right-image. The resulting pressure distributions are plotted in the upper part of this graph. The application of AFC on this flap was consequently studied numerically (not shown). The results revealed that the new flap is more effective than the best found retrofit at low blowing momentum coefficients, but delivers similar lift enhancement at moderate and high actuation intensity. Additionally, the reduced flap deflection of the optimized flap allows for a significant reduction in drag where the lift remains mostly retained, which was not possible with a retrofit shape. Nevertheless, the benefits of this optimized flap shape were proven over the complete airfoil polar. This is considered to be a small example of what could be the future of high-lift system design, taking into account the potential benefits offered by modern flow control.

Conclusions and prospects

This overview highlights some important aspects for high-lift modern flow control that have been recently investigated at DLR. It shows experimental and numerical results for two control technologies, namely pulsed blowing by skewed round jet actuators for leading edge stall delay and by slot-actuators for flap trailing edge separation control. These technologies have matured over the last decade, concerning the evaluation of the aerodynamic performance. Most of the studies concern the implementation, on a state-of–the-art supercritical high-lift airfoil, up to flight relevant inflow conditions. One major objective was to recover the maximum lift loss due to the slat retraction, by using active flow control. It was shown that the combined actuation systems can support significant lift increments at moderate, as well as for high, Reynolds number flows. The numerical method based on the Navier-Stokes equations was validated with wind tunnel experiments and a first complex study of high-lift wing body configuration with flow control was successfully conducted.

The flow control technologies by pulsed blowing showed significant potential for flight relevant separation control. However, further efforts are needed, especially for system design and integration, as well as for the optimization of energetic requirements prior to use on future transport aircraft ■

Acknowledgements

The authors would like to acknowledge the contributions of the Technical Universities of Berlin and Braunschweig for the achievement of these results. Thus, we would like to thank Marcus Casper, Frank Haucke, Philipp Hühne and Peter Scholz for their efforts in performing the common wind tunnel testing at DNW facilities. Moreover, the experimental work and part of the numerical studies have been conducted within the framework of the German national project LuFo IV M-Fly (Luftfahrtforschungsprogramm IV, Multidisziplinäre flugphysikalische Optimierung) and the support of BMWi is acknowledged herewith. Some of the computational work was performed within the scope of European projects and the financial support from the Seventh Framework Programme of the European Community (Clean Sky Joint Technology and AVERT) is also acknowledged.

References

[1] M. GAD-EL HAK - *Flow Control: Passive, Active, Reactive Flow Management*. Cambridge Univ. Press, New York, 2000.
[2] D. GREENBLATT, I. WYGNANSKI - *The Control of Flow Separation by Periodic Excitation.* Progress in Aerospace Sciences, Vol. 36, No. 7, pp. 487–545, 2000.
[3] J.D. MCLEAN, J.D. CROUCH, R.C. STONER, S. SAKURAI, G.E. SEIDEL, W.M. FEIFEL, H.M. RUSH - *Study of the Application of Separation Control by Unsteady Excitation to Civil Transport Aircraft*. NASA Technical Report CR 209338, 1999.
[4] R. JOSLIN, D. MILLER - *Fundamentals and Applications of Modern Flow Control*. Progress in Astronautics and Aeronautics, Vol. 231, AIAA, Inc., Reston, Virginia, 2009.
[5] P.K.C. RUDOLPH - *High-Lift Systems on Commercial Subsonic Airliners*. NASA Technical Report CR 4746, 1996.
[6] F. TINAPP, W. NITSCHE - *Separation Control on a High-Lift Configuration by Periodic Excitation.* New Results in Numerical and Experimental Fluid Mechanics III, Vol. 77, Springer-Verlag, Heidelberg, 2002.
[7] R. PETZ, W. NITSCHE - *Active Separation Control on the Flap of a Two-Dimensional Generic High-Lift Configuration*. Journal of Aircraft, Vol. 44, No. 3, pp. 865–874, 2007.
[8] R. BECKER, R. KING, R. PETZ, W. NITSCHE - *Adaptive Closed-Loop Separation Control on a High-Lift Configuration Using Extremum Seeking*. Journal of Aircraft, Vol. 44, No. 3, pp. 865–874, 2007.
[9] J. ORTMANNS, C.J. KÄHLER - *Investigations of Pulsed Actuators for Active Flow Control Using Phased Locked Stereoscopic Particle Image Velocimetry*. Presented at the 12th. Intl. Symposium for Application of Laser Techniques to Fluid Mechanics, Lisbon, Portugal, 12-15 June, 2004.
[10] P. SCHOLZ, J. ORTMANNS, C.J. KÄHLER, R. RADESPIEL - *Leading Edge Separation Control by Means of Pulsed Jet Actuators.* AIAA-Paper 2006-2850, 2006.
[11] V. TOGITI, V. CIOBACA, B. EISFELD, T. KNOPP - *Numerical Simulation of Steady Blowing Active Flow Control Using a Differential Reynolds Stress Model*. In Proceedings of CEAS/KATnet II Conference on Key Aerodynamics Technologies, Bremen, Germany, 2009.
[12] V. CIOBACA - *Simulation of Active Flow Control on the Flap of a 2D High-Lift Configuration.* Notes on Numerical Fluid Mechanics and Multidisciplinary Design, Vol. 112, Springer–Verlag, Berlin, pp. 209–216, 2010.
[13] V. CIOBACA - *Parameter Study for a Slatless 2D High-Lift Airfoil with Active Separation Control using a URANS Approach*. Notes on Numerical Fluid Mechanics and Multidisciplinary Design, Springer– Verlag, Vol. 121, pp. 135-142, Berlin, 2013.
[14] G. DARGEL, H. HANSEN, J. WILD, T. STREIT, H. ROSEMANN, K. RICHTER - *Aerodynamische Flügelauslegung mit multifunktionalen Steuerflächen*. DGLR, Bonn [Hrsg.]: DGLR Jahrbuch 2002, DGLR-2002-096, Vol. I, pp. 1605, 2002.
[15] J. WILD, G. WICHMANN, F. HAUCKE, I. PELTZER, P. SCHOLZ - *Large Scale Separation Flow Control Experiments within the German Flow Control Network*. AIAA Paper 2009-530, 2009.
[16] J. WILD - *Experimental Investigations of Mach- and Reynolds-Number Dependencies of the Stall Behavior of 2-Element and 3-Element High-Lift Wing Sections*. AIAA Paper 2012-108, 2012.
[17] P. SCHOLZ, C.J. KÄHLER, R. RADESPIEL, J. WILD, G. WICHMANN - *Active Control of Leading-Edge Separation within the German Flow Control Network*. AIAA Paper 2009-0529, 2009.
[18] C.P. HÜHNE, P. SCHOLZ, R. RADESPIEL, J. WILD, V. CIOBACA - *Active Control of Leading Edge Flow Separation for a Swept High-Lift Airfoil.* In Proceedings of 61 Deutscher Luft- und Raumfahrtkongress, Berlin 10-12 September, 2012.
[19] F. HAUCKE, M. BAUER, T. GRUND, W. NITSCHE, B. GÖLLING - *An Active Flow Control Strategy for High-Lift Flaps.* KATnet II. In Proceedings of CEAS/KATnet II Conference on Key Aerodynamics Technologies, Bremen, Germany, 2009.
[20] P. POISSON-QUINTON - *Recherches théoriques et expérimentales sur le contrôle de couche limite*. 7th Congress of Applied Mechanics, London, September 1948.
[21] R.J. ENGLER - *Two-Dimensional Subsonic Wind Tunnel Investigations of a Cambered 30 Percent Thick Circulation Control Airfoil*. AD913411 Report, 1972.
[22] M. CASPER, P. SCHOLZ, R. RADESPIEL, J. WILD, V. CIOBACA - *Separation Control on a High-Lift Airfoil Using Vortex Generator Jets at High Reynolds Numbers*. AIAA Paper 2011-3442, 2011.
[23] F. HAUCKE, W. NITSCHE - *Active Separation Control on a 2D High-Lift Wing Section towards High Reynolds Number Application*. To be published at 31st AIAA Applied Aerodynamics Conference, San Diego, CA, 2013.
[24] Clean Sky European Project, URL, http://www.cleansky.eu/
[25] M. MEUNIER - *Simulation and Optimization of Flow Control Strategies for Novel High-Lift Configurations*. AIAA Journal, 47(5):1145–1157, 2009.
[26] J. DANDOIS, E. GARNIER, P. SAGAUT - *Unsteady Simulation of a Synthetic Jet in a Crossflow.* AIAA Journal, 44(2):225–238, 2006.
[27] S.G. ANDERS, W-L. SELLERS III, A.E. WASHBURN - *Active Flow Control Activities at NASA Langley.* AIAA Paper 2004-2623, 2004.
[28] A. SHMILOVICH, Y. YADLIN - *Flow Control Techniques for Transport Aircraft*. Journal of Aircraft, 49(3):489–502, 2011.
[29] F. VON STILLFRIED, S. WALLIN, A.V. JOHANSSON - *Vortex-Generator Models for Zero- and Adverse-Pressure-Gradient Flows.* AIAA Journal, 4(50): 855-866, 2012.

[30] T. GERHOLD - *Overview of the Hybrid RANS Code TAU. MEGAFLOW* . Numerical Flow Simulation for Aircraft Design, Vol. 89 of Notes on Numerical Fluid Mechanics and Multidisciplinary Design, Springer, pp. 81-92, 2005.
[31] O. BRODERSEN, M. HEPPERLE, A. RONZHEIMER, C.-C. ROSSOW, B. SCHÖNING - *The Parametric Grid Generation System MegaCads.* In Proceedings of the 5th Intern. Conf. On Numerical Grid Generation in Comp. Field Simulation, National Science Foundation (NSF), pp. 353-362, 1996. http://www.megacads.dlr.de.
[32] J. WILD - *Smooth Mixed Meshes for Acceleration of RANS CFD in Aircraft Analysis and Design.* AIAA Paper 2011-1267, 2011.
[33] Centaursoft, https://www.centaursoft.com (accessed 2012)
[34] A. SEIFERT, A. DARABI AND I. WYGNANSKI - *Delay of Airfoil Stall by Periodic Excitation.* Journal of Aircraft, 33(4):691–698, 1996.
[35] V. CIOBACA, T. KÜHN, R. RUDNIK, M. BAUER, B. GÖLLING, W. BREITENSTEIN - *Active Flow Separation Control on a High-Lift Wing-Body Configuration.* Journal of Aircraft, 50(1):56-72,2013.
[36] T. HOELL, E. WASSEN, F. THIELE - *Numerical Investigation of Spatially Distributed Actuation on a Threee-Element High-Lift Configuration.* In R. King, editor, Active Flow Control II - NNFM 108, Notes on Numerical Fluid Mechanics and Multidisciplinary Design, pages 109–123. Springer, 2010.
[37] F. HAUCKE, W. NITSCHE - *Active Flow Control on the Flap of a 2D High-Lift Wing Section at Re=1·10⁶*. AIAA-Paper 2011-3359, 2011.

Acronyms

AFC	(Active Flow Control)
DLR	(Deutsches Zentrum für Luft- und Raumfahrt) (German Aerospace Center)
DLR F15	(DLR Forschungskonfiguration Nr. 15) (DLR research configuration No. 15)
CFD	(Computational Fluid Dynamics)
DNW	(Deutsch-Niederländische Windkanäle) (German Dutch Wind Tunnels)
NWB	(Niedergeschwindigkeits-Windkanal Braunschweig) (Low Speed Wind Tunnel Braunschweig)
KKK	(Kryo Kanal Köln) (Cryogenic Windtunnel Cologne)
ProHMS	(Prozesskette Hochauftrieb mit multifunktionalen Steuerflächen (process chain for high-lift applying multi-functional control surfaces)
LE	(Leading Edge)
TE	(Trailing Edge)
TUB	(Technische Universität Berlin)
TUBS	(Technische Universität Braunschweig)

AUTHORS

Vlad Ciobaca received his diploma in 2005 from the University Politehnica Bucharest, Faculty of Aerospace Engineering and he has been a PhD candidate (TU Berlin) since 2011. He is a Research Scientist within the DLR Institute of Aerodynamics and Flow Technology, Transport Aircraft Department and High-Lift Group. His field of research is High-Lift Aerodynamics, with a focus on Flow Control, including Mesh Generation, Numerical Simulations and Experimental Aerodynamics, and Wind Tunnel Simulations.

Jochen Wild received his diploma from TH Darmstadt in 1995, and his PhD from TU Braunschweig in 2001 on “Numerical Optimization of High-Lift Airfoils by solution of RANS equations (transl.)”. He is a “High-Lift” Research Scientist and Team Leader within DLR Institute of Aerodynamics and Flow Technology, Transport Aircraft Department. His field of research is High-Lift Aerodynamics, including Numerical Simulation and Design Optimization, Mesh Generation, Experimental Aerodynamics and Flow Control.